Multiwavelength Characterization of the Brown Dwarf Auroral Phenomenon - Establishing the Nature of the Electrodynamic Engine

Thesis by
John Sebastian Pineda

In Partial Fulfillment of the Requirements for the
degree of
Doctor of Philosophy

CALIFORNIA INSTITUTE OF TECHNOLOGY
Pasadena, California

2017
Defended September 14, 2016

John Sebastian Pineda
ORCID: 0000-0002-4489-0135

ACKNOWLEDGEMENTS

This thesis represents the culmination of many, many years of work, not just the past six years as a graduate student at Caltech, but all of my efforts ever since I embarked on this continual journey to learn about and understand nature, and the universe around us. I have been blessed to be able to undertake this endeavor and could not have gotten here as a mathematician, physicist and astronomer without the constant love and support of my friends and family over the years.

First and foremost, I thank my mother, Norelia Garcia, for instilling in me a strong work ethic, believing in me through everything, and encouraging me to pursue my goals. She pushed me to excel and I would not be the person that I am without her influence in my life. Thank you, Gus Horwith and Jamie Rennar for being my steadfast friends and companions, taking me in and making me feel like family. Thank you, Dr. Swickard, your dedication and unwavering support bolstered my drive to always keep learning.

I thank my friends and housemates at MIT for their interesting discussions, late night revelry and general silliness. Derreck Barber, Martyna Józwiak, Naomi Stein, Stephanie Cheng, Sara Dahan, Jessie Mueller, Michelle Bentivegna, Julia Moffett, Jennifer De Bruijn, and Vazrik Chiloyan, I could not have asked for a more compassionate and supportive community with which to tackle the challenges of undergraduate life at MIT.

Everyone knows that Caltech can be a difficult place to pursue a PhD, but I was fortunate to be surrounded by a caring and tight-knit community of astronomy graduate students. I want to point out my classmates in particular, Sirio Belli, Michael Bottom and Jackie Villadsen; together we made it through all the problem sets, late nights, exams, and general scientific and philosophical inquiries that one encounters in graduate school. My group mates, Kunal Mooley, Marin Anderson, Michael Eastwood, Ryan Monroe, Melodie Kao, and Jackie Villadsen, have been instrumental throughout grad school, making sure I didn't take things too seriously, providing thoughtful feedback and giving me a different perspective on things as we slogged through our research, plus making sure I took plenty of breaks. I must also thank Jackie in particular, as my officemate throughout our time at Caltech, partner in crime, sounding board for both research and life, and general wonderful human being. I have learned a great deal from our interactions and I'm positive my Caltech

experience would not have been nearly as rich without her presence.

Now this brings me to my advisor, Gregg Hallinan. It has been a long but short three years of research. I am indebted to him for taking me in as his student and pointing me toward a particularly interesting set of research projects. I have learned a lot, as this thesis can attest, but more than our scientific achievements, I want to thank him for continually putting his students first and making a concerted effort to provide for our scientific and career development. We are all a little bit different but we have managed to thrive thanks to his attention to our differences and concern for our well being. I thank my committee members, Chuck Steidel, Davy Kirkpatrick, Heather Knutson, and Sterl Phinney, for there consideration and thoughtful feedback throughout my dissertation.

I also want to thank Katherine Saad, for everything she has done for me these last couple of years. Always supportive and considerate, encouraging me when I falter and bringing out the best in me, I cannot imagine getting through my PhD without her.

Framed copy of JPL Travel Poster to Jupiter, signed by everyone.

ABSTRACT

Stellar coronal activity has been shown to persist into the low-mass star regime, down to late M-dwarf spectral types. However, there is now an accumulation of evidence suggesting that at the end of the main sequence there is a transition in the nature of the magnetic activity from chromospheric and coronal to planet-like and auroral, from local impulsive heating via flares and MHD wave dissipation to energy dissipation from strong large-scale magnetospheric current systems. In this dissertation, I examine the effects of these processes on the atmospheres of brown dwarfs across multiple different wavebands and investigate the underlying mechanisms powering the electrodynamic engine responsible for auroral emission in brown dwarfs. I conduct observational surveys looking for the emission features of Hα and H_3^+ as indicative of auroral systems across the ultracool dwarf regime. I further provide a comprehensive view of brown dwarf magnetic activity and auroral phenomena, detailing the various emission processes, and expectations for auroral brown dwarfs. I also initiate a preliminary analysis of the detailed emission features and discuss the constraints imposed on the electrodynamic engine of these objects.

PUBLISHED CONTENT AND CONTRIBUTIONS

Pineda, J. S., M. Bottom, and J. A. Johnson. 2013. "Using High-resolution Optical Spectra to Measure Intrinsic Properties of Low-mass Stars: New Properties for KOI-314 and GJ 3470." *ApJ* 767, 28 (April): 28.

J.S.P was the lead author, who in collaboration with Michael Bottom developed the spectroscopic templates used in the study, while John Johnson provided the data. I wrote the article and did the entire rest of the analysis. doi:10.1088/0004-637X/767/1/28. arXiv: 1302.6231 [astro-ph.SR].

Pineda, J. S., G. Hallinan, J. D. Kirkpatrick, G. Cotter, M. M. Kao, and K. Mooley. 2016. "A Survey for Hα Emission from Late L Dwarfs and T Dwarfs." *ApJ* 826, 73 (July): 73.

J.S.P conducted the observational survey, reduced the data, analyzed the results and wrote the paper. The various co-authors helped with data acquisition, target selection and/or data reduction. doi:10.3847/0004-637X/826/1/73. arXiv: 1604.03941 [astro-ph.SR].

TABLE OF CONTENTS

LIST OF ILLUSTRATIONS

LIST OF TABLES

"...imitating in this the Astronomers, who, although their assumptions are almost all false or uncertain, nevertheless, because these assumptions refer to different observations which they have made, never cease to draw many very true and well-assured conclusions from them. "

René Descartes

Optics

First Discourse

1637

Translated by Olscamp, P. J.

"Astronomers, like other men, spend most of their lives in hard and often tedious work. They are, however, sometimes fortunate enough to take part in a great adventure, and it is of such an adventure that I am now writing."

George Ellery Hale

Building the 200-Inch Telescope

1929

Chapter 1

INTRODUCTION

Many people interpret the field of astrophysics to be defined as the study of astronomical objects to uncover the principles of fundamental physics. Although this definition captures the aims of many scientists studying, for example, neutron stars, black holes, dark matter, or dark energy, it fails to encompass a large swath of astrophysicists and the astronomical community as a whole. Instead, many astrophysicists can be described as using our understanding of physics to illuminate the processes governing the nature of astronomical objects. The methods include both observation and theory, but either way, at its core, the process seeks to uncover the physical truths of nature. In this dissertation, I cast the focus of our scientific enterprise on the nature of brown dwarf magnetic phenomena.

However, before delving into that topic, I must address the question: what is a brown dwarf? Brown dwarfs were theorized as stellar bodies incapable of sustained hydrogen fusion in their cores (Kumar 1963b, 1963a). They formed from the direct collapse of molecular clouds, the same way stars do, as the low-mass end of the initial mass function, with masses $\lesssim$0.08 $M_\odot$ (e.g., Stevenson 1991; Burrows et al. 1993, 2001). The first confirmed brown dwarfs were discovered in 1995, separately by Rebolo, Zapatero Osorio, and Martín (1995) and Nakajima et al. (1995). Rebolo, Zapatero Osorio, and Martín (1995) located a brown dwarf in the Pleiades star cluster and inferred a mass below the hydrogen burning limit, however despite the low luminosity, the spectroscopic features still resembled those of low-mass stars. The observations by Nakajima et al. (1995), discovered a companion to the low-mass star GL229, and demonstrated the existence of astrophysical objects, in the field, down to effective temperatures as cool as ~1000 K with a mass ~50 M_{Jup}. Follow-up observations of this target confirmed dramatically different spectroscopic features and heralded the detailed study of brown dwarfs as interesting astrophysical objects e.g., Geballe et al. 1996; Allard et al. 1997. Thus, also began the dedicated hunt for more sub-stellar objects and the search to fill in the observational gap between low-mass stars and the 'methane' dwarf GL229B.

Since these initial detections more and more sub-stellar objects have been discovered, aided by all sky surveys in the infrared, like the Two Micron All Sky Survey

(2MASS; Cutri 2003). Using the infrared photometry and knowledge of the very red spectral energy distributions of the sub-stellar objects, brown dwarf candidates can be identified and vetted spectroscopically. Furthermore, a spectroscopic sample of these objects allowed Kirkpatrick et al. (1999) to define distinguishing features in their spectra that separate these objects from low-mass stars. The absence of significant TiO and VO in the optical spectra and the strengthening of alkali metal absorption, from Na I and K I, became the defining features of the 'L' spectral type on the traditional MK stellar classification system (Kirkpatrick et al. 1999; Kirkpatrick 2005). Similarly, the methane features seen in the spectrum of GL229B became the defining feature of the 'T' spectral type (Kirkpatrick et al. 1999; Kirkpatrick 2005). Since then, observations have refined these classifications further and pushed to lower and lower temperature objects, including the recent discovery of 'Y' dwarfs, distinguished by their prominent NH_3 and H_2O features (Cushing et al. 2011; Kirkpatrick et al. 2012). This brings the full stellar classification system to OBAFGKMLTY in order of hottest to coldest, reflecting the spectroscopic signatures and the effective temperature of the atmospheres.

The study of brown dwarfs has thus been a natural extension of stellar astrophysics into sub-stellar astrophysics, with many scientists viewing the data with this perspective. However, the properties of brown dwarfs extend from the stellar regime at the boundary at which objects sustain hydrogen fusion in their cores, $M \sim 80$ M_{Jup}, down to the boundary at which objects are capable of sustaining deuterium fusion in their cores, $M \sim 13$ M_{Jup} (Burrows et al. 2001). Moreover, the observable properties of brown dwarfs often overlap between stars on one end of the mass scale and planets on the other. For example, high mass brown dwarfs show effective temperatures that overlap with the lowest mass stars, brown dwarf radii are often similar to Jupiter and cool brown dwarfs have temperatures consistent with what is seen on young gas giant planets and hot jupiters (Burrows et al. 2001). Without knowing the mass, the age and luminosity of these systems are required to differentiate between stars and brown dwarfs. For the coolest brown dwarfs, it is the formation mechanism that distinguished them from the largest planets, whether the object formed through gravitational collapse, like stars and brown dwarfs form, or through core-accretion, like planets (Chabrier and Baraffe 2000). Regardless of these distinctions, the physical properties of brown dwarfs overlap with both star and planet regimes and thus their study requires a distinct approach that takes into account the full set of processes that can take place between planets and stars. This feature has made the study of brown dwarfs a dynamic and rich field, encompassing

the various challenges presented by these objects, including cloud dynamics, dust condensation, extensive molecular and ionic chemical networks, plasma physics, and non-ideal magnetohydrodynamics (MHD).

One interesting feature that has gained recent attention is their magnetic activity, the properties and emission related to the presence of magnetic fields on these objects. Viewed predominantly from the perspective of stellar activity, many puzzles have emerged in understanding the brown dwarf observations (see Chapter 2). However, the perspective of planetary phenomena, specifically auroral emissions, can provide new insight.

In this introduction, I will discuss the development of our understanding of stellar magnetic activity and contrast that with what we know about auroral phenomena to set the stage for delving into brown dwarf magnetism spanning the divide between stars and planets. In Chapter 2, I will survey current developments in the study of magnetic activity in very-low mass stars and brown dwarfs and how they depart from the standard paradigms established in studies of stellar activity. In Chapter 3, I describe our study of Hα emission in late L dwarfs and T dwarfs. In Chapter 4, I report on our search for auroral H_3^+ emission. In Chapter 5, I present a preliminary analysis of recent high-resolution observations investigating the detailed emission line structure of the benchmark brown dwarf LSR J1835+3259. In Chapter 6, I put together the complete multi-wavelength perspective on auroral phenomena in brown dwarf atmospheres. Lastly, in Chapter 7, I discuss the culmination of our findings and the future directions of research into the magnetic and auroral phenomena of very-low mass stars and brown dwarfs. Additionally, the appendix includes my investigation into using high-resolution optical spectra to discern the physical properties of low-mass stars.

1.1 Stellar Activity in Low-Mass Stars

To put the magnetic activity of brown dwarfs in context it is essential to discuss the current understanding of stellar activity in low-mass stars. Like much of stellar astrophysics, this begins with the Sun. Solar observations of a host of phenomena have formed the basis for interpreting observations of similar activity in other stars, especially low-mass stars (e.g., Haisch, Strong, and Rodono 1991). These processes include sunspot activity, coronal and chromospheric emission features, flares, coronal mass ejections, the solar wind, radio bursts, and the solar cycle. Despite a long history of studying the Sun, recent space-borne observatories, for example, the Solar

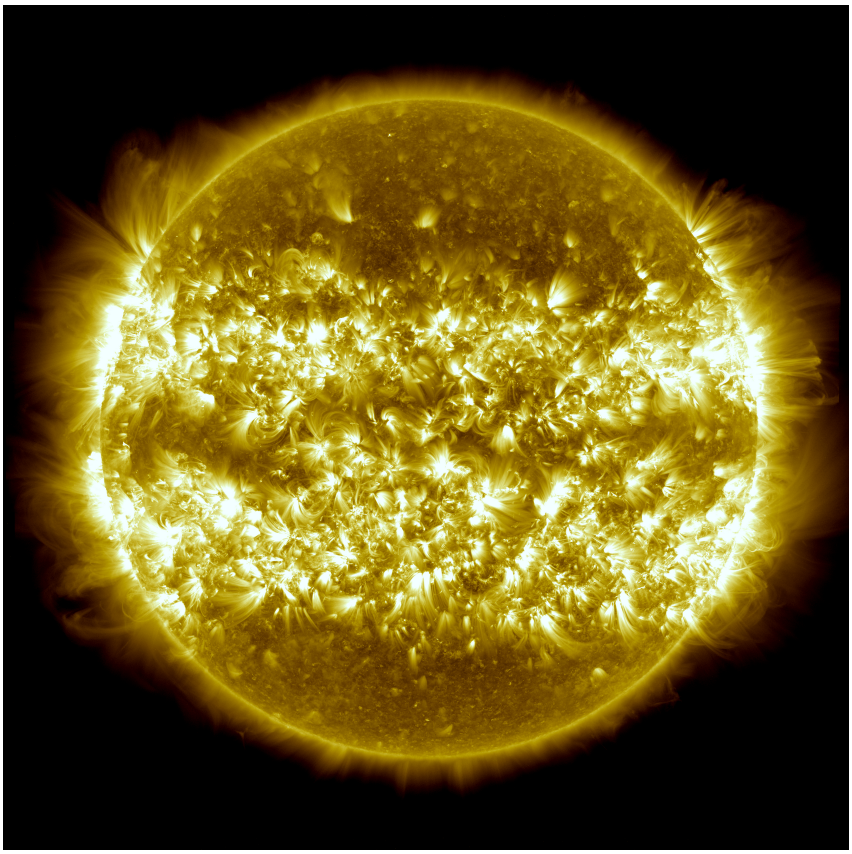

Figure 1.1: Solar Dynamics Observatory composite image of the Sun taken at 171 Å, illustrating the complex field structures above the Solar surface and the Sun's active equatorial latitudes, where the majority of sunspots emerge. The image is composed of 25 images taken from April 16, 2012, to April 15, 2013. Image courtesy of NASA/SDO and the AIA, EVE, and HMI science teams; NASA/SDO/AIA/S. Wiessinger.

and HelioSpheric Observatory and the Solar Dynamics Observatory, have greatly expanded our ability to study the Sun in depth, at high resolution, in both time and space (see Figure 1.1; e.g. Aschwanden, Poland, and Rabin 2001). Although there remain many open questions in heliophysics, a standard picture has emerged describing the Sun's magnetic phenomena (see Solanki, Inhester, and Schüssler 2006, and references therein).

The activity begins with the creation of a stable large-scale magnetic field through an internal magnetic dynamo. In the Sun, the α-Ω dynamo mechanism generates this global field through the interchange and regeneration of meridional and azimuthal field components in turbulent convective flows (Solanki, Inhester, and Schüssler 2006) . The shearing layer between the radiative core and the differentially rotating

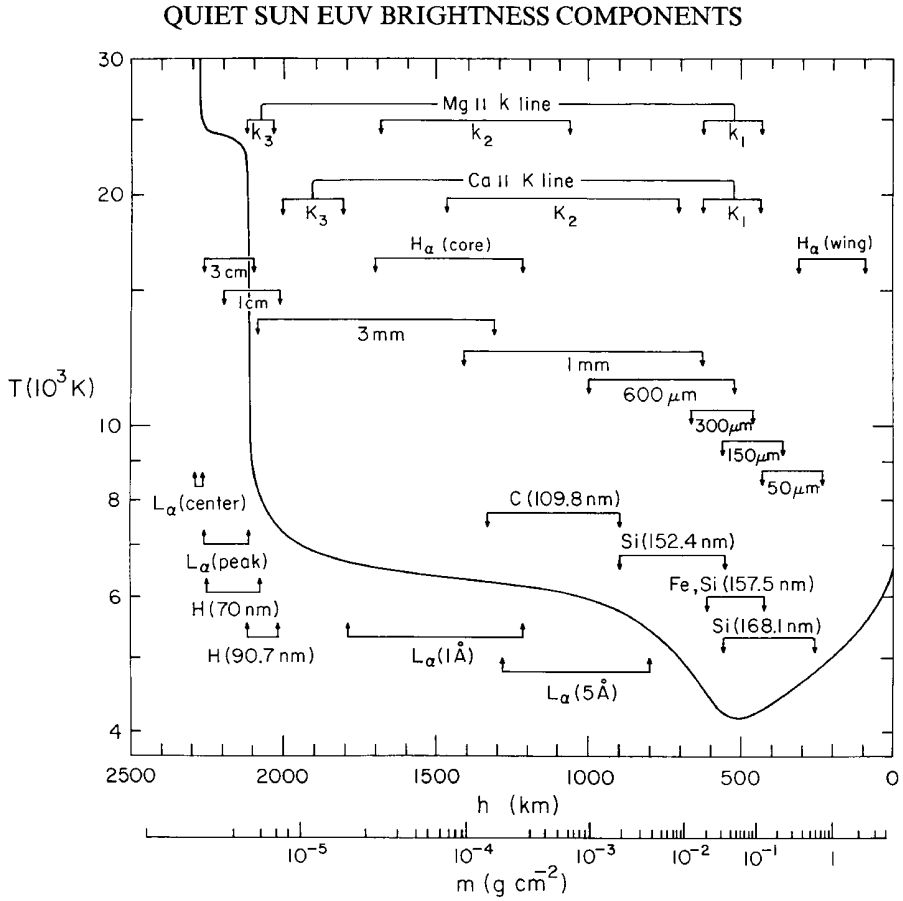

Figure 1.2: A semi-emperical model chromosphere from Vernazza, Avrett, and Loeser (1981), reproduced by permission of the AAS. This idealized model shows the location within the rising temperature profile at which many emission lines are formed, as well as regions of continua produced at long wavelengths from free-free emission (Vernazza, Avrett, and Loeser 1981). For important lines multiple locations are indicated which correspond to the core and the wings of the line (Vernazza, Avrett, and Loeser 1981).

convective exterior acts to strengthen and anchor the global magnetic field (Charbonneau 2014). This mechanism ties the interior field generation to the rotational evolution of the star. The dynamo results in a field with significant multi-polar components at the stellar surface and a large scale field capable of carrying the particle flux of the stellar wind on open field lines (Solanki, Inhester, and Schüssler 2006). The Sun also generates buoyant flux tubes deep in its interior that emerge to produce sunspots at their foot points with enhanced magnetic field strengths and depressed photospheric temperatures (e.g., Solanki, Inhester, and Schüssler 2006; J. C. Hall 2008). These magnetic loops twist and rise and can initiative impul-

sive multi-wavelength flare events when the field lines reconnect and release their energy (e.g., Solanki, Inhester, and Schüssler 2006). These impulsive events are also capable of lifting plasma up from the Sun and initiating coronal mass ejections, jettisoning large quantities of plasma from the solar surface (see Zhang and Low 2005, and references therein). The flares can generate X-ray emission, optical light, and radio bursts of multiple varieties (e.g., Bastian, Benz, and Gary 1998; Solanki, Inhester, and Schüssler 2006). In concert with MHD wave dissipation, these impulsive events also locally heat the outer atmosphere (see Aschwanden, Poland, and Rabin 2001, and references therein). This heating is sufficient to invert the atmospheric temperature-pressure profile and create the chromospheric, transition region, and coronal structures, where the temperatures rise to $\sim 10^4$ K, 10^5 K, and over $\sim 10^6$ K, respectively (e.g., Linsky 1980; Aschwanden, Poland, and Rabin 2001). The chromosphere is where low temperature magnetic emission lines are generated, such as Hα, Lyα, and the Ca II H and K lines. The tenuous plasma of the corona and transition region also emit characteristic emission lines, usually in the ultraviolet or X-ray, such as Mg II, C IV, and Fe XII (e.g., Linsky 1980; Testa, Saar, and Drake 2015). Collectively, these different properties and mechanisms define the general host of Solar activity.

Crucially, similar magnetic emissions have been detected from other stars. Of particular relevance to brown dwarf magnetism is the activity seen on low-mass stars, classified as M dwarfs, with masses $M \lesssim 0.6 M_\odot$ and effective temperatures $T_{eff} \lesssim 4000$ K. Models of stellar interiors suggests that stars down to masses of $\sim 0.35\ M_\odot$ have interiors with radiative cores and convective envelopes, like the Sun, and likely generate magnetic dynamos through the same α-Ω effect (Chabrier and Baraffe 2000; Ossendrijver 2003; Browning et al. 2006). This theory indicates that there should be a strong connection between stellar angular momentum evolution and magnetic phenomena. Indeed, observations of M-dwarf activity have revealed a significant correlation between rotation rates and tracers of magnetic activity. Younger and more rapidly rotating M dwarfs flare more frequently than similar older stars, depositing energy in their upper atmospheres at a higher rate early in their lifetimes (Hilton et al. 2010). Also, the majority of the well-studued nearby flare stars, like AD Leo, are early-to-mid M dwarfs, displaying frequent and energetic flares (Lacy, Moffett, and Evans 1976).

The connection is further observed as a strong correlation between stellar rotation/age and emission lines that trace upper atmospheric heating (e.g., Skumanich

1972). In Figure 1.2, I show a plot from Vernazza, Avrett, and Loeser (1981) illustrating the temperature profile of an active dwarf and the locations of prominent emission line formation. Emission features such as Hα, and Ca II H and K are more prevalent and stronger in faster rotating M dwarfs as compared to slower rotators (Delfosse et al. 1998; Mohanty and Basri 2003; West et al. 2008; Browning et al. 2010; West et al. 2015).

Similarly, stellar X-ray emission tracing the hot coronal gas is observed to correlate with age and rotation. Looking at a sample of dwarf stars from open clusters Pizzolato et al. (2003) demonstrated that the observed X-ray emission from *Rosat* declined with the stellar rotation period. Moreover, below a period of ~5 d for M dwarfs, the X-ray emission was at consistently high levels and declined rapidly for slower rotators (James et al. 2000; Pizzolato et al. 2003; Cook, Williams, and Berger 2014). These observations have been confirmed and extended to the UV showing that after an age of about 500 Myr the tracers of hot chromospheric and coronal gas begin to decline (Shkolnik and Barman 2014). These observations reflect a decline in the upper atmospheric heating mechanisms (flares and MHD wave dissipation) with age/rotation, likely a consequence of the influence of rotation on the magnetic dynamo and field generation.

Additionally, stellar radio emission, usually attributed to gyrosynchrotron radiation, has been shown to be closely tied to the X-ray emission (see Güdel 2002, and references therein). From F-type dwarf stars to early M-type dwarf stars, the Güdel-Benz relation demonstrates a tight empirical relation between coronal X-ray and quiescent radio emission, illustrating a deep connection between the coronal plasma producing the X-ray emission and the non-thermal energetic electrons responsible for the radio emission (Guedel and Benz 1993). This connection is underpinned by the association of the emission and heating processes with turbulent magnetic field structures and transient magnetic loops (e.g., Aschwanden, Poland, and Rabin 2001). These complex field structures are apparent in Zeeman Doppler Imaging (ZDI) reconstructions of the magnetic field, and indicate that much of the fields on early M dwarfs exhibit complicated non-axisymmetric multi-polar fields similar to what is seen on the Sun (e.g., Donati et al. 2008).

The magnetic activity also drives a strong stellar wind, which removes angular momentum from the system and increases the rotational period. This closes the feedback loop with the magnetic dynamo by which the activity influences the rotation in addition to the rotation determining the field strength and activity. Ultimately,

the star spins down and the activity declines. However, even slowly rotating early M dwarfs display UV emission features characteristic of coronal and transition region atmospheres. In far UV and near UV observations of several early M dwarfs with the *Hubble Space Telescope*, France et al. (2013) detected emission features indicating the presence of magnetically heated atmospheres, despite weak Ca II H and K emission lines and no Hα emission (see also France et al. 2016). Thus, early M dwarfs, even at field ages, are capable of sustaining significant magnetic heating.

Although the basic elements of low-mass stellar activity match what is seen on the Sun, there are significant differences in the observations that reflect the differences in M dwarfs, such as lower atmospheric temperatures and stronger magnetic field strengths, as well as different star spot distributions. Accordingly, there still remain many open questions regarding the details of M dwarf magnetic phenomena. Nevertheless, this paradigm represents the point of departure when examining the observations of magnetic emissions in brown dwarf atmospheres. Conversely, the planet-auroral perspective represents a new lens with which to understand brown dwarf magnetism.

1.2 Auroral Processes in Planetary Magnetospheres

Electrodynamic Engine

In contrast to the stellar paradigm, planetary auroral emissions are associated with large-scale current systems that pervade the extended magnetosphere, connecting the planetary atmosphere to energetic processes in the middle magnetosphere. In the Solar System, there are three main mechanisms that generate auroral currents (see Keiling et al. 2012, and references therein).

- Firstly, the interaction between the solar wind and a planetary magnetosphere triggers magnetic reconnection events that accelerate electrons along the magnetic field lines. This mechanism dominates the aurorae of the Earth and Saturn (e.g, Cowley, Bunce, and Prangé 2004). The energy dissipated is a function of the solar wind density and velocity, and the cross section of interaction with the planetary magnetosphere (Zarka 2007).

- Secondly, the relative motion of an orbiting satellite through a planet's magnetosphere creates a current system in the flux tube connecting the moon and the planet. This mechanism produces the auroral emission associated with the moons Io and Enceladus of Jupiter and Saturn, respectively (e.g., Saur

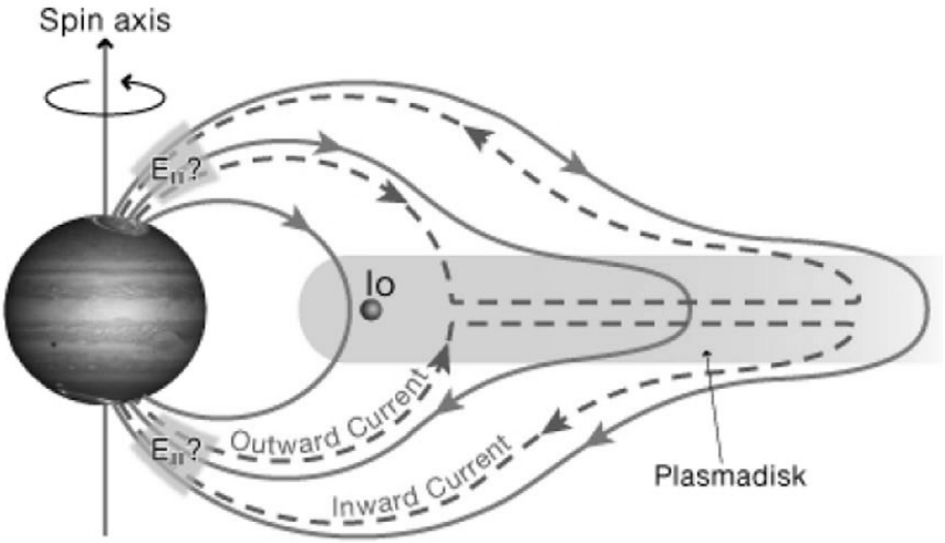

Figure 1.3: A diagram of the Jovian magnetosphere adapted from Bagenal et al. (2014), see also Cowley and Bunce (2001). This figure illustrates the main magnetic field configuration of the electrodynamic engine corresponding to the breakdown of co-rotation (see texts). The magnetic field lines are shown in blue, stretched in the central plane due to the effect of the plasma disk. The plasma in the disk is tied to the rotating magnetic field of the planet. At large radii along the disk plane the plasma can no longer keep up with the rotation of the magnetic field and begins to drag, creating strong electric fields and generating the currents shown as dashed lines (Cowley and Bunce 2001).

et al. 2004). The dissipated energy is a function of the relative velocity of the satellite through the magnetosphere, the magnetic field strength at the satellite location and the cross section of interaction, usually defined by the size of the lunar obstacle (Zarka 2007). In the case of a moon without an intrinsic magnetic field (ex. Io), the cross section is defined by the exo-ionosphere of the moon (Zarka 2007). If the moon does have its own magnetosphere (ex. Ganymede), the cross section is defined by the magnetopause radius of the moon relative to the planet's magnetosphere (Zarka 2007).

- Lastly, the breakdown of co-rotation between a rotating plasma disk and the planetary magnetosphere can create a shearing layer that drives auroral currents. This is the mechanism that powers the main Jovian auroral oval (e.g., Cowley and Bunce 2001). The energy dissipated in this case is dependent on the differential velocity between the co-rotating magnetosphere and the

extended plasma disk and the magnetic field of the planet (Cowley and Bunce 2001; Nichols et al. 2012). I depict this last mechanism in Figure 1.3, excerpted from Bagenal et al. (2014), to show the magnetic field configuration and illustrate the generation of the current systems of the Jovian main auroral oval.

Additionally, the different mechanisms can overlap, as they do in the Jovian magnetosphere. Each of these electrodynamic engines generates strong field-aligned currents that drive accelerated electron beams, the fundamental ingredient of auroral emission processes.

ECMI Radio Emission

The acceleration of the electrons creates an energetic non-thermal energy distribution and can lead to the onset of the electron cyclotron maser instability (ECMI). The necessary criteria are an energy distribution dominated by the non-thermal component and a cyclotron frequency,

$$\omega_{ce} = \frac{eB}{m_e c} , \tag{1.1}$$

larger than the plasma frequency,

$$\omega_{pe} = \sqrt{\frac{4\pi n_e e^2}{m_e}} , \tag{1.2}$$

such that,

$$\frac{\omega_{pe}^2}{\omega_{ce}^2} = \frac{4\pi n_e m_e c^2}{B^2} \leq 1 , \tag{1.3}$$

where n_e is the electron density, B is the magnetic field strength, m_e is the electron mass, e is the charge of the electron, and c is the speed of light (see Treumann 2006). As the ratio of Equation 1.3 approaches unity, the maser becomes weaker and less efficient. However, under the conditions of a dilute plasma immersed in a strong magnetic field, the energetic electrons become an efficient radiation source. The result is a strong coherent radio source emitting near the local cyclotron frequency that is highly circularly polarized and radiates into a thin ($\sim$1°) conical sheet with large opening angles, nearly perpendicular to the magnetic field direction, $\gtrsim$80°

(Dulk 1985; Treumann 2006). Consequently, the observations of this non-thermal radiation are subject to geometric beaming effects and are rotationally modulated as the emission cone sweeps into and out of view (Badman et al. 2015).

ECM radio emission has been observed in the magnetized planets of the Solar System, signaling the presence of non-thermal energetic electron distributions in the regions around the planetary magnetic poles, near the top of the atmosphere (e.g., Wu and Lee 1979). In Figure 1.4, I show a diagram, excerpted from Bagenal et al. (2014) illustrating the Jovian auroral system and the various ECM radio sources and emission cones, including the main oval and the flux-tube aurorae of the Jupiter-Io system (see also Zarka 2000). For Jupiter, the total power emitted at radio wavelengths is less than 0.1% of the total energetic output of the auroral emission (Bhardwaj and Gladstone 2000). Radio observations thus provide important constraints on the magnetic field but only limited constraints on the energetics of the auroral mechanisms. The bulk of the energy emerges at other wavebands (Bhardwaj and Gladstone 2000).

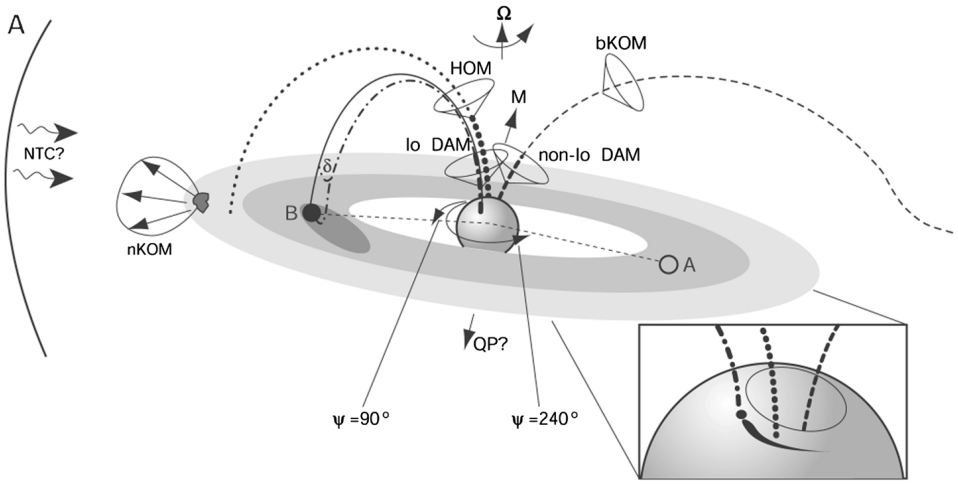

Figure 1.4: Diagram of the Jovian auroral system showing the various kinds of auroral radio emission of Jupiter, including the decametric emission (DAM), hectometric component (HOM), and the broadband kilometric component (bKOM), excerpted from Bagenal et al. (2014), see also Zarka (2000).

Atmospheric Impact

The energetic electron beams responsible for the radio emission precipitate into the atmosphere and generate a cascade of additional auroral emission processes (see Badman et al. 2015, and references therein). In Figure 1.5, I depict the overall

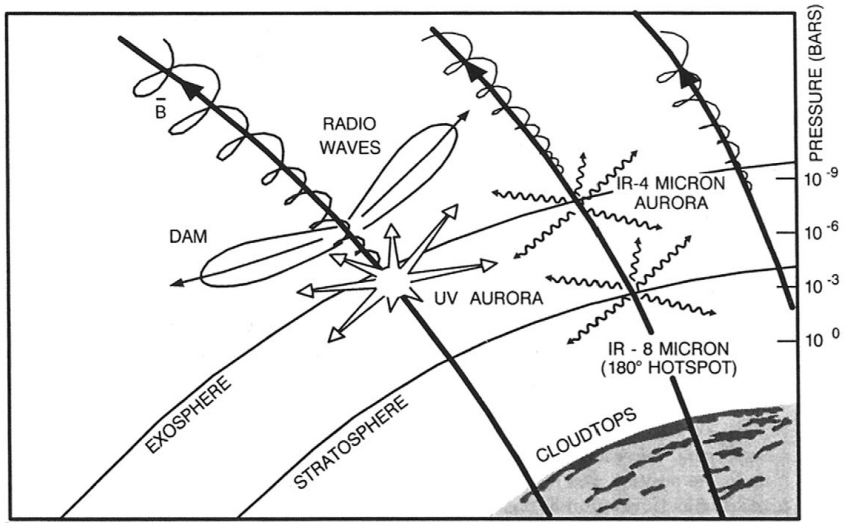

Figure 1.5: A diagram of the upper atmosphere of Jupiter, excerpted from Bagenal et al. (2014), illustrating the various interactions of the precipitating electrons with the atmospheric gas. The electrons spiral down along the magnetic field lines emitting radio waves (DAM - decametric radiation) and when they hit the atmosphere they deposit the bulk of their energy, creating the ultraviolet, optical, and infrared aurorae.

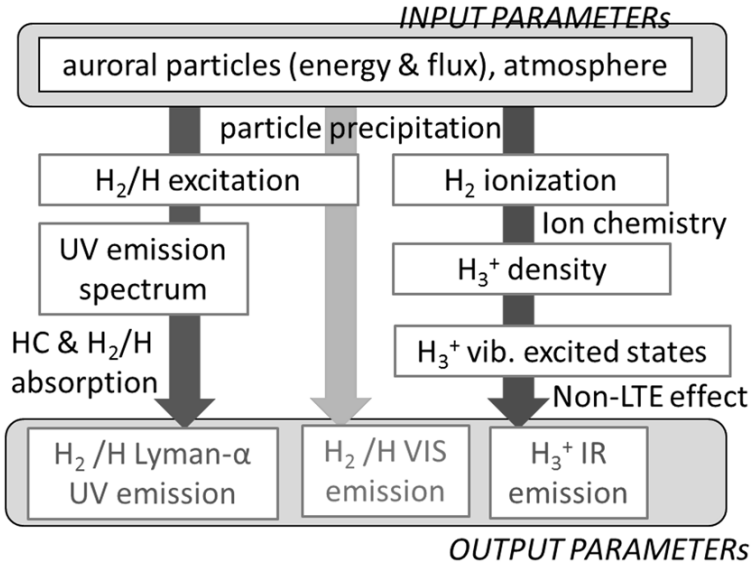

Figure 1.6: A chart, adapted from Badman et al. (2015), summarizing the radiative emissions and processed resulting from auroral particle precipitation and energy deposition in a cool hydrogen dominated atmosphere.

picture and subsequent auroral emissions in the diagram exceprted from Bagenal et al. (2014). In Jupiter and Saturn, where the atmospheres are predominantly hydrogen, the collision of the energetic electrons with the atmospheric gas leads to excitation and ionization of H/H_2 and subsequent emissions at UV and optical wavelengths (Perry et al. 1999; Vasavada et al. 1999; Grodent et al. 2003; Gustin et al. 2013; Dyudina et al. 2016). The chart in Figure 1.6, adapted from Badman et al. (2015), summarizes atmospheric auroral processes and the related emissions.

Ultraviolet Aurorae

The ultraviolet (UV) spectrum is defined by emission from the Lyman and Werner bands of excited molecular hydrogen (Gustin et al. 2013). The Lyα emission line produced by dissociative excitation is also prominent, although it may only contribute ~10% of the total UV energy (Perry et al. 1999). The UV auroral spectrum is further shaped by the column of hydrocarbon absorption above the auroral emission region in the atmosphere (Gustin et al. 2013). In Figure 1.7, I show an image of the UV auroral emission of Jupiter taken with the *Hubble Space Telescope* (*HST*) from Grodent et al. 2003, demonstrating the auroral oval morphology. Because the time scale for the radiation of UV emission is so short (~10^{-2} s; see Figure 1.8), this UV radiation is very responsive to changes in the properties of the electron beam energies and fluxes (Tao, Badman, and Fujimoto 2011; Badman et al. 2015). In Jupiter, the power released in the UV emissions can be ~15% of total auroral energy (Bhardwaj and Gladstone 2000).

Figure 1.7: An HST-STIS image of Jupiter's UV aurorae from Grodent et al. (2003). The auroral oval is the main emission feature with more variable polar emission visible within the oval as well as the footpoint of the flux tube connecting to Io (Grodent et al. 2003).

Optical Aurorae

The study of auroral emissions at visible wavelengths in the solar system giant planets has been hampered by the effects of reflected light from the Sun. Nevertheless, imaging studies of the planet night side aurorae have shown that there are enhanced optical emissions coincident with the main auroral oval of Jupiter (Ingersoll et al. 1998). The optical emission is likely from the Balmer series of hydrogen, a consequence either of direct interaction with the electron beam or of fluorescence (Ingersoll et al. 1998). For Jupiter, the total amount of energy released at visible wavelengths is less than ∼1% of the total auroral energy (Bhardwaj and Gladstone 2000).

Infrared Aurorae

The creation of ionized species in the Jovian and Kronian auroral regions also leads to significant ion chemistry within the atmosphere and the creation of the strongly emitting species H_3^+ (e.g., Perry et al. 1999).

$$H_2^+ + H_2 \rightarrow H_3^+ + H\,. \tag{1.4}$$

The ro-vibrational transitions of H_3^+, with bands around 2 μm and 4 μm, serve to effectively cool the atmosphere and regulate Jovian exospheric temperatures (Maillard and Miller 2011). These emissions represents about a fifth of the total IR auroral emissions of Jupiter (Bhardwaj and Gladstone 2000). Moreover, because of their thermal nature, the H_3^+ emission lines can serve as a diagnostic of the atmospheric conditions and probe the upper atmospheric structure (Tao, Badman, and Fujimoto 2011; Badman et al. 2015). Indeed, Tao et al. (2012) showed how the properties of the electron beam and the background atmospheric temperature can be determined from a study of just the H_3^+ emission lines. In Figure 1.8, I show a chart, from Badman et al. (2015), illustrating the atmospheric interactions that generate the UV and IR emission lines and their timescales. Critically, because the presence of H_3^+ depends on the ion chemistry in the atmosphere, it is sensitive to processes that drive its destruction, like electron recombination in the presence of large electron number densities or reactions with larger molecules like methane or water in the deeper atmospheric layers (e.g., Perry et al. 1999). The deposition of energy from the electron beam into the atmosphere also leads to a significant thermal contribution to the auroral emissions between 7 μm and 14 μm, representing the

bulk of the IR emission and ~85% of the total auroral emission energy (Bhardwaj and Gladstone 2000).

X-ray Emission

X-rays have also been detected from the giant planets in connection with aurorae (Bhardwaj and Gladstone 2000; Badman et al. 2015). Largely a product of charge exchange reactions of highly ionized species of oxygen and sulfur, the X-ray emission constitutes a very tiny portion of the total auroral energy, $\lesssim$0.1%, less than the total radio contribution (Bhardwaj and Gladstone 2000; Badman et al. 2015).

Given the similarities between brown dwarfs and planets, it is not unreasonable to suggest that these kinds of processes may be taking place in brown dwarf magnetospheric systems. This analogy has been further strengthened by the recent discoveries of planets around brown dwarfs, confirming the notion that the brown dwarfs could be considered scaled up versions of the Jovian system with its satellites (Udalski et al. 2015; Gillon et al. 2016). In the next chapter we consider the observational trends in brown dwarf magnetic activity and why the data suggest the emergence of auroral processes in brown dwarf atmospheres.

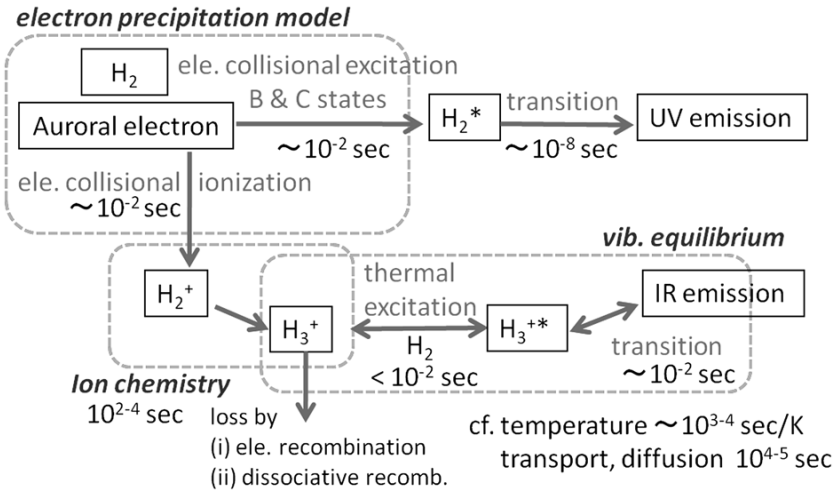

Figure 1.8: A chart, adapted from Badman et al. (2015), summarizing the network of different collisional and chemical processes that generate the atmospheric auroral emissions with important timescales indicated.

Chapter 2

MAGNETIC ACTIVITY TRENDS IN BROWN DWARFS

The cumulative history of observations of low-mass stars and very-low mass stars provides an important context for the developments of magnetism in ultracool dwarfs (UCDs), objects with spectral types ≥M7.

2.1 Magnetic Field Topology

In going from early M-dwarf stars toward lower-mass stars, the magnetic activity properties change. Studies of the magnetic field topology through ZDI of low-mass stars has revealed that early M dwarfs (M0-M4) typically exhibit large-scale fields of moderate strength with significant toroidal components and high degrees of asymmetry, whereas late M dwarfs (M5-M8) often show much stronger axisymmetric large-scale fields dominated by their dipolar component (Donati et al. 2008; Morin et al. 2011). The lower mass regime, however, also shows evidence for both non-axisymmetric and axisymmetric large-scale field configurations which may be evidence for a bimodal dynamo (Morin et al. 2011). The transition appears to take place around spectral type dM4 which corresponds to the transition from a partially convective interior to a fully convective interior (Chabrier and Baraffe 2000). Accordingly, this transition must coincide with a change in the underlying magnetic dynamo. Instead of an α-Ω dynamo mechanism, the fully convective objects likely generate their large-scale field structures with an α^2 dynamo, in which the turbulent convective motions create and regenerate the field (Browning 2008; Yadav et al. 2015).

2.2 Rotation Rates

This transition also leads to an increase in the rotation rates of low-mass stars (Reiners and Basri 2008; Reiners and Mohanty 2012). Stars below this boundary lose angular momentum less efficiently than higher mass stars and retain their high rotation rates for longer (Reiners and Mohanty 2012). Reiners and Mohanty (2012) showed that the change in rotation rates can be attributed to the change in stellar radius across the convective boundary and does not require a change in the magnetic field topology. The high rotations rates are observed in the large values of $v \sin i$ measurements for samples of UCDs (e.g., Reiners and Basri 2010; McLean, Berger, and Reiners 2012;

Crossfield 2014). This shift in the rotation rates is especially apparent comparing L dwarfs to the earlier spectral type stars (Basri and Marcy 1995). I illustrate this in Figure 2.1, adapted from Reiners and Basri (2008), showing the observed projected rotational velocities as a function of spectral type for the objects in their sample. There is a clear increase for the cooler objects. This is interesting because of the usual connection between rotation and activity in stellar coronal and chromospheric atmospheres. Reiners and Basri (2010), however, show that for fast rotating objects the magnetic flux is not correlated with the rotation, indicating that the rotation may be decoupled from the magnetic dynamo in fully convective stars and thus be decoupled from the chromospheric activity indicators that are related to the mean surface magnetic strength. This was first revealed by initial Hα observations that should no emission despite fast rotation rates (Basri and Marcy 1995). Observations of Zeeman broadening of magnetically sensitive lines have shown that these stars are capable of sustaining kG magnetic field strengths over large portions of their surfaces (e.g., Reiners and Basri 2007, 2010).

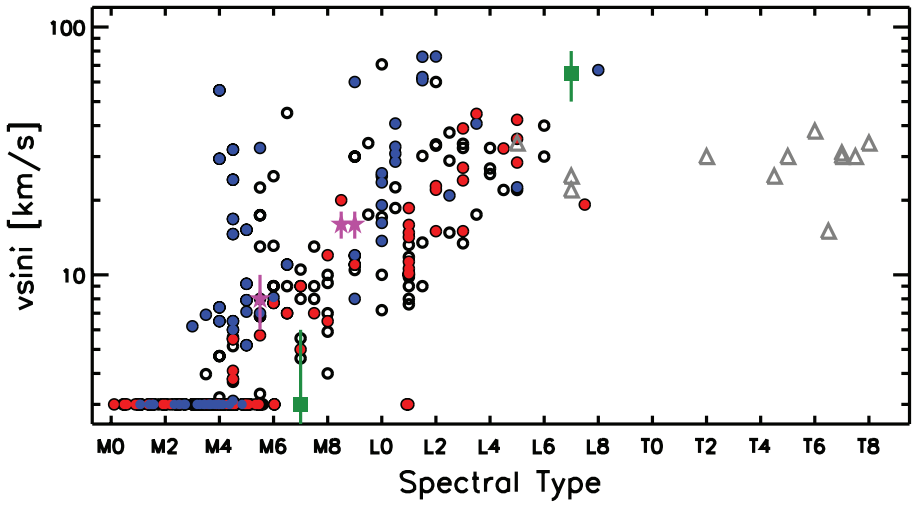

Figure 2.1: The distribution of projected rotational velocities as a function of spectral type, adapted from Reiners and Basri (2008) and reproduced by permission of the AAS, showing the relatively high rotation rates amongst the UCD populations relative to earlier type stars. The different symbols indicate objects with indications of youth (blue circles), field objects (red circles) and, objects with no age information (empty symbols). The stars correspond to the members of LHS1070 system, and squares are a couple of sub dwarfs. The triangles correspond to data from Zapatero Osorio et al. (2006).

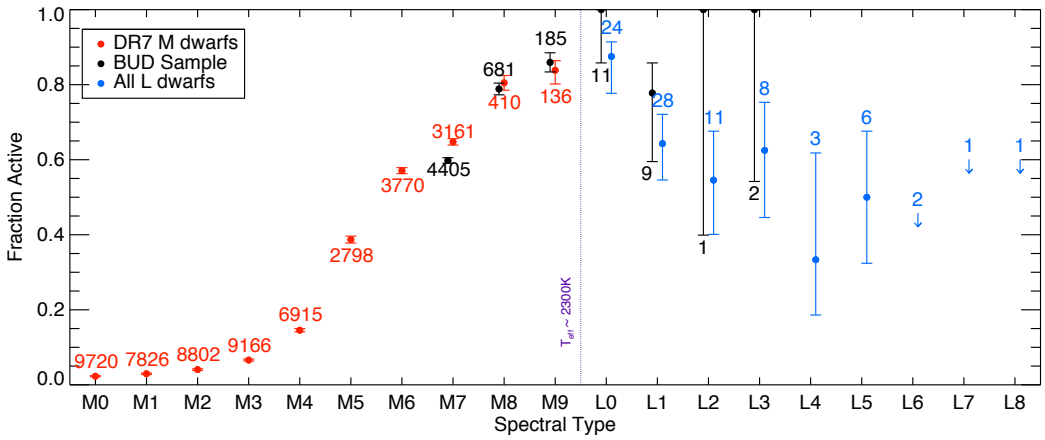

Figure 2.2: The Hα activity fractions, from Schmidt et al. (2015), reproduced by permission of the AAS, as a function of spectral time across the M dwarf and L dwarf regimes. Objects are deemed 'active' if they show Hα emission in excess of 0.75 Å. The plots shows a peak in the active fraction between M9 and L0 spectral types.

2.3 Hα

Trends in chromospheric activity have been examined through studies of Hα emission. Looking at a spectroscopic sample of M dwarfs from the Sloan Digital Sky Survey, West et al. (2008) showed that the fraction of active stars, as traced by Hα emission, rises from early M dwarfs to late M dwarfs, with a significant jump at a spectral type of dM4. Only 2% of M0 dwarfs are observed in the active state, whereas up to ~85% of M9 dwarfs show activity (Pineda et al. 2013). This has been attributed to a rise in the active lifetimes of these stars across the boundary dividing partially convective and fully convective stars (West et al. 2008). This is likely a consequence of the slower spin-down rates of the lowest mass stars (Reiners and Mohanty 2012). Thus, although the rotation is not strongly coupled to the strength of activity in late M dwarfs, there could be a rotation threshold for which objects orbiting below a certain period are 'active' and those rotating more slowly are 'inactive', similar to what is observed in mid-M dwarfs (West et al. 2015). Extending these studies into the L dwarf regime, Schmidt et al. (2015) revealed a peak in the activity fractions at early L dwarfs and the subsequent decline going to later spectral types. I illustrate these findings in Figures 2.2-2.3, showing the activity fraction of Hα detections and the strength of the Hα emission relative to the objects bolometric luminosity, respectively, from Schmidt et al. (2015). Moreover, the strength of the emission relative to the object's bolometric luminosity also steadily declines. These results have been interpreted as a decline of activity due to the increasingly neutral

atmospheres of brown dwarfs being unable to sustain significant chromospheric heating (Mohanty et al. 2002).

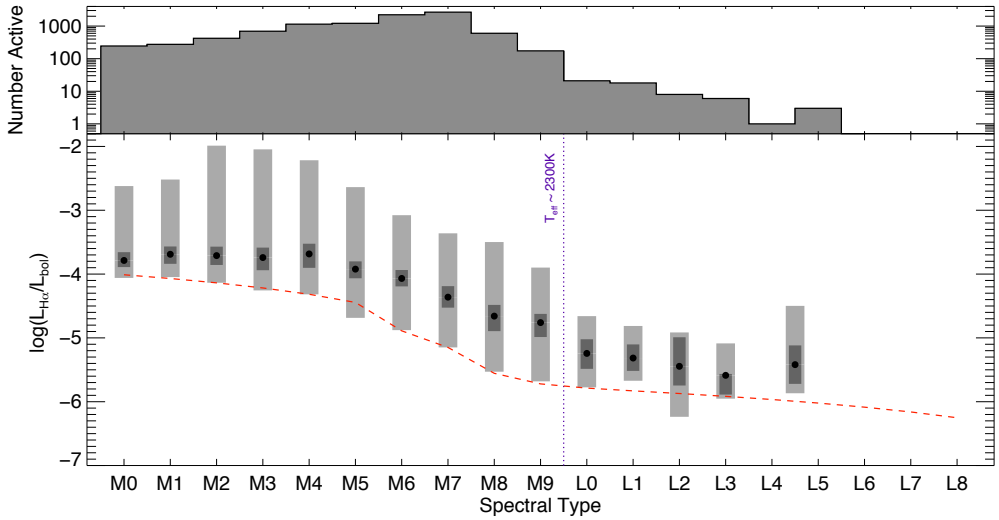

Figure 2.3: The normalized Hα luminosity as a function of spectral type from M dwarfs to L dwarfs, from Schmidt et al. (2015), reproduced by permission of the AAS. The plot points show the median activity level, the interquartile range (dark grey), and the min/max (light grey), for each spectral type bin. The dashed line indicates the observational detection threshold.

2.4 Ultraviolet

UV observations of M dwarfs have also been used to examine the chromospheres of low-mass stars. There are only a handful of UV observations of M dwarfs, but *Hubble Space Telescope* spectra have shown that even old stars that are inactive in Hα exhibit strong UV emission with prominent fluxes in Lyα (France et al. 2013, 2016). These results point to the presence of chromospheres and transition regions across dM0-dM6 stars (France et al. 2013, 2016). Although UV observations of field UCDs are limited, the M8 dwarf VB 10 has been observed to flare in the UV (Linsky et al. 1995; Helling and Casewell 2014).

2.5 X-ray

Coronal X-ray emission is known to be tied to rotation in early M dwarfs, with greater X-ray emission for faster rotators up to a saturation level (Pizzolato et al. 2003). In late M dwarfs, X-ray emission drops off despite the consistently high rotation rates (Berger et al. 2010; Cook, Williams, and Berger 2014). There may also be evidence for a decline in X-ray activity with increasing rotation rates for very-late M dwarfs

(dM6.5-dM9; Cook, Williams, and Berger 2014). X-ray observations of UCDs have also shown detections in short duration flares (e.g., Berger et al. 2010).

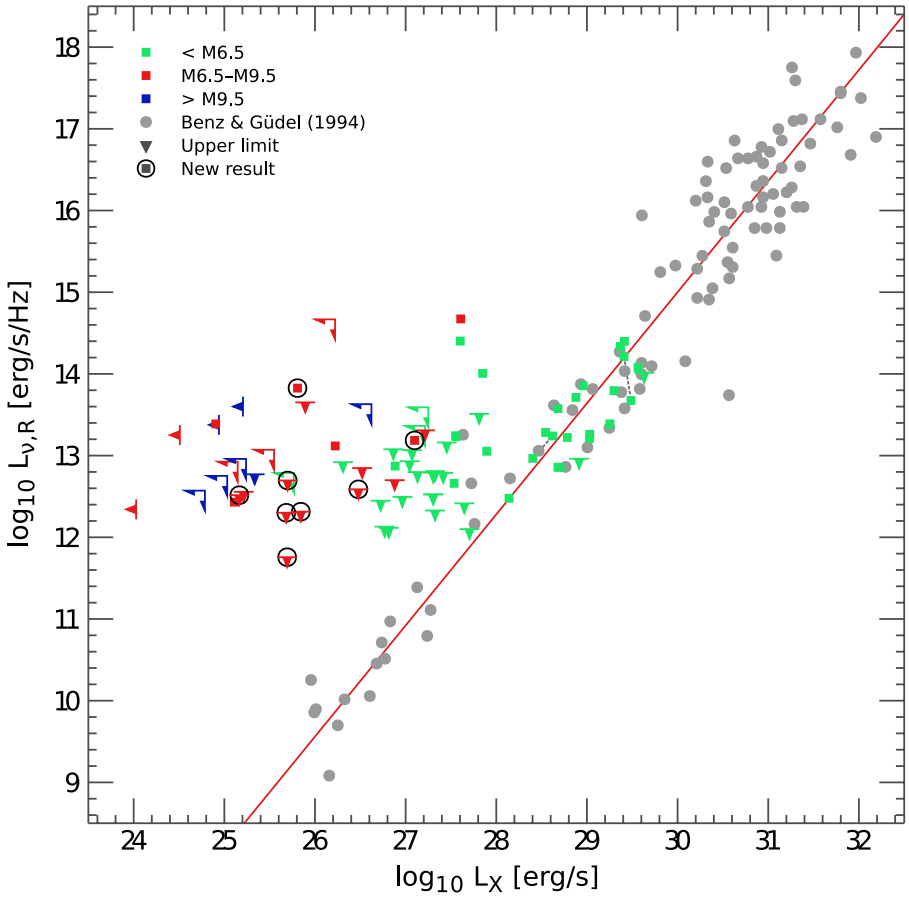

Figure 2.4: From Williams, Cook, and Berger 2014, reproduced by permission of the AAS, I show here the correlation of X-ray luminosity and radio luminosity for stars with solar-like magnetic activity and how the lowest mass stars show many examples of deviations from this relation (shown as a red line).

2.6 Radio

The trends in X-ray luminosity are of particular importance because of their tight connection to radio luminosities in the standard coronal paradigm (Güdel 2002). Stellar X-ray and radio luminosities were shown to be tightly correlated in what became known as the Güdel-Benz relation (Guedel and Benz 1993). This relation, applicable to solar-like magnetic activity, extends down to early M dwarfs but begins to break down for late M dwarfs (see Figure 2.4; Williams, Cook, and Berger 2014). Williams, Cook, and Berger (2014) argue that the observations show a mix of ultracool dwarfs (UCDs; spectral types $\gtrsim$dM6.5) that are consistent with the Güdel-

Benz relation and a group of radio bright objects with low X-ray activity levels. They suggest that these two populations can be explained by different emission regimes corresponding to different magnetic field topologies, UCDs with large-scale fields have high X-ray activity and UCDs with smaller scale fields power relatively bright radio gyro-synchrotron sources (Williams, Cook, and Berger 2014). However, the connection of these field topologies to the emission mechanisms remains to be proven. Moreover, these authors likely have the relationship backwards (see Chapter 6).

Collectively, the array of observations present a somewhat conflicted view of the ability of UCDs to sustain stellar-like magnetic activity. In some case's observations reflect the coronal picture of activity; however in other ways the observations deviate considerably.

2.7 Evidence for Ultracool Dwarf Aurorae

Despite the emergence of new behavior at the end of the main sequence, the activity observations were still predominantly interpreted within the solor-stellar paradigm. Significant discrepancies with this picture first emerged with the discovery of unexpectedly strong radio emission from the brown dwarf LP944-20 (Berger et al. 2001). Follow up studies have revealed a population of radio bright brown dwarfs within a population of brown dwarfs with radio emission upper limits (e.g., McLean, Berger, and Reiners 2012; Antonova et al. 2013; Route and Wolszczan 2013; Lynch et al. 2016). The strong radio emitters typically display coherent polarized periodic pulses, attributed to the ECMI, the same mechanism that is responsible for the Jovian radio aurorae (Hallinan et al. 2007, 2008; Kao et al. 2016). This process generates 100% circularly polarized radiation at the local cyclotron frequency, see Equation 1.1. ECMI is also capable of reaching extremely high brightness temperatures $T_b \lesssim 10^{20}$ K (Güdel 2002). The detectability of objects with radio pulses is likely subject to beaming and geometric effects, naturally explaining at least some of the population of radio non-detections (Hallinan et al. 2008). However, the underlying conditions generating this kind of emission in brown dwarfs is an open question. Radio pulses have even been detected from a T6.5 dwarf with an effective temperature of ~900 K (Route and Wolszczan 2012). Stellar atmospheric models for such low temperature objects have difficulties recreating the kinds of magnetic conditions typically responsible for radio emission features (Mohanty et al. 2002; Rodriguez-Barrera et al. 2015). Instead, the presence of ECMI emission uniquely points toward the existence of energetic non-thermal electron populations, produced

by field-aligned current systems, analogous to what is found in the auroral regions of the gas giant planets of the Solar System.

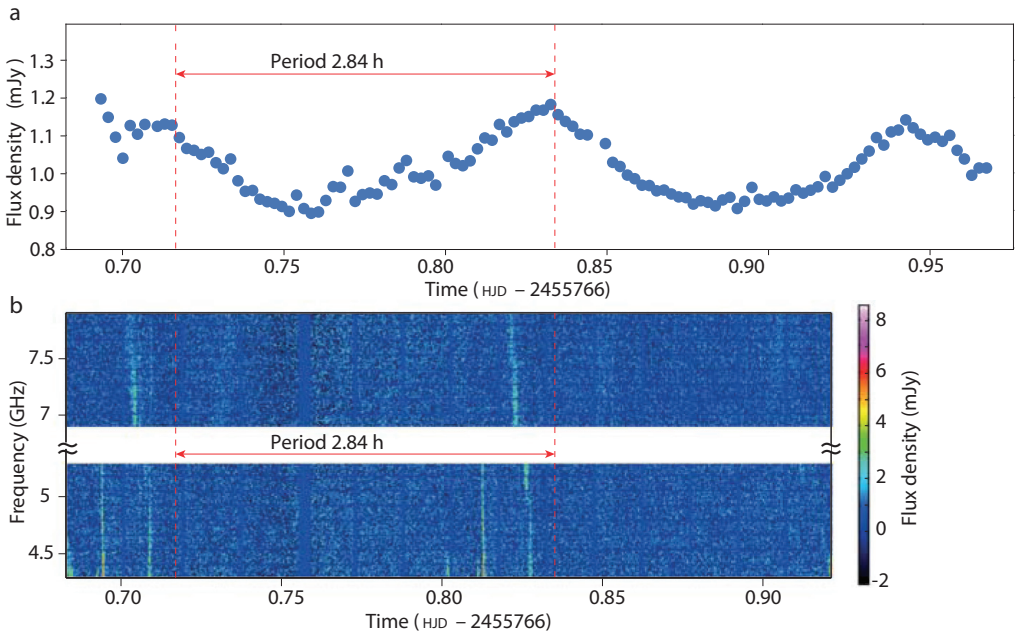

Figure 2.5: Plot from Hallinan et al. (2015), showing the Hα light curve from the Hale 200' at Palomar Observatory with the simultaneous radio dynamic spectrum intensity from the VLA of the benchmark UCD LSR J1835+3259. The radio pulses are clear and distinct, rotating with an period of 2.84, the same as the optical light curve with a well-defined phase offset.

Brown dwarf studies in the optical have also revealed indicators of magnetic activity despite low atmospheric temperatures. Burgasser et al. 2003 reported Hα detections from three T dwarfs. They show that the low Hα luminosity levels (see Figure 2.3) generally extend into the T dwarf regime, but unexpectedly there are still a couple of objects with clear detections; these objects do not fit the trend of decreasing emission established from L dwarf observations generally attributed to chromospheric activity (Schmidt et al. 2014). For example, the multiple attempts to investigate the underlying emission mechanism of the bright Hα emission in the T6.5 dwarf, 2MASS J12373919+6526148, ruled out several scenarios but did not find a satisfactory solution (Burgasser, Kirkpatrick, Reid, et al. 2000; Burgasser, Kirkpatrick, Brown, Reid, Burrows, et al. 2002; Liebert and Burgasser 2007). Based on a stellar activity perspective these emissions are puzzling.

Interestingly, the connection of optical Hα emission with radio aurorae is evident from recent work by Hallinan et al. (2015). From simultaneous measurements in

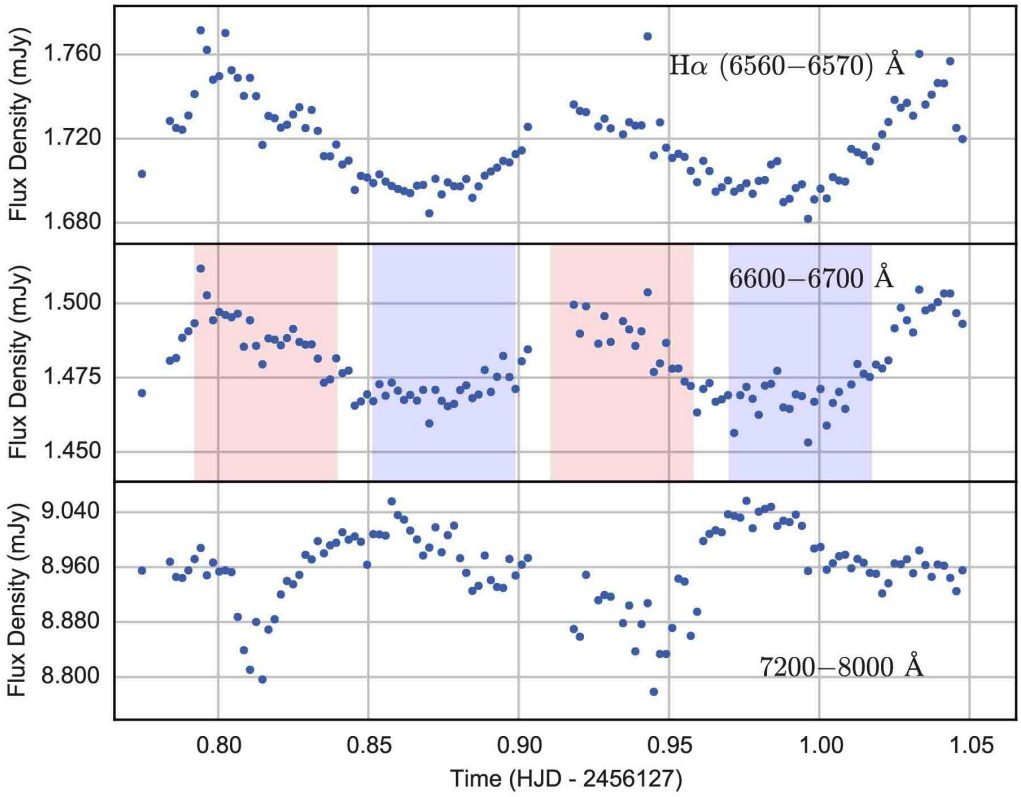

Figure 2.6: Light curves, from Hallinan et al. (2015), showing the emission in different bands from the spectroscopic monitoring of LSR J1835+3259. The top panel is Hα, the middle covers 6600-6700 Å and the bottom corresponds to 7200-8000 Å. The light curves reveal broadband variability that is correlated and anti-correlated to the Hα emission. Hallinan et al. (2015) use these spectra to determine the properties of the emitting surface region.

the optical and the radio of an M8.5 dwarf, they show that the optical emission line features are rotationally modulated at the same period as the coherent radio pulses with a fixed phase offset (see Figure 2.5, Hallinan et al. 2015). With Keck-LRIS monitoring of the target Hallinan et al. (2015), further assessed the spectrophotometric variability of the surface emission region. These observations revealed broadband photometric variability in phase with the rotational modulation of the emission line features Hallinan et al. (2015). The modulations show that different portions of the spectrum were either correlated or anti-correlated with the Hα emission (see Figure 2.6). The authors were able to determine that the surface emission region was well modeled by a blackbody-like feature, instead of a low-mass star photospheric spectrum (see Figure 2.7). Hallinan et al. (2015) conclude that the energetic electrons generating the radio emission precipitate into the atmosphere

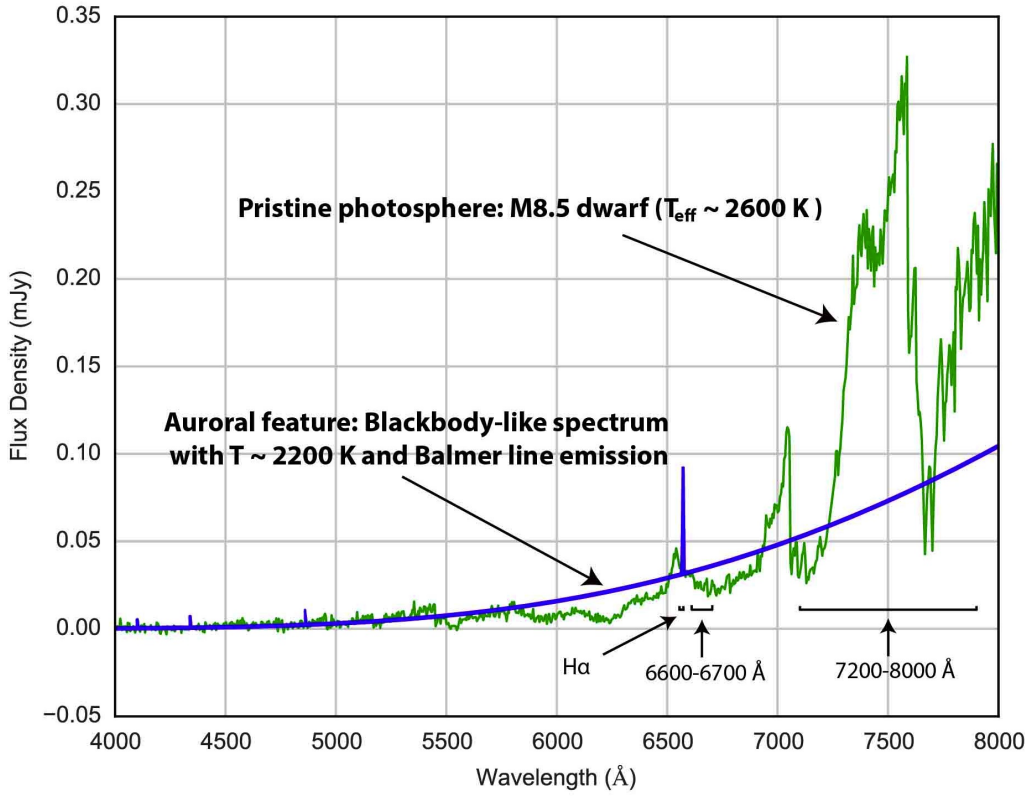

Figure 2.7: Data and model spectrum, from Hallinan et al. (2015), for LSR J1835+3259 used to explain the observed spectrophotometric variability in their study. The different emission levels at different wavelengths between the surface feature and the photosphere explain the light curves shown in Figure 2.6

and generate the auroral surface region responsible for the Hα emission.

Additionally, Harding, Hallinan, Boyle, et al. 2013 observe broadband optical photometric periodicity in a long-term study of several radio detected brown dwarfs. These results point toward the likely association of optical periodicity (in continuum and emission lines) with auroral radio pulses, perhaps via the same mechanisms put forward by Hallinan et al. (2015).

Using Hα detections and the presence of photometric variability to define an UCD sample to observe with the Jansky Very Large Array (VLA), Kao et al. (2016) detected additional sources of polarized radio emission, including 2MASS J12373919+6526148. Biasing the target selection with indicators of magnetic phenomena has proven successful in expanding the number of radio detected brown dwarfs in the T dwarf regime, adding greater significance to the connection between radio aurorae and surface magnetic emissions (Kao et al. 2016). This array of observational features, set apart by the ECMI radio pulses, is not found in the standard picture of magnetic

activity in low-mass stars and points to a different explanation in the substellar regime which can be coherently described as a consequence of large scale magnetospheric currents driving auroral activity. These auroral processes are analogous to what is found in the gas giant planets of the Solar System (see Chapter 1.2).

Given these findings, I have embarked on a research program designed to investigate magnetic activity in the ultracool dwarf regime and understand the manifestations of auroral phenomena in brown dwarf atmospheres. The primary studies are,

- first, a survey for auroral Hα emission in late L dwarfs and T dwarfs,
- second a search for the auroral infrared emission lines of H_3^+ from radio detected brown dwarfs,
- third, a detailed study of the emission line morphology of the benchmark object LSR J1835+3259 to discern the auroral electrodynamic engine, and
- fourth, a comprehensive multi-wavelength description of brown dwarf auroral phenomena.

These studies are outlined in Chapters 3-6 of this dissertation.

Chapter 3

A SURVEY FOR Hα EMISSION FROM LATE L DWARFS AND T DWARFS

Pineda, J. S., G. Hallinan, J. D. Kirkpatrick, G. Cotter, M. M. Kao, and K. Mooley. 2016. "A Survey for Hα Emission from Late L Dwarfs and T Dwarfs." *ApJ* 826, 73 (July): 73. doi:10.3847/0004-637X/826/1/73. arXiv: 1604.03941 [astro-ph.SR].

Recently, studies of brown dwarfs have demonstrated that they possess strong magnetic fields and have the potential to produce radio and optical auroral emissions powered by magnetospheric currents. This emission provides the only window on magnetic fields in the coolest brown dwarfs and identifying additional benchmark objects is key to constraining dynamo theory in this regime. To this end, we conducted a new red optical (6300 - 9700 Å) survey with the Keck telescopes looking for Hα emission from a sample of late L dwarfs and T dwarfs. Our survey gathered optical spectra for 29 targets, 18 of which did not have previous optical spectra in the literature, greatly expanding the number of moderate resolution (R~2000) spectra available at these spectral types. Combining our sample with previous surveys, we confirm an Hα detection rate of $9.2\pm^{3.5}_{2.1}$ % for L and T dwarfs in the optical spectral range of L4 - T8. This detection rate is consistent with the recently measured detection rate for auroral radio emission from Kao et al. (2016), suggesting that geometrical selection effects due to the beaming of the radio emission are small or absent. We also provide the first detection of Hα emission from 2MASS 0036+1821, previously notable as the only electron cyclotron maser radio source without a confirmed detection of Hα emission. Finally, we also establish optical standards for spectral types T3 and T4, filling in the previous gap between T2 and T5.

3.1 Introduction

Twenty years ago, the discovery of the first brown dwarfs opened up the study of sub-stellar objects as interesting astrophysical targets spanning the gap between stars and planets (Nakajima et al. 1995; Oppenheimer et al. 1995). Since then, our understanding of brown dwarfs has developed considerably, including their

atmospheric properties, evolution, and internal structure (e.g., Burrows et al. 2001; Kirkpatrick 2005; Marley and Robinson 2015 and references therein). Many of these developments are based on detailed spectroscopic analyses examining brown dwarf spectra at infrared (IR) wavelengths, where the photospheric flux is the brightest, and where the effects of absorption bands, such as CH_4, H_2O, and NH_3, are most prominent (e.g., Burgasser, Kirkpatrick, Brown, Reid, Burrows, et al. 2002; Burgasser, Burrows, and Kirkpatrick 2006; Burgasser et al. 2006, 2010; McLean et al. 2003; Knapp 2004; Cushing, Rayner, and Vacca 2005; Cushing et al. 2008, 2011; Stephens et al. 2009; Kirkpatrick et al. 2012; Mace 2013). By comparison, the flux at red optical wavelengths (600 nm - 1000 nm) is much fainter because of the cool effective temperatures, especially for late L dwarfs, T dwarfs, and Y dwarfs ($T_{\rm eff} < 1500$ K). Consequently, there have been far fewer studies looking at cool brown dwarfs at these wavelengths.

One feature of particular interest in the optical spectrum is Hα emission at 6563 Å, which has often been used as an indicator of chromospheric emission in the spectra of M dwarfs and early L dwarfs (e.g., Reiners and Basri 2008; Schmidt et al. 2015). For early M dwarfs, the chromospheric nature of the Balmer emission is substantiated by accompanying evidence in X-ray and UV data, revealing high temperature atmospheric regions consistent with a transition region between the photosphere and a corona (e.g., Linsky et al. 1982; Fleming et al. 1988; Walkowicz, Johns-Krull, and Hawley 2008). For late M dwarfs, L dwarfs and cooler objects, despite very few detections in the X-ray and UV, the presence of chromospheres has been inferred in the population based on detections of Hα emission and the analogy with the warmer stars. However, X-ray and optical observations of ultracool dwarfs (UCD; spectral type $\geq$M7) show a drop in their X-ray and Hα luminosities (Berger et al. 2010; Williams, Cook, and Berger 2014; Schmidt et al. 2015). The decline in these X-ray and Hα emissions, has been seen as indicative of a decline in the ability of UCDs to sustain much magnetic activity in their cool atmospheres with a transition taking place around the boundary between stars and brown dwarfs (Mohanty et al. 2002; Reiners and Basri 2008; Berger et al. 2010).

Despite the cool atmospheric temperatures, recent surveys have revealed that many brown dwarfs also show strong radio emission, indicating that they can sustain strong magnetic fields throughout the whole spectral sequence from L dwarfs to T dwarfs (Hallinan et al. 2008; Berger et al. 2010; Route and Wolszczan 2012; Williams, Cook, and Berger 2014; Kao et al. 2016). Early efforts to understand this radio

emission invoked standard Solar-like magnetic processes (Berger 2006; Berger et al. 2009; Route and Wolszczan 2012). Building on those efforts, continued monitoring of the radio brown dwarfs and observations of the coolest UCDs have now shown that the pulsed radio emission is entirely consistent with being a consequence of the electron cyclotron maser instability (ECMI) as part of auroral currents in the magnetosphere (Hallinan et al. 2008, 2015; Williams and Berger 2015; Lynch, Mutel, and Gudel 2015; Kao et al. 2016). Furthermore, Hallinan et al. (2015) demonstrated that certain optical spectral features, Balmer series emission lines and broadband variability, can be directly tied to the auroral process in some objects. The connection is further corroborated by the association of radio aurorae with Hα emission, suggested by a high detection rate of radio brown dwarfs in the late L dwarf and T dwarf regime, when selecting the observational sample based on potential auroral activity indicators (Kao et al. 2016). This survey is in stark contrast to the very low detection rate of numerous previous surveys that looked for radio emission from brown dwarfs (Berger 2006; McLean, Berger, and Reiners 2012; Antonova et al. 2013; Route and Wolszczan 2013).

Within the UCD regime, many objects may indeed exhibit chromospheric emissions, especially for the late M dwarfs and early L dwarfs, in which the atmospheres are warmest. However, many studies have now shown that auroral processes are also possible throughout the brown dwarf sequence. This leads to the question: what governs brown dwarf magnetic activity and what drives potential auroral activity? Amongst late M dwarfs and early L dwarfs, disentangling the different processes requires dedicated monitoring of known benchmark objects like 2MASS 0746+2000 and LSR 1835+3259 (Berger et al. 2009; Hallinan et al. 2015). Another way to examine the question is to observe late L dwarfs and T dwarfs, objects in which the local stochastic heating of the upper atmosphere that generates chromospheric emission, as seen on the Sun, is difficult to generate. A study of the activity in these objects allows us to understand the prevalence of magnetic processes, assess the viability of the auroral mechanism and find new potential benchmark targets for dedicated monitoring. If the Hα emission in these objects is associated with the same processes that produce auroral radio emission, surveys in the optical provide an additional means to look for brown dwarfs potentially harboring auroral activity. The advantage of surveying for magnetic activity in the optical, over the radio, is that at radio wavelengths the emission may be highly beamed, as in the auroral case, and thus a detection can be highly dependent on the viewing geometry of the system, but is less dependent on geometry at optical wavelengths (Treumann 2006). These

factors motivate the search for Hα emission, potentially of an auroral nature, in the optical spectrum. We note that optical variability due to weather phenomena is also a compelling reason to observe and monitor the spectra of objects in this spectral range (Heinze, Metchev, and Kellogg 2015).

Our focus is on late L dwarfs and T dwarfs which have received less followup at optical wavelengths than the warmer brown dwarfs but are much brighter in the optical than the cooler Y dwarfs. Much of these initial efforts took place ~10 years ago, prominently by Kirkpatrick et al. (1999), Burgasser et al. (2003) and Cruz et al. (2007), hereafter K99, B03 and C07, respectively. The early studies were not able to get detailed optical spectra for all of the brown dwarfs that emerged from early wide-field infrared sky surveys like the Two Micron All Sky Survey (2MASS; Skrutskie 2006). Moreover, since then, numerous all sky surveys, including the Sloan Digital Sky Survey (SDSS; York 2000), the DEep Near-Infrared Survey of the Southern Sky (DENIS; Epchtein 1997), the Wide-field Infrared Survey Explorer (WISE; Wright 2010), the Panoramic Survey Telescope and Rapid Response System (Pan-STARRS; Kaiser 2002), the United Kingdom Infrared Telescope Deep Sky Survey (UKIDDS; Lawrence 2007), and the Canada-France Hawaii Telescope Legacy Survey (CFHTLS; Delorme et al. 2008), have greatly expanded the number of known late L dwarfs and T dwarfs, many of them bright enough to observe with large ground based telescopes. The growing number of late L dwarfs and T dwarfs, thus allows for a comprehensive assessment of the prevalence of Hα activity for objects of this effective temperature range.

Due to the small number of T-dwarf studies at optical wavelengths, our current observational understanding of their spectra remains defined by the early works, like B03, and the few handful of targets they observed. These early spectra set the optical spectral sequence in this regime and provide the observational archetypes for T dwarf optical spectral features (Kirkpatrick 2005). The prominent features include the pressure-broadened wings of the K I resonant doublet at 7665/7699 Å, other alkali lines from Cs I and Rb I, as well as molecular band-heads of CrH and H_2O (B03; Kirkpatrick 2005). These features are physically interesting because they are sensitive to temperature, gravity, metallicity and the rainout of cloud condensates (Burrows et al. 2002). An expanded collection of optical spectra will thus allow us to examine these features in greater detail.

In this article, we present the results of a new survey of late L dwarfs and T dwarfs at red optical wavelengths looking for Hα emission. In Section 3.2, we discuss

our observations and the target selection for our data sample. In Section 3.3, we present the collection of optical spectra, including literature data and examine the variety of optical spectral features. In Section 3.4, we focus in particular on the Hα emission and the prevalence of potential auroral activity. In Section 3.5, we discuss our findings for a series of particularly interesting objects in our data sample. Lastly, in Section 6.5, we summarize and discuss our results.

Table 3.1: Observing Log

Object	SpT NIR/Opt[a]	UT Date	Filter	Instrument	t_{exp} (s)	Air Mass	References[b]
SDSS J000013.54+255418.6	T4.5/ T5	2014 Dec 22	OG550	DEIMOS	2400	1.18 - 1.25	15, 5
2MASS J00361617+1821104[c]	L3.5/L3.5	2012 Jul 19	Clear	LRIS	5400	1.00 - 1.10	16/13, 17
SIMP J013656.5+093347.3	T2.5/ T2	2014 Dec 22	OG550	DEIMOS	3600	1.01-1.10	1
		2014 Aug 27	OG550	LRIS	2400	1.02 - 1.03	
2MASS J02431371-2453298	T6/ T5.5	2014 Dec 22	OG550	DEIMOS	2400	1.47-1.52	4, 5
SDSS J042348.57-041403.5	T0/ L7.5	2014 Dec 22	OG550	DEIMOS	1800	1.10	11, 5
2MASS J05591914-1404488	T4.5/ T5	2014 Dec 22	OG550	DEIMOS	2400	1.21-1.23	3, 5
WISEP J065609.60+420531.0	T3/ T2	2014 Dec 22	OG550	DEIMOS	2400	1.08	14
2MASS J07003664+3157266[d]	– / L3.5	2014 Feb 03	GG400	DEIMOS	1200	1.24	20
2MASS J07271824+1710012	T7/ T8	2014 Feb 03	GG400	DEIMOS	1800	1.27	4, 5
SDSS J075840.33+324723.4	T2/ T3	2014 May 05	GG495	DEIMOS	2400	1.21 - 1.28	15, 5
WISE J081958.05-033528.5	T4/ T4	2014 May 05	GG495	DEIMOS	2400	1.09-1.10	14
2MASSI J0835425-081923	– / L5	2014 Feb 03	GG400	DEIMOS	1200	1.35	7
SDSSp J092615.38+584720.9	T4.5/ T5	2014 Dec 22	OG550	DEIMOS	2400	1.35-1.38	11, 5
2MASS J09393548-2448279	T8/ T8	2014 Feb 03	GG400	DEIMOS	2000	1.57	19, 5
2MASS J10430758+2225236	– / L8	2014 Dec 22	OG550	DEIMOS	2400	1.03-1.06	8
SDSS J105213.51+442255.7	T0.5/ L7.5	2014 May 05	GG495	DEIMOS	3600	1.10-1.12	6
2MASS J11145133-2618235	T7.5/ T8	2014 Feb 03	GG400	DEIMOS	2000	1.47	19, 5

Continues on next page ...

Object	SpT NIR/Opt[a]	UT Date	Filter	Instrument	t_{exp} (s)	Air Mass	References[b]
2MASS J12314753+0847331	T5.5/ T6	2014 Dec 22	OG550	DEIMOS	2400	1.18-1.25	15, 5
SDSS J141624.08+134826.7	L6/ L6	2014 May 05	GG495	DEIMOS	1800	1.05	2
WISEP J150649.97+702736.0	T6/ T6	2014 May 05	GG495	DEIMOS	2000	1.42	14
2MASSW J1507476-162738	L5.5/ L5	2014 May 05	GG495	DEIMOS	900	1.25	16/13, 15
SDSSp J162414.37+002915.6	T6/ T6	2014 May 05	GG495	DEIMOS	1800	1.07	18, 5
PSO J247.3273+03.5932[e]	T2/ T3	2014 May 05	GG495	DEIMOS	1800	1.12	9
WISEP J164715.59+563208.2	L9p/ L7	2014 May 05	GG495	DEIMOS	2000	1.42	14
2MASS J17502484-0016151	L5.5/ L5	2014 May 05	GG495	DEIMOS	900	1.07	12
2MASS J17503293+1759042	T3.5/ T4	2014 May 05	GG495	DEIMOS	1200	1.07	11, 5
2MASS J17545447+1649196	T5.5/ T5.5	2014 May 05	GG495	DEIMOS	1800	1.11	16
2MASS J21392676+0220226	T1.5/ T2	2014 Aug 27	OG550	LRIS	2400	1.07 - 1.09	10
2MASS J22541892+3123498	T4/ T5	2014 Dec 22	OG550	DEIMOS	2400	1.12-1.17	4, 5

[a] Optical spectral types are from this paper. For NIR spectral types see references.

[b] The first entry is the discovery reference and second the NIR spectral type reference unless otherwise noted.

[c] 2MASS J00361617+1821104 - optical spectral type from Kirkpatrick et al. (2000); observations were taken with the LRIS Dichroic, D560.

[d] 2MASS J07003664+3157266 - optical spectral type from Thorstensen and Kirkpatrick (2003).

[e] RA, = 16 29 18.409, DEC = +03 35 37.10 .

REFERENCES. – (1) Artigau et al. 2006; (2) Bowler, Liu, and Dupuy 2010; (3) Burgasser, Wilson, et al. 2000; (4) Burgasser, Kirkpatrick, Brown, Reid, Burrows, et al. 2002; (5) Burgasser et al. 2006; (6) Chiu et al. 2006; (7) Cruz et al. 2003; (8) C07; (9) Deacon et al. 2011; (10) Faherty et al. 2012; (11) Geballe 2002; (12) Kendall et al. 2007; (13) Kirkpatrick et al. 2000; (14) Kirkpatrick 2011; (15) Knapp 2004; (16) Reid et al. 2000; (17) Reid et al. 2001 ; (18) Strauss 1999; (19) Tinney et al. 2005; (20) Thorstensen and Kirkpatrick 2003

3.2 Data

Sample

We selected our target sample by examining the collection of known brown dwarfs in the literature and culling targets that already had observations at red optical wavelengths. We used the compendium of brown dwarfs at `DwarfArchives.org` as a resource in this endeavor, including new updates to the archive (private communication – Chris Gelino) and also cross checked the Ultracool RIZzo Spectral Library[1]. We gave priority to the brightest and closest targets, using the Database of Ultracool Parallaxes[2] to verify the distances (Dupuy and Liu 2012). We further combined our new observations of these targets with literature T dwarf spectra (discussed in Section 3.2). All together this resulted in the largest compilation of late L dwarf and T dwarf red optical spectra yet assembled.

Observations

We observed our target brown dwarfs at the W. M. Keck Observatory using either the Low Resolution Imaging Spectrometer (LRIS) on Keck I or the DEep Imaging Multi-Object Spectrograph (DEIMOS) on Keck II during the course of several observing nights, mostly in 2014 (Oke et al. 1995; Faber 2003). The observations were designed predominately for the purposes of searching for Hα emission in objects without previous observational limits on the emission strength. However, in our survey we also looked at some objects with previous limits, testing for variability, as well as at targets that may have only had marginal detections, which we sought to confirm. The full observing log for the 29 objects is presented in Table 3.1. We also display the spectra of the 18 objects without previous optical spectra in Figure 3.1 and Figure 3.2.

DEIMOS

The majority of our survey was conducted with Keck/DEIMOS, a multi-slit imaging spectrograph designed for acquiring optical wavelength spectra of faint objects. DEIMOS operates at the Nasmyth focus and includes a flexure compensation system for increased stability. The multi-slit capability utilizes pre-milled masks; however we used the instrument in longslit mode with the standard longslit masks, placing the targets in the 1" (8.4 pixels) wide slit. This mode is regularly used for spectroscopic

[1]Data from the Library Available at `http://dx.doi.org/10.5281/zenodo.11313`

[2]Database accessible at `http://www.as.utexas.edu/~tdupuy/plx/Database_of_Ultracool_Parallaxes.html`

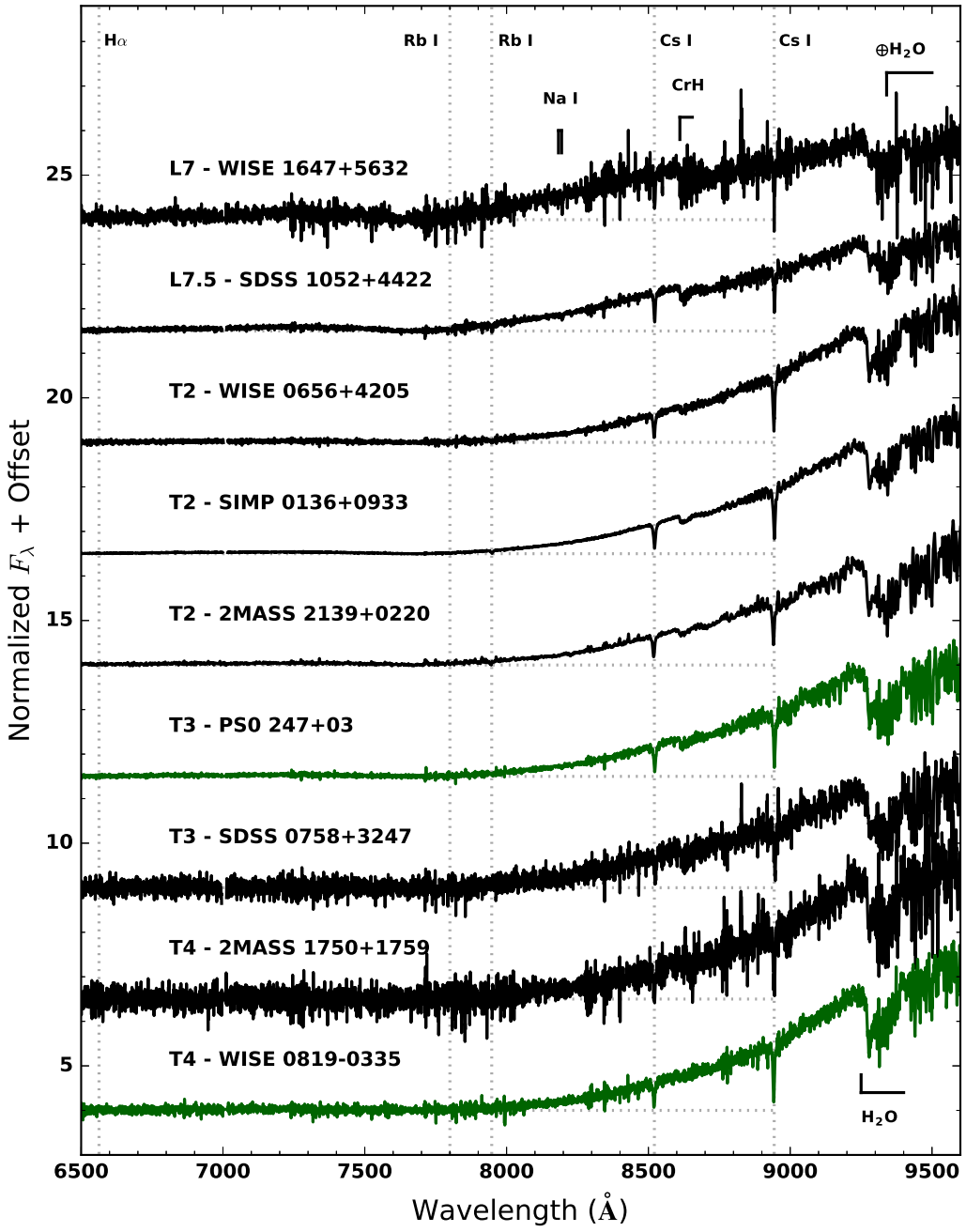

Figure 3.1: Sequence of spectra for objects in our sample without optical spectra in the literature, arranged according to the optical spectral type. The spectra are normalized at 8750 Å with some of the main spectral features noted; see also Figure 3.3. We also note the spectra of objects PSO 247+03 and WISE 0819-0335 as candidates for the optical T3 and T4 spectral standards (shown in green). Note that there is a slight break in the DEIMOS spectra at 7010 Å due to a gap in the DEIMOS detector. All the spectra plotted here were taken with DEIMOS, except for the spectrum of 2MASS J2139+02, which was taken with LRIS.

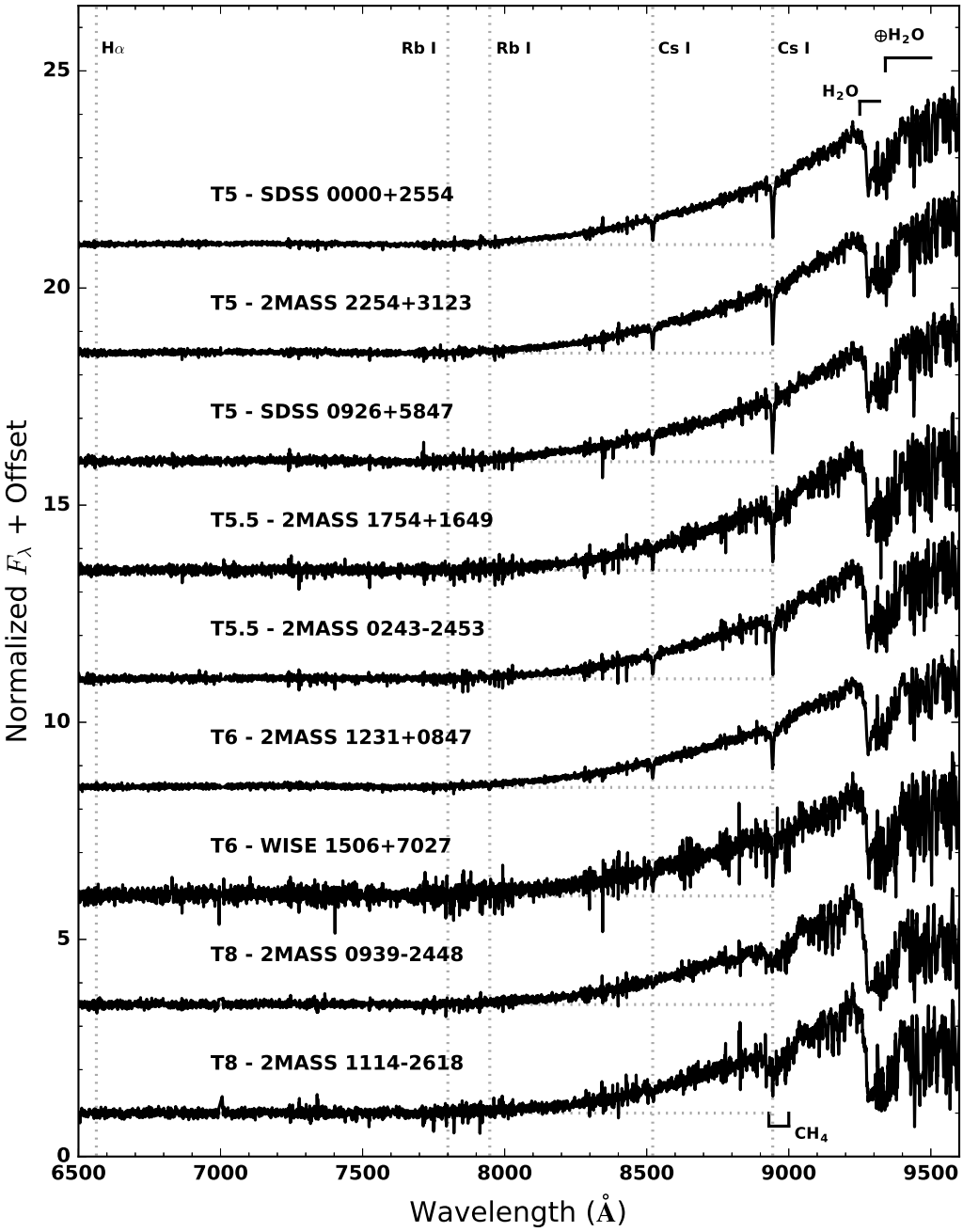

Figure 3.2: Continued from Figure 3.1

followup for the Palomar Transient Factory (PTF; Law 2009). The detector uses a large format 8k x 8k CCD mosaic, consequently the blue and red ends of a single spectroscopic exposure fall on different CCD chips with a small gap between them.

For our observations we used the 600 line mm^{-1} grating blazed at 7000 Å yielding a wavelength coverage from 5000 - 9700 Å and a resolution of 3.5 Å (R $\sim$ 2000) with a dispersion of 0.62 Å pixel^{-1}. The blue extent of the spectra were also limited by the use of order blocking filters to limit the effects of second order light (see Table 3.1). In comparison to the earlier observations in K99, B03 and C07, our observations are at a slightly higher resolution.

Data reduction for these observations was initiated with a modified version of the DEEP2 pipeline utilized by PTF (Cooper et al. 2012; Newman 2013). The pipeline uses the overscan region to bias subtract the raw frames, median combines the dome flats to flat field the raw data, determines the wavelength solution from NeArKrXe arc lamps and returns the 2D spectrum of each slit for both the red and blue CCD chips with cosmic ray rejection routines applied.[3] The rest of the data reduction was handled by custom routines in `Python` with `PyRAF` to rectify the frames, extract the spectra, and flux calibrate.[4]

Since the ultracool dwarfs have very red spectra, up to a couple orders of magnitude flux difference between 7000 Å and 9000 Å, for most targets the spectral flux is barely seen toward the blue end of the detector ($\lambda \lesssim 7000$ Å). Thus, the extractions for each CCD chip were done independently and we therefore used the location of the centroid of the target trace on the red chip in the rectified frames as the central location for the blue chip. We verified that this produced accurate results based on the calibration targets and the brighter L dwarfs with plenty of flux for $\lambda \lesssim 7000$ Å.

Our observations took place on 2014 February 3rd, 2014 May 5th and 2014 December 22nd (UT). At the beginning of the observing night for February 3rd there was fog at the summit; however the dome opened up half way through the night with typical seeing conditions of 1.2". Conditions on May 5th were more favorable, low humidity and 0.8" seeing. December 22nd was also a good observing night with good conditions throughout and 0.7" seeing. Typical exposure times varied between 900 s for the L dwarfs and up to 1800 s for the fainter T dwarfs with

[3]The longslit masks that we used have short breaks along the length of the slit to prevent the slitmask from buckling.

[4]Python Software Foundation. Python Language Reference, version 2.7.10. Available at `http://www.python.org`. PyRAF is a product of the Space Telescope Science Institute, which is operated by AURA for NASA.

multiple exposures for some of the targets. We also observed a standard star from Hamuy et al. (1994) or Massey and Gronwall (1990) each night for the purposes of flux calibrating the spectra. These calibrators were Hiltner 600, HZ44, and Feige 110, respectively, for the three nights. We note that the specific order blocking filter varied for each of the three nights, GG400, GG495, and OG550, respectively.

Although, this did not effect the primary goal of surveying for Hα emission, unlike the other filters, the use of the GG400 filter (observations on Feb. 3rd) limited the ability to flux calibrate the red end of the spectrum due to contamination from second order short wavelength light in the standard star observations. Consequently, we had to make adjustments in order to get flux calibrated spectra for that observing night. We took advantage of the fact that a couple of L dwarf targets we observed that evening, were part of the Ultracool RIZzo spectral library. To get a sensitivity curve for the red chip on that night, we divided the raw extracted spectrum by the literature spectra of the same targets, 2MASSI J0835425-081923 and 2MASS J07003664+3157266AB, took the median of the respective curves and fit a low order polynomial. We subsequently scaled the resulting curve to match the sensitivity function from the blue chip where there was no effect from the second order light. The resulting sensitivity curve agreed reasonably well with similar curves from the other observing nights and the reduced spectra from the night of Feb. 3rd proved to match the expected optical standards rather well (see Section 3.3).

The red end of the DEIMOS spectrum cuts off at ~9700 Å in the middle of a broad telluric H_2O absorption band. This presented an added difficulty in determining the flux calibration for a given night because the telluric band could not be interpolated over when determining the sensitivity function from the spectrophotometric standards. Consequently, the sensitivity function for $\lambda > 9300$ Å is based solely on the polynomial fit at shorter wavelengths. The effect this has on the spectral shape is only significant beyond ~9400 Å where the spectrum is also significantly effected by telluric absorption. Additionally, we did not correct for telluric absorption in any of the DEIMOS spectra. Thus, the effects of the telluric absorption are most prominent in the same region where the flux calibration is most unreliable. This has no impact on the bulk of our analysis as we focus on short wavelength regions; however it does have a small effect on the measurement of the H_2O feature at 9250 Å (see Section 3.3; B03).

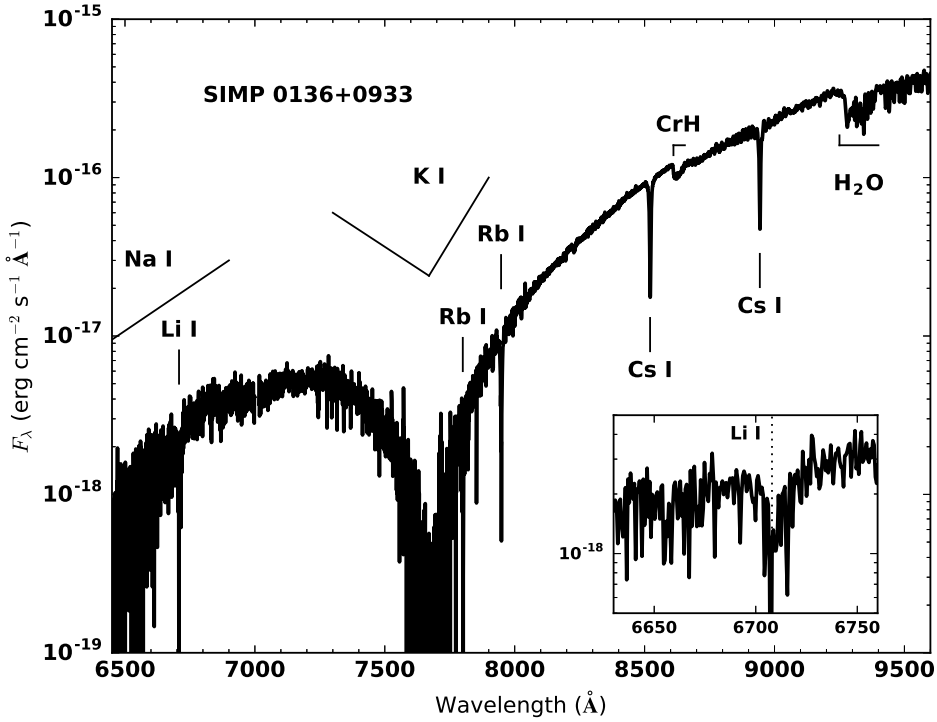

Figure 3.3: The DEIMOS spectrum of SIMP 0136+0933, a T2 brown dwarf. The figure indicates the location of prominent alkali absorption lines and molecular features that shape the optical spectra of T dwarfs and define the T dwarf optical spectral sequence. The inset shows the spectral region around the Li I line, which is clearly detected in this target; see Section 3.5.

LRIS

We observed the spectrum of 2MASS J00361617+1821104 (2MASS 0036+1821) on 2012, July 19th. These observations used the 1200 line mm $^{-1}$ grating blazed at 6400 Å through a 0.7" slit, yielding a wavelength coverage of 5600-7200 Å, and a resolution of $\sim$ 1.7 Å ($R \sim 3700$). The detector was readout with 2x2 binning, yielding a dispersion of 0.81 Å pixel^{-1}. The target was observed for 5400 seconds split into six 900 s exposures. The observations also used the LRIS dichroic D560 with a clear filter through the red arm of the instrument. We also took data with the blue side of LRIS; however, we do not present that data in this paper. These data were reduced with the `longslit` routines in IRAF.[5] The individual exposures were bias subtracted, corrected for pixel-to-pixel gain variation and slit illumination via

[5]IRAF, version 2.16, is distributed by the National Optical Astronomy Observatories, which are operated by the Association of Universities for Research in Astronomy, Inc., under cooperative agreement with the National Science Foundation. Available at `http://iraf.noao.edu`.

dome flats, transformed onto a rectilinear wavelength-sky position grid via internal arc lamps, and finally sky-subtracted by interpolating a polynomial along each row in the sky direction, excluding the target from the fit by sigma-clipping.

We acquired LRIS spectra of SIMP J013656.5+093347.3 (SIMP 0136+0933) and 2MASS J21392676+0220226 (2MASS 2139+0220) on 2014 August 27th. Although LRIS is designed to use a beamsplitter to allow independent and simultaneous observations in a red channel and a blue channel, these observations made use of only the red channel. Since the work of K99 and B03, which used LRIS to obtain optical spectra of late L dwarfs and T dwarfs, the red channel detector has been upgraded, improving the sensitivty (Rockosi 2010).

Our observations on 2014 August 27th used the 400 line mm^{-1} grating blazed at 8500 Å through a 0.7" slit, yielding a wavelength coverage of 6300 - 10100 Å, a resolution of $\sim$ 5 Å ($R \sim 1700$), and a dispersion of 1.33 Å $pixel^{-1}$. The data were taken through a companion program, and accidentally left out the order blocking filter, which meant the flux calibration was not viable from that night's observing (the dichroic was also set to clear). As we did with the February 3rd DEIMOS observations (see Section 3.2), we used the flux calibrated DEIMOS observations of SIMP 0136+0933 from 2014 December 22nd, to calibrate for the rough shape of the LRIS sensitivity function. This did not effect the blue end of the spectrum, nor our ability to measure the Hα emission; however, it created an effective upper limit to the LRIS wavelength coverage of 9700 Å. We reduced the data using standard routines in `PyRAF`. Since the spectral trace becomes very faint in the red, we used the trace for calibration white dwarfs taken before and after the science observations to define the extraction trace for our target brown dwarfs.

In our sample we also include the archival data of the 7 T dwarfs with red optical spectra from the WISE followup of Kirkpatrick (2011), in order to bolster the sample size of T dwarf optical spectra and provide comparisons of the optical features across the full optical sequence to the latest T dwarf spectral types. These objects are the T5, WISE 1841+7000, the T7s, WISE 1019+6529 and WISE 2340-0745, the T8s, WISE 1617+1807, WISE 1457+5815, and WISE 1653+4444, and the T9, WISE 1741+2553. These observations also used Keck/LRIS with similar settings but a wider 1" slit. The reductions and calibrations of those data are described in K99 and Kirkpatrick et al. (2006). These objects were incorporated into the analysis of the optical spectral features (Section 3.3) but not for Hα emission (Section 3.4).

We also used the archival spectra of SDSSp J083717.22-000018.3, SDSSp J102109.6-

030419, and 2MASS J12095613-1004008 to get additional measurements of T dwarf Hα emission (Kirkpatrick et al. 2008). These objects already had measurements of the important optical spectral features (see Section 3.3) but required flux estimates of their Hα emission instead of just equivalent widths (see Section 3.4).

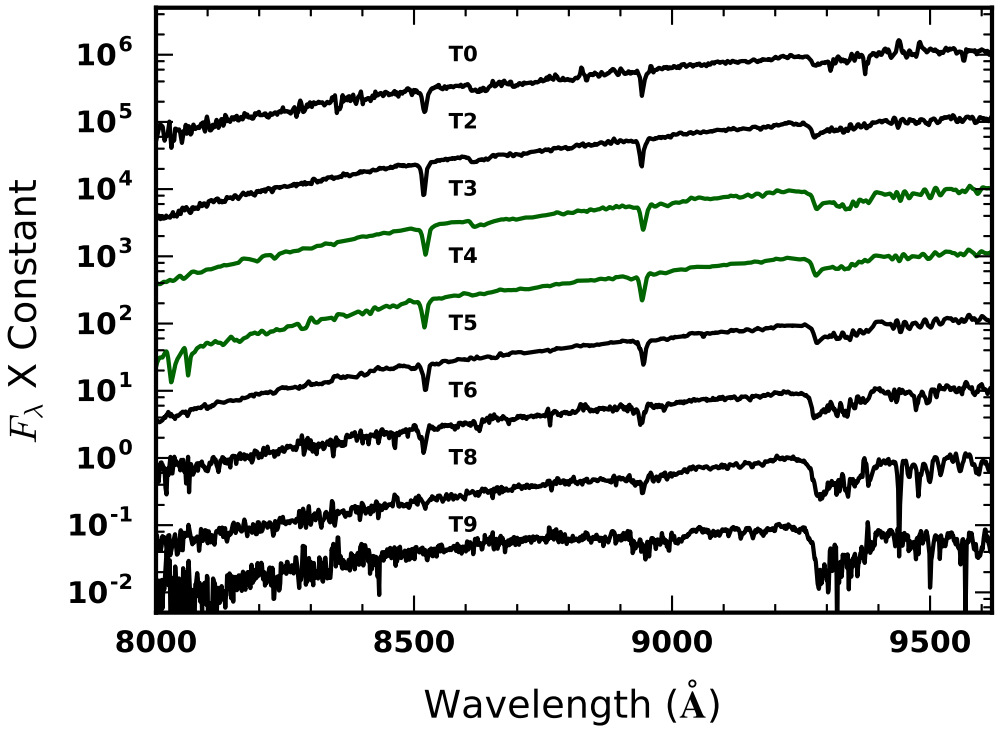

Figure 3.4: The T dwarf optical spectral standards including our new additions for types T3 and T4. The T0 standard is from Kirkpatrick et al. (2008) and the T9 is from Kirkpatrick (2011), while the rest are from B03. The T3 and T4 spectra have not been corrected for telluric absorption but have been convolved here to match the resolution of the literature standards.

3.3 Optical Spectra

Spectral Sequence

To determine the optical spectral types for each object with new optical spectra, we compared the spectra visually with the set of optical spectral standards from L5 to T8. The optical standards are DENIS 1228-1547, for L5 (K99), 2MASS 0850+1057, for L6 (K99), DENIS 0205-1159, for L7 (K99), 2MASS 1632+1904, for L8 (K99), SDSS 0837-0000, for T0 (Kirkpatrick et al. 2008), SDSS 1254-0122, for T2 (B03), 2MASS 0559-1404, for T5 (B03), SDSS 1624+0029, for T6 (B03), 2MASS 0415-0935, for T8 (B03), and WISE 1741+2553, for T9 (Kirkpatrick 2011).

To aid in the visual classification we also convolved the DEIMOS spectra down to the same resolution as the optical standards using a Gaussian kernel. We verified the results of the convolution process by matching our convolved DEIMOS spectra to the literature spectra of the same targets matching the resolution of the standards (ex. 2MASS 0559-1404). The new optical spectral types are included in the Table 3.1 alongside the near-infrared spectral types from Burgasser et al. (2006) or Kirkpatrick (2011). We also show the spectra in Figure 3.1 and Figure 3.2, with the important spectral features detailed closely in Figure 3.3.

Through this comparison we discovered that four of the spectra display features that are clearly between those of the T2 and T5 spectral standards. The morphology is best illustrated by the strength of the CrH absorption, Cs I lines, and the H_2O absorption. This last water feature is at wavelengths that are influenced by telluric absorption in our spectra; however the astrophysical signal completely dominates (see B03). The objects PSO 247+03 and SDSS 0758+3247 showed slightly weaker CrH absorption relative to the T2 standard and slightly stronger H_2O absorption but not as strong as the T5 standard while maintaining strong Cs I absorption. Both of these brown dwarfs have NIR spectral types of T2. 2MASS 1750+1759 and WISEP 0819-0335 show no CrH absorption like the T5 standard but with slightly weaker H_2O and stronger Cs I lines. These two targets have NIR spectral types of T3.5 and T4 respectively. These targets fill the gap in spectral morphologies between T2 and T5 and we propose that PSO 247+03 and WISEP 0819-0335 be considered the optical spectral standards for T3 and T4, respectively. We plot the standards for the T dwarf optical spectral sequence in Figure 3.4. Using these standards, we also update the optical spectral types of SDSSp J102109.6-030419 and 2MASS 12095613-1004008 of T3.5 from Kirkpatrick et al. (2008) to T4.

Spectral Features

Alkali Lines

We measured the set of alkali absorption lines in our new spectra. These are the Cs I lines at 8521 Å and 8943 Å and the Rb I lines at 7800 Å and 7948 Å (K99). Following B03, to measure the absorption strength of each line we simultaneously fit a Lorentz distribution to the line profile and a linear continuum to the 120 Å region centered at the nominal wavelength position of each line. We used a maximum likelihood estimate and a MCMC routine implemented in `Python` to determine the best fit parameters of the model (Patil, Huard, and Fonnesbeck 2010). The

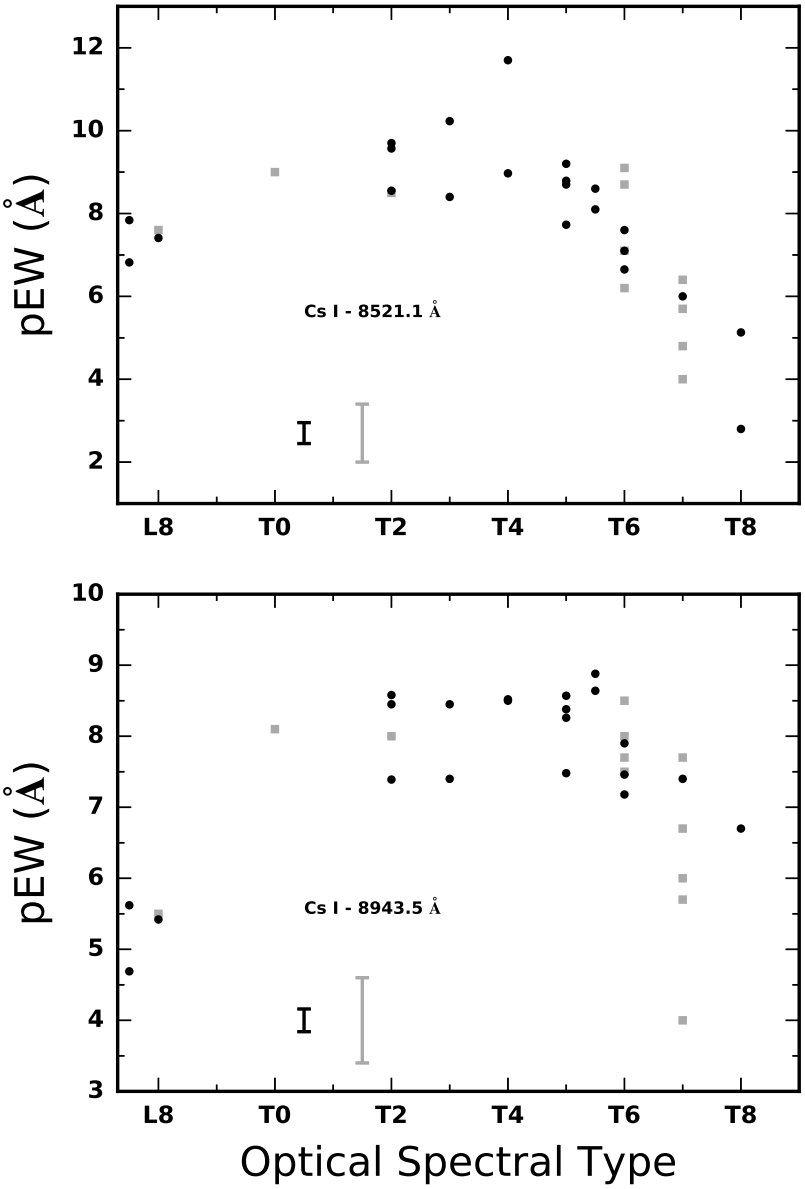

Figure 3.5: The measured pEWs of the Cs I absorption lines at 8521 Å (top) and 8943 Å (bottom) as a function of optical spectral type across the T dwarf sequence. We plotted the values listed in Tables 3.2-3.5 (black circles), and also the literature measurements from B03 (grey squares), including new measurements for the L8 and T0 standards, 2MASS 1632+1904 and SDSS 0837-0000, respectively. We only plot the values with less than 20% uncertainties and include the median full errorbar length in the lower left of each plot. The absorption peaks for T2-T4 objects and declines in late T dwarfs. The scatter at a given spectral type is likely associated with differences in gravity and/or metallicity between the different brown dwarfs. The larger scatter for late T dwarfs in the Cs absorption line at 8943 Å has to do with the onset of a CH_4 band around the location of the Cs line.

likelihood was constructed from the product of the probability of each datum which was assumed to be described by a normal distribution centered at the measured flux for each wavelength with the standard deviation given by the error spectrum. The model is given as

$$S_\lambda = b + m(\lambda - \lambda_0) + \frac{A}{\pi}\frac{\gamma}{(\lambda - \lambda_0)^2 + \gamma^2}\ , \tag{3.1}$$

where λ_0 is the center of the absorption line, A is the total flux absorbed by the line, γ defines the width of the Lorentz distribution, m is the slope of the continuum, and b is the level of the continuum at the center of the line. The pseudo-equivalent widths, pEWs, for each line are computed as

$$\text{pEW} = A/b\ . \tag{3.2}$$

Additionally, we compared the corresponding fit using a Voigt line profile (the convolution of a Lorentz profile with a Gaussian profile) to the Lorentz profile fits. Although the Gaussian component is typically dominant in the core whereas the Lorentz profile dominates in the wings of the line from pressure broadening, we found that in all cases the fit using the Voigt line profile model tended to the Lorentz profile with little to no contribution from the Gaussian component. Gaussian line profile fits also did a poor job of fitting the data compared to the Lorentz profile. Additionally, there is a systematic bias in the measured pEWs depending on the assumed shape of the line profile. An assumed Gaussian profile yields lower pEWs than the corresponding fit using a Lorentz line profile with differences of up to 15%. These results signify the importance of pressure broadening in determining the shape of the absorption line profiles for these high gravity atmospheres.

We report the pEWs for our line profile fits in Tables 3.2-3.5, where we include, in addition to 28 of the targets we observed from Table 3.1 (all except 2MASS 0036+1821), measurements for 3 of the 7 WISE T dwarfs (see Section 3.2) for which we could get decent line fits, and measurements for the L8, T0, and T6 optical standards (using the literature spectra). The T2 and T8 optical standards already have alkali line fitting measurements from B03. Not every line was visible in every spectrum due to the lower flux in the fainter parts of the spectrum. If a line was clearly identified, we fit the line profile as described above. If we detected the continuum but were not able to distinguish a clear absorption line, we determined a 3σ upper limit from the uncertainty in the continuum and the sum of the residuals

in a 40 Å region around the line center after the linear continuum was subtracted. When there was no clear continuum we left the entry in Tables 3.2-3.5 blank. All included, the table includes 34 distinct targets. In Figure 3.5, we plot the pEWs of the Cs I lines as a function of optical spectral type for the T dwarfs with black circles representing our new measurements and the grey squares representing literature data. The peak Cs I absorption across the T dwarf sequence occurs for mid T dwarf spectral types.

Table 3.2: Pseudo-Equvalent Widths: Cs I - 8521 Å

Object	Opt. Spectral Type	λ_0 (Å)	pEW (Å)
2MASS 0700+3157	L3.5	8521.72 ± 0.02	3.64 ± 0.04
2MASS 0835-0819	L5	8521.68 ± 0.01	4.72 ± 0.03
2MASS 1507-1627	L5	8520.42 ± 0.01	5.81 ± 0.03
2MASS 1750-0016	L5	8522.00 ± 0.01	5.84 ± 0.04
SDSS 1416+1348	L6	8519.99 ± 0.01	6.43 ± 0.03
WISE 1647+5632	L7	8521.6 ± 0.2	7.2 ± 0.5
SDSS 0423-0414	L7.5	8521.81 ± 0.02	7.84 ± 0.07
SDSS 1052+4422	L7.5	8521.96 ± 0.06	$6.82 \pm {}^{0.17}_{0.16}$
2MASS 1043+2225	L8	8520.68 ± 0.06	7.41 ± 0.18
2MASS 1632+1904	L8	8520.7 ± 0.1	7.6 ± 0.3
SDSS 0837-0000	T0	8520.5 ± 0.3	$9.0 \pm {}^{0.7}_{6}$
SIMP 0136+0933	T2	8521.77 ± 0.02	9.70 ± 0.06
		8519.07 ± 0.02	10.16 ± 0.06
WISE 0656+4205	T2	8520.52 ± 0.07	9.57 ± 0.23
2MASS 2139+0220	T2	8518.75 ± 0.06	8.55 ± 0.17
SDSS 0758+3247	T3	8524.2 ± 0.3	$8.4 \pm {}^{0.9}_{0.8}$
PSO 247+03	T3	8522.18 ± 0.07	10.23 ± 0.23
WISE 0819-0335	T4	8519.97 ± 0.12	8.97 ± 0.42
2MASS 1209-1004	T4	8522.6 ± 0.3	12.2 ± 0.6
2MASS 1750+1759	T4	8521.1 ± 0.3	$11.7 \pm {}^{1.2}_{1.1}$
SDSS J0000+2554	T5	8521.48 ± 0.07	8.79 ± 0.23
2MASS 0559-1404	T5	8521.565 ± 0.029	7.73 ± 0.10

Continues on next page ...

Object	Opt. Spectral Type	λ_0 (Å)	pEW (Å)
SDSS 0926+5847	T5	8521.07 ± 0.15	9.2 ± 0.4
WISE 1841+7000	T5	$8519. \pm 2.$	$7 \pm \frac{4}{3}$
2MASS 2254+3123	T5	8521.29 ± 0.10	8.7±0.3
2MASS 0243-2453	T5.5	8521.5 ± 0.1	8.6 ± 0.4
2MASS 1754+1649	T5.5	8521.44 ± 0.17	$8.1 \pm \frac{0.6}{0.5}$
2MASS 1231+0847	T6	8521.01 ± 0.13	7.1 ± 0.3
WISE 1506+7027	T6	8522.19 ± 0.28	7.6 ± 0.8
SDSS 1624+0029	T6	8520.68 ± 0.10	$6.65 \pm \frac{0.28}{0.27}$
WISE 1019+6529	T7	. . .	< 19
WISE 2340-0745	T7	8519.9 ± 0.7	6 ± 1
2MASS 0727+1710	T8	8521.2 ± 0.2	$5.13 \pm \frac{0.35}{0.34}$
2MASS 0939-2448	T8	8521.7 ± 0.6	2.8 ± 0.5
2MASS 1114-2618	T8	8523.1 ± 0.5	$4.7 \pm \frac{1.0}{0.8}$

Table 3.3: Pseudo-Equvalent Widths: Cs I - 8943 Å [a]

Object	Opt. Spectral Type	λ_0 (Å)	pEW (Å)
2MASS 0700+3157	L3.5	8943.98 ± 0.02	2.32 ± 0.04
2MASS 0835-0819	L5	8943.903 ± 0.022	$2.56 \pm \frac{0.04}{0.03}$
2MASS 1507-1627	L5	8942.596 ± 0.014	3.41 ± 0.03
2MASS 1750-0016	L5	8944.21 ± 0.02	3.47 ± 0.04
SDSS 1416+1348	L6	8942.07 ± 0.01	3.91 ± 0.03
WISE 1647+5632	L7	8943.8 ± 0.3	4.2 ± 0.6
SDSS 0423-0414	L7.5	8943.86 ± 0.03	5.62 ± 0.06
SDSS 1052+4422	L7.5	8944.27 ± 0.08	4.69 ± 0.16
2MASS 1043+2225	L8	8942.77 ± 0.07	$5.42 \pm \frac{0.16}{0.15}$
2MASS 1632+1904	L8	8942.2 ± 0.3	5.5 ± 0.5
SDSS 0837-0000	T0	8942.5 ± 0.3	8.1 ± 0.7
SIMP 0136+0933	T2	8943.969 ± 0.014	8.58 ± 0.04

Continues on next page ...

Object	Opt. Spectral Type	λ_0 (Å)	pEW (Å)
		8941.35 ± 0.01	8.45 ± 0.04
WISE 0656+4205	T2	8942.54 ± 0.05	8.45 ± 0.15
2MASS 2139+0220	T2	8941.11 ± 0.05	7.39 ± 0.12
SDSS 0758+3247	T3	8946.3 ± 0.2	7.4 ± 0.6
PSO 247+03	T3	8944.17 ± 0.06	8.45 ± 0.16
WISE 0819-0335	T4	8942.00±0.10	8.52±0.26
2MASS 1209-1004	T4	8945.4 ± 0.3	9.7 ± 0.5
2MASS 1750+1759	T4	8942.95±0.27	8.5±0.7
SDSS J0000+2554	T5	8943.81±0.06	8.38±0.15
2MASS 0559-1404	T5	8943.66 ± 0.02	7.48 ± 0.07
SDSS 0926+5847	T5	8943.6 ± 0.1	8.57 ± 0.25
WISE 1841+7000	T5	$8942 \pm 1.$	$13.822077 \pm \frac{4}{3}$
2MASS 2254+3123	T5	8943.59±0.07	8.26±0.18
2MASS 0243-2453	T5.5	8943.71 ± 0.10	8.88 ± 0.23
2MASS 1754+1649	T5.5	8943.68 ± 0.15	8.64 ± 0.37
2MASS 1231+0847	T6	8942.93 ± 0.09	7.46 ± 0.21
WISE 1506+7027	T6	8945.0 ± 0.3	7.9 ± 0.6
SDSS 1624+0029	T6	8942.78 ± 0.09	7.18 ± 0.21
WISE 1019+6529	T7	$8944 \pm \frac{1}{20}$	$5 \pm \frac{5}{3}$
WISE 2340-0745	T7	8942.4 ± 0.5	7.4 ± 0.8
2MASS 0727+1710	T8	8943.43 ± 0.15	6.7 ± 0.3
2MASS 0939-2448	T8	. . .	. . .
2MASS 1114-2618	T8	. . .	. . .

[a] For the L dwarfs the line is confused with a broader molecular absorption band. For the latest T dwarfs the line is obscured by CH_4 absorption.

Table 3.4: Pseudo-Equvalent Widths: Rb I - 7800 Å

Object	Opt. Spectral Type	λ_0 (Å)	pEW (Å)
2MASS 0700+3157	L3.5	7800.96 ± 0.03	4.62 ± 0.08
2MASS 0835-0819	L5	7800.79 ± 0.04	6.51 ± 0.11
2MASS 1507-1627	L5	7799.76 ± 0.04	$9.01 \pm {}^{0.16}_{0.15}$
2MASS 1750-0016	L5	7801.20 ± 0.05	$9.63 \pm {}^{0.20}_{0.19}$
SDSS 1416+1348	L6	7799.24 ± 0.06	11.11 ± 0.22
WISE 1647+5632	L7	...	< 42
SDSS 0423-0414	L7.5	7801.0 ± 0.2	$9.3 \pm {}^{0.7}_{0.6}$
SDSS 1052+4422	L7.5	...	< 23
2MASS 1043+2225	L8	...	...
2MASS 1632+1904	L8	...	...
SDSS 0837-0000	T0	...	...
SIMP 0136+0933	T2	7801.40 ± 0.27	$10.6 \pm {}^{1.2}_{1.1}$
		7798.8 ± 0.6	14 ± 2
WISE 0656+4205	T2	...	< 56
2MASS 2139+0220	T2	...	...
SDSS 0758+3247	T3	...	...
PSO 247+03	T3	...	< 41
WISE 0819-0335	T4	...	< 51
2MASS 1209-1004	T4	...	...
2MASS 1750+1759	T4	...	...
SDSS J0000+2554	T5	...	< 48
2MASS 0559-1404	T5	7800.1 ± 0.5	$12 \pm {}^{3}_{2}$
SDSS 0926+5847	T5	...	< 69
WISE 1841+7000	T5	...	...
2MASS 2254+3123	T5	...	< 108
2MASS 0243-2453	T5.5	...	...
2MASS 1754+1649	T5.5	...	...
2MASS 1231+0847	T6	...	< 35

Continues on next page ...

Object	Opt. Spectral Type	λ_0 (Å)	pEW (Å)
WISE 1506+7027	T6	...	...
SDSS 1624+0029	T6	...	< 44
WISE 1019+6529	T7	...	...
WISE 2340-0745	T7	...	...
2MASS 0727+1710	T8	...	< 23
2MASS 0939-2448	T8	...	...
2MASS 1114-2618	T8	...	...

Table 3.5: Pseudo-Equvalent Widths: Rb I - 7948 Å

Object	Opt. Spectral Type	λ_0 (Å)	pEW (Å)
2MASS 0700+3157	L3.5	7948.38 ± 0.03	4.34 ± 0.06
2MASS 0835-0819	L5	7948.22 ± 0.02	6.18 ± 0.06
2MASS 1507-1627	L5	7947.01 ± 0.02	8.13 ± 0.07
2MASS 1750-0016	L5	7948.485 ± 0.025	$8.15 \pm {}^{0.09}_{0.08}$
SDSS 1416+1348	L6	7946.54 ± 0.02	9.13 ± 0.08
WISE 1647+5632	L7	7947 ± 2	$12 \pm {}^{16}_{6}$
SDSS 0423-0414	L7.5	7948.30 ± 0.07	9.22 ± 0.20
SDSS 1052+4422	L7.5	7948.7 ± 0.3	$8.6 \pm {}^{1.0}_{0.9}$
2MASS 1043+2225	L8	7947.2 ± 0.3	9.6 ± 0.9
2MASS 1632+1904	L8	...	...
SDSS 0837-0000	T0	...	...
SIMP 0136+0933	T2	7948.58 ± 0.12	9.96 ± 0.32
		7945.81 ± 0.13	10.96 ± 0.38
WISE 0656+4205	T2	7948 ± 1	12 ± 3
2MASS 2139+0220	T2	7944.2 ± 0.5	10 ± 1
SDSS 0758+3247	T3	...	< 37
PSO 247+03	T3	$7951 \pm {}^{2}_{1}$	$10 \pm {}^{5}_{3}$
WISE 0819-0335	T4	...	< 33

Continues on next page ...

Object	Opt. Spectral Type	λ_0 (Å)	pEW (Å)
2MASS 1209-1004	T4	...	< 10
2MASS 1750+1759	T4	...	< 89
SDSS J0000+2554	T5	$7950 \pm ^{2}_{1}$	$10 \pm ^{10}_{3}$
2MASS 0559-1404	T5	7948.15 ± 0.25	11.5 ± 0.7
SDSS 0926+5847	T5	...	< 32
WISE 1841+7000	T5	...	...
2MASS 2254+3123	T5	...	< 25
2MASS 0243-2453	T5.5	...	< 41
2MASS 1754+1649	T5.5	...	< 69
2MASS 1231+0847	T6	7946 ± 1	11 ± 3
WISE 1506+7027	T6	...	< 40
SDSS 1624+0029	T6	$7945 \pm ^{1}_{2}$	$10 \pm ^{4}_{3}$
WISE 1019+6529	T7	...	...
WISE 2340-0745	T7	...	...
2MASS 0727+1710	T8	$7949.1 \pm ^{0.5}_{0.6}$	8 ± 2
2MASS 0939-2448	T8	...	< 25
2MASS 1114-2618	T8	...	...

Spectral Ratios

We also examined the series of spectral ratios summarized by B03 in their Table 5, in particular CsI(A), CrH(A), $H_2$0, and Color-e. The ratios measure the respective spectral features indicated, with Color-e corresponding to the overall spectral slope of the pseudo-continuum between 8450 Å and 9200 Å. Before measuring the features, we convolved down our DEIMOS spectra to the same resolution as their LRIS sample, as in Section 3.3, in order to compare their measurements with ours. We also used the line center measurements from the alkali line fitting (Section 3.3) to shift each spectrum to a consistent frame in line with the expected positions of the absorption features. The results are presented in Table 3.6, where we show measurements from 28 of our newly observed targets, all except 2MASS 0036+1821

Table 3.6: Spectral Ratios

Object	SpT Opt	CsA	H_2O	CrH/H_2O	Color-e
2MASS 0700+3157	L3.5	1.3	1.08	1.37	1.71
2MASS 0835−0819	L5	1.41	1.12	1.72	1.56
2MASS 1507−1627	L5	1.56	1.12	1.79	1.56
2MASS 1750−0016	L5	1.53	1.18	1.5	1.56
SDSS 1416+1348	L6	1.61	1.14	1.58	1.78
WISE 1647+5632	L7	1.63	1.29	1.1	1.72
SDSS 1052+4422	L7.5	1.65	1.23	0.98	2.45
SDSS 0423−0414	L7.5	1.77	1.24	1.2	2.02
2MASS 1043+2225	L8	1.66	1.28	0.95	2.16
SIMP 0136+0933	T2	2.3	1.39	0.752	4.06
WISE 0656+4205	T2	2.01	1.42	0.693	4.54
2MASS 2139+0220	T2	2.11	1.61	0.64	3.8
SDSS 0758+3247	T3	1.93	1.63	0.713	3.54
PSO 247+03	T3	2.03	1.65	0.648	3.87
WISE 0819−0335	T4	1.98	1.55	0.615	4.89
2MASS 1750+1759	T4	2.53	1.47	0.663	4.64
SDSS J0000+2554	T5	1.91	1.68	0.55	4.85
2MASS 0559−1404	T5	1.75	1.59	0.579	4.61
SDSS 0926+5847	T5	1.88	1.55	0.59	4.49
WISE 1841+7000	T5	1.87	1.88	0.429	4.87
2MASS 2254+3123	T5	1.84	1.55	0.607	4.9
2MASS 0243−2453	T5.5	1.83	2.17	0.409	5.26
2MASS 1754+1649	T5.5	1.84	2.16	0.412	5.57
2MASS 1231+0847	T6	1.58	2.14	0.42	4.42
WISE 1506+7027	T6	1.77	2.4	0.37	4.23
SDSS 1624+0029	T6	1.62	2.18	0.404	4.26
WISE 1019+6529	T7	2.05	2.57	0.447	4.57
WISE 2340−0745	T7	1.76	2.35	0.381	4.15
2MASS 0727+1710	T8	1.43	2.65	0.329	4.32
2MASS 0939−2448	T8	1.21	5.85	0.147	4.77
2MASS 1114−2618	T8	1.25	5.77	0.151	4.76
WISE 1457+5815	T8	1.47	2.55	0.364	3.62
WISE 1617+1807	T8	1.92	3.15	0.252	3.14
WISE 1653+4444	T8	1.16	2.11	0.408	4.17
WISE 1741+2553	T9	1.07	5.24	0.157	2.46

for which the spectrum did not cover the selected spectral regions, plus the ratios measured for the 7 late T dwarfs in the the literature from WISE (see Section 3.2). We also plot the ratios as a function of optical spectral type in Figure 3.6, focusing on the T dwarf sequence with our newly expanded sample.

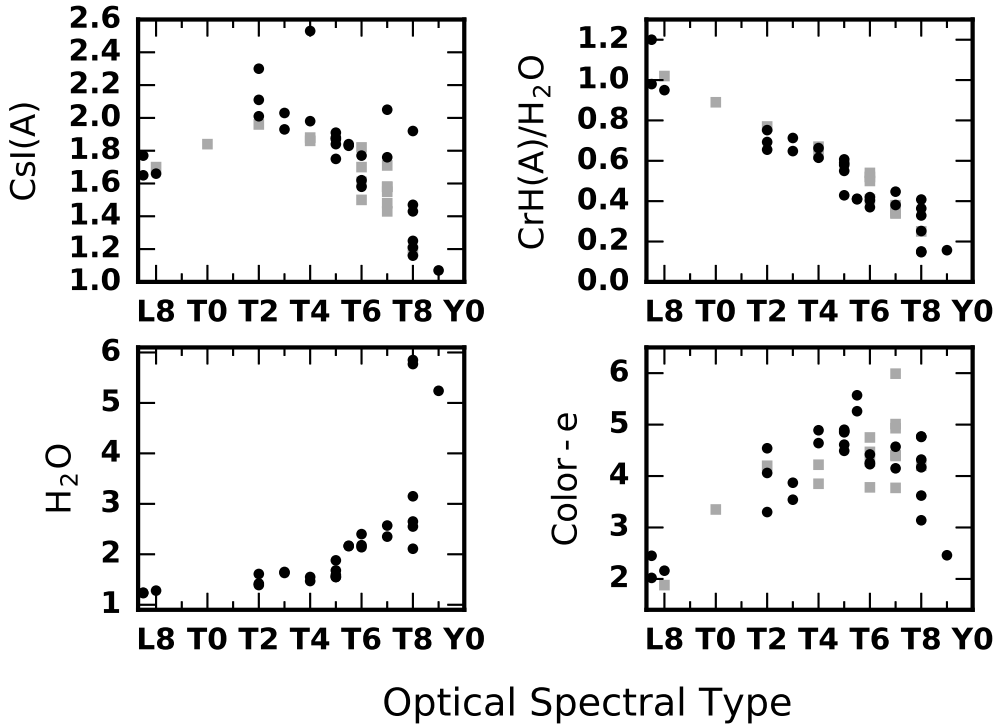

Figure 3.6: The spectral ratios of Table 3.6 as a function of optical spectral type. The black points are our new measurements and the grey squares comprise literature values from B03 and Kirkpatrick et al. (2008). We focus on the T dwarf sequence but show the points down to L7.5 to illustrate how the ratios change across the L/T transition. The CrH(A)/ H_2O ratio shows the clearest and tightest trend with spectral type.

As demonstrated by B03, the ratio of the CrH(A) feature to the H_2O feature tracks the T dwarf optical spectral sequence most clearly (see Figure 3.6, top right). With our expanded data sample, we show that the relation is rather tight throughout the whole T dwarf optical sequence, despite the influence of weak telluric absorption in the H_2O index in our new data (See Section 3.3). A quadratic fit to the spectral types as a function of CrH(A)/H_2O yields a residual scatter that is less than 1 full spectral type. This particular ratio is the best predictor of the overall spectral morphology, whereas features like the overall optical slope or the alkali line depths show considerably

more scatter. Moreover, this ratio combination continues smoothly across the L/T transition.

The H_2O feature, shown in the lower left of Figure 3.6 grows gradually through the optical spectral sequence before greatly increasing for spectral types after T8. Two of our targets with new optical spectra, 2MASS 1114−2618 and 2MASS 0939−2448, showed absorption in line with the T9 optical standard WISE 1741+2553 from Kirkpatrick (2011). These spectra match the overall shape of the T8 standard, however the H_2O band is slightly stronger and agrees well with the T9 standard. Because the overall shape so closely matches the T8 standard, we retain the T8 optical spectral type for these objects, however they likely represent a transition to cooler objects, T9s and even Y dwarfs. These remarks are in line with the results of Burgasser, Burrows, and Kirkpatrick (2006), which determine that these two objects have effective temperatures cooler than the T8 standard with an upper limit of $T_{\rm eff} \lesssim 700$ K.

3.4 Hα Activity

Of particular interest in this study is the prevalence of Hα emission in late L dwarfs and T dwarfs. Most of the spectra did not show a clear indication of Hα emission, see Table 3.7. From our observations, only 2MASS 0036+1821, 2MASS 1750−0016, SDSS 0423−0414, and 2MASS 1043+2225 had excess emission around the location of Hα. We plot the corresponding Hα profiles in Figure 3.7 and in Figure 3.8. To measure this flux we fit a line to the 40 Å region around the nominal location of the emission line, excluding the 6 Å region centered at 6563 Å. We subtracted the linear fit from the spectrum and summed the flux between 6560 and 6566 Å as the flux in the emission line. The uncertainty was determined from the error spectrum for the sum of that region with the uncertainty in the continuum below the line added in quadrature. In Table 3.7, we report the flux measurements with the 1σ uncertainty level as well as the 3σ upper limits.

For these measurements we did not apply the line fitting procedure developed in Section 3.3 for a couple of reasons. Firstly, This approach allowed us to compare our measurements to the values in the literature in a consistent way. Secondly, the line fitting assumes a particular shape for the line profile, which is justified for the absorption lines but not for these emission lines. We did attempt to fit example profiles, Gauss, Lorentz and Voigt, however one did not particularly outperform the

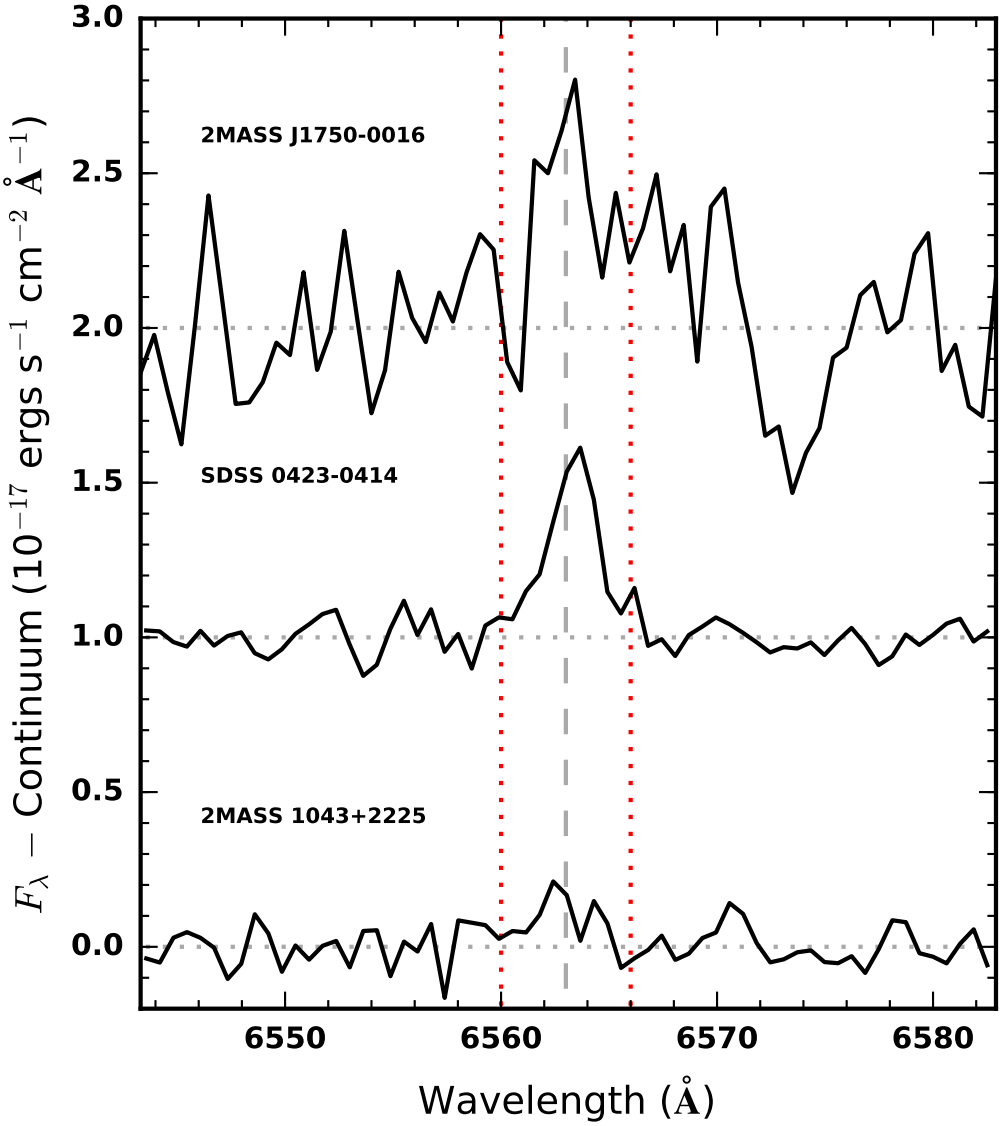

Figure 3.7: Zoom in of the region around the 6563 Å Hα emission line (vertical dashed line) for the spectra of 2MASS J1750-0016, SDSS 0423-0414 and 2MASS 1043+2225. The spectra have the local continuum subtracted and are offset by a constant for clarity with the line center marked by a dashed line. The vertical dotted lines delineate the region used to sum the Hα flux. We report the measurements of these fluxes in Table 3.7.

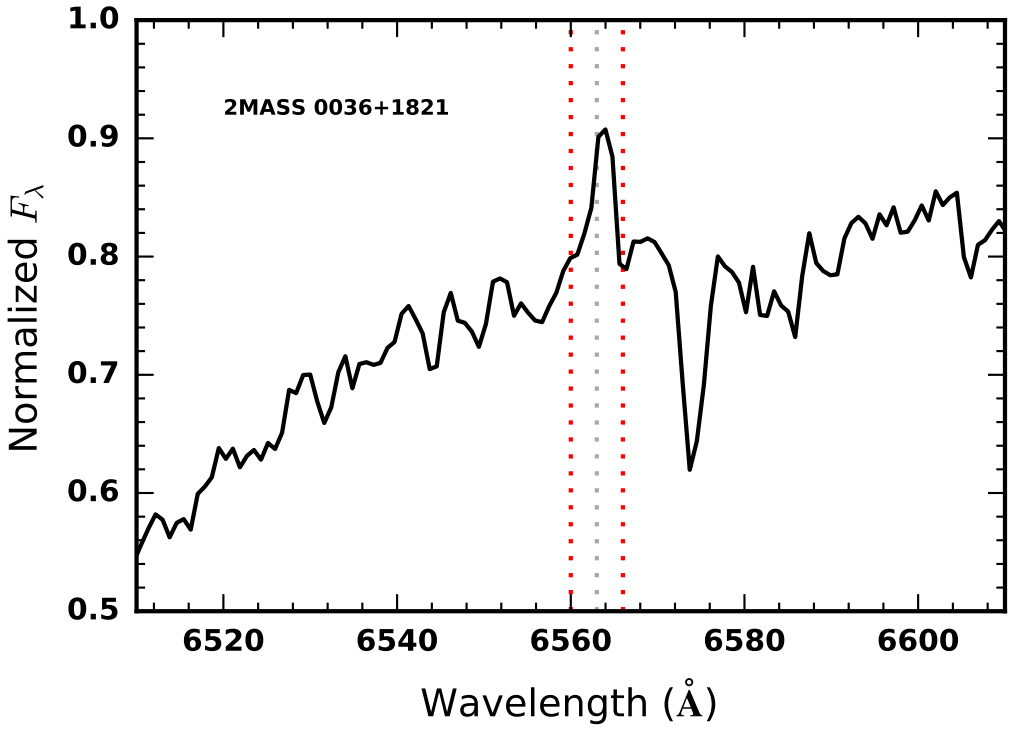

Figure 3.8: The normalized spectrum of 2MASS 0036+1821 in the region around Hα. The dashed line marks the expected position of the emission line and the dotted lines denote the region used to add up the emission line flux once the continuum has been subtracted. Unlike the observations for the targets in Figure 3.7, the spectrum for 2MASS 0036+1821 was not flux calibrated.

others.

We calculated the ratio of the luminosity in Hα to the brown dwarf's bolometric luminosity, $L_{\mathrm{H}\alpha}/L_{\mathrm{bol}}$, by making use of new bolometric corrections from Filippazzo et al. (2015), which uses the newly defined absolute magnitude scale ($M_\odot = +4.74$)[6]. We use the J band bolometric correction as a function of spectral type to determine the bolometric luminosity since it has the least amount of scatter for the field T dwarfs (Filippazzo et al. 2015). The values of $L_{\mathrm{H}\alpha}/L_{\mathrm{bol}}$ for our observations are also listed in Table 3.7. We have also compiled the literature measurements from Burgasser, Kirkpatrick, Reid, et al. (2000), Burgasser, Liebert, et al. (2002), and B03, and report them in Table 3.8, with updated values of $L_{\mathrm{H}\alpha}/L_{\mathrm{bol}}$ based on the new bolometric corrections. For three of the objects with literature measurements shown in Table 3.8, we took new spectra in our current survey with Hα measurements shown in Table 3.7:

[6]The new bolometric corrections are consistent with previous efforts by Liu, Dupuy, and Leggett (2010)

2MASS 0559−1404, SDSS 1624+0029, and 2MASS 0727+1710. Table 3.8 also includes flux measurements for SDSSp J083717.22-000018.3, SDSSp J102109.6-030419, and 2MASS J12095613-1004008, based on archival spectra, which we reanalyzed to provide new limits on the Hα flux.

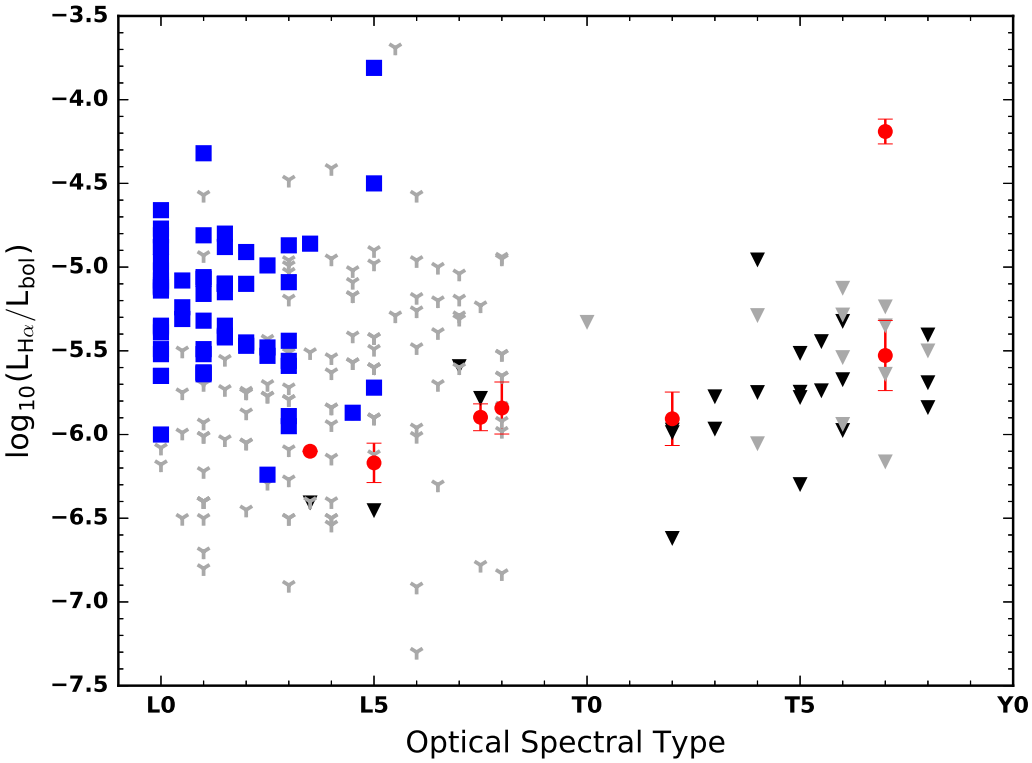

Figure 3.9: The logarithm of the luminosity in Hα relative to an object's bolometric luminosity as a function of optical spectral type. The red points mark measurements listed in Table 3.7 and Table 3.8. Downward triangles mark the upper limits of the same tables with the darker points corresponding to new measurements from this paper and the lighter ones to previous studies of T dwarfs from Burgasser, Kirkpatrick, Reid, et al. (2000) and B03. Literature values for L dwarf emissions as compiled by Schmidt et al. (2015) and supplemented by new measurements from Burgasser et al. (2015a) are included as squares and tri symbols respectively for measurements and upper limits.

In Figure 3.9, we plot $L_{\mathrm{H}\alpha}/L_{\mathrm{bol}}$ as a function of optical spectral type. Measurements in Table 3.7 and Table 3.8 are plotted as red filled circles with new limits as black downward triangles and limits from the literature as grey downward triangles. In the instances in which there were multiple measurements for a single target, either from our observations or in the literature, we plotted a detection, if available, or the most stringent limit for the non-detections. For comparison with earlier spectral types,

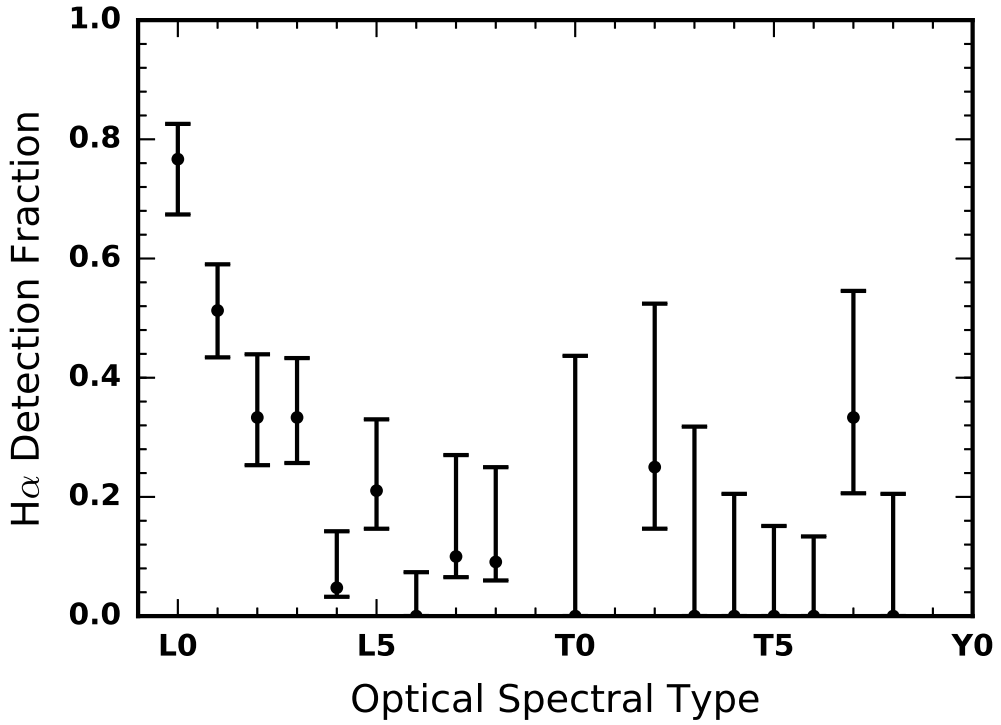

Figure 3.10: The detection fraction of objects as a function of optical spectral type from L dwarfs to T dwarfs based on the compilations by Schmidt et al. (2015), Burgasser et al. (2015a), and this paper. Half spectral types have been rounded down to earlier spectral types and the errorbars represent the 68% confidence interval of the corresponding binomial distribution. At spectral types later than about L4/L5 the prevalence of Hα detections is low.

we have also included measurements (blue squares) and limits (grey tri-symbols) compiled by Schmidt et al. (2015) and supplemented by Burgasser et al. (2015a). These values include measurements from K99, Kirkpatrick et al. (2000), P. B. Hall (2002), Liebert et al. (2003), Schmidt et al. (2007), Reiners and Basri (2008), Burgasser et al. (2011), and Schmidt et al. (2015). We do not distinguish binaries in this plot, but note that for those objects, the optical spectrum is dominated by the warmer component and thus the points are representative of the position corresponding to the primary.

In Figure 3.10, we plot the fraction of objects shown in Figure 3.9 that have Hα detections as a function of optical spectral type from L dwarfs through to T dwarfs. Since the data comes from a variety of sources and surveys with different sensitivity limits there are observational biases inherent to this detection fraction. Additionally, many brown dwarfs have been demonstrated to exhibit variability in their Hα

emission, potentially from rotation (Berger et al. 2009; Hallinan et al. 2015) or longer timescales (see Section 3.5). Thus, objects with only non-detections may yet display emission from further monitoring and/or more sensitive observations, so the detection fractions of Figure 3.10 are systematically low. With these caveats, our extended brown dwarf sample allows us to assess the prevalence of the Hα emission, going from L dwarfs to T dwarfs. The data in Figure 3.10 demonstrates that the declining prevalence of Hα emission, demonstrated for early-to-mid L dwarfs in Schmidt et al. (2015), declines to a low level by L4/L5 spectral types and is consistent with this low level through to late T dwarfs. Although the complete sample presented here does not have the virtue of a consistent detection threshold, as the subsample analyzed by Schmidt et al. (2015) does for the L dwarf activity fractions, putting everything together allows for a straightforward comparison between the T dwarfs and the L dwarfs.

It is clear that the number of objects with Hα emission for spectral types later than about mid-L is low. For all of the L dwarfs in this compilation, 67/195, $34\pm^{3.5}_{3.2}$%, show Hα emission. This detection fraction, however, is skewed by the high number of active early L dwarfs. For mid-to-late L dwarfs (L4-L8), only 7/75, $9.3\pm^{4.5}_{2.4}$%, show Hα emission. For comparison, despite nearly doubling the number of measurements available in the literature for T dwarfs, our results show that most T dwarfs show no emission or very weak emission. Only 3/34, $8.8\pm^{7.4}_{2.8}$%, distinct systems with T dwarf optical spectral types show Hα emission (see Table 3.7 and Table 3.8). Luhman 16B, the nearby T dwarf, also has an EW limit, EW $<$ 1.5 Å, but no flux limit, so we did not include it in Table 3.8 (Faherty et al. 2014). Additionally, the 7 WISE T dwarfs with optical spectra from Kirkpatrick (2011), but no flux measurements, also do not show any indication of Hα emission. Inclusion of these targets leads to the statistic that only 3/42, $7.1\pm^{6.2}_{2.2}$%, of T dwarf systems show this emission feature. Given the broad similarities between the Hα detections of T dwarfs and late L dwarfs, we can also group them together to get an overall detection fraction for optical spectral types L4 - T8 of 10/109, $9.2\pm^{3.5}_{2.1}$%. Inclusion of the additional 8 T dwarfs without flux limits gives, for L4-T9, a detection rate of 10/117, $8.5\pm^{3.3}_{1.9}$%. Since we do not treat binaries separately, these figures could even decrease when accounting for each component in multiple systems.

Interestingly, these detection rates for late L dwarfs and T dwarfs are comparable to the total detection rate, ∼7 %, in surveys looking for brown dwarf radio emission in objects ≥L6 (Kao et al. 2016; Lynch et al. 2016). If auroral processes are

the dominant mechanisms responsible for magnetic emission in late L dwarfs and T dwarfs, these results suggest that geometric beaming of the radio emission is potentially totally absent or may not significantly affect the auroral detection rates.

3.5 Interesting Individual Objects

2MASS 0036+1821

This target is one of the few L dwarfs to exhibit detectable quiescent radio emission, as well as periodic highly polarized radio pulses (Berger 2002; Berger et al. 2005; Hallinan et al. 2008; McLean, Berger, and Reiners 2012). Consequently, there have been numerous studies examining the magnetic activity of this object, looking for X-ray, radio and Hα emission (Berger et al. 2005; Hallinan et al. 2008; Reiners and Basri 2008). Previous studies in the optical report limits on the Hα emission of EW $<$ 0.5 Å and $<$ 1.0 Å from Kirkpatrick et al. (2000) and Reiners and Basri (2008), respectively. The most stringent previous limit comes from a 4 hr monitoring observation by Berger et al. (2005) in which they do not detect anything to a limit of $\log(L_{\mathrm{H}\alpha}/L_{\mathrm{bol}}) \lesssim -6.7$. As the only radio pulsing brown dwarf to not show Hα emission, we decided to observe it further due to the potential association of the radio emission to Hα emission. Our new observations on 2012 July 19th (UT), clearly show an emission feature at 6563 Å with EW = 0.59 ± 0.08 and $\log(L_{\mathrm{H}\alpha}/L_{\mathrm{bol}})$ = -6.1 (see Figure 3.8). Since our spectrum of 2MASS 0036+1821 was not flux calibrated, we did not measure the flux of Hα emission, instead, we used the revised χ factors of Schmidt et al. (2014) to convert the measured EW to $\log(L_{\mathrm{H}\alpha}/L_{\mathrm{bol}})$. This measurement is in line with some of the previous limits; however, the detection greatly exceeds the limit placed by Berger et al. (2005). Although many L dwarfs have been shown to exhibit variable Hα emission, as evidenced in the compilation by Schmidt et al. (2015), the emission is generally not as weak as we have detected for 2MASS 0036+1821, nor have most of these targets been monitored over their full rotational periods. Thus, the intermittent variability that we are detecting, at timescales definitively exceeding the rotational period, represents a new phenomena.

To explain their observed radio emission, Berger et al. (2005) considered the possibility that it could be the result of enhanced activity due to a tidal interaction with a close in companion which orbits on a timescale consistent with the 3 hr period in their data. More recent results, however, positively attribute the radio emission to the ECMI and the periodic signature to a combination of the brown dwarf's rotation and the beaming effect of the emission mechanism (Hallinan et al. 2008). Additionally,

Table 3.7: New Hα Measurements

Object	SpT Opt	f_α (10^{-18} erg s^{-1} cm^{-2})	$\log(L_{H\alpha}/L_{bol})$
2MASS 0036+1821[a]	L3.5	...	−6.1
2MASS 0700+3157	L3.5	< 15	< −6.4
2MASS 0835−0819	L5	< 12	< −6.5
2MASS 1507−1627	L5	< 17	< −6.5
2MASS 1750−0016	L5	21.4 ± 4.8	−6.2 ± 0.1
SDSS 1416+1348	L6	< 18	< −6.6
WISE 1647+5632	L7	< 4.6	< −5.6
SDSS 0423−0414	L7.5	16.3 ± 1.7	−5.9 ± 0.1
SDSS 1052+4422	L7.5	< 4.7	< −5.8
2MASS 1043+2225	L8	4.7 ± 1.5	−5.8 ± 0.2
SIMP 0136+0933[b]	T2	< 4.9	< −6.6
WISE 0656+4205	T2	< 3.1	< −6.0
2MASS 2139+0220	T2	< 4.8	< −6.0
SDSS 0758+3247	T3	< 9.6	< −5.8
PSO 247+03	T3	< 4.5	< −6.0
WISE 0819−0335	T4	< 6.6	< −5.7
2MASS 1750+1759	T4	< 13	< −5.0
SDSS J0000+2554	T5	< 5.7	< −5.7
2MASS 0559−1404	T5	< 5.1	< −6.3
SDSS 0926+5847	T5	< 4.5	< −5.5
2MASS 2254+3123	T5	< 4.8	< −5.8
2MASS 0243−2453	T5.5	< 3.8	< −5.7
2MASS 1754+1649	T5.5	< 5.1	< −5.4
2MASS 1231+0847	T6	< 8.4	< −5.3
WISE 1506+7027	T6	< 5.8	< −6.0
SDSS 1624+0029	T6	< 4.0	< −5.7
2MASS 0727+1710	T8	< 4.2	< −5.7
2MASS 0939−2448	T8	< 2.8	< −5.8
2MASS 1114−2618	T8	< 6.8	< −5.4

[a] The value of $L_{H\alpha}/L_{bol}$ for 2MASS 0036+18 was determined using the measured EW and a χ value 1.415×10^{-6} from (Schmidt et al. 2014), taking the averages for the median χ of spectral types L3 and L4

[b] The value listed for this object is only from the DEIMOS spectrum taken on 2014 December 22nd

Table 3.8: Literature T dwarf Hα Emission

Object	SpT Opt	f_α (10^{-18} erg s^{-1} cm^{-2})[a]	$\log(L_{H\alpha}/L_{bol})$
SDSS 0837−0000[b]	T0	< 4.4	< 5.3
SDSS1254−0122	T2	7.5 ± 2.5	−5.9 ± 0.2
SDSS 1021−0304[bc]	T4	< 8.3	< −5.3
2MASS 1209−1004[bc]	T4	< 1.7	< −6.1
2MASS 0559−1404	T5	< 6.1	< −6.2
2MASS 0755+2212	T6	< 12	< −5.1
2MASS 1225−2739	T6	< 6.7	< −5.5
2MASS 1503+2525	T6	< 9.6	< −5.9
2MASS 1534−2952	T6	< 17	< −5.3
SDSS 1624+0029	T6	< 4	< −5.7
2MASS 0937+2931	T7	< 3.9	< −6.2
2MASS 1047+2124	T7	5.9 ± 2.7	−5.5 ± 0.2
2MASS 1217-0311	T7	< 7.7	< −5.4
2MASS 1237+6526[d]	T7	74.4 ± 0.8	−4.2 ± 0.1
SDSS 1346−0031	T7	< 7	< −5.2
GL570D	T7	< 6.5	< −5.6
2MASS 0415−0935	T8	< 7.9	< −5.5
2MASS 0727+1710	T8	< 3.6	< −5.9

[a] Unless otherwise noted, flux measurements are from Burgasser, Kirkpatrick, Reid, et al. (2000) or B03
[b] Flux values are newly determined from archival spectra
[c] Optical Spectral types are from this paper, updating values presented in Kirkpatrick et al. (2008)
[d] We report the average for this source taken from Burgasser, Liebert, et al. (2002)

the new Hα emission suggests the presence of long-term variability to the magnetic processes.

In the context of auroral radio emission and its potential connection to Hα emission, the intermittent variability of this object can be coherently explained via a potential flux tube interaction between the brown dwarf and a satellite, whose orbit modulates the long-term Hα emission. Energetic electrons moving along the field lines are responsible for the radio pulses and generate the Hα emission when they precipitate into the atmosphere and deposit their energy at the flux tube footpoint. This scenario is analogous to the interaction between Jupiter and its moon Io (e.g. Vasavada et al. 1999). For this scenario to be consistent with the data, the satellite must orbit with a period $\gtrsim$ 8 hrs, or else the monitoring campaign of Berger et al. (2005) should have

seen some indication of Hα emission.

The presence of a potential companion is also consistent with the inclination, i, of this system. Crossfield (2014) report a $v \sin i$ of 40.0 ± 2.0 km s^{-1}, which is a weighted average of the consistent measurements from Jones et al. (2005), Zapatero Osorio et al. (2006) , and Reiners and Basri (2008). Early efforts to understand the magnetic emission from 2MASS 0036+1821 were confounded by the low $v \sin i$ = 15 ± 5 km s^{-1} measurement from Schweitzer et al. (2001). However, Reiners and Basri (2008) attributed that outlying value to mismatches between the observed spectra and the atmospheric models used by Schweitzer et al. (2001). Using a rotational period of 3.08 hrs, $v \sin i$ of 40 km s^{-1} and a radii range between 0.9 $R_{\rm Jup}$ and 1 $R_{\rm Jup}$, for this field brown dwarf, gives the range of inclinations, $i \sim$ 80-90° (Hallinan et al. 2008). During the course of the satellite's orbital evolution, the corresponding flux tube footpoint, the location of the Hα emission, traces a path around the magnetic axis of the brown dwarf. Since the magnetic axis is not likely to be very misaligned with the rotational axis (for example, Jupiter's magnetic axis differs by only $\sim 10°$ from its rotational axis Badman et al. 2015), and since the brown dwarf has a high inclination, it is very plausible that a hidden satellite could be modulating the Hα for this target, the emission being visible during certain orbital phases but hidden on the opposite face of the brown dwarf during others.

Depending on its orbital semi-major axis and orbital inclination, there is a possibility that such a satellite could be transiting the system. For example, an Earth sized satellite around a Jupiter sized brown dwarf would produce a transit depth of $\delta = (R_\oplus / R_{\rm Jup})^2 = 0.008$. Photometric monitoring from the ground by Harding, Hallinan, Boyle, et al. (2013) detected rotational variability in two 5 hour observations in I band observations of 2MASS 0036+1821 with 1% photometric precision, however they did not see any transits. *Spitzer* monitoring with 0.1% photometric precision also detected variability but no transits in their 14 hr observation (Metchev et al. 2015). These observing campaigns could have missed the transit for a longer period satellite, or the object may not be transiting at all. By comparison, Io orbits Jupiter with an 1.77 day period. If an Earth sized planet is placed in a 1.77 day orbit around a 50 $M_{\rm Jup}$ brown dwarf of radius $R_{\rm Jup}$, it would orbit at a distance of about 22 $R_{\rm Jup}$. The plane of the orbit would need to be inclined at an angle, i_p, such that the $\cos i_p < (R_\star + R_p)/r$, for the planet to transit (for $i_p = 0$, the plane of the orbit coincides with the plane of the sky, face on; Winn 2010). Using these orbital parameters gives an inclination of $i_p > 87.1°$; assuming that all orbital inclination

are equally likely gives such a satellite a 3% probability of transiting. If the orbital inclination is consistent with the rotation axis, as it is in many exoplanetery systems, the chances of transiting are much higher Morton and Winn (2014). The current data is suggestive, but more extensive monitoring is required to confirm whether a satellite body is responsible for the long-term modulation of the Hα emission.

J1750−0016

2MASS 1750−0016 is a L5.5 dwarf discovered by Kendall et al. (2007). Only recently was this target observed at optical wavelengths by Burgasser et al. (2015a) and they place an Hα EW emission limit of < 0.4 Å. On the other hand, we detect excess emission at the location of Hα in our DEIMOS spectrum of this target and measure an emission strength of EW = 0.46 ± 0.10 Å (see Figure 3.7 and Table 3.7). Although this emission is rather weak, Burgasser et al. (2015a) report detections of a similar level in some of the other targets in their sample. Our new findings suggest that this target could have variable Hα emission like 2MASS 0036+1821 or many of the variable targets compiled by Schmidt et al. (2015).

SDSS 0423-0414AB

This target was revealed to be a binary system by Burgasser et al. (2005) in HST NICMOS imaging, with a L6 primary and T2 secondary. The target also showed strong Hα emission, with EW = 3 Å and strong Li I absorption, with EW = 11 Å (Kirkpatrick et al. 2008). We used our new DEIMOS observations to once again measure these features, looking for indications of variability. We measured the Hα emission, as described in Section 3.4, to be EW = 2.95 ± 0.30. This value is consistent with the values reported in the literature, suggesting that the emission may be steady across several year time scales.

We also compared the different measurements of the Li I absorption. We applied the alkali line fitting from Section 3.3 to both our new DEIMOS spectrum and the previous LRIS spectrum from Kirkpatrick et al. (2008). Both spectra yielded consistent results; however they were systematically higher than the reported values in the literature. This is likely due to the fact that the Lorentz line profile includes absorption in the wings of the distribution that may not be included by simply subtracting a continuum and adding up the flux in a predefined region around the line center. For consistency with the literature, we report an EW = 11.1 ± 0.4, in line with the literature value.

SDSS 1052+4422

This target had been designated as an early T dwarf (T0.5) by Chiu et al. (2006) in their discovery paper, based on the NIR spectrum. However, Dupuy et al. (2015) showed that SDSS 1052+4422 is actually a binary system from adaptive optics imaging. Their detailed study was able to determine dynamical masses of each component based on astrometric monitoring (Dupuy et al. 2015). They also decomposed the composite NIR spectrum from the IRTF/SpeX library and determine spectral types of L6.5 ± 1.5 and T1.5 ± 1.0 (Dupuy et al. 2015). Our new integrated light optical spectrum of this target fit between the L7 and L8 optical standards, and we assigned it a spectral type of L7.5. Our observations are thus consistent with the binary decomposition of L6.5 and T1.5, and provide further constraints on the properties of these objects. Binary systems like these, straddling the L/T transition, are important benchmarks for understand the evolution of brown dwarfs. For a given system, a large discrepancy between the NIR integrated light spectral type and the optical integrated light spectral type can be used as an indicator of a potential binary. This highlights the ability of optical spectra, as a counterpart to the NIR spectra, to be a useful diagnostic in verifying binary systems (see also Manjavacas et al. 2015).

2MASS 1043+2225

2MASS 1043+2225 is a late L dwarf reported by C07 to have tentative indications of Hα emission. Although they see excess flux at the location of Hα, their results were inconclusive. Our new observations of this target confirm that this object does indeed exhibit weak Hα emission at a level of $\log(L_{\mathrm{H}\alpha}/L_{\mathrm{bol}}) = -5.8 \pm 0.2$ (see Table 3.7). The detection is only just at the 3.1σ level, very similar to the weak detections of 2MASS 1047+2124 and 2MASS 1254-0122 from B03. We show the spectrum of this target around the Hα line in Figure 3.7.

For this object, we also report a tentative detection of Li I at 6708 Å. In Figure 3.11, we show this region of the spectrum alongside the the spectrum of C07, taken from the Ultracool RIZzo Spectral Library. We measured the absorption to have an EW = 10 ± 3 Å, in line with the typical EW of L8 dwarfs with Li I detections (Kirkpatrick et al. 2008). Our more recent, higher resolution, observation shows that there may be an absorption feature there; however, the earlier spectrum does not. We consider this to be a tentative detection which will require deeper observations to confirm. If the absorption is real, this target would be added to the few very late L dwarfs and T dwarfs to display this important physical indicator of mass and age.

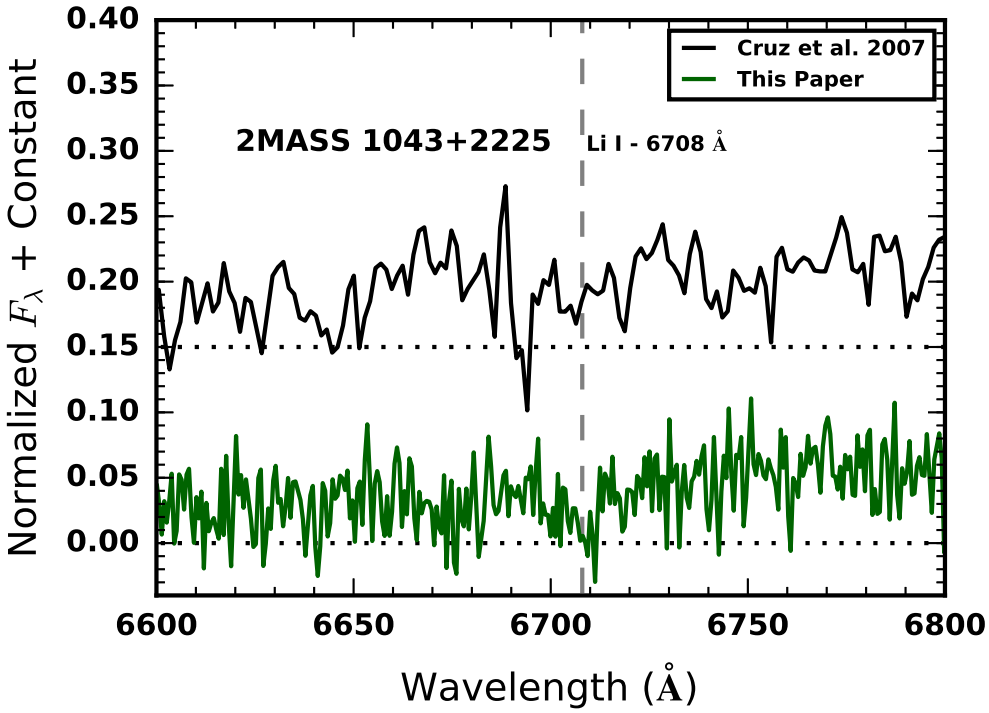

Figure 3.11: The spectra of 2MASS 1043+2225 zoomed in around the location of the Li I line at 6708 Å, showing both the spectrum from C07 (top; from the Ultracool RIZzo Spectral Library) and our DEIMOS spectrum (bottom). Our new spectrum shows a dip in the observed flux that could be Li I absorption; however the previous spectrum from C07 only shows a small trough, in line with the continuum noise. We consider the corresponding lithium detection for this target as tentative.

WISE 1647+5632

This target is included in the WISE discoveries from Kirkpatrick (2011) and has a preliminary parallax placing it within 10 pc of the Sun. Kirkpatrick (2011) assigned this object a NIR spectral type of L9 peculiar from an IRTF/SpeX spectrum, noting the discrepancies at H and K band between the spectrum and the standards. They added this object to a collection of unusually red L dwarfs. However, our optical spectrum of this target matches the L7 standard very well (see Figure 3.12). Our findings suggest that WISE 1647+5632 is likely an unresolved binary system straddling the L/T transition.

2MASS 2139+0220

This target is one of the prominent T dwarfs with high amplitude variability in the J band, displaying up to 26% variability (Radigan et al. 2012). We included it in

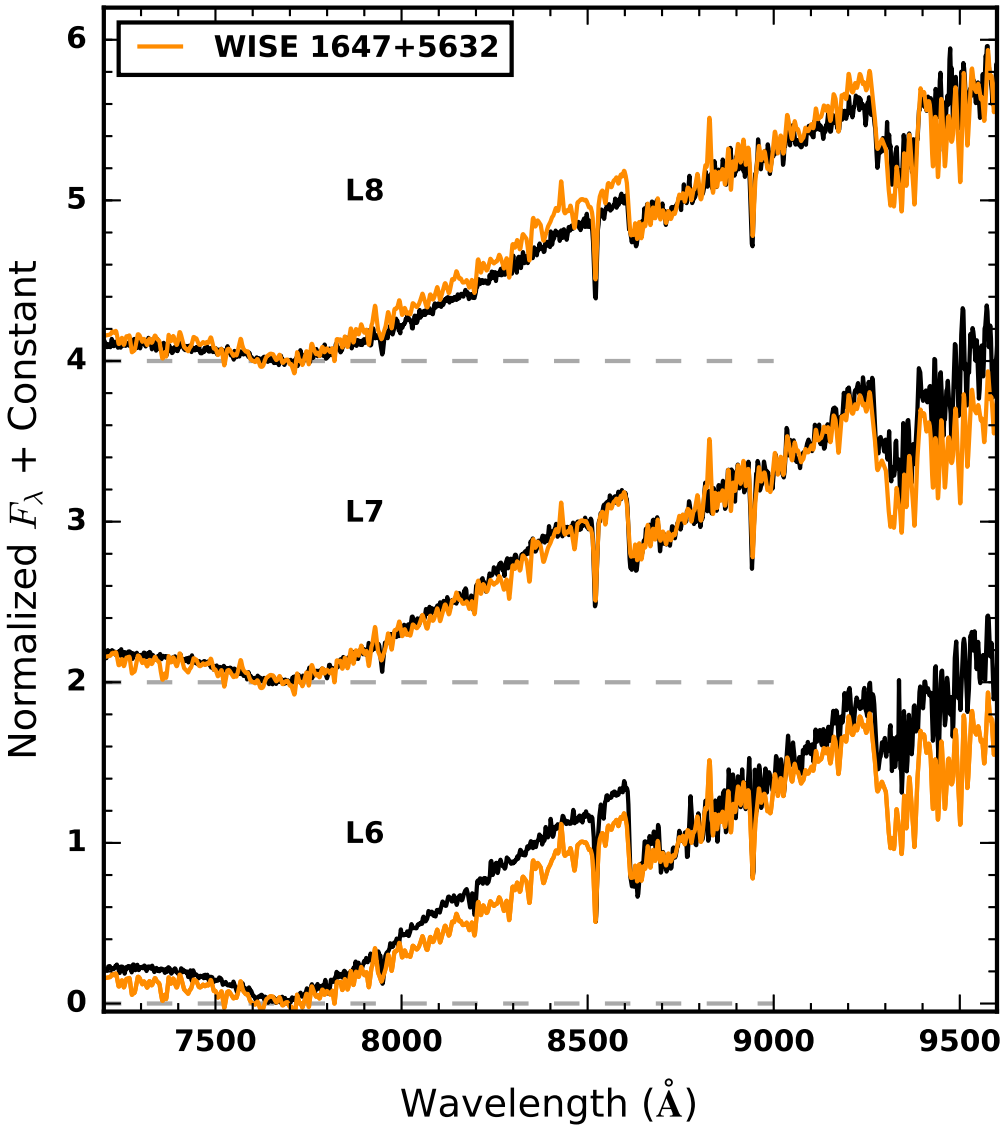

Figure 3.12: A comparison of the DEIMOS spectrum of WISE1647+5632 (orange) against the optical standards for spectral types L6, L7 and L8 (black). The best match is produced by the L7 standard. This spectral type differs greatly from the NIR spectral type of L9p, and suggests that this target may be an unresolved binary (see Section 3.5)

the sample to investigate if there could be any connection between the magnetic emissions and the cloud phenomena. We did not find any Hα emission and report an emission upper limit of EW < 8 Å. There have also been some suggestions that this object could be a binary due to its somewhat peculiar NIR spectrum (Bardalez Gagliuffi et al. 2014). Our observed spectrum matches the T2 optical spectral standard very well. This corroborates findings by Manjavacas et al. (2015) which rule out this scenario. The peculiar spectrum is thus, likely a consequence of a patchy atmosphere and the impact of cloud variability on the emergent spectral flux.

SIMP 0136+0933

SIMP 0136+0933 is one of the archetypes for cloud variability at the L/T transition; it was found to exhibit 50 mmag photometric variability in J band and has since been followed up throughout the infrared to characterize the patchy cloud structures of its atmosphere (Artigau et al. 2009; Apai et al. 2013; Radigan et al. 2014). As a potentially very interesting object in the context of auroral activity, we observed it with LRIS on 2014 August 27th, and again with DEIMOS on 2014 December 22nd. In the first epoch we took two consecutive 1200 s exposures, whereas in the second epoch we took two exposures of 1800 s each, separated by 1.5 hrs.

In no exposure did we detect any excess flux at the location of the Hα line. We measured stringent limits on the corresponding emission line flux of SIMP 0136+0933 from the co-added DEIMOS spectrum (see Table 3.7). Because we detect the underlying continuum in the combined spectra, for this target, we also report EW emission limits of < 3.2 Å and < 3.5 Å for the August and December nights, respectively. In the context of auroral emission, which may be rotationally modulated, the 1.5 hrs of separation between the exposures in December correspond to a phase shift of 0.63, using the photometric rotational period of 2.39 hrs (Apai et al. 2013). Although, it remains possible that we missed potential optical auroral emission from this source, the series of observations at different phases suggest that it may indeed lack Hα emission.

Our high signal-to-noise ratio spectrum, S/N ~ 6 at 6800 Å and S/N ~ 96 at 8600 Å, of SIMP 0136+0933 also allowed us to look for the presence of Li at 6708 Å. We plot this spectrum in Figure 3.3 with the inset zoomed in on the location of

[7] Disentangling the effective temperature, gravity and cloud effects remains a challenging problem in brown dwarf atmospheric modeling and depending on the different assumptions can yield differing answers, even when good data are available (Marley, Saumon, and Goldblatt 2010; Apai et al. 2013; Faherty et al. 2014; Marley and Robinson 2015).

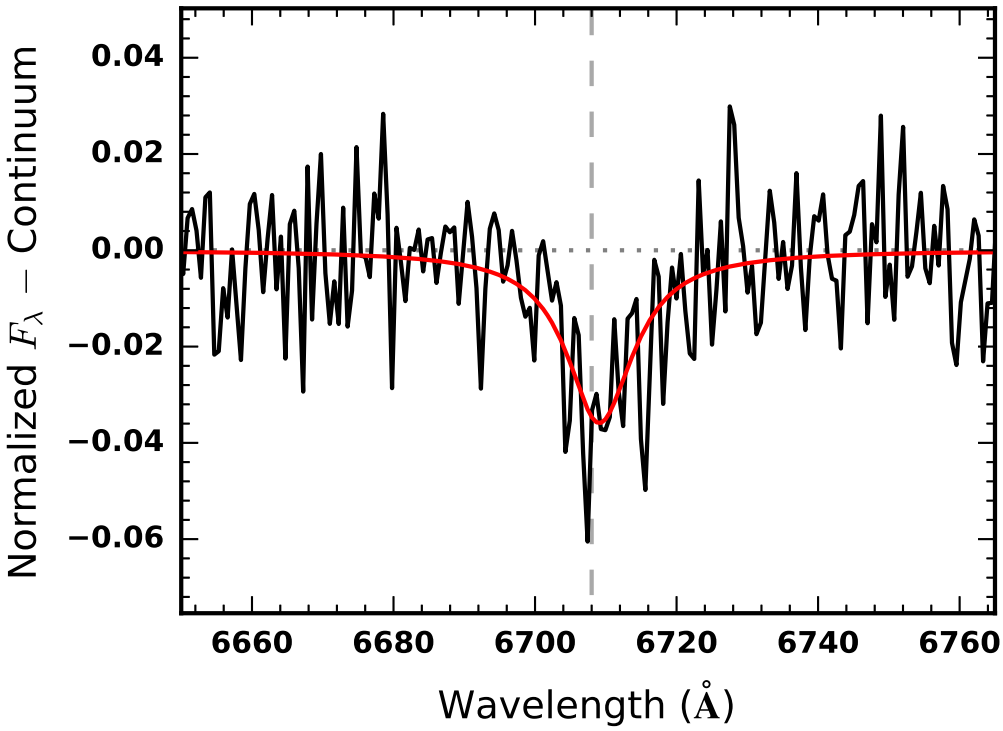

Figure 3.13: The spectrum of SIMP 0136+0933 around the Li I line at 6708 Å. The spectrum is normalized with the continuum profile subtracted. The line corresponds to a Lorentz line profile model fit of the data (see Section 3.3).

the Li I absorption. It is clearly present. We fit the absorption line as we fit the other alkali lines in Section 3.3 with a Lorentz line profile and over-plotted the model result in Figure 3.13. As in the case of SDSS 0423-0414, we report EW values not based on the fit but a simple summation of the absorption line region (see Section 3.5). We measure EW values of 6.6 ± 1.0 Å and 7.8 ± 1.0 Å for the August and December observations respectively. SIMP 0136+0933 joins the T0.5 dwarf, Luhman 16B (EW = 3.8 ± 0.4), as the second T dwarf and the latest spectral type object with a clear lithium detection in its atmosphere (Faherty et al. 2014). Although the spread of the values between the two objects is in line with the spread of detections for L8 dwarfs from Kirkpatrick et al. (2008), this absorption appears to be particularly strong by comparison given that SIMP 0136+0933 has a later spectral type and possibly cooler atmosphere[7]. As Lodders (1999) discussed, the Li I in the atmosphere becomes readily depleted by the formation of LiCl gas and other Li bearing substances like LiOH in cool dwarf atmosphere below temperatures of about 1600 K. Kirkpatrick et al. (2008) showed that the peak of Li I absorption takes

place around a spectral type of L6.5 and declines for later spectral types.

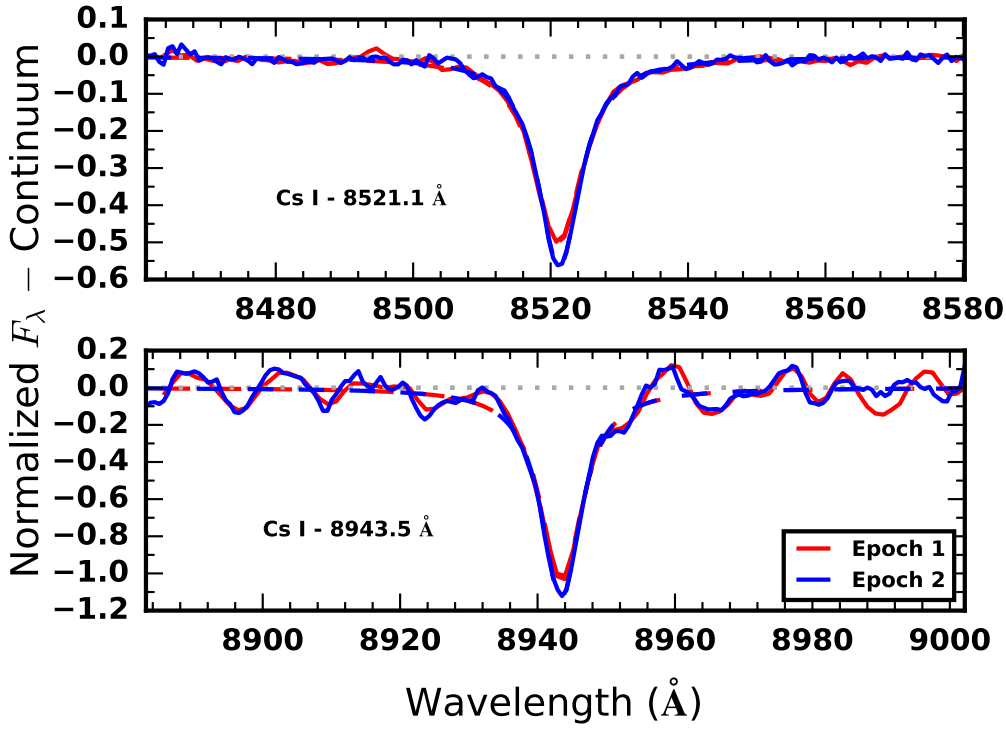

Figure 3.14: The Cs I absorption lines of SIMP 0136+0933 between the observations in August and December plotted as solid lines and the Lorentz line profile model fits plotted as dashed lines. The pEWs of the lines are significantly different and likely reflect spectroscopy variability between the two observations for this photometrically variable target; see Section 3.5

Thus, the strong Li I of SIMP 0136+0933 is somewhat anomalous; howevers it is interesting to note that in addition to SIMP 0136+0933, Luhman 16B also exhibits cloud variability (Crossfield et al. 2014; Burgasser et al. 2014). The presence of Li may be related to the transition from L to T spectral types within a patchy cloud atmosphere [8]. Indeed, although our Li I EW measurements from the different epochs are formally in agreement within the 2σ level, the central values differ by 15%. If this is due to cloud phenomena in the atmosphere, the spectra from the different epochs could be dominated by flux from atmospheric levels with differing Li I depletion.

The two different epochs did allow us to observe spectroscopic variability in the other optical absorption lines. We note that the difference of the pEWs in the

[8] We did not see any indication of Li I in our LRIS spectrum of 2MASS 2139+0220; however there was not enough signal in the continuum to definitively rule it out.

co-added spectra from the two epochs, for the lines reported in Tables 3.2-3.5, are statistically significant. This is especially true of the Cs I lines where the signal-to-noise ratio is greatest. For the first epoch, 2014 August 27th, we measured pEWs of 10.16 ± 0.06 Å and 8.45 ± 0.04 for the Cs I lines at 8521 Å and 8943 Å respectively. For the second epoch, 2014 December 22nd, we measured pEWs of 9.70 ± 0.06 Å and 8.58 ± 0.04 for the same lines, respectively. The difference between the pEW measurements for the Cs I line at 8521 Å is different from 0 at the 5.4σ level and similarly at the 2.3σ level for the Cs I line at 8943 Å. The Rb I lines at 7948 Å were measured to have pEWs of 10.96 ± 0.38 Å and 9.96 ± 0.32 Å for epoch 1 and epoch 2, respectively, yielding a difference that is significant at the 2σ level. In Figure 3.14, we plot a comparison of these spectral line profiles with the continuum subtracted and the corresponding Lorentz profile model fits (see section 3.3).

The pEW measurements track the changes in the absorption relative to the nearby pseudo-continuum. The two different Cs I line observations did not show the same degree of variation, suggesting that this variability may be driven as much by differences in the relative continuum in the different parts of the spectrum as in the individual absorption line strength. These results provide support for the interpretation of cloud variability in the atmosphere of this object and supports the idea that there could be significant optical variability to coincide with the large-amplitude NIR variability, potentially even in the Li I absorption. In fact, Heinze, Metchev, and Kellogg (2015) showed that photometric optical variability in brown dwarfs could be stronger than the NIR variability and Buenzli et al. (2015) used *Hubble Space Telescope* grism observations to demonstrate spectroscopic variability from 0.8 μm to 1.15 μm in both components of Luhman16AB.

3.6 Discussion and Summary

We have conducted a new survey at red optical wavelengths (6300 Å - 9700 Å) looking for Hα emission in a large sample of late L dwarfs and T dwarfs. We acquired new optical spectra for 18 targets without previous spectra and several additional spectra looking for potential variability in the emission features. We have nearly doubled the number of red optical spectra available for T dwarfs and used our new observations, in conjunction with available spectra, to examine prominent spectral features and the optical T dwarf sequence.

Our findings include two objects that fill the gap between the T dwarf optical spectral standards from T2 - T5. We proposed PSO 247+03 as the T3 spectral standard and

WISE 0819-0335 as the T4 spectral standard. These two targets are relatively bright and are both near the equatorial plane, allowing for observational access from both the northern and southern hemispheres.

We also observed Li I absorption at 6708 Å in the spectrum of SIMP 0136+0933, one of the most prominent IR photometric variable brown dwarfs. This object becomes only the second T dwarf and the latest type object to display this feature. We also see spectroscopic variability in the strength of the absorption lines that is likely related to the heterogeneous cloud phenomena present in the atmosphere.

Our survey included new Hα detections for 2MASS 0036+1821, 2MASS 1750−0016, and 2MASS 1043+2225 and many more limits on the Hα flux for late L dwarfs and T dwarfs (see Section 3.4). Our focus on these objects has allowed us to investigate the prevalence of magnetic activity in objects with low temperature atmospheres. The persistent magnetic emissions of many objects in this regime and the discovery of continued activity, even in late T dwarfs points to deficiencies in the understanding of magnetic atmospheric processes and/or new phenomena that fall outside of the standard paradigm of stellar activity.

For the warmer UCDs, chromospheric emission may still persist. Recent work by Rodriguez-Barrera et al. (2015) on the ability of UCD atmospheres to become magnetized suggests that the plasma conditions may allow for objects to remain magnetized down to an $T_{\rm eff} \sim 1400$ K, 900 K cooler than the similar magnetization threshold considered by Mohanty et al. (2002). This lower threshold is similar to the typical effective temperatures of L4/L5 dwarfs (Kirkpatrick 2005) and would coincide with where we see the detection of Hα emission bottom out (see Figure 3.10). However, for even cooler objects, the strong optical and radio emissions of some objects remain difficult to explain.

The emergence of the ECMI as a coherent explanation for the periodic radio emissions of numerous studies across the UCD regime provides an alternative. These studies argue that auroral processes are capable of driving the periodic radio and optical emissions that have been observed and are also consistent with potential long-term variability (see Section 3.5). The benchmark objects that have been used to investigate these processes have predominantly been systems of either late M or early L spectral types. These kinds of objects might exhibit both auroral and/or chromospheric emissions, requiring detailed study to distinguish. This confusion is alleviated when examining the population of late L dwarfs and T dwarfs with atmospheres for which standard Solar-like magnetic processes have difficulty generating

chromospheric emissions, due to the highly neutral atmospheres. If the Hα emission in these objects is connected to the radio auroral emission, then the prevalence of this emission provides an estimate of the overall occurrence rate of auroral activity.

Our measurements of T dwarf Hα emission revealed that this activity indicator is less common than previously thought. B03 found three T dwarfs in about a dozen objects to exhibit this emission: two weak emitters and one very strong emitter. Our new observations and other work since their initial efforts show that the emission in this regime is actually much rarer and likely only seen in ~7% of T dwarf systems. When considering objects of spectral type from L4-T8, the detection rate remains only $9.2\pm^{3.5}_{2.1}$ % (as low as $8.5\pm^{3.3}_{1.9}$% for L4-T9). It is possible that some of these targets exhibit variability and we did not observe the targets at the right point in time to catch the emission; however that is unlikely to be the case for all of the targets. Nevertheless, only extended monitoring of each target will be able to rule out that scenario.

Even if the occurrence rate of auroral activity is well characterized by our Hα detection rate of ~10 %, the question of the nature of the underlying mechanism that governs the emission still remains. Rodriguez-Barrera et al. (2015) point out that, despite having less magnetized atmospheres, objects with $T_{\rm eff} < 1400$ K are capable of sustaining significant ionospheres and driving auroral emission processes. Schrijver (2009) and Nichols et al. (2012) point to a rotation dominated magnetospheric-ionospheric coupling current system as the underlying mechanism for the auroral emissions capable of generating strong surface emission features near the magnetic poles. However, what determines whether an object displays auroral emission or not? One clue might be the long-term variability we have detected in the Hα emission of 2MASS 0036+1821. Within the auroral context, if this emission is proved to be related to the presence of satellites, then our observed detection rate for late L dwarfs and T dwarfs may reflect the satellite occurrence rate.

Comparing our overall Hα detection rate to surveys of brown dwarf radio emission revealed that radio and Hα detection rates in late L dwarfs and T dwarfs are comparable, suggesting that if the emission is auroral then geometric beaming may not play a prominent role in the detectability of the radio aurorae. Consequently, the sample of Hα emitting brown dwarfs are potentially excellent targets to pursue with sensitive radio telescopes, like the *Jansky Very Large Array*. These magnetically active brown dwarfs will be important benchmark objects for understanding not only magnetospheric processes across the brown dwarf regime from planets to stars

but also for understanding magnetic dynamos in fully convective objects (Kao et al. 2016) and examining the upper atmospheric structures of brown dwarfs.

Acknowledgments

The authors wish to recognize and acknowledge the very significant cultural role and reverence that the summit of Mauna Kea has always had within the indigenous Hawaiian community. We are most fortunate to have had the opportunity to conduct observations from this mountain.

The authors would like to thank the anonymous referee for helpful comments strengthening this contribution. J.S.P would like to thank Yi Cao for assistance in DEIMOS data reduction. J.S.P was supported by a grant from the National Science Foundation Graduate Research Fellowship under grant No. (DGE-11444469).

This research has benefitted from the M, L, T, and Y dwarf compendium housed at DwarfArchives.org. This research has benefitted from the Ultracool RIZzo Spectral Library maintained by Jonathan Gagné and Kelle Cruz. This researched has benefitted from the Database of Ultracool Parallaxes maintained by Trent Dupuy.

PyRAF is a product of the Space Telescope Science Institute, which is operated by AURA for NASA. PyFITS is a product of the Space Telescope Science Institute, which is operated by AURA for NASA.

The data presented herein were obtained at the W.M. Keck Observatory, which is operated as a scientific partnership among the California Institute of Technology, the University of California and the National Aeronautics and Space Administration. The Observatory was made possible by the generous financial support of the W.M. Keck Foundation.

This publication makes use of data products from the Two Micron All Sky Survey, which is a joint project of the University of Massachusetts and the Infrared Processing and Analysis Center/California Institute of Technology, funded by the National Aeronautics and Space Administration and the National Science Foundation.

Chapter 4

SEARCHING FOR H_3^+ EMISSION IN AURORAL BROWN DWARFS

Recent observations have demonstrated that very-low mass stars and brown dwarfs are capable of sustaining strong magnetic fields despite their cool and neutral atmospheres. The electron cyclotron maser instability has been the key mechanism invoked to explain the strong radio emission and infer kG field strengths. Crucially, these observations imply the existence of energetic non-thermal electron populations, associated with strong current systems, as are found in the auroral regions of the magnetized planets of the Solar System. If these auroral electrons precipitate into the brown dwarf atmospheres, as they do on Jupiter and Saturn, the electron collisions with the H_2 gas will generate the ion H_3^+. With this motivation, we targeted a sample of ultracool dwarfs, known to exhibit signatures associated with aurorae, in search of the K-band emission features of H_3^+ using the Keck telescopes on Mauna Kea. From our sample of 9 objects, we found no clear indication of H_3^+ emission features. The results of our survey imply that the energy breakdown of auroral emissions may differ significantly in brown dwarf atmospheres as compared to Jupiter. Furthermore, we discuss the implications of our findings for brown dwarf aurorae, and the mean of the auroral electron energy distribution.

4.1 Introduction

The discovery of strong radio emission from brown dwarfs (e.g., Berger et al. 2001; Hallinan et al. 2007, 2008; Berger et al. 2009; Route and Wolszczan 2012; Burgasser, Melis, et al. 2015; Kao et al. 2016) has opened up a new window into the magnetic activity of ultracool dwarfs (UCDs; spectral type $\geq$ M7). Whereas typical tracers of stellar activity, like Hα and X-ray, appear to decline into the UCD regime, such objects with radio emission appear to display consistent flux levels from late M dwarfs to T dwarfs, allowing for continued investigation into the magnetic fields and dynamos operating in brown dwarfs (Kao et al. 2016; Route and Wolszczan 2016b). Furthermore, detailed study of individual objects such as LSR J1835+3259 and TVLM513-46546 has revealed the importance of the electron cyclotron maser instability (ECMI) as the key mechanism generating the highly polarized coherent strong periodic radio pulses (Hallinan et al. 2008; Lynch, Mutel, and Gudel 2015;

Hallinan et al. 2015; Williams and Berger 2015). Concurrently, multiple studies have also observed these objects displaying periodic optical variability consistent with the rotational period seen in the radio pulses (e.g., Littlefair et al. 2008), with Harding, Hallinan, Boyle, et al. (2013) suggesting a possible correlation between the optical variability and the radio emission.

To test this potential connection, Hallinan et al. (2015) observed LSR J1835+3259 simultaneously at radio and optical wavelengths, demonstrating that the object's Hα emission was periodic and consistent with the rotational period determined from the radio observations. Through spectroscopic monitoring they also demonstrated that the broadband optical variability was connected with the Hα emission and generated both correlated and anti-correlated light curves in broadband photometry, depending on the wavelengths of the observations. They concluded that the electron beam responsible for the radio emission impacted the atmosphere and created the surface feature seen both in Hα and broadband optical monitoring, analogous to what is observed in the auroral emissions of the magnetized planets of the Solar System (Hallinan et al. 2015).

This analogy suggests that brown dwarfs are capable of hosting auroral phenomena in their hydrogen dominated atmospheres similar to what is seen on Jupiter and Saturn. In these gas giant planets, the ECMI radio emission is generated by a strong magnetospheric current system that produces an energetic non-thermal electron beam that precipitates into the atmosphere depositing the bulk of its energy (see Keiling et al. 2012; Badman et al. 2015, and references therein). This atmospheric interaction generates a cascade of auroral emission processes at ultraviolet, optical, and infrared (IR) wavelengths (see Badman et al. 2015, and references therein).

Table 4.1: Targets and Observations for our H_3^+ MOSFIRE Survey

Target	Spectral Type	UT Date	t_{exp} (s)	Total Time (s)	Selection	Seeing	Slit Width	References
LSR J1835+3259	M8.5	2013 March 30	23	186	Hα/ Radio	1".0	0".5	7
TVLM513-46546	M9	2013 March 30	23	186	Hα/Radio	1".0	0".5	8
2MASS J0746+2000	L0+L1.5	2013 October 11	25	1508	Hα/Radio	0".9	0".5	4
DENIS J1058-1548	L3	2014 March 17	29	1513	Hα/Variable[a]	0".8	0".7	3
2MASS J0036+1821	L3.5	2013 October 12	25	2910	Hα/Radio	0".8	0".3	4, 6
2MASS J1254-0122	T2	2013 June 14	29	1513	Hα/Variable[a]	0".4	12"	5
SIMP J0136+0933	T2.5	2013 October 12	29	1047	Radio/Variable[a]	0".9	0".5	1
2MASS J1237+6526	T6.5	2014 March 17	60	1192	Hα/Radio	0".8	0".7	2
2MASS J1047+2124	T6.5	2013 March 30	119	1432	Weak Hα/ Radio	1".0	1".0	1

[a] Variable targets are objects with known near infrared photometric variability.

REFERENCES. – (1) Artigau et al. 2006, (2) Burgasser et al. 1999, (3) Delfosse et al. 1997, (4) Kirkpatrick et al. 2000, (5) Leggett et al. 2000, (6) Reid et al. 2000, (7) Reid et al. 2003, (8) Tinney, Mould, and Reid 1993.

Of particular importance is the collisional ionization of molecular hydrogen and the subsequent production of H_3^+, through the chemical reaction

$$H_2^+ + H_2 \rightarrow H_3^+ + H\,. \tag{4.1}$$

In auroral atmospheric regions, this reaction proceeds very rapidly creating large quantities of the triatomic hydrogen ion from the impact of the electron beam. H_3^+ does not have an electric dipole moment but instead emits strongly from the rotational-vibrational modes of its fundamental band at 4 μm and in the overtone band at 2 μm (Maillard and Miller 2011). This ion of hydrogen plays a significant role in regulating the exospheric temperature, as one of the most strongly emitting species in the Jovian ionosphere (Maillard and Miller 2011). Moreover, the long timescale and the thermal nature of the transitions means that the H_3^+ emission is sensitive to the properties of the atmosphere (Tao, Badman, and Fujimoto 2011; Badman et al. 2015). Indeed, Tao et al. (2012) showed how the properties of the electron beam and the background atmospheric temperature can be determined from a study of the H_3^+ emission lines of Jupiter.

If brown dwarfs can generate auroral emissions, as suggested by the ECM radio emission, then they become strong candidates for the search for H_3^+ emission in atmospheres beyond the Solar System. These efforts have focused on known hot jupiters (e.g., Shkolnik, Gaidos, and Moskovitz 2006; Lenz et al. 2016), where the intense radiation and close proximity to their host stars could strengthen the signatures of auroral processes as the planet interacts with the star's stellar wind (e.g., Zarka 2007). However, these efforts have not yet yielded any detections (Shkolnik, Gaidos, and Moskovitz 2006; Lenz et al. 2016).

Brown dwarfs, on the other hand, could be potentially more favorable targets for the detection of H_3^+. Unlike the hot jupiters, isolated brown dwarfs can be studied directly without having to remove the effect of a bright stellar host. Moreover, based on the observed radio emissions, the strength of the auroral emission in brown dwarfs can be several orders of magnitude greater than what is seen in the Solar System, because of their rapid rotation rates and strong kG magnetic field strengths (Hallinan et al. 2015). Because of the similar atmospheric temperatures, the potential detection of H_3^+ in brown dwarf atmospheres could also be used as a stepping stone toward the exploration of H_3^+ in hot jupiter atmospheres and an understanding of the physics underlying auroral processes in an entirely new parameter space.

These developments motivate the current study looking for H_3^+ emission in the IR spectra of auroral UCDs. We focus on the overtone band at 2 μm, K-band, which is readily accessible from the ground and has recently seen improved sensitivity from the completion of new IR instruments. In Section 4.2, we present our survey sample. In Section 4.3, we review our observing strategy and data reduction. In Section 4.4, we present the results of our survey. Lastly, in Section 4.5 we discuss our findings and the implications for studies of auroral phenomena in the UCD regime.

4.2 Targets

We selected a sample of UCD targets with indications of potential auroral activity, usually radio emission and Hα, but also photometric variability, to look for H_3^+ emission. These targets are summarized in Table 4.1; we discuss each in detail here. We also include here literature reports of effective temperature and gravity to be used in a comparison between our spectra and model atmospheres (See Section 4.4).

LSRJ 1835+3259

Discovered by Reid et al. (2003), LSRJ 1835+3259 (hereafter LSR 1835), a M8.5 dwarf with a K-band magnitude of 9.171 at a distance of 5.67 pc, has been studied extensively for its magnetic activity (Cutri 2003). LSR 1835 is known to emit sinusoidally varying Hα emission and displays steady long-term photometric variability with a period of 2.84 hrs (Harding, Hallinan, Boyle, et al. 2013; Hallinan et al. 2015). LSR 1835 also shows both quiescent radio emission and periodically pulsed highly polarized radio emission, spanning 4 - 8 GHz (Hallinan et al. 2008, 2015). Despite the presence of strong magnetic fields, as indicated by the radio emission, no X-ray detections have been observed from LSR 1835 (Berger et al. 2008, 2010). Berger et al. (2008) also report near ultraviolet ($\lambda_{\rm eff}$ = 2600 Å) measurements from *Swift* consistent with photospheric emission. Filippazzo et al. (2015) report an effective temperature, T_{eff}, of 2316 ± 51 K and gravity, log g, of 5.22 ± 0.11 (cgs), based on a semi-empirical approach using recent evolutionary models and measured bolometric luminosities from multi-wavelength observations spanning the bulk of the spectral energy distribution of the target.

TVLM513-46546

TVLM513-46546 (hereafter TVLM 513) is a M8.5 dwarf with a K-band magnitude of 10.706 at a distance of 10.59 pc (Kirkpatrick, Henry, and Simons 1995; Dahn et al. 2002; Cutri 2003). TVLM 513 has been studied extensively for its magnetic

activity, including both Hα and radio emission and has become a benchmark object for activity at the end of the main sequence. TVLM 513 displays highly polarized periodic pulses at a rotation period of 1.958 hr and quiescent radio emission (Hallinan et al. 2007, 2008). Extensive follow-up at radio wavelengths has shown this emission and period to be very stable and long-lasting (Wolszczan and Route 2014). TVLM 513 also shows stable photometric variations over long time periods at optical wavelengths, that could be connected to the process emitting the radio emission (Harding, Hallinan, Boyle, et al. 2013; Wolszczan and Route 2014). TVLM 513 has an effective temperature and log gravity of 2242 ± 55 K and 5.22 ± 0.11 (cgs), respectively (Filippazzo et al. 2015).

2MASS J07464256+2000321

2MASS J07464256+2000321 (hereafter J0746+20AB) is a binary system comprising L0 and L1.5 dwarfs at a distance of 12.2 pc with a K-band magnitude of 10.468 (Dahn et al. 2002; Cutri 2003; Bouy et al. 2004). Extensive mulit-wavelength monitoring of this target has revealed periodic radio pulses and Hα emission that are offset in phase by 0.25 within a period of 2.07 hr, as well as non-detections in the X-ray and UV (Berger et al. 2009). Photometric monitoring of the binary by Harding, Hallinan, Konopacky, et al. (2013) indicated that the primary component is photometrically variable at optical wavelengths and rotates with a period of 3.3 hr, whereas the faster rotating secondary is the source of the radio emission.

DENIS J1058.7-1548

Discovered by Delfosse et al. (1997), DENIS J1058.7-1548 (hereafter DENIS 1058-15) is a L3 dwarf at a distance of 17.3 pc with a K-band magnitude of 12.532 (Kirkpatrick et al. 1999; Dahn et al. 2002; Cutri 2003). Spectroscopic studies detected weak Hα emission from DENIS 1058-15 Kirkpatrick et al. (e.g., 1999). This target also displays J-band variability in photometric monitoring with similar periodic variation in the *Spitzer* bands at 3.6 and 4 μm (Heinze et al. 2013; Metchev et al. 2015). DENIS 1058-15 has an effective temperature and log gravity of 1809 ± 68 K and 5.20 ± 0.19 (cgs), respectively (Filippazzo et al. 2015).

2MASS J00361617+1821104

2MASS J00361617+1821104 (hereafter J0036+18) is an L3.5 dwarf at a distance of 8.76 pc with a K-band magnitude of 11.058 (Reid et al. 2000; Kirkpatrick et al. 2000; Dahn et al. 2002; Cutri 2003). Initial studies demonstrated that J0036+18

displayed strong radio emission and periodic highly circularly polarized pulses (Berger 2002; Berger et al. 2005; Hallinan et al. 2008). However, simultaneous monitoring campaigns showed no X-ray emission and an apparent lack of Hα (Berger et al. 2005, 2010). Recent results from Pineda et al. (2016), however, did detect Hα emission, indicating variability timescales much longer than the rotation period of 3.08 hr (Hallinan et al. 2008). Harding, Hallinan, Boyle, et al. (2013) detected periodic variability, consistent with the rotational period in optical photometric monitoring. Additionally, Metchev et al. (2015) detected irregularly periodic photometric variability in *Spitzer* monitoring of J0036+18 at both 3.6 and 4 μm. J0036+18 has T_{eff} = 1869 ± 64 K and log g = 5.21 ± 0.17 (cgs; Filippazzo et al. 2015).

2MASS J12545393-0122474

Discovered by Leggett et al. (2000), 2MASS J12545393-0122474 (hereafter J1254-01) is a brown dwarf with an infrared spectral type of T2 at a distance of 13.21 pc with a K-band magnitude of 13.84 (Cutri 2003; Vrba et al. 2004; Burgasser et al. 2006). Burgasser et al. (2003) report the detection of weak Hα emission from J1254-01. Further monitoring at radio wavelengths yielded no detections in two 2 hr observing blocks (Kao et al. 2016). *Spitzer* observations looking for photometric variability at 3.6 and 4 μm also did not yield positive results (Metchev et al. 2015). J1254-01 has T_{eff} = 1219 ± 94 K and log g = 5.02 ± 0.47 (cgs; Filippazzo et al. 2015).

SIMP J013656.5+093347.3

Discovered by Artigau et al. (2006), SIMP J013656.5+093347.3 (hereafter SIMP 0136+09) is a T dwarf at the L/T transition, with a K-band magnitude of 12.562, displaying strong photometric variability in the J-band interpreted as heterogenous cloud cover in its atmosphere (Cutri 2003; Artigau et al. 2009). At a distance of 6.1 pc, SIMP 136+09 is one of the closest cool brown dwarfs and a benchmark object for atmospheric modeling (Weinberger et al. 2016). Efforts to find Hα emission have only produced upper limits despite multiple observations at different rotational phases (Pineda et al. 2016). However, radio monitoring at 4 GHz by Kao et al. (2016) has detected quiescent emission and multiple highly circularly polarized radio pulses. Kao et al. (2016) use an updated version of the spectral index methods of Burgasser, Burrows, and Kirkpatrick (2006) to measure $T_{eff} = 1089 \pm^{62}_{54}$ K and log $g = 4.79 \pm^{0.26}_{0.33}$ (cgs) for SIMP 0136+09.

2MASS J12373919+6526148

Since its discovery, 2MASS J12373919+6526148 (hereafter J1237+65), a brown dwarf at 10.4 pc with a K-band magnitude of 16.4, has been an unusual T6.5 (infrared spectral type) because of it's exceedingly strong Hα emission (Burgasser et al. 1999; Cutri 2003; Burgasser et al. 2003; Vrba et al. 2004; Burgasser et al. 2006). Many follow-up efforts have attempted to understand the cause of the emission, however there have been few definitive conclusions (Burgasser, Kirkpatrick, Brown, Reid, Burrows, et al. 2002; Liebert and Burgasser 2007). More recently, the search for ECM radio emission in cool brown dwarfs has revealed J1237+65 to be a radio source with moderate levels of circular polarization (Kao et al. 2016). J1237+65 has T_{eff} = 851 ± 74 K and log g = 4.95 ± 0.5 (cgs; Filippazzo et al. 2015).

2MASS J10475385+2124234

First reported in Burgasser et al. (1999), 2MASS J10475385+2124234 (J1047+21 hereafter) is a brown dwarf with a spectral type of T6.5 in the infrared, at a distance of 10.56 pc, with a K-band magnitude of 16.2 (Cutri 2003; Vrba et al. 2004; Burgasser et al. 2006). Burgasser et al. (2003) detected weak Hα emission from this target, as one a few T dwarfs with this emission feature. J1047+21 was also the first T dwarf to be detected in radio emission (Route and Wolszczan 2012). Follow-up efforts have since confirmed the radio detection, measured quiescent emission levels and characterized the periodic pulses of the object with a period of 1.77 hr (Williams and Berger 2015; Kao et al. 2016; Route and Wolszczan 2016b). J1047+21 has an effective temperature and log gravity of 880 ± 76 K and 4.96 ± 0.49 (cgs), respectively (Filippazzo et al. 2015).

4.3 Observations and Data

H_3^+ K-band Energy

The detection of auroral radio emission in brown dwarf atmospheres indicates that auroral processes may be creating significant quantities of H_3^+ in their upper atmospheric regions. Using the relative energy scaling observed in the Jovian atmosphere between the different multi-wavelength auroral emissions, we can estimate the amount of energy in H_3^+ K-band emission features we expect to see from UCDs. In Jupiter, about a ∼10% of the total auroral energy emerges in H_3^+ emission lines, with the total emission around 4 μm comprising ∼85%-90% of the H_3^+ energy (Bhardwaj and Gladstone 2000). However, compared to the energy in Hα ($\lesssim$1% of total) and radio ($\lesssim$0.1% of total), the H_3^+ features carry considerably more energy.

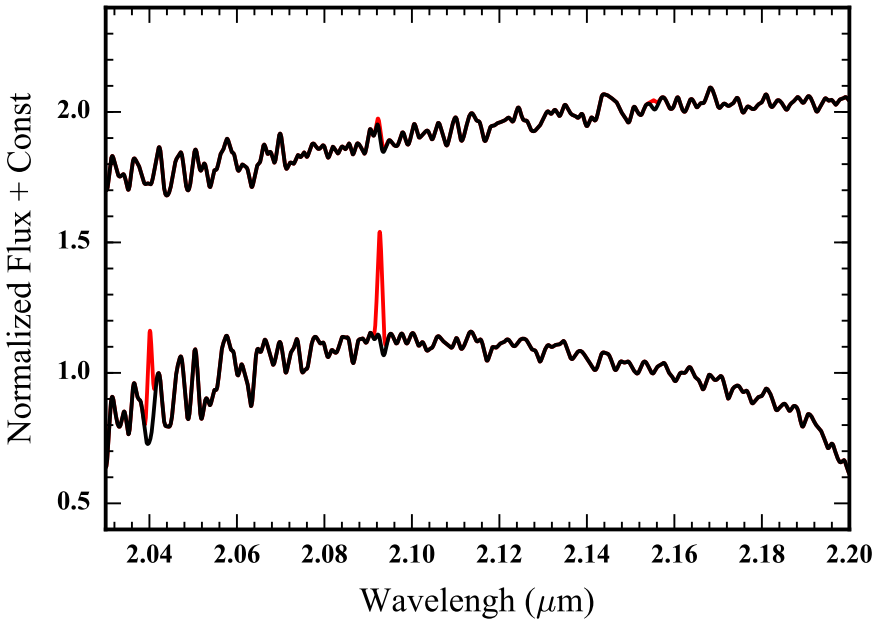

Figure 4.1: PHOENIX model spectra of log g = 5 (cgs) and effective temperatures 2300 K and 1200 K, top line and lower line respectively, with H_3^+ emission lines superimposed. The models are representative of the typical stars in our target sample (see Section 4.2) and indicate what the spectra would look like if the prominent H_3^+ emission lines carried as much energy as is found in Hα emission ($L_{\mathrm{H}\alpha}/L_{\mathrm{bol}} \sim 10^{-5.5}$; see Section 4.3). The spectra are normalized by the mean flux between 2.1 and 2.2 μm. The emission is more difficult to detect in the warmer objects which have more photospheric flux in the K-band than in the cooler brown dwarfs.

If we assume that all of the visible auroral energy on Jupiter (~100 GW) emerges as Hα and that only 10% of the H_3^+ energy emerges in K-band (~600 GW), then the expected energy in the overtone band is at least several factors (~6) greater than the Hα energy. However, the Hα emission is only a portion of the visible aurorae, additional features of H_2 and broadband variations likely contribute to the total visible flux (Ingersoll et al. 1998). Thus, the K-band H_3^+ lines likely carry at least as much energy as Hα and are possibly several factors stronger. The clear Hα detections of our target objects suggests that the H_3^+ emission features could be strong enough to detect despite the thermal photospheric emission in K-band.

We show an example of H_3^+ emission features with energy equivalent to that of Hα, $L_{H\alpha}/L_{\mathrm{bol}} \sim 10^{-5.5}$, in Figure 4.1, sitting on top of the K-band photospheric emission represented by PHOENIX BT-Settl model spectra (Baraffe et al. 2015). The figure shows two representative spectra normalized by the mean flux between

2.1 and 2.2 μm and offset by a constant, the top having T_{eff} = 2300 K and log g = 5 and the lower line having T_{eff} = 1200 K and log g = 5. Because of the bright photospheric flux in the K-band the emission features are harder to distinguish for the warmer object than they are for the cooler object in which the emission stands out clearly. Similar calculations can be done using the radio emission; however, any auroral Hα is physically associated with the atmospheric conditions producing the H_3^+ and is more likely to yield an accurate estimate.

Although UCDs have been observed extensively at IR wavelengths in the past, these observations have predominantly been very-low resolution ($\sim$ 500), or have not focused on potentially auroral brown dwarf targets with deep K-band observations, precluding the successful identification of these features (e.g., McLean et al. 2003; Rayner, Cushing, and Vacca 2009; Blake, Charbonneau, and White 2010). Furthermore, the H_3^+ emission features are likely to be very narrow, requiring highly sensitive and at least medium resolution spectrographs. The deep observations are essential, especially for late M dwarfs and early L dwarfs, in order to distinguish from the photospheric emission. Although this is not an issue for the cooler objects, the faint K-band magnitudes of the T dwarfs makes high resolution observations difficult. The recent development of new highly sensitive IR instruments provides a the opportunity to look for these features in brown dwarf atmospheres.

Data

In order to search for H_3^+ emission features, we focused on the $2\nu_2$ overtone band around 2 μm in the K-band, where we expect potentially strong H_3^+ emission features. We observed our target sample (see Table 4.1) using the Mulit-Object Spectrometer For Infrared Exploration (MOSFIRE) on the Keck Telescopes on Mauna Kea (McLean et al. 2010, 2012). MOSFIRE is a multi object spectrograph with a configurable slitmask unit (CSU) with movable bars that can be repositioned as desired during the observations. MOSFIRE uses a highly sensitive teledyne H2RG HgCdTe detector with 2k x 2k pixels within a 6'.1 x 6'.1 field of view, and is designed to provide NIR spectra of faint objects (usually galaxies), but has been used for careful spectrophotometric work during exoplanet transits (e.g., Crossfield et al. 2013). MOSFIRE provides a resolution of R$\sim$3600 in the K-band with a nominal 0".7 wide slit, spanning 1.95-2.4 μm. The resolution in each of our observations varied according to the slit width we used, from $\sim$2500 to $\sim$8400 (see Table 4.1 and below for discussion).

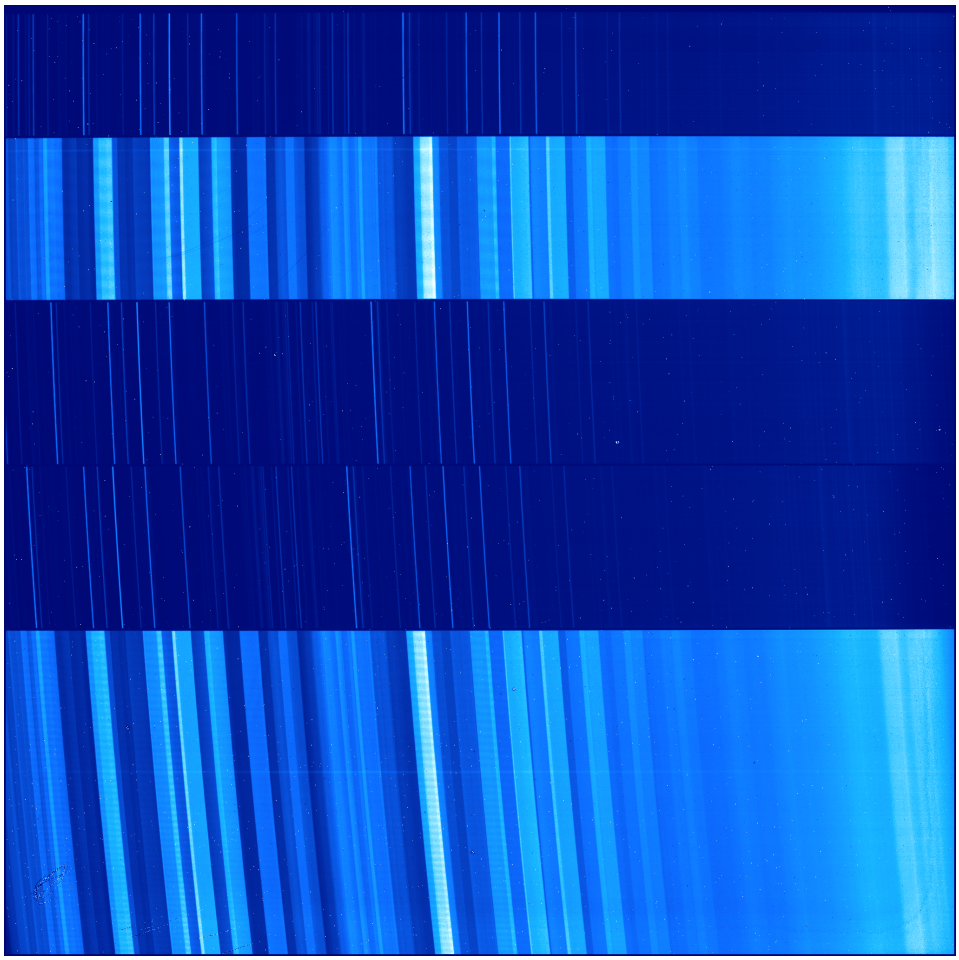

Figure 4.2: A raw MOSFIRE exposure from the observing night of 2014 June 14, targeting J1254-01. The raw frame illustrates the combination of narrow slits and wide slots on the CSU which enable multi-functional observing sequences by dithering between an open slit, for spectrophotometry and in order to limit the effects of narrow sky emission features, and a narrow slit, for precise control of spectral resolution. Bright dots in the data correspond to hot pixels.

Our observations took place over the course of 2013 and 2014 (see Table 4.1), usually only one or two objects on a given night with total exposure times ranging from 3 minutes, for the two bright M dwarfs in our sample, and up to 50 minutes for one of our targets, but usually only about 25 minutes. Our program was clouded out on dedicated observing nights; however we were able to take advantage of cooperation with companion programs looking for photometric variability in brown dwarfs and/or exoplanet transmission spectroscopy. During periods between transits and/or when specific targets were not yet sufficiently high in the sky we were able to collect deep K-band spectra of our sample target list. Consequently, the time available on each target varied considerably and we were not always able to acquire telluric

calibrators to correct the K-band spectra. However, the prominent H_3^+ emission features avoid the regions of intense telluric absorption in the K-band around 2.02 and 2.07 μm (see for example Figure 4.4). We present these spectra in Section 4.4.

We configured the CSU to contain additional reference targets to provide a check on any astrophysical variations we observed and included both narrow slit and wide slit sections of the slit mask. These can been seen in the raw exposure example, shown in Figure 4.2. The bright bands in the image correspond to the sky emission lines seen through the wide open slit (width ~10") and can be traced vertically to the sections with narrow sky lines from the narrow slit width (~0".7). During the observations we were able to dither along the slit direction on the mask to change between one mode and the other. This proved more expedient than moving the CSU bars, because it was quicker and slight differences between the repositioning of the CSU bars can introduce systematics into the observations from frame to frame (Crossfield et al. 2013). Although there can be differences introduced from the dithering due to slight shifts in the pointing potentially shifting the target slightly within the wide slits, these proved inconsequential for the search for H_3^+ emission.

The use of both slit widths allowed us to provide precise control of the observed spectral resolution with the narrow slits while using the wide slits for spectrophotometry and to help distinguish between sky lines and narrow H_3^+ emission features. Although the the wide slits increase the background noise by spreading out the bright night sky lines, it eliminates any issues dealing with residual sky line subtraction and confusing a poorly subtracted narrow skyline with potential astrophysical emission features. The sky emission varies on the order of 1-2 minutes and we found that for careful sky line subtraction, we required exposures of $\leq$30 s (see Table 4.1). Nevertheless, we were able to use our wide slit exposures as a verification when assessing any narrow features in the observed spectra. Additionally, the most prominent H_3^+ features avoid the major OH sky lines. We illustrate this in Figure 4.3, showing the error spectrum from our observations of DENIS1058-15 with an H_3^+ spectrum overlaid. The spikes in the error spectrum correspond to the locations of sky emission lines, with the strongest H_3^+ lines usually located between sky features. In Section 4.4, we present our best co-added spectra (based on S/N and resolution) for each object, usually from narrow slit observations. Our observations of J1254-01 were conducted under good seeing conditions (see Table 4.1) and we thus present the wide slit observations of that target because of their high resolution and high signal-to-noise ratio.

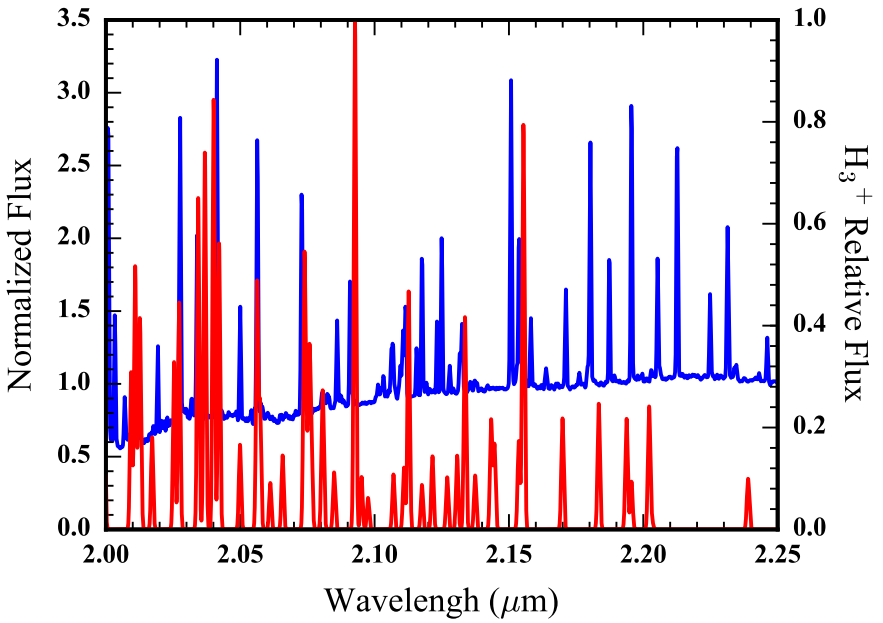

Figure 4.3: The error spectrum (left axis), normalized to its median level, of our observations of DENI1058-15, illustrating the locations of the sky emission lines as narrow peaks in the uncertainty with a relative flux spectrum (right axis) of H_3^+ overlaid (T = 1800 K), showing the locations of the K-band emission features. The H_3^+ spectrum's most prominent feature is the emission line at 2.09 μm which falls between sky emission lines.

For each target we used an ABBA nodding pattern, to allow clean background subtraction between adjacent frames with typical nodding sizes of at least 4". The IR detector was readout in the multiple correlated double sampling mode (MCDS), 4, 8, or 16, depending on the exposure time, available observing time and the brightness of the object. While additional readouts help limit the read noise in each exposure, it adds additional overhead which may limit the total signal to noise that is ultimately achieved over the course of many exposures within a given amount of time. For the brighter objects, we typically used MCDS 4 and MCDS 16 for the fainter objects with longer exposures.

The data were reduced using the MOSFIRE Data Reduction Pipeline (DRP) [4] to perform the flat fielding, background subtraction through frame differencing, cosmic ray rejection, co-addition, and wavelength calibration. We took flat fields and any necessary arc lamps at the beginning and end of the night with the CSU configured to our science masks, and when possible prevented changes to the CSU between

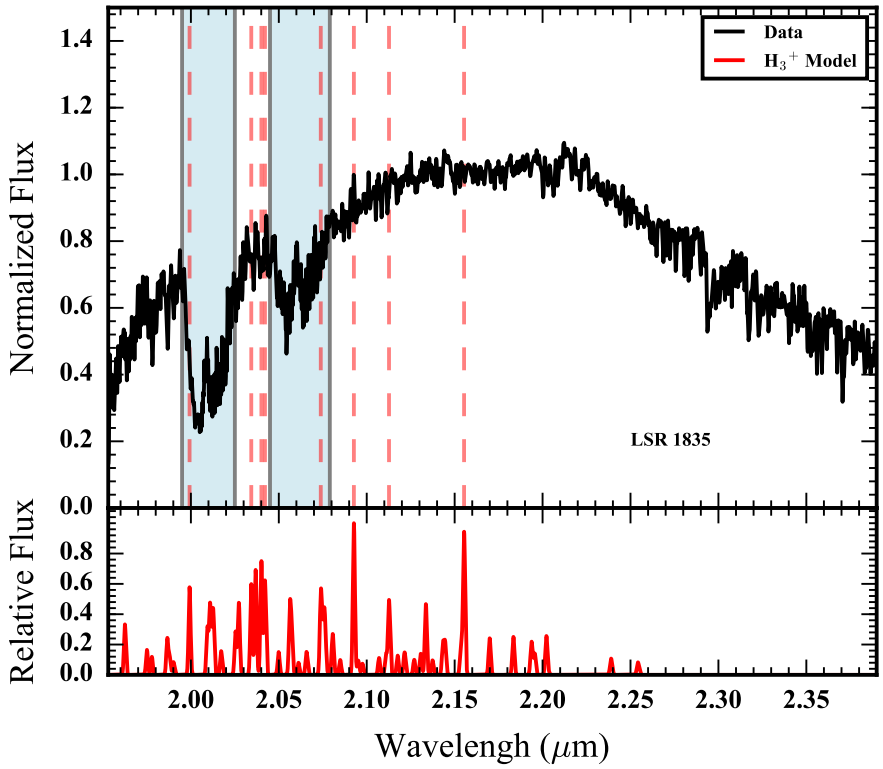

Figure 4.4: The MOSFIRE spectrum of LSR 1835 in the K band, in black, normalized to the median flux level between 2.1 and 2.2 μm. The bottom panel shows a simulated spectrum of H_3^+, with a rotational and vibrational temperature of 2300 K. The shaded regions denote significant telluric absorption and the dashed lines trace the locations of the eight strongest lines of H_3^+.

calibration and science exposures to limit systematic effects. The flats in K-band require the use of dome lamp exposures and additional 'lamp off' exposures to assess the thermal background contribution to the 'lamp-on' signal. Additionally, because the lamps were too bright to properly calibrate the wide slits, we took many additional (~50) lamp-off exposures to construct accurate flat fields with the wide slits [5]. In the K-band, the OH sky lines are used for the primary wavelength calibration, however they become scarce at the long wavelength end of the band and are thus supplemented by arc lamp spectra with the solutions being merged and corrected for the lamp optical path differing from the astrophysical signal path. The DRP produces 2D spectra from which we use optimal extraction to create our

reduced science spectra.

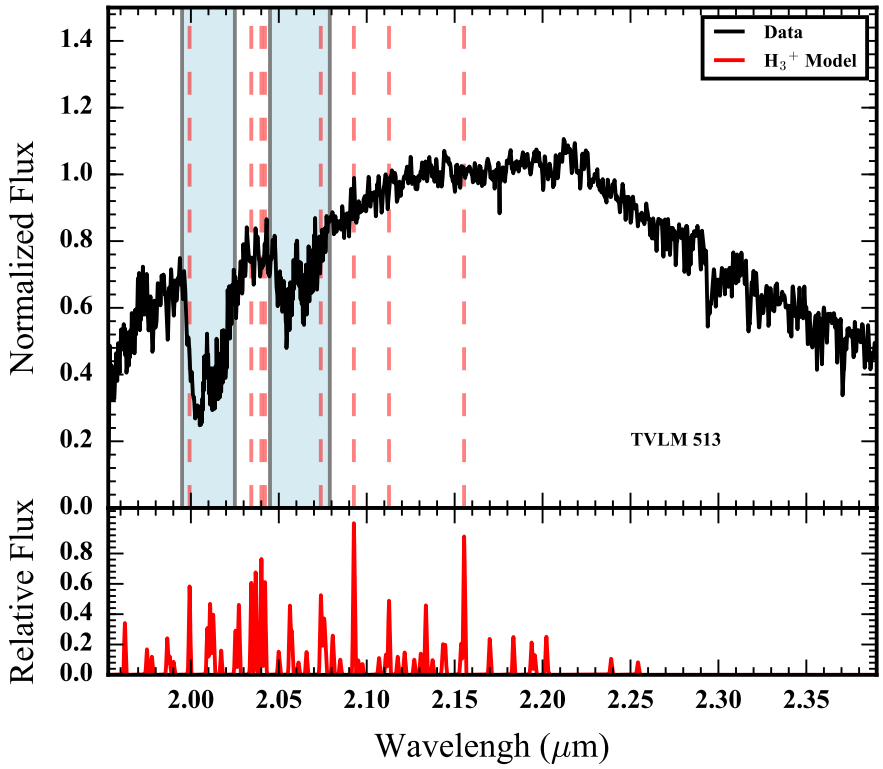

Figure 4.5: Same as in Figure 4.5 but for TVLM 513. The simulated H_3^+ spectrum uses rotational and vibrational temperatures of 2200 K.

4.4 Results

We report the results of our survey here, plotting each of the spectra from our MOSFIRE observations in Figures 4.4-4.12. In each of these plots, we show in the top panel our K-band spectrum and in the lower panel an expected H_3^+ spectrum. The shaded region marks off where there is significant telluric absorption and the dashed lines show the location in the top panel of the eight highest peaks of the H_3^+ spectrum below. The expected H_3^+ spectrum is taken from the intensity calculator of the H_3^+ Resource Center [6]. The calculator uses input rotational and vibrational temperatures and a computed line list to construct the intensity spectra following Neale, Miller, and Tennyson (1996). We use equivalent rotational and vibrational

[4] https://keck-datareductionpipelines.github.io/MosfireDRP/

[5] Since these observations, Keck Observatory has provided variable power lamps to more easily use wide slit observing modes see http://www2.keck.hawaii.edu/inst/mosfire/

[6] http://h3plus.uiuc.edu/

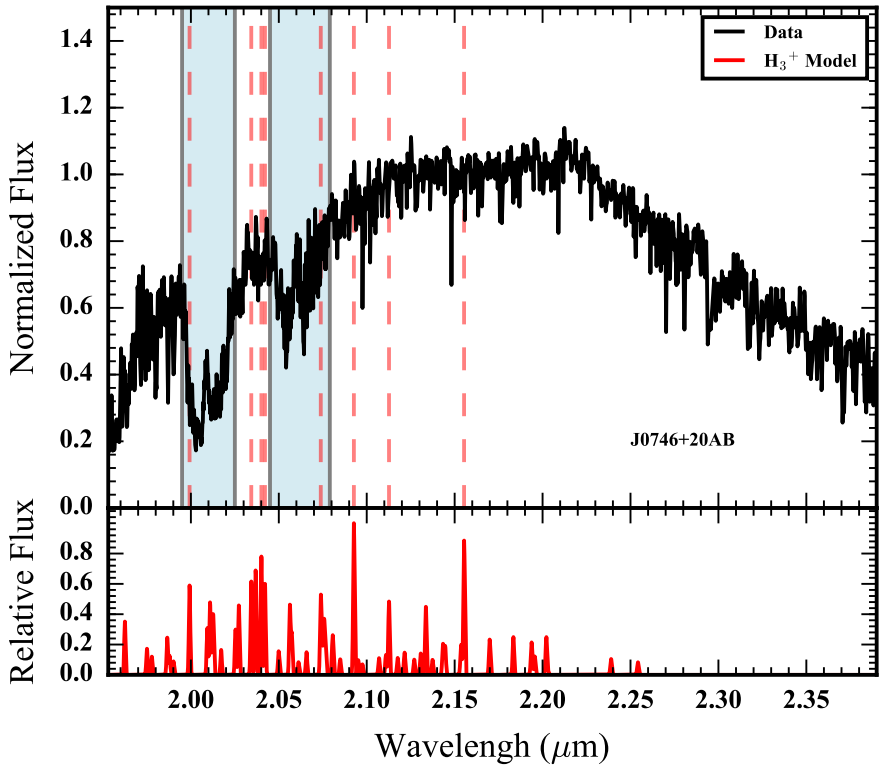

Figure 4.6: Same as in Figure 4.4 but for J0746+20AB. The simulated H_3^+ spectrum uses rotational and vibrational temperatures of 2100 K.

temperatures consistent with the photospheric temperatures of the UCDs (see Section 4.2). Equating the two temperatures assumes the molecule has thermalized in the atmosphere, which is consistent with the Jovian observations Miller, Joseph, and Tennyson (e.g., 1990). Although the exospheric temperature is likely warmer, as is seen in Jupiter, there can be large variations and the photosphere presents a representative value for the atmosphere. The shape of the spectrum and the prominent lines do not change considerably with changes in the temperature; this is evident by comparing the H_3^+ spectra plotted for each of the targets with different temperatures spanning 800-2300 K.

In these spectra, for all but the faint T dwarf targets, J1237+65 and J1047+21, which have lower signal-to-noise observations, the variations reflect the the physical features shaping the K-band flux of these objects — the jagged appearance of the data in these plots is not noise but the collection of closely spaced absorption lines.

To examine the spectra in detail, we compared the observations to BT-Settl PHOENIX

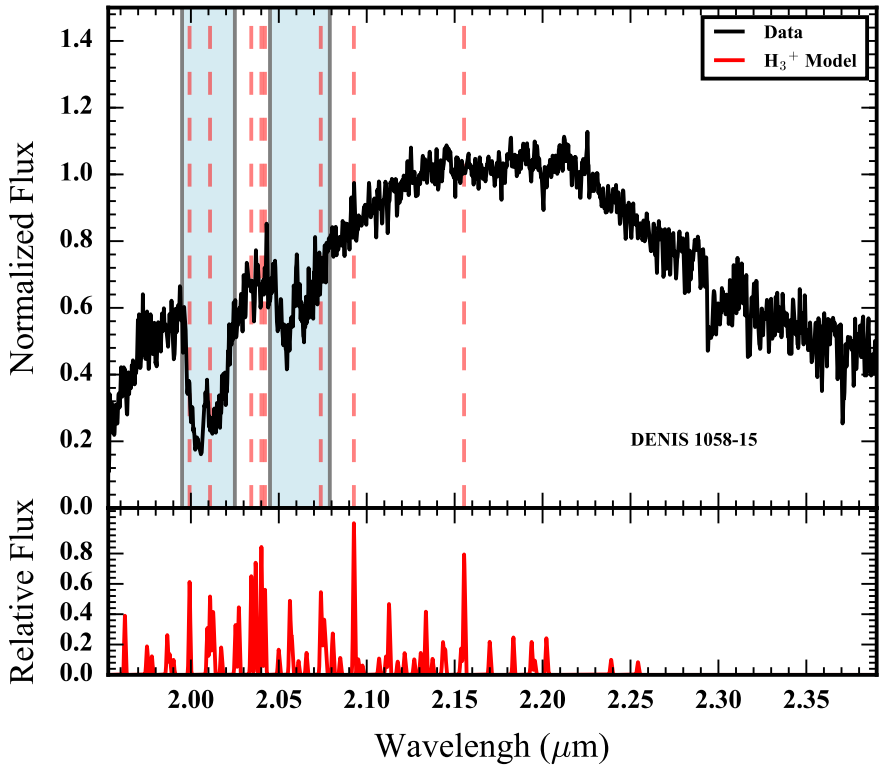

Figure 4.7: Same as in Figure 4.4 but for DENIS 1058-15. The simulated H_3^+ spectrum uses rotational and vibrational temperatures of 1800 K.

model spectra convolved to the resolution of the data and zoomed in on the region with the strongest expected H_3^+ line (Baraffe et al. 2015). These plots are shown in Figures 4.13-4.21. In each plot, we show the data as a black solid line and the models as lighter solid and dashed lines. Vertical dashed lines mark off the same H_3^+ features from Figures 4.4-4.12. The models chosen are those from the model grids that best represent the atmospheric properties as determined in the literature (see Section 4.2).

For LSR 1835 and TVLM 513 (see Figures 4.4-4.5), the model spectra match the data very well, each of the spectroscopic features can be matched clearly to corresponding features in the model spectra. Although there is a slight excess in emission near the location of the H_3^+ feature at 2.093 μm, we do not see corresponding excesses at the locations of the other features in line with the relative ratios of the different emission line strengths. Moreover, a comparison between these two similar temperature M dwarfs reveals the same features in both atmospheres, suggesting that neither shows

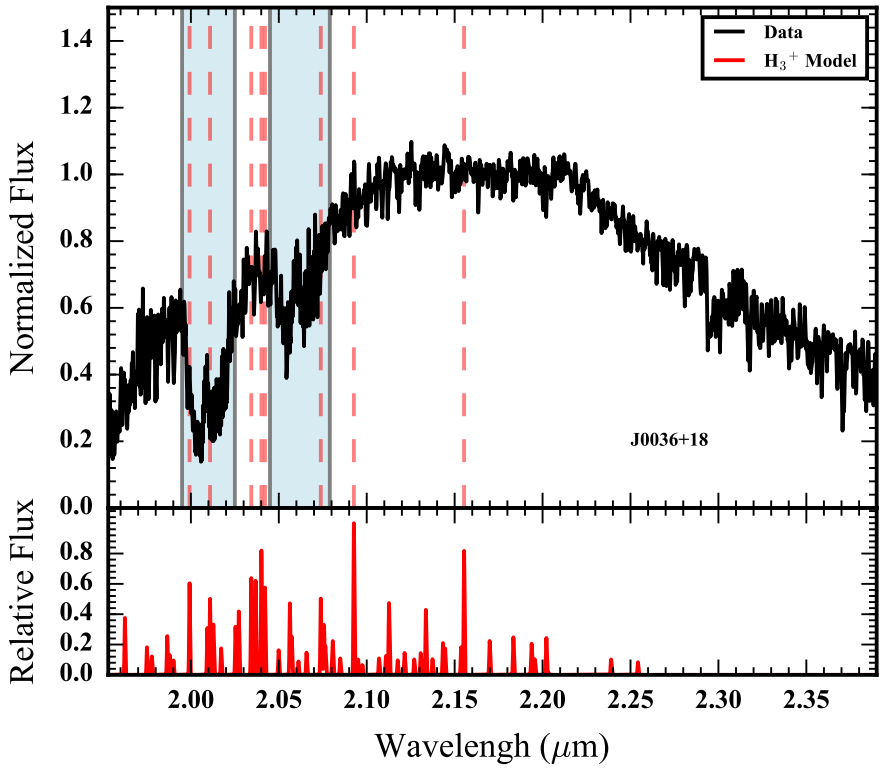

Figure 4.8: Same as in Figure 4.4 but for J0036+18. The simulated H_3^+ spectrum uses rotational and vibrational temperatures of 1900 K.

evidence for H_3^+.

For J0746+20AB, we used a representative model atmosphere of T_{eff} = 2100 K for the combined light spectrum of this nearly equal temperature binary system, consistent with an L1 combined light spectral type. Like the two previous targets, the features in the spectrum closely match those seen in the model with similar deviations as noted for LSR 1835 and TVLM 513, likely photospheric.

Our plot of the comparison between our spectrum for DENIS 1058-15 and the model in Figure 4.16, shows a broad difference in the K-band spectral shape. Because observing conditions for this target were not ideal, there were intermittent clouds and we were not observing at the parallactic angle, this difference is likely systematic. However, this target is also known to be photometrically variable in the NIR, potentially due to brown dwarf clouds and these could potentially cause spectroscopic variations in the emergent flux (e.g., Heinze et al. 2013; Buenzli et al. 2014). Nevertheless the absorption features in the spectrum are clear and are consistent with

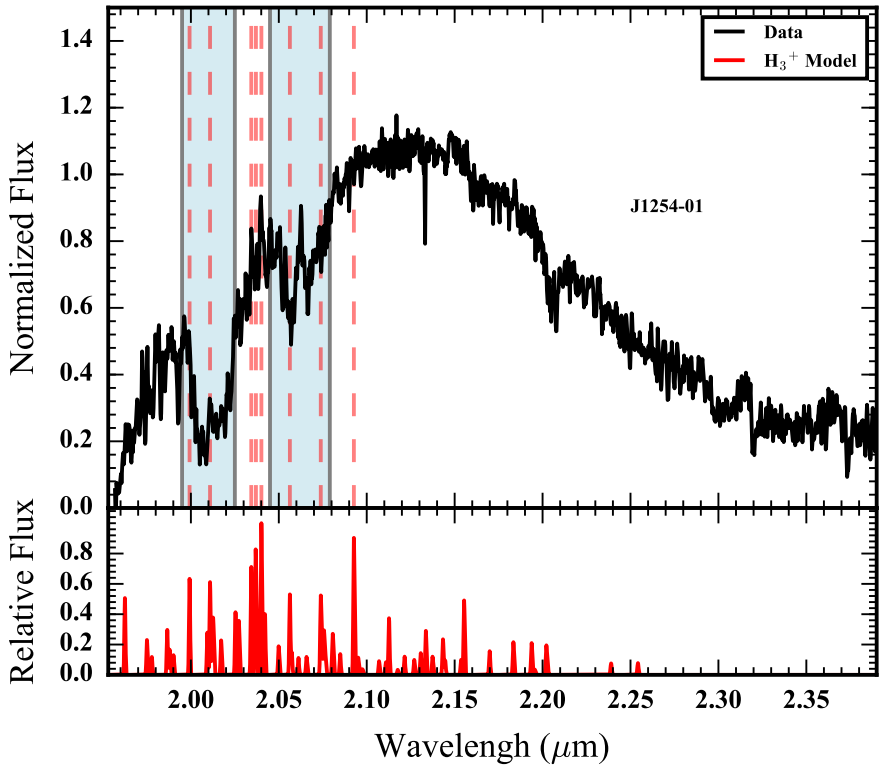

Figure 4.9: Same as in Figure 4.4 but for J1254-01. The simulated H_3^+ spectrum uses rotational and vibrational temperatures of 1200 K.

the features evident in the model spectrum.

Our spectrum of J0036+18, shown in Figure 4.17 is similar to those of LSR 1835 and TVLM 513. The spectral features are well distinguished and are in line with the model spectra. The same feature near 2.093 μm is apparent and observed with a similar shape as the other late M dwarfs and early L dwarfs. H_3^+ emission fluxes consistent with this excess are not seen at their expected locations. J0036+18 shows no indication of H_3^+ emission features.

For the cooler T dwarfs in our sample, J1254-01, SIMP 0136+09, J1237+65, and J1047+20, the expected emission levels of H_3^+ based on typical Hα emission strengths should be easily detected in our moderate resolution spectra. In Figures 4.18-4.21, we plot the data as compared to the model PHOENIX spectra. These plots focus on the region around 2.04 μm where the most prominent H_3^+ lines are for temperatures below ~1300 K. In each of these spectra, we do not see any indication of H_3^+ emission features.

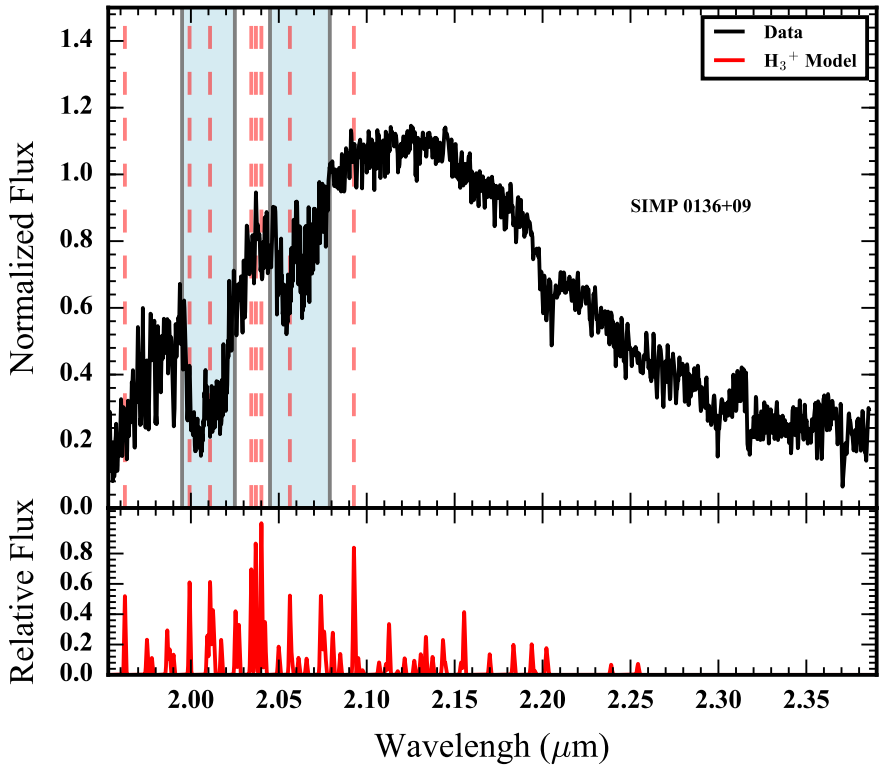

Figure 4.10: Same as in Figure 4.4 but for SIMP0136+09. The simulated H_3^+ spectrum uses rotational and vibrational temperatures of 1100 K.

4.5 Discussion

Our results indicate that the brown dwarfs with known signatures of auroral emissions, predominantly radio, do not emit appreciable amounts of H_3^+ in the K-band. Although we expected these targets to display these emission features, there are several possible explanations. Since the radio pulses and optical variability imply the existence of an energetic electron beam interacting with the atmosphere, we consider this as a given and consider scenarios that limit the emission of H_3^+ features.

Our assumed auroral energy scaling was based on the auroral emissions of Jupiter, the known system most resembling the brown dwarfs in our sample. However, important differences in the atmospheric properties and potentially the auroral electron distribution may lead to diminished H_3^+ emissions. When auroral H_3^+ was first observed from Saturn, the lower than expected emissions were attributed to a potentially high homopause altitude, the layer in the atmosphere up to which the gas is totally mixed (Geballe, Jagod, and Oka 1993). More recent observations by Melin

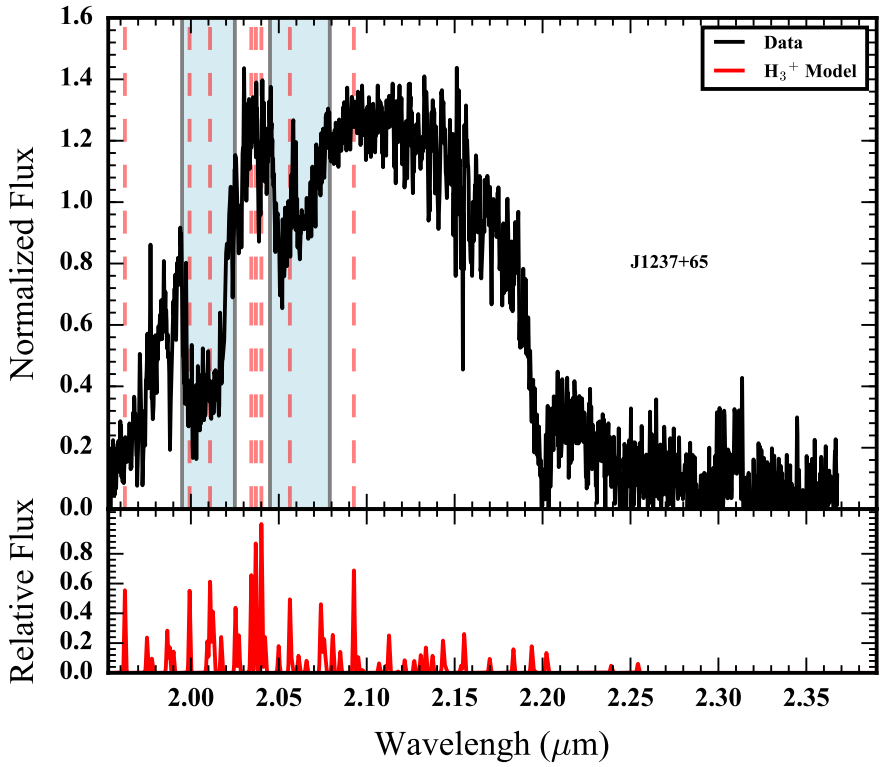

Figure 4.11: Same as in Figure 4.4 but for J1237+65. The simulated H_3^+ spectrum uses rotational and vibrational temperatures of 900 K.

et al. (2007), however, demonstrate that the lower emission strength is not due to the height of the homopause layer but rather a much lower exospheric temperature on Saturn as compared to Jupiter. These Solar System observations illustrate two important effects that can have significant consequences for H_3^+ emission: the atmospheric mixing and the atmospheric temperature.

The amount of H_3^+ emission is sensitive to the atmospheric temperature on both Jupiter and Saturn, as seen in auroral atmospheric models, with emissions generally increasing with higher temperatures and the Kronian emissions being more sensitive to temperature than the Jovian ones (Tao, Badman, and Fujimoto 2011). However, auroral modeling has not yet considered the higher atmospheric temperatures expected in the brown dwarfs, and it is unclear, although perhaps unlikely, if the effect continues to temperatures as high as ~2000 K. Nevertheless, we can comment on the influence of temperature on the T dwarf emissions. Despite upper atmospheres that have temperatures, not likely too much higher than Jovian exosphere temperatures

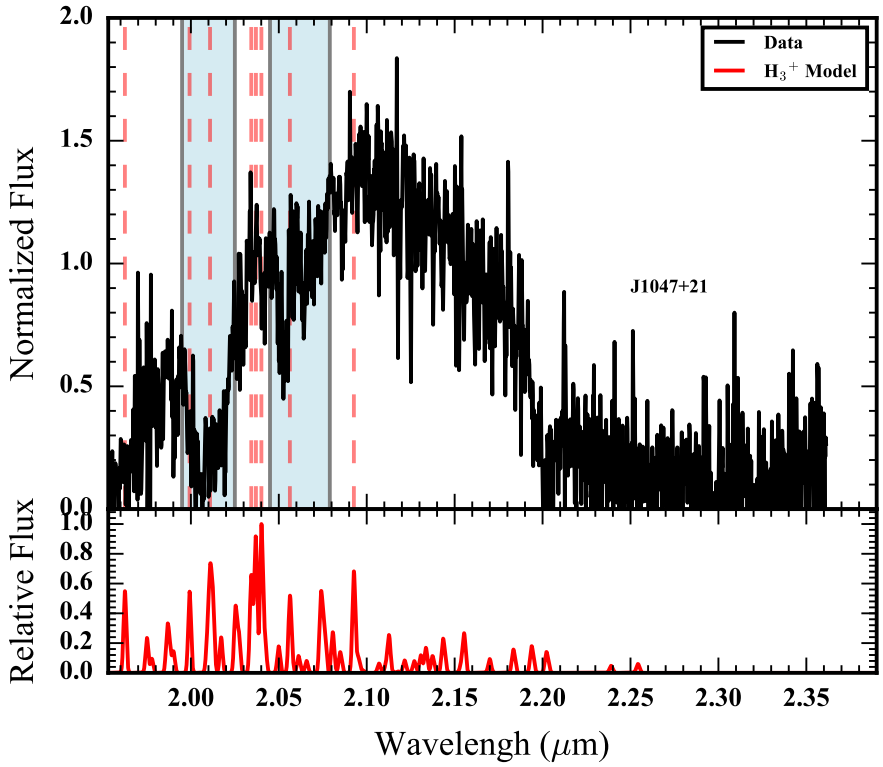

Figure 4.12: Same as in Figure 4.4 but for J1047+21. The simulated H_3^+ spectrum uses rotational and vibrational temperatures of 900 K.

(T ~ 1000 K), we do not see any emission in the T dwarfs (e.g., Lam et al. 1997; Grodent, Waite, and Gérard 2001). Consequently, the difference in temperatures does not likely drive the differences in H_3^+ emission.

Non-LTE effects suppress the strength of emission features, especially at high latitudes where the densities are low (Melin et al. 2005; Tao, Badman, and Fujimoto 2011). This effect could be significant in the brown dwarfs which have higher gravity and warmer atmospheres, but requires detailed modeling to understand. Additionally, our model spectrum assumed LTE conditions, and is likely incorrect; however our rough estimates were conservative in nature and the effect of the non-LTE conditions is only a factor of a few on the assumed total energy (Tao, Badman, and Fujimoto 2011). Despite this caveat, there should still have been significant H_3^+ emission, if the processes were identical to the Jovian case.

Atmospheric mixing has an important influence because it can drive the rapid destruction of H_3^+ through interactions with abundant atmospheric gases. Although

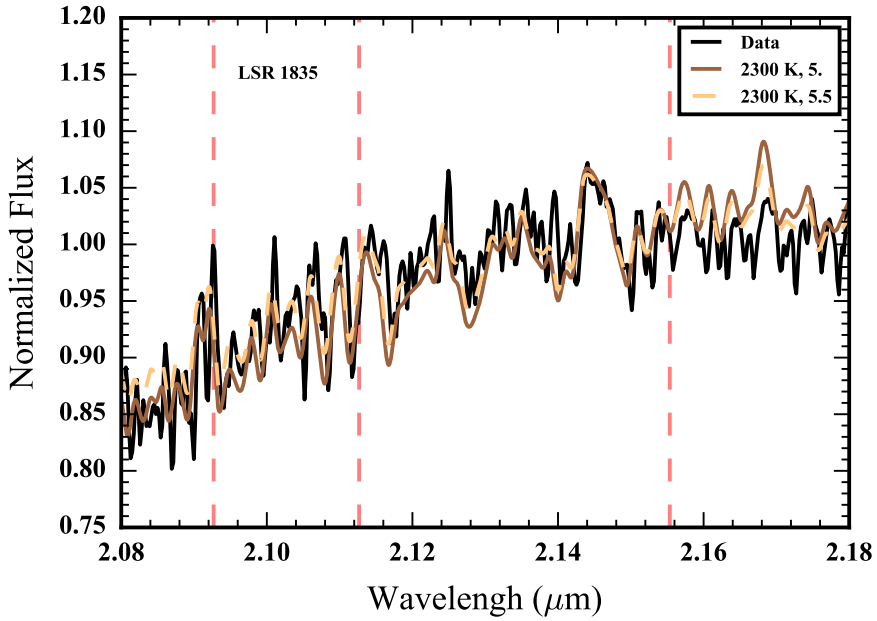

Figure 4.13: A close in view of our MOSFIRE spectrum of LSR 1835 highlighting the locations of the strongest expected H_3^+ features with PHOENIX model spectra overlaid. The solid model line uses an effective temperature of 2300 K and a gravity of log g = 5, while the dashed line uses an effective temperature of 2300 K and a gravity of log g = 5.5. The features in the data closely follow the features seen in the model spectra, indicating the absence of any H_3^+ emission features (see Section 4.4).

the H_3^+ ion emits readily on time scales $\lesssim$0.01 s, high density environments can lead to rapid reactions that remove H_3^+ before it has an opportunity to emit (Badman et al. 2015). In Saturn's atmosphere, H_2O plays this role, whereas in Jupiter, CH_4 is the dominant reacting species (Perry et al. 1999; Tao, Badman, and Fujimoto 2011; Badman et al. 2015). When the homopause layer is high, or conversely when the electron energy deposition layer is deep, the site of dominant collisional ionization and H_3^+ creation becomes a region of frequent collisions with neutral species. This has the effect of limiting the amount of H_3^+ emission possible.

Similarly, through electron recombination, a large electron number density will destroy any H_3^+ that is produced. In the absence of heavy molecules like H_2O or CH_4, this recombination process is the dominant loss mechanism for H_3^+ (Badman et al. 2015). Although the brown dwarfs are warmer and can sustain more thermally ionized atmospheres than what is expected for giant planets, the atmospheres are still predominantly neutral and are not likely to suppress H_3^+ entirely through electron

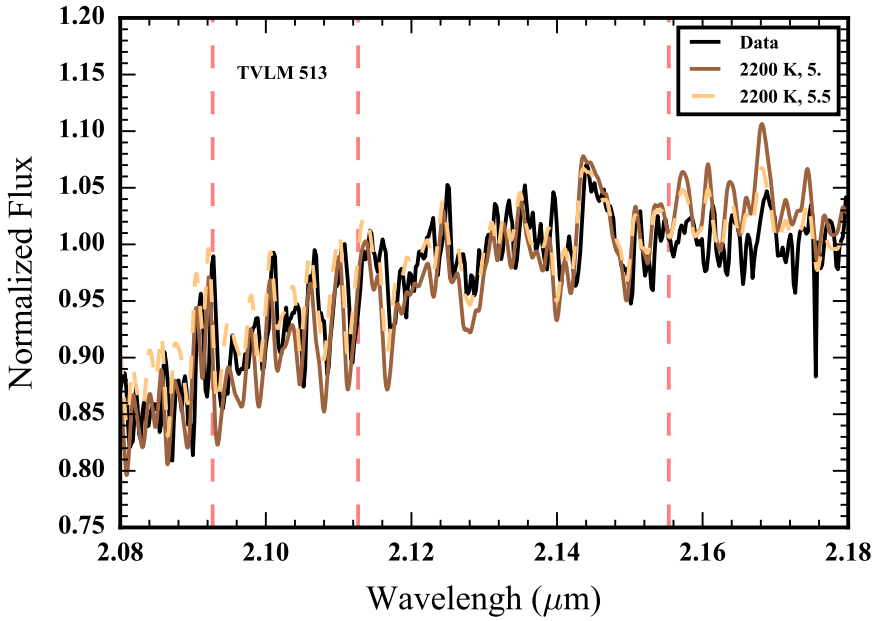

Figure 4.14: Same as Figure 4.13 but for TVLM 513 with model spectra corresponding to an effective temperature of 2200 K and gravities of log g = 5 and log g = 5.5 for the solid and dashed lines respectively. No clear indication of H_3^+ emission features are visible.

recombination (Rodriguez-Barrera et al. 2015).

The weak H_3^+ emission inferred by our observations is consistent with enhanced ion losses through collisions with neutral species. Whereas the homopause layer is set by the atmospheric properties, the depth reached by the electron energy beam is set by the mean energy of the electron energy distribution; for a given atmosphere, an electron beam with greater mean electron energies reaches deeper into the atmosphere to deposit the bulk of its energy (Tao, Badman, and Fujimoto 2011). The absence of H_3^+ emission potentially indicates that the brown dwarf electron energy distributions have sufficient energy to penetrate into the deeper well mixed atmospheric gas. This would then set a lower limit on the electron energies. A higher energy beam relative to Jovian auroral emissions is consistent with the faster rotation of the brown dwarfs, a few hours relative to the 10 hr Jovian rotation period and the stronger magnetic field strengths, kG fields instead of 10 G fields (e.g., Hallinan et al. 2008; Bagenal et al. 2014). These physical conditions are likely to generate larger potential drops and more energetic magnetospheric currents and lead to stronger radio aurorae, as is seen in many of the radio brown dwarfs

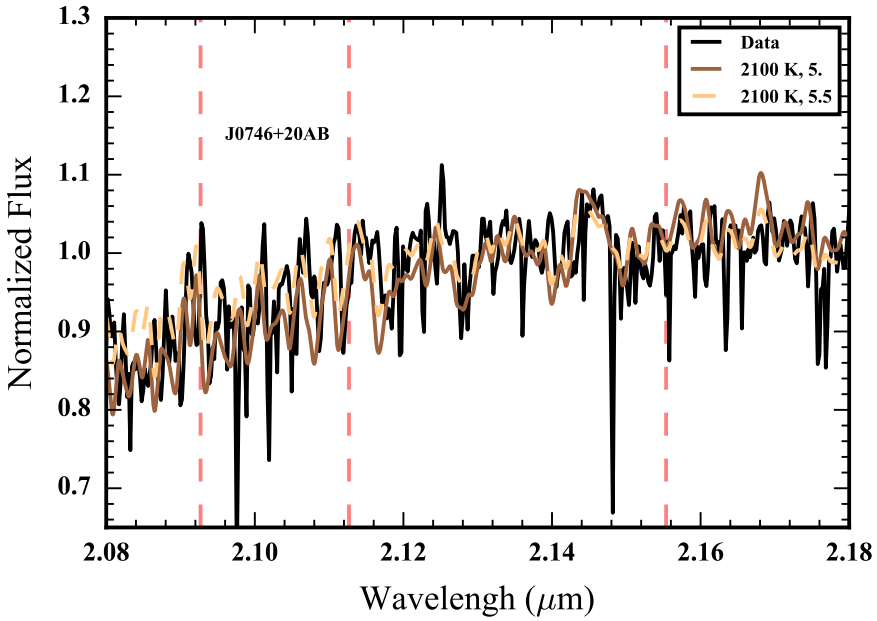

Figure 4.15: Same as Figure 4.13 but for J0746+20AB with model spectra corresponding to an effective temperature of 2100 K and gravities of log g = 5 and log g = 5.5 for the solid and dashed lines respectively. No clear indication of H_3^+ emission features are visible.

(e.g., Hallinan et al. 2015). Additionally, this scenario would predict diminished ultraviolet aurorae due to significant hydrocarbon absorption in the column of gas above the auroral energy deposition layer (Gustin et al. 2013).

Another reason for the observed absence of the K-band auroral emission lines could simply be due to the variability of the aurorae with rotational period. As demonstrated by Hallinan et al. (2015), the auroral surface features rotate in and out of view, and because our observations do not all span a rotational period, it is possible that we missed the emission by observing at the wrong time. Although this is somewhat unlikely for all of the targets in our sample, it remains a possibility. Additionally, Pineda et al. (2016) demonstrated that the emission features may vary on timescales exceeding the rotational period, requiring long-term monitoring and recurring observations to rule out completely. Nevertheless, it is not unreasonable to consider our observed targets to be missing appreciable H_3^+ emission.

Our results suggest that the emergent auroral emission of brown dwarfs are distinct from those of Jupiter. The energy scalings between different wavelength regimes are different, potentially due to a much stronger electron beam generated by the

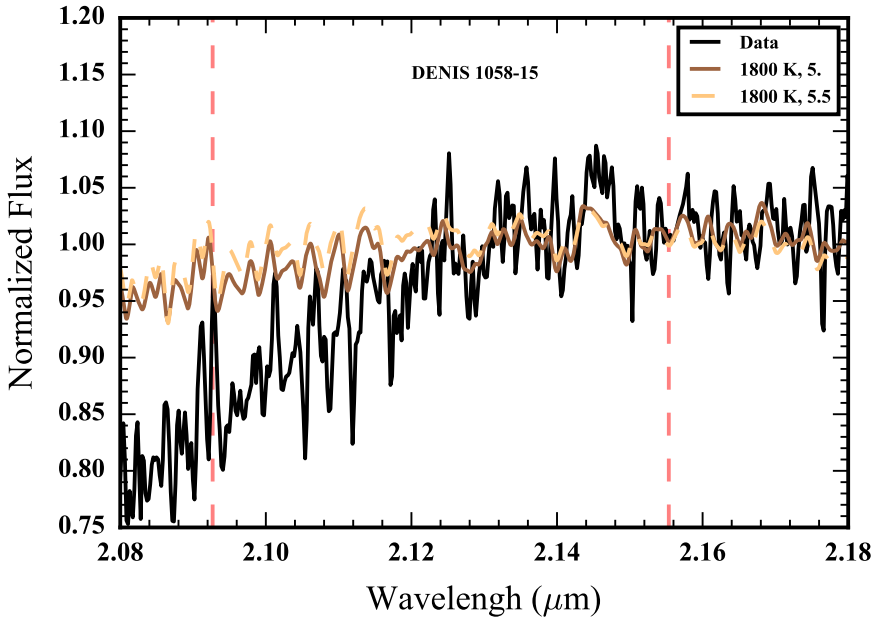

Figure 4.16: Same as Figure 4.13 but for DENIS 1058-15 with model spectra corresponding to an effective temperature of 1800 K and gravities of log g = 5 and log g = 5.5 for the solid and dashed lines respectively. The mismatch in model and data on the left-hand side could be due to partly to spectrophotometric variations and the need for heterogenous cloud models to fit photometrically variable targets. However, observing conditions were not ideal, clouds were prominent and could be an effect of systematics. Nevertheless, no clear indication of H_3^+ emission features are visible.

brown dwarf magnetospheric current systems. This scenario needs to be confirmed through further observations, potentially examining the H_3^+ fundamental emissions at 4 μm with high sensitivity and resolution. These kinds of observations will be made possible with the *James Webb Space Telescope* and its suite of NIR instruments. Additionally, auroral atmospheric modeling of brown dwarfs will be key in understanding the various physical processes that are taking place and how they change in the brown dwarf regime relative to gas giant planets. Only through these efforts will we be able to use auroral processes to probe the upper atmospheric conditions of brown dwarfs and provide physical constraints on the physics of auroral processes in brown dwarf atmospheres.

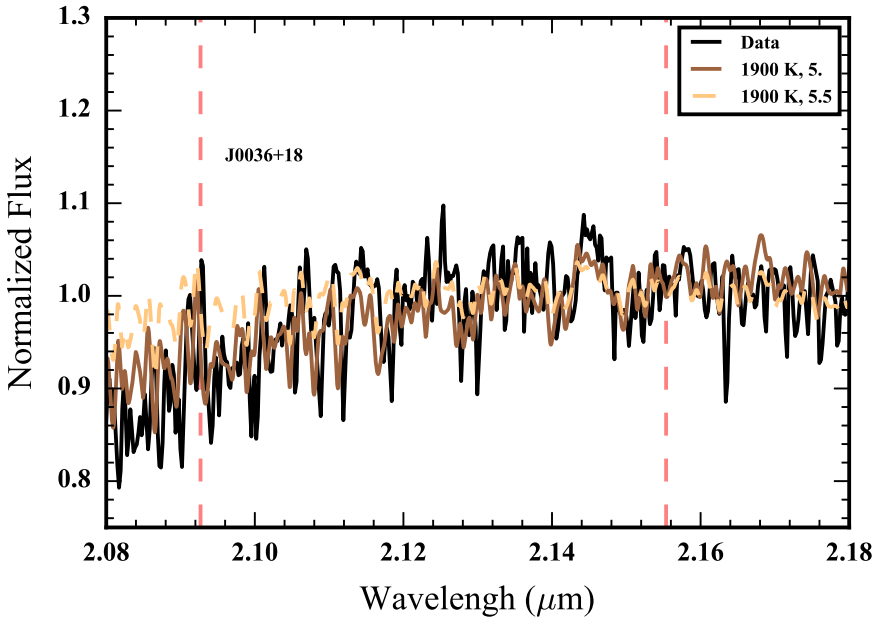

Figure 4.17: Same as Figure 4.13 but for J0036+18 with model spectra corresponding to an effective temperature of 1900 K and gravities of log g = 5 and log g = 5.5 for the solid and dashed lines respectively. No clear indication of H_3^+ emission features are visible.

Acknowledgments

The authors wish to recognize and acknowledge the very significant cultural role and reverence that the summit of Mauna Kea has always had within the indigenous Hawaiian community. We are most fortunate to have the opportunity to conduct observations from this mountain.

J.S.P would like to thank Jean-Michel Desert for assistance in developing the observing program and coordinating observations.

J.S.P would like to thank Chuck Steidel and Gwen Rudie for their assistance preparing observations with MOSFIRE, as well as Nick Konidaris for help with the data reduction.

J.S.P was supported by a grant from the National Science Foundation Graduate Research Fellowship under grant No. (DGE-11444469).

The data presented herein were obtained at the W.M. Keck Observatory, which is operated as a scientific partnership among the California Institute of Technology, the University of California and the National Aeronautics and Space Administration.

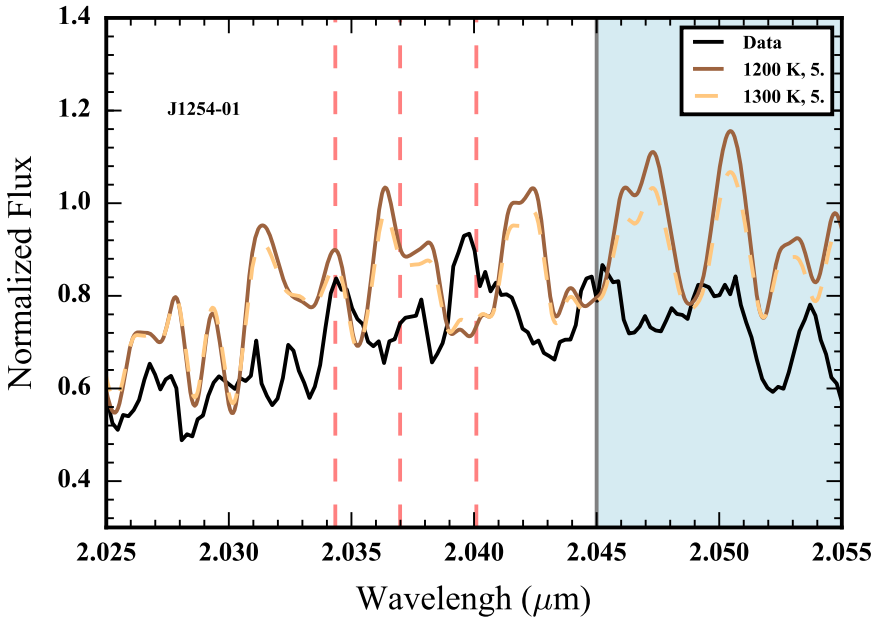

Figure 4.18: Same as Figure 4.13 but for J1254-01 with model spectra corresponding to effective temperatures of 1200 K and 1300 K, with a gravity of log g = 5, for the solid and dashed lines respectively. The shaded region marks off the region of significant telluric absorption. No clear indication of H_3^+ emission features are visible.

The Observatory was made possible by the generous financial support of the W.M. Keck Foundation.

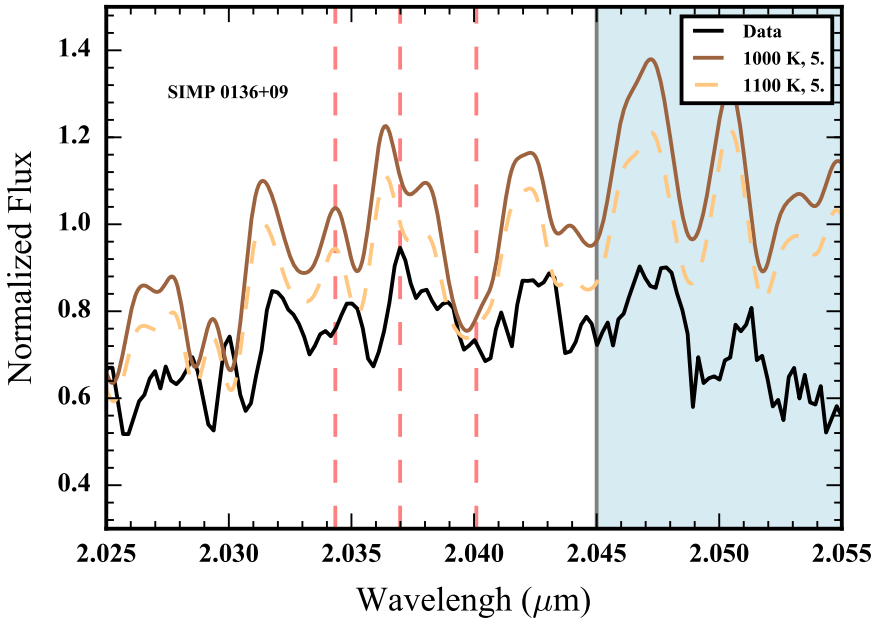

Figure 4.19: Same as Figure 4.13 but for SIMP 0136+09 with model spectra corresponding to effective temperatures of 1000 K and 1100 K, with a gravity of log g = 5, for the solid and dashed lines respectively. No clear indication of H_3^+ emission features are visible.

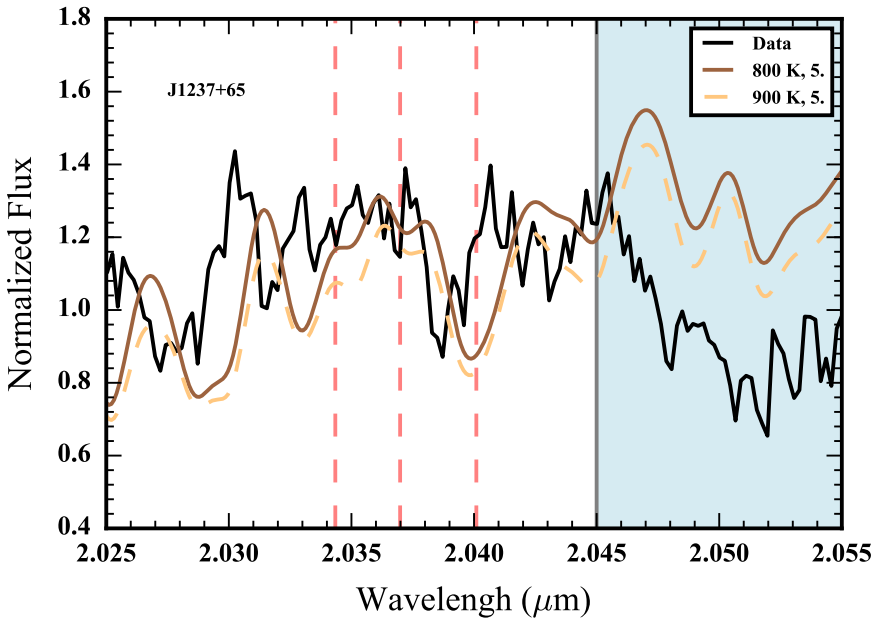

Figure 4.20: Same as Figure 4.13 but for J1237+65 with model spectra corresponding to effective temperatures of 800 K and 900 K, with a gravity of log g = 5, for the solid and dashed lines respectively. No clear indication of H_3^+ emission features are visible. Despite relatively noisy spectrum, no large emission lines are observed that are consistent with H_3^+, given known Hα emission.

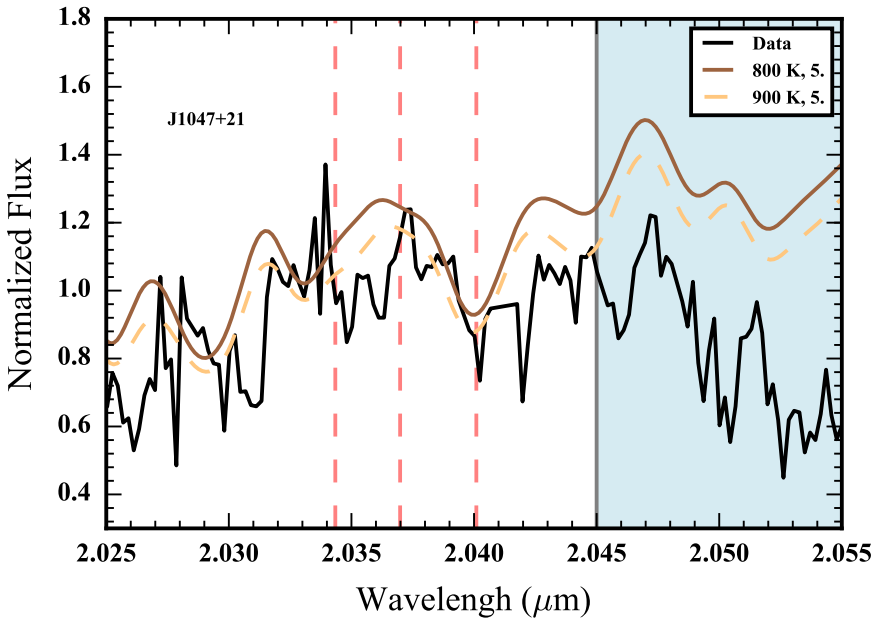

Figure 4.21: Same as Figure 4.13 but for J1047+21 with model spectra corresponding to effective temperatures of 800 K and 900 K, with a gravity of log g = 5, for the solid and dashed lines respectively. No clear indication of H_3^+ emission features are visible. Despite relatively noisy spectrum, no large emission lines are observed that are consistent with H_3^+, given known Hα emission.

Chapter 5

PRELIMINARY INVESTIGATION INTO THE MORPHOLOGY AND TEMPORAL VARIABILITY OF AURORAL Hα EMISSION FROM LSR J1835+3259

The emergence of auroral phenomena at the end of the main sequence has been heralded by the detections of strong radio pulses in the atmospheres of ultracool dwarfs. These findings have been led by the detailed study of benchmark targets, like LSR J1835+3259, displaying the key observations indicative of auroral radio emission and the corresponding auroral surface features (Hallinan et al. 2015). Building on these findings, I present a preliminary investigation into the morphology and variability of the Hα emission of LSR J1835+3259 using high-resolution optical spectroscopy. We monitored the target for a full night to determine the shape of the Hα line profile and examine how the profile changes with rotational period. We examine these profiles to determine the nature of the emission and reconstruct the stellar emission surface through doppler imaging techniques. We use this data to constrain the properties of the electrodynamic engine powering brown dwarf auroral phenomena, potentially confirming co-rotation breakdown as the key underlying physical mechanism.

5.1 Introduction

Observations of the magnetic activity of very-mow mass stars has revealed significant departures at the end of the main sequence from the activity observed in earlier-type stars. Numerous surveys have reported a decline in the prevalence and strength of typical stellar activity tracers, like X-ray and Hα, in this ultracool dwarf (UCD; spectral type $\geq$ M7) regime, despite rapid rotation rates (e.g., Reiners and Basri 2008; Berger et al. 2010; McLean, Berger, and Reiners 2012; Antonova et al. 2013; Williams, Cook, and Berger 2014; Schmidt et al. 2015). These changes track the decreasing atmospheric temperatures of UCDs and the low fractional ionization of their atmospheres (Mohanty et al. 2002; Rodriguez-Barrera et al. 2015). However, many objects in this regime display unexpectedly strong emission features, raising questions regarding the physical mechanisms driving the activity (e.g., Burgasser, Kirkpatrick, Reid, et al. 2000; Berger et al. 2001).

The activity at the beginning of the UCD sequence near the transition between M

dwarfs and L dwarfs (T_{eff} ~ 2300 K) is of particular interest because of the complex overlapping physical regimes that prevail. These objects straddle the stellar versus substellar boundary with masses near ~0.08 $M_{\odot}$ (e.g., Chabrier and Baraffe 2000). Since the atmospheres are becoming cooler and increasingly neutral, the influence of dust condensates and clouds (ex. silicate grains) in the atmospheric opacities can be significant (e.g., Burrows et al. 2001; Marley and Robinson 2015). Despite the cool temperatures, the atmospheres are sufficiently ionized and magnetically heated to sustain chromospheric structures (Schmidt et al. 2015; Rodriguez-Barrera et al. 2015). These objects are also capable of sustaining both strong large-scale and small-scale magnetic fields (Morin et al. 2010, 2011; Yadav et al. 2015).

Furthermore, these objects may be capable of hosting auroral phenomena. Crucial to this development has been the detailed study of benchmark targets and the physics governing their emission processes. The discovery of radio emission from LP944-20 provided evidence for the continued magnetization of very-low mass stars and brown dwarfs (Berger et al. 2001). The characterization of the periodic circularly polarized radio pulses from objects such as TVLM513-46546 and 2MASS J00361617+1821104 revealed the electron cyclotron maser instability (ECMI) as a significant process in UCD atmospheres (Hallinan et al. 2008). The discovery of similar radio emissions in the T6.5 dwarf, 2MASS 10475385+2124234, confirmed the pervasiveness of the ECMI throughout the UCD regime (Route and Wolszczan 2012).

Table 5.1: Properties of LSR J1835+3259

Parameter	Value	References
Spectral Type	M8.5	1
Parallax	176.5 ± 0.5 mas	1
Mass	77.28 ± 10.34 M_{Jup}	2
L_{bol}	$10^{-3.5} L_{\odot}$	2
T_{eff}	2316 ± 51 K	2
$\log g$ (cgs)	5.22 ± 0.11	2
Radius	1.07 ± 0.05 R_{Jup}	2
Age	0.5 - 10 Gyr	2
$v \sin i$	43.9 ± 2.2 km s^{-1}	3
Period	2.84 ± 0.01 hr	4

References. – (1) Reid et al. 2003, (2)Filippazzo et al. 2015, (3) Crossfield 2014, (4) Hallinan et al. 2008

More recently, Hallinan et al. (2015) conducted simultaneous radio and optical observations of LSR J1835+3259 to investigate a connection between highly circularly polarized radio pulses and optical Hα emission. With their optical spectroscopic monitoring, they showed that the Hα emission was periodic and commensurate with the radio pulses. Their work reasoned that the energetic electrons responsible for the radio emission impacted the stellar surface and created a surface feature responsible for the optical emission lines and optical broadband variability of LSR J1835+3259. Hallinan et al. (2015) concluded that these observations were consistent with auroral phenomena, as seen in the gas giant planets of the Solar System, in which large-scale magnetospheric currents drive both radio and optical auroral emissions. The currents generate an energetic electron beam that emits strongly in the radio, and ultimately precipitates into the atmosphere, colliding with the predominately neutral hydrogen gas (H and H_2) to generate Hα and other auroral emission features.

Through these studies the possibility of auroral phenomena in UCD atmospheres has developed, however there still remain many open questions. Most prominently, the nature of the electrodynamic engine powering the magnetospheric currents is unknown. In the case of brown dwarfs the most likely mechanisms are either co-rotation breakdown of a magnetized plasma disk or the flux tube interaction between the brown dwarf and a nearby satellite (Schrijver 2009; Nichols et al. 2012; Hallinan et al. 2015).

In order to distinguish these processes and the mechanisms powering the activity at the end of the main sequence, we undertook a spectroscopic monitoring campaign to closely examine the surface feature detailed in Hallinan et al. (2015), measuring with high-resolution the Hα emission profile and how it changes with the rotation period of the UCD benchmark target LSR J1835+3259. In Section 5.2, we provide the details and physical characteristics of our target. In Section 5.3, we review the data from our high resolution spectroscopic monitoring campaign. In Section 5.4, we report the the results of our observations and the important spectral features. In Section 5.5, we apply doppler imaging techniques to our data set to reconstruct an image of the surface in Hα emission. In Section 5.6, we consider the implications of our findings on the nature of the brown dwarf auroral electrodynamic engine. Lastly, in Section 5.7 we discuss our conclusions.

5.2 Target: LSR J1835+3259

LSR J1835+3259 is a M8.5 dwarf at a distance of 5.67 ± 0.02 pc discovered by Reid et al. (2003). Filippazzo et al. (2015) recently reported fundamental parameters for this target based on a semi-empirical approach using evolutionary models and the measured bolometric luminosity from spectroscopic and photometric observations spanning the bulk of the spectral energy distribution. They determine a bolometric luminosity of $L_{\rm bol} = 10^{-3.5}\ L_{\odot}$, an effective temperature of $T_{eff} = 2316 \pm 51$ K, a mass of $M = 77.28 \pm 10.34$ $M_{\rm Jup}$, a surface gravity of $\log g = 5.22 \pm 0.11$ (cgs), and a radius of $R = 1.07 \pm 0.05$ $R_{\rm Jup}$. The error bars on their parameters reflect the range of the values consistent with the evolutionary models and an assumed field age between 0.5 and 10 Gyr. These values are tabulated in Table 5.1.

Previous studies have revealed LSR J1835+3259 to emit strongly pulsed radio emission with a period of 2.84 ± 0.01 hr, attributed to the object's rotation (Hallinan et al. 2008). Using the range of permissible radii (see Table 5.1), we can determine the likely equatorial velocity of the target to be $v = 47 \pm 2$ km s^{-1}. Furthermore, measurements of the projected rotational velocity, as compiled by Crossfield (2014), suggest $v \sin i = 43.9 \pm 2.2$ km s^{-1}, indicating that the system is likely inclined by more than 60° and possibly close to 90° (Hallinan et al. 2008).

5.3 Data

We observed LSR J1835+3259 on the night of 2016, July 09 (UT) for a total of ~8.5 hr using the Keck telescopes on Manua Kea. Our observational settings were set to similar parameters as have been deployed in the past to observe late M-dwarfs by many authors (e.g., Reiners and Basri 2010); we summarize our approach below. We used the High Resolution Echelle Spectrometer (HIRES) in the red configuration with a 1".148 wide slit providing a resolution of ~ 37,000 (Vogt et al. 1994). The echelle and cross disperser angles were set to -0.235 and 1.736, respectively, allowing us to span a wavelength range from 570 nm to 1000 nm across the 3 different CCD chips of HIRES. The detector gain was set to low and the pixels binned 2x1, in the spatial versus the spectral directions. We also used the order blocking filter OG 530. The conditions for our observing run were favorable all night with a seeing of ~ 0".75. We took exposures of 600 s for each frame, corresponding to rotational smearing of ~ 6% of the phase curve, assuming a period of 2.84 hr. We got a total of 50 exposures in the single night, spanning ~3 rotational periods.

We reduced the spectra using the MAKEE pipeline for HIRES[1]. The pipeline bias

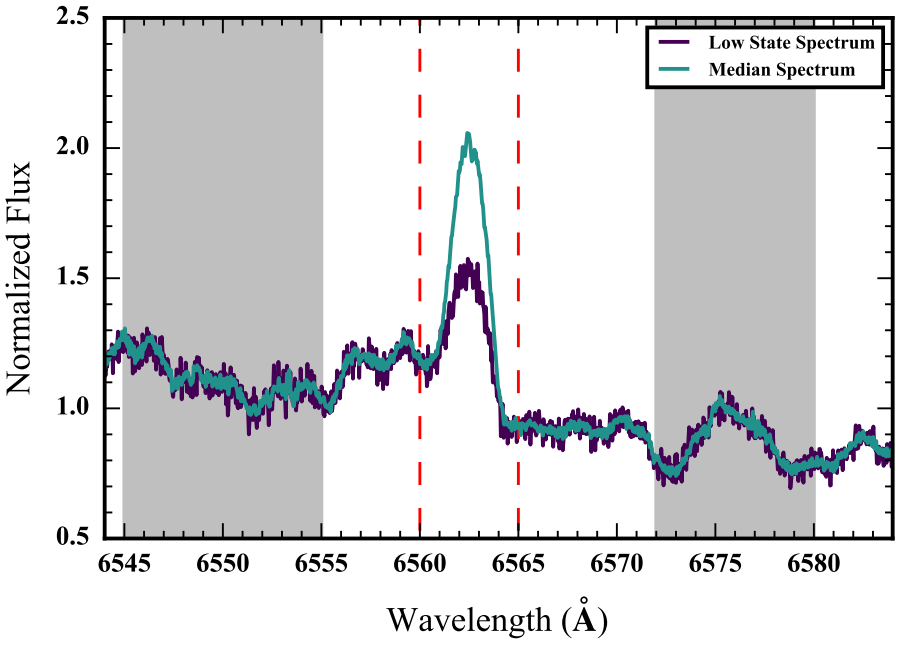

Figure 5.1: Spectral profiles of LSR J1835+3259 centered on the Hα region, showing both the spectrum in its low state and the median from the full observing run. The grey region to the left marks off the region used to normalize the spectra and the dashed lines bound the region use to compute the Hα equivalent widths, see Figure 5.2.

subtracts the data, averages together the flat field calibration images taken at the beginning and end of the night, divides each data exposure by the combined flat field, and computes a wavelength solution from ThAr arc lamp exposures taken before and after the observing run. MAKEE then extracts the spectra for each order of the dispersed spectrum, subtracting the nearby sky emission.

Our primary focus was on the emission of Hα at 6563 Å, which fell in the middle of the first CCD chip, covering the shortest wavelengths of the spectrum. The typical signal to noise in each exposure for this spectral region was $\gtrsim$10 in the continuum and $\sim$18 in the line center, with greater signal during the high Hα emission states over the course of the night. We plot an example of the Hα emission profile in Figure 5.1, showing the normalized spectrum for the median of all our data and a low state spectrum (see Section 5.4).

[1] See `http://www.astro.caltech.edu/~tb/ipac_staff/tab/makee/index.html`

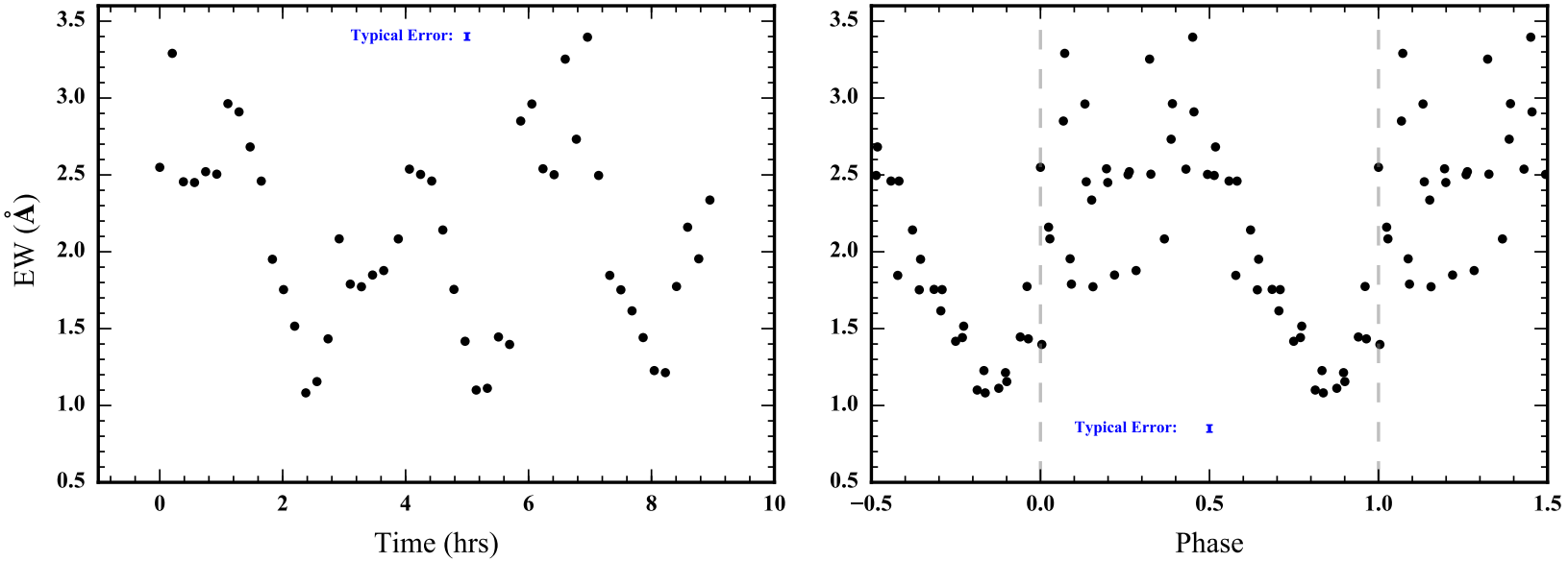

Figure 5.2: The light curves of Hα emission for our observations of LSR J1835+3259. *Left* - The EW as a function of time with the points plotted at the middle of each 600 s exposure with the reference time set to the middle of our first data point, 2016-07-09 05:52:53.26 UT. *Right* - Same data as the left figure but with the points phased at the 2.84 hr period. The phased curve is plotted twice and wrapped around to visualize the periodicity. The light curves show multiple bright increases in the flux during the rising portion of the light curve.

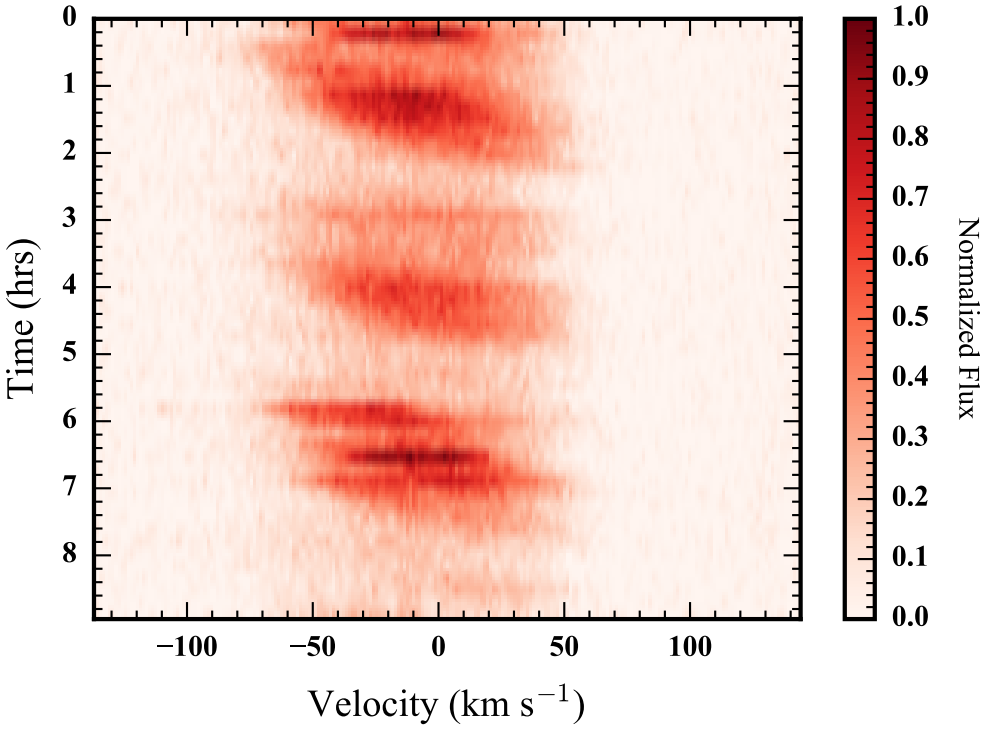

Figure 5.3: The dynamic spectrum from our observations of LSR1835+32 centered around Hα for the night of 2016 July 09. Each row corresponds to the observed flux in 600 s exposures, with the continuum emission subtracted off. The plot shows how the peak of the Hα emission traverses the stellar surface, from blue shifted to redshifted, over the course of several rotational periods.

5.4 Measurements

Hα EW Time Series

For each of our spectra we also computed the Hα equivalent width (EW) to illustrate the total changes in the line flux over the course of the night. We normalized the spectra, following Reiners and Basri (2010), by taking the median of the flux from 6545-6555 Å and 6572-6580 Å (see Figure 5.1). In the normalized spectra we add up the flux between 6560 Å and 6565 Å to determine the EW; this region is denoted by dashed lines in Figure 5.1. These bounds were chosen to encompass the full width of the line profiles for all of the spectra at different rotational phases. The resulting light curve is plotted in Figure 5.2, showing the EWs as a function of time in the left plot and the phased light curve assuming a period of 2.84 hr in the right plot, with each data point shown twice to wrap the data around in phase (the dashed lines mark a single period of data).

The time series shows a clear periodicity in the Hα emission, as has been seen in previous studies, consistent with the established rotational period from Hallinan et al. (2015). The periodic variations appear to be sinusoidal with numerous bursts superimposed on top (see Section 5.4). In the phased light curve (right-hand side in Figure 5.2), it is clear that the bursts are located predominantly during the brighter half of the phase curve, with comparatively consistent emission during the trough of the sinusoidal Hα variations.

Line Profiles

Our high resolution spectra additionally allow us to measure the Hα line profiles and how they change with the rotation of LSR J1835+3259. We demonstrate these results with the dynamic spectrum in Figure 5.3 showing the line emission at different times as a function of velocity centered at 6562.7 Å. The spectra have been continuum subtracted by a second order polynomial fit to the continuum regions from 6559.7-6560.0 Å and 6565-6569.5 Å, and then normalized by the maximum value of all of the spectra. We observe clear structures in the shape of the line profiles. With time increasing downward, we see well defined sweeps from negative velocities (blue shifted) toward positive velocities (red shifted) in the sinusoidal emission.

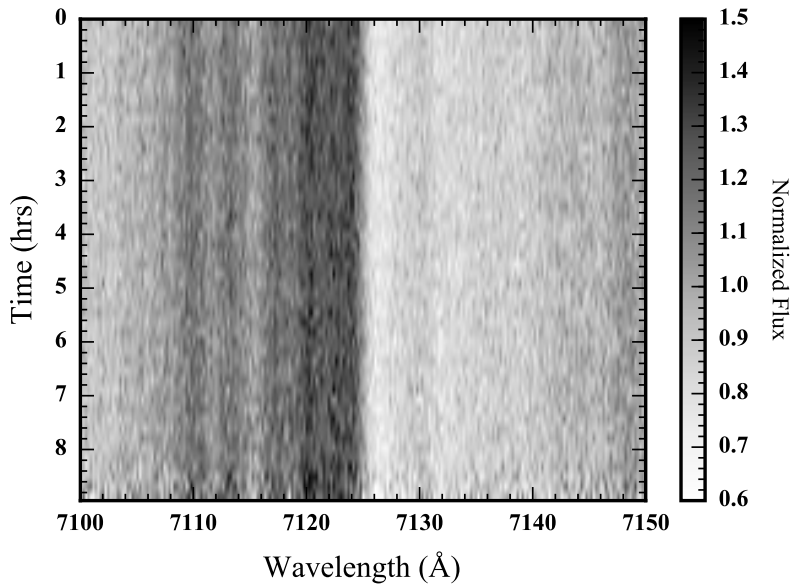

Figure 5.4: The dynamic spectrum of LSR J1835+3259, as in Figure 5.3, centered around the TiO molecular absorption bandheads near 7125 Å. Spectroscopic regions dominated by absorption features do not display the spectroscopic drifts evident in the Hα emission line.

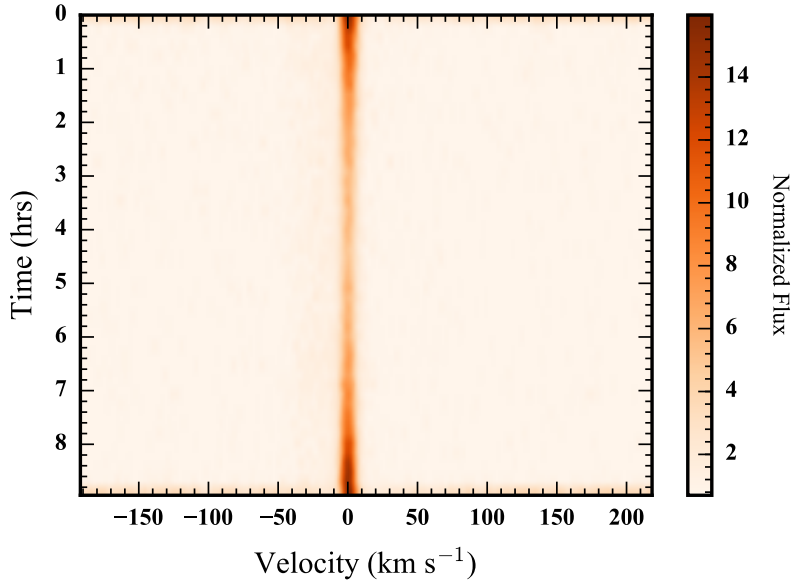

Figure 5.5: The dynamic spectrum from our observations, like Figure 5.3, but for just the sky emission centered on the position of Hα. The Earth's emission of Hα is clearly present, seen as a steady background level that increases during twilight. The changes in the position and shape of the Hα line profile for LSR J1835+3259 are astrophysical and cannot be due to drifts in the wavelength solution and/or background emission.

As a check on this observed structure, we compared these features against the data for different molecular features in the late M dwarf spectra. In Figure 5.4, we show the dynamic spectrum for the TiO features near 7100 Å. The edge of the band head is seen clearly as the steady streak across the center of the plot. The other regions of the spectrum do not show the structure evident in the Hα line. Moreover, an examination of the sky emission, shows terrestrial Hα (see Figure 5.5), as a constant background to our astrophysical observations, with the sky emission brighter at the beginning and end of the night around twilight. These checks confirm that the structure seen in Figure 5.3 is particular to Hα and it not due to systematic changes in the sky background.

The dynamic spectrum of Figure 5.3 reveals emission features traversing the stellar surface with the stellar rotation. A surface feature with enhanced Hα emission creates the ribbons evident in Figure 5.3, with Hα bursts occurring preferentially when the surface feature is in view (phases 0.0-0.5 in Figure 5.2). The bright ribbons sit upon Hα emission that remains present throughout the observations, which is characterized as the low-state in Figure 5.1. This emission extends out

nearly to velocities ~50 km s^{-1}. Considering the observed $v \sin i$ of 43.9 km s^{-1}, the emission flux at large velocities suggest that the low-state emission is consistent with being fully rotationally broadened by the full stellar disk. To understand the surface features generating this emission we further apply doppler imaging methods in Section 5.5.

Hα Bursts

In addition to the smooth variations of the Hα emission evident in the dynamic spectra, there were several Hα bursts captured in our observations, for example, near the beginning of the observing night at the top of Figure 5.3. We plot the line profiles, in Figure 5.6, of the exposures with the 8 greatest Hα EW measurements, organized according to their phase, normalized and offset by a constant. The plot includes a dashed line indicating the central location of Hα at 6562.7 Å, with each profile including the low-state of Figure 5.1 as a comparison in grey.

That these bursts coincide with the phases at which the Hα surface feature traverses the line-of-sight, suggests that the bursts likely emerge from the same surface feature. However, a close look at the phases of the bursts reveals that the burst centroids do not perfectly track the velocity centroid of the underlying surface feature. Nevertheless, the burst locations do appear preferentially on the blue side at low phases and more centrally at phases closer to 0.5. Additionally, the light curves of Figure 5.2 show that in our observations the bursts never took place while the surface feature was rotating out of view (phases 0.5-0.75), suggesting that the bursts may be preferentially located toward the leading edge of the surface feature.

These burst profiles indicate that the enhances emission is typically localized at particular velocities but remains rather broad in many instances, spanning regions encompassing tens of km s^{-1}. Alternatively, the intrinsic emission line profile may be rather broad, potentially exceeding the thermal contribution of ~5 km s^{-1}, based on the stellar photospheric effective temperature. Interestingly, the shapes of some of these bursts appear to be relatively flat, indicating that the burst emission may not be dominated by the region at the velocity centroid and instead could be dominated by the contributions from the edges of the bursting regions.

5.5 Doppler Imaging

We applied doppler imaging techniques to reconstruct the stellar surface in Hα from our HIRES spectra of LSR J1835+3259, as presented in Figure 5.3. As our initial attempt, we selected a set of spectra relatively free of bursts during the

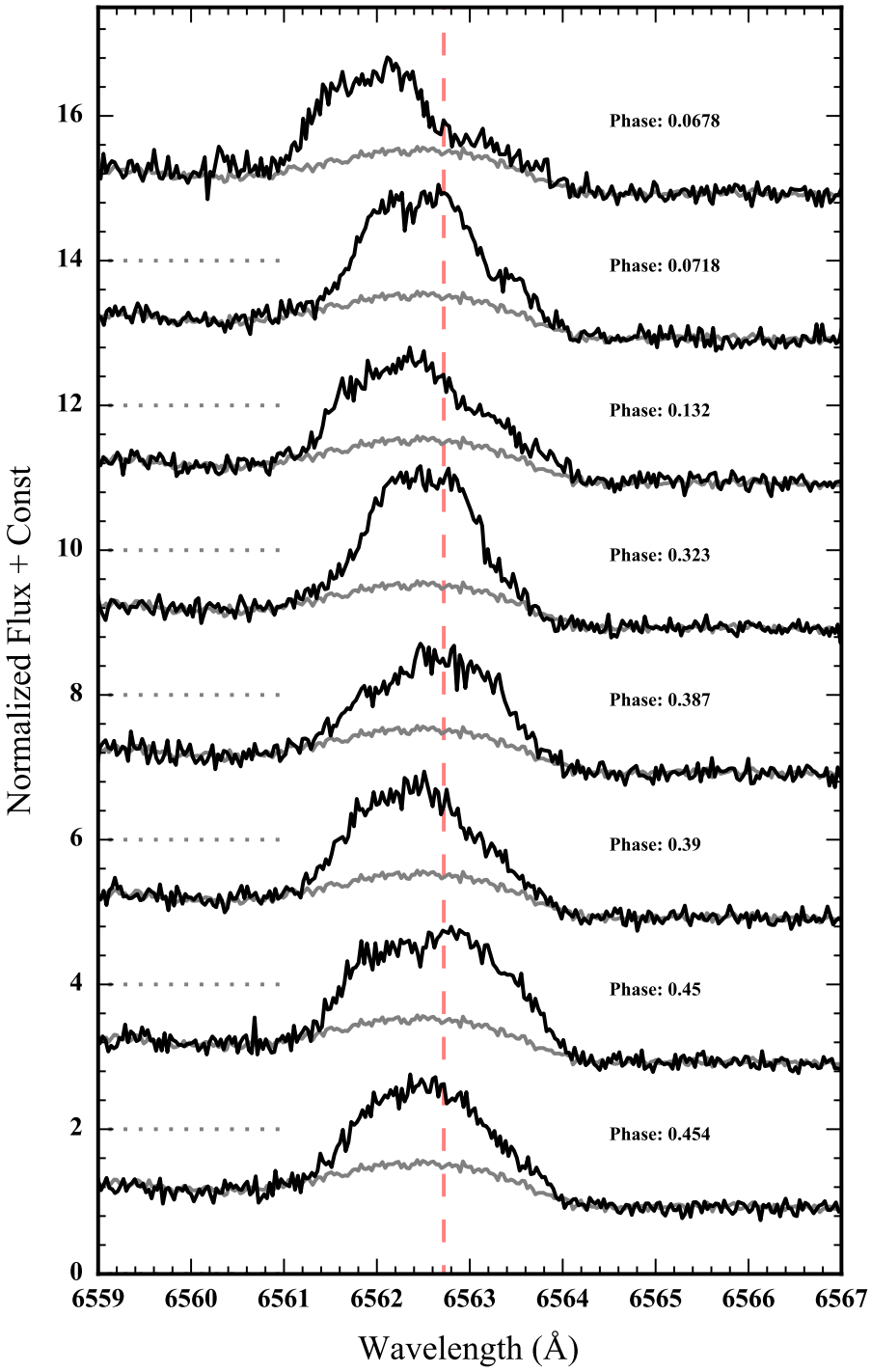

Figure 5.6: The Hα emission line profiles for the exposures with the 8 brightest EW measurements, plotted in order of their corresponding phase (see Figure 5.2) compared to the profile for the average low state in grey. The center location of Hα is marked by the dashed line and the constant offsets are plotted with the dotted line. These profiles show the emission during Hα bursts with show narrower profiles and different velocity centroids at different rotational phases.

middle of the observations from 1.60 to 5.85 hr to do the reconstruction. Because, the reconstruction relies on viewing the same stellar features at different rotational phases over time, the time variable bursts become problematic in the inversion process and could lead to unphysical features in the resulting image. We also removed a small burst around $t = 3$ hr (see Figure 5.2) for this reason.

The image reconstruction uses a tiled stellar surface with individual flux contributions from each surface and a forward model to generate a simulated spectrum as a function of velocity and rotational phase. The model spectrum is then compared to the data to determine how closely the model fits. Iteratively, the model stellar surface tile flux levels are adjusted to maximize the likelihood of the data, given the model parameters. Additionally, an entropy function is used to penalize the fit statistic when adjusting the surface image to the data. This process maximizes the entropy of the image to produce the best fit image that is also the simplest and makes the image relatively smooth (see Berry 1993). These methods are regularly employed in image reconstruction and doppler tomography (e.g., Hill et al. 2016).

We summarize our doppler imaging reconstruction in Figure 5.7. We set the period to 2.84 hr and the inclination to 80° and let iterative fitting determine the stellar radius. We used an intrinsic line profile of 5 km s^{-1} and an instrumental resolution of 8 km s^{-1}. In Figure 5.7, we show projections of the resulting best fit map at different rotational phases and a comparison of the model to the data. Despite, being an initial attempt at the image reconstruction, the doppler imaging results give a good fit to the data and reveals a high latitude feature. We show a close up of the stellar surface in Figure 5.8.

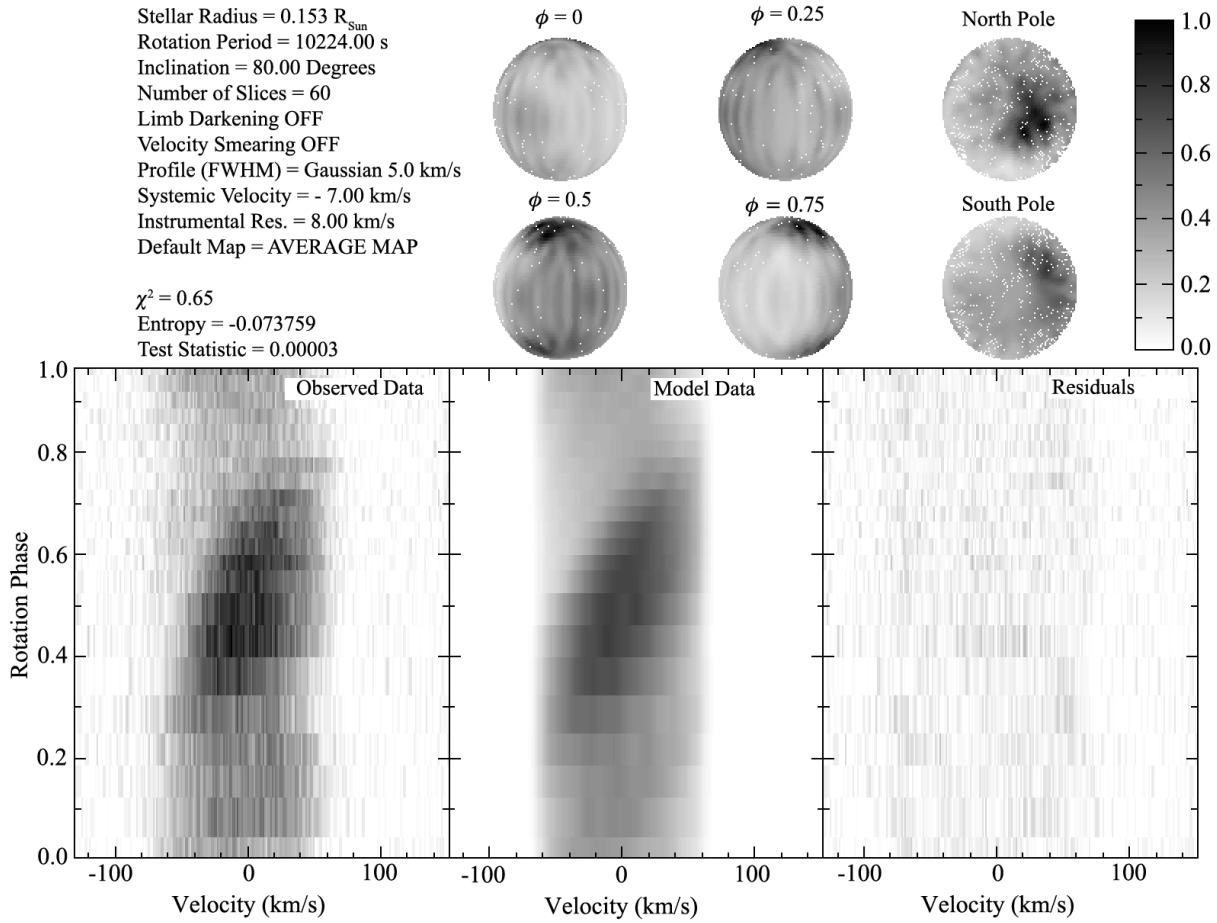

Figure 5.7: The results of our doppler imaging analysis. The parameters and statistics are listed in the upper left with projections of the stellar surface shown on the upper right. The darker regions are those with a greater contribution to the flux. The data have been all normalized to the peak value. The lower left plot shows the data phase folded over the 2.84 hr rotational period. The lower center plot shows the model data produced from the image reconstruction. The lower right plot shows the residuals between the model and the observations.

The surface map shows low-level full disk emission and a spot feature with the brightest Hα emission near the rotational axis. Although this is a preliminary look at the reconstructed surface image, the quality of the fit and the consistency of the features indicates that a more in depth analysis will not deviate too much from the basic picture presented here. The surface shows both full disk emission responsible for the low-state and the Hα wings, as well as a strongly emitting feature near the rotational axis, at about a latitude of $\sim$70°. There are longitudinal streaks in the map (see Figure 5.8), which are a consequence of trying to fit noise in the data and the degeneracy inherent to the inversion between emission latitude and velocity. Likewise, the south pole features are also a consequence of mirroring from the northern hemisphere emission and are likely spurious. As an additional caveat, the best fit model required an inflated radius of 0.153 $R_\odot$ to fit well. This is a consequence of the large wings of the Hα emission, exceeding the suggested rotational velocities, based on the period and radius (see Table 5.1). Although this will require resolution, it will not influence the resulting surface map, but is needed to match the width of emission in the data. A possible resolution lies in the assumed intrinsic width of the Hα emission, which could be potentially much large than assumed in the initial doppler image reconstruction.

5.6 The Electrodynamic Engine

Our observations of LSR J1835+3259 allow us to constrain the electrodynamic engine driving the auroral emission of this object. Crucially, the different mechanisms, either co-rotation breakdown or a flux-tube interaction with a satellite would produce different observational signatures in the Hα line profile. Additionally, although disfavored, reconnection with the ISM, as a kind of interstellar wind, would also provide a distinct profile (Schrijver 2009; Nichols et al. 2012). In Figure 5.9, we plot some potential scenarios for the emission line features and compare them to a fully rotational broadened line. The plot shows the profile for the emission from a magnetic polar cap, consistent with an ISM wind, with an opening half-angle of 20° (subtending 40° in diameter), compared to the profile of an auroral oval with an width of 2° and a opening half-angle of 19°. The plot shows that the line shapes for an auroral oval are distinct from a polar cap. The auroral oval produces a flatter profile than the polar cap and when the instrumental resolution is higher or when the intrinsic profile width is narrower leads to a depression at the line center due to the missing emission from the interior of the oval.

The examination of our HIRES emission line profiles and the doppler image recon-

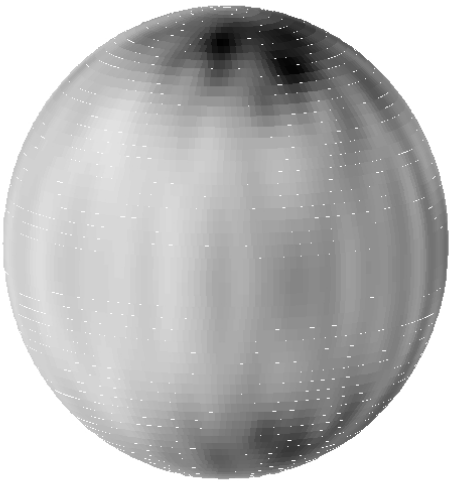

Figure 5.8: The doppler image map of LSR J1835+3259 based on the Hα emission at a phase of 0.65. The data is normalized to the peak value, as in Figure 5.7. The map highlights the high latitude feature ~70° where the bulk of the time variable emission emerges. Longitudinal streaks are due to the noise in the data and degeneracies in the transformation between surface latitude and velocity in the observed spectrum (see Section 5.5).

structions (see Section 5.5) indicates the presence of a high latitude surface feature which rotates with the stellar surface. Although, this is inconsistent with the satellite interaction, it is consistent with either an auroral oval or a polar cap. If we consider the center of the surface feature to coincide with the brown dwarf's magnetic axis, this suggests a potential 20° offset between the magnetic and rotational axes. Furthermore, the width of the surface feature appears to extend ~10° either way of the central location. If the surface feature is created by an auroral electron beam, in a dipolar dominated magnetic filed, this angle corresponds to the particular field lines that map to the electrodynamic acceleration regions along the magnetic equator. The corresponding distance along this equator, for the dipolar field, is then given by

$$L = (\sin\theta)^{-2}\, R_* \,, \tag{5.1}$$

where θ is the half-angle of the auroral oval or polar cap, and R_* is the object's radius. For $\theta = 10°$, the distance along the magnetic equator is 33.2 stellar radii. In the case of a polar cap, this determines the separation between open and closed

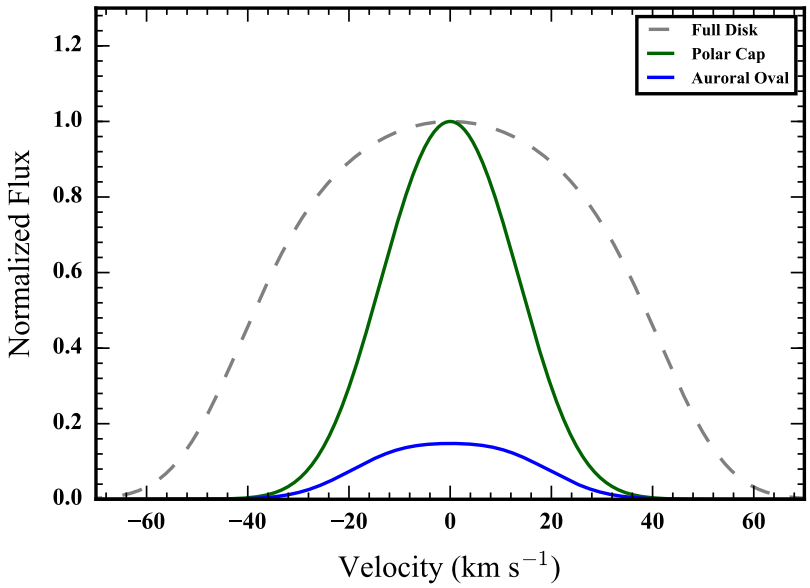

Figure 5.9: Line profile comparison of a polar cap and an aurora oval, as compared to a fully rotationally broadened disk with equatorial velocity of 46.9 km s^{-1} and inclination $i = 90°$. The cap is created from a surface feature centered at a latitude of 75° with a half-angle of 20°. The oval consists of a surface feature centered at a latitude of 75° with a half-angle of 19° and a width of 2°. The emission line profile assumed accounts for an intrinsic width of 5 km s^{-1} and an instrumental resolution of 8 km s^{-1}. The oval emission is normalized to the peak of the polar cap emission.

field lines and the distance at which the field reconnection takes place. The doppler image from Section 5.5 indicates strong high-latitude features that are not uniform but appear to be broad. Image reconstructions with the full data set may yield more refined results but currently resemble a polar cap. Interestingly, the burst profiles are relatively flat and may provide insight into the exact shape of the emission surface during the bursts. If these correspond to the filled cap, it would confirm that the feature is a polar cap; however if the burst appear enhanced along a ring of emission, the feature may indeed be an auroral oval; additional analysis is required.

5.7 Conclusions

We have monitored the benchmark auroral brown dwarf LSR J1835+3259 with high resolution optical spectra to examine the morphology and time variability of the auroral Hα emission line. Our observations revealed sinusoidally varying emission sitting on top of a low-level emission that is consistent with being fully rotationally broadened, with possibly extended wings. Our observations also showed multiple Hα bursts localized at particular velocities that were correlated with the

sinusoidally varying emission. Preliminary doppler image reconstructions of the stellar surface in Hα emission indicate the presence of a high latitude surface feature that is responsible for the bright sinusoidally varying emission. The surface feature appears to be at a latitude of about $\sim$70° and subtend about 20° total. Because this emission is consistent with being auroral in nature, as discussed in Hallinan et al. (2015), the extent of the surface feature can be mapped directly to the regions of auroral electron acceleration. The $\sim$10° half-angle would correspond to an L-shell of 33.2, assuming the center of the surface feature coincided with the magnetic axis.

In our preliminary analysis, we were not able to distinguish between the polar cap and the auroral oval but the cumulative evidence and a more detailed analysis of the line shapes, may yet be able to make this distinction for LSR J1835+3259. Considered in light of evidence that the ISM wind cannot supply sufficient energy to power auroral radio emissions, the data may point to co-rotation breakdown as the key mechanism (Schrijver 2009; Nichols et al. 2012; Hallinan et al. 2015). If so, we would be able to potentially confirm the nature of the electrodynamic engine powering the auroral emission of this object. This will have important implications for the nature of brown dwarf magnetic phenomena.

Additionally, other studies examining the detailed line profiles of late M dwarfs, have also shown that high latitude features are present. Barnes et al. (2015) performed a doppler imaging analysis on high-resolution spectra of two late M dwarfs, including LP944-20, the first brown dwarf discovered to exhibit radio emission. Their surface reconstructions showed features near the rotational axis consistent with a circumpolar oval. Moreover, our preliminary surface image of LSR J1835+3259, strongly resembles their surface map of LP944-20. In contrast to our analysis, their work used spectral templates of differing effective temperatures to fit the spotted surface regions and the photospheric emissions through large sections of the optical spectrum. From Hallinan et al. (2015), it is clear that the auroral region also influences the multi-wavelength spectral emission. However, their model implied a blackbody-like spectrum whereas Barnes et al. (2015) used model photospheres, although they did not consider the possibility of aurorae. Nevertheless, these results demonstrate that auroral phenomena may be widespread among late M dwarfs and the underlying electrodynamic engine in each case could be co-rotation breakdown.

Acknowledgments

J.S.P was supported by a grant from the National Science Foundation Graduate Research Fellowship under grant No. (DGE-11444469).

J.S.P would like to thank Evan Kirby for assistance with the HIRES data reduction.

J.S.P would like to thank Gibor Basri for providing useful comments in interpreting the observed spectra.

J.S.P would like to thank Stuart Littlefair and Christopher Watson for developing the doppler imaging tools and providing the initial surface image for this study.

The data presented herein were obtained at the W.M. Keck Observatory, which is operated as a scientific partnership among the California Institute of Technology, the University of California and the National Aeronautics and Space Administration. The Observatory was made possible by the generous financial support of the W.M. Keck Foundation.

Chapter 6

A PANCHROMATIC VIEW OF BROWN DWARF AURORAE

Stellar coronal activity has been shown to persist into the low-mass star regime, down to late M-dwarf spectral types. However, there is now an accumulation of evidence suggesting that at the end of the main sequence there is a transition in the nature of the magnetic activity from chromospheric and coronal to planet-like and auroral, from local impulsive heating via flares and MHD wave dissipation to energy dissipation from strong large-scale magnetospheric current systems. We examine this transition and the prevalence of auroral activity in brown dwarfs through a compilation of multi-wavelength surveys of magnetic activity, including radio, X-ray, and optical. We compile the results of those surveys and place their conclusions in the context of auroral emission as the consequence of large-scale magnetospheric current systems that accelerate energetic electron beams and drive the particles to impact the cool atmospheric gas. We explore the different manifestation of auroral phenomena in brown dwarf atmospheres, like Hα, and define their distinguishing characteristics. We conclude that large amplitude photometric variability in the near infrared is a consequence of clouds in brown dwarf atmospheres, but that auroral activity may be responsible for long-lived stable surface features. We report a connection between auroral Hα emission and quiescent radio emission in ECMI pulsing brown dwarfs, suggesting a potential underlying physical connection between the quiescent and auroral emissions. We also discuss the possible electrodynamic engines powering brown dwarf aurorae and the possible role of satellites around these systems.

6.1 Introduction

Within the past 15 years, the discovery and follow up observations of radio emission from brown dwarfs (e.g., Berger et al. 2001, 2010; Hallinan et al. 2008, 2015) have heralded a shift in our understanding of magnetic activity in low-mass stars and ultracool dwarfs (UCDs; spectral type $\geq$ M7). The accumulating evidence now suggest that there may be a transition at the end of the main sequence away from coronal Solar-like magnetic activity towards auroral planet-like phenomena. Moreover, the progress of several observational surveys of brown dwarfs across the electromagnetic spectrum allows us to put together a comprehensive view of UCD auroral phenomena, for the first time, in this article. However, in order to put these

observations in context, it is essential to discuss both the standard coronal picture of stellar magnetic activity and the underlying processes that govern aurorae in the gas giant planets of the Solar System.

Stellar Activity in Low-Mass Stars

Our understanding of stellar magnetic activity is rooted in our understanding of the Sun. Solar observations of a host of phenomena, from impulsive flare events to long-term monitoring of sunspots as well as the study of coronal and chromospheric structures have formed the basis for interpreting observations of similar activity in M dwarfs (e.g., Haisch, Strong, and Rodono 1991). Observations indicate that a version of the same mechanisms powering Solar magnetic activity operates in low-mass stars. The process requires an internal dynamo that generates the persistent magnetic field anchored deep in the stellar interior and non-thermal local heating of the upper atmosphere, above the photosphere, through magnetic reconnection and/or MHD wave dissipation (e.g., Linsky 1980).

In early M-dwarfs, with partially convective interiors, the dynamo is thought to be the same as operates in the Sun, the α-Ω dynamo, in which the shearing layer between the radiative core and the convective exterior acts to strengthen and regenerate the global magnetic field, linking the magnetic activity to the rotation and the internal structure of the star (e.g., Ossendrijver 2003; Browning et al. 2006). This leads to a strong feedback between a star's rotational evolution, due to angular momentum loss in a stellar wind, and observable tracers of magnetic phenomena (e.g., Covey et al. 2011; Reiners and Mohanty 2012). For example, younger and more rapidly rotating M dwarfs flare more frequently than similar older stars, depositing energy in their upper atmospheres at a higher rate early in their lifetimes (Hilton et al. 2010). The connection is further observed as a strong correlation between stellar rotation/age and emission lines that trace upper atmospheric heating (e.g., Skumanich 1972). Emission features such as Ca II H and K, and Hα are more prevalent and stronger in faster rotating M dwarfs as compared to slower rotators (Delfosse et al. 1998; Mohanty and Basri 2003; West et al. 2008; Browning et al. 2010; West et al. 2015).

Although these features, for early M dwarfs, are indicative of chromospheric atmospheric structures, their disappearance in slowly rotating stars does not indicate the vanishing of inverted atmospheric temperature profiles. As indicated by observations at ultraviolet (UV) wavelengths, chromospheric, transition region, and coronal emission lines, such as Mg II, at 2796 Å, N V, at 1239 Å and 1243 Å, and

Fe XII, at 1242 Å, are prevalent in M dwarf atmospheres, even for slowly rotating M dwarfs that are 'inactive' in Hα (France et al. 2013, 2016). The presence of coronal structures, like those of the Sun, in M dwarf atmospheres, is further corroborated by the detections of X-ray emission in observations of early M dwarfs (e.g., James et al. 2000; Pizzolato et al. 2003). Like the the optical emission features, UV and X-ray emission is also strongly correlated with rotation/age, with observations showing constant emission levels for young objects rotating more quickly than ~5 d, and the emission declining for more slowly rotating objects as they age (Pizzolato et al. 2003; Shkolnik and Barman 2014; Cook, Williams, and Berger 2014).

Early M-dwarf radio emission also appears to be consistent with this coronal picture. From F-type dwarf stars to early M-type dwarf stars, the Güdel-Benz relation demonstrates a tight empirical relation between coronal X-ray and quiescent radio emission, illustrating a deep connection between the coronal plasma producing the X-ray emission and the non-thermal energetic electrons responsible for the radio emission (Guedel and Benz 1993). Additionally, the results of Zeeman Doppler Imaging (ZDI) studies demonstrate that active flaring M dwarfs exhibit complicated non-axisymmetric multi-polar large-scale fields similar to what is seen on the Sun (e.g., Donati et al. 2008).

Auroral Processes in Planetary Magnetospheres

In contrast to the stellar paradigm, planetary auroral emissions are associated with large-scale field-aligned current systems that pervade the extended magnetosphere, connecting the planetary atmosphere to energetic processes in the middle magnetosphere. In the Solar System, there are three main mechanisms that generate auroral currents (see Keiling et al. 2012, and references therein). Firstly, the interaction between the solar wind and a planetary magnetosphere triggers magnetic reconnection events that accelerate electrons along the magnetic field lines. This mechanism dominates the aurorae of the Earth and Saturn (e.g, Cowley, Bunce, and Prangé 2004). Secondly, the relative motion of an orbiting satellite through a planet's magnetosphere creates a current system in the flux tube connecting the moon and the planet. This mechanism produces the auroral emission associated with the moons Io and Enceladus of Jupiter and Saturn, respectively (e.g., Saur et al. 2004). Lastly, the breakdown of co-rotation between a rotating plasma disk and the planetary magnetosphere can create a shearing layer that drives auroral currents. This is the mechanism that powers the main Jovian auroral oval (e.g., Cowley and Bunce 2001). Moreover, the different mechanisms can overlap, as they

do in the Jovian magnetosphere. Each of these electrodynamic engines generates strong field-aligned currents that drive accelerated electron beams, the fundamental ingredient of auroral emission processes.

The acceleration of the electrons creates an energetic non-thermal energy distribution and can lead to the onset of the electron cyclotron maser instability (ECMI). The necessary criteria are an energy distribution dominated by the non-thermal component and a cyclotron frequency larger than than the local plasma frequency,

$$\frac{\omega_{pe}^2}{\omega_{ce}^2} = \frac{4\pi n_e m_e c^2}{B^2} \leq 1 \,, \tag{6.1}$$

where n_e is the electron density, B is the magnetic field strength, m_e is the electron mass and c is the speed of light (see Treumann 2006). As the ratio of Equation 6.1 approaches unity, the maser becomes weaker and less efficient. However, under the conditions of a dilute plasma immersed in a strong magnetic field, the energetic electrons become an efficient radiation source. The result is a strong coherent radio source emitting near the local cyclotron frequency that is highly circularly polarized and radiates into a thin ($\sim$1°) conical sheet with large opening angles, nearly perpendicular to the magnetic field direction, $\gtrsim$80° (Dulk 1985; Treumann 2006). ECM radio emission has been observed in the magnetized planets of the Solar System, signaling the presence of non-thermal energetic electron distributions in the regions around the planetary magnetic poles, near the top of the atmosphere (e.g., Wu and Lee 1979).

The energetic electron beams responsible for the radio emission precipitate into the atmosphere and generate a cascade of additional auroral emission processes (see Badman et al. 2015, and references therein). In Jupiter and Saturn, where the atmospheres are predominantly hydrogen, the collision of the energetic electrons with the atmospheric gas leads to excitation and ionization of H/H_2 and subsequent emissions at UV and optical wavelengths, including Lyman and Balmer line emissions (Perry et al. 1999; Vasavada et al. 1999; Grodent et al. 2003; Gustin et al. 2013; Dyudina et al. 2016). The creation of ionized species in the Jovian and Kronian auroral regions also leads to significant ion chemistry within the atmosphere and the creation of the strongly emitting species H_3^+ (e.g., Perry et al. 1999). The ro-vibrational transitions of H_3^+ serve to effectively cool the atmosphere and regulate exospheric temperatures (Maillard and Miller 2011). The deposition of energy from the electron beam into the atmosphere also leads to a significant thermal contribution to the auroral emis-

sions between 7 μm and 14 μm (Bhardwaj and Gladstone 2000). X-ray emission has also been detected in the auroral polar regions, a consequence of charge exchange reactions of highly ionized species such as oxygen and sulfur, likely created during ion precipitation in auroral currents (e.g., Gladstone et al. 2002; Hui et al. 2009).

These different multi-wavelength auroral emission processes are the consequence of the energy dissipation from the electrodynamic engine operating in the planetary magnetosphere. In the Jovian system the bulk of the energy, ~85% goes into atmospheric heating and thermal radiation (Bhardwaj and Gladstone 2000). Most of the remaining ~15% emerges as part of the UV emission, with less than ~1% of the energy going into the optical aurorae (Bhardwaj and Gladstone 2000). Additionally, the radio contribution only represents $\lesssim$0.1% of the total auroral energy, and the X-rays even less (Bhardwaj and Gladstone 2000).

Between Stars and Planets

The divide between stars and planets reflects the different natures of the atmospheres and physical properties of these objects. However, brown dwarfs, as objects which span this separation, constitute a regime in which there must be a transition from the planetary regime to the stellar one. Observationally, many of the the atmospheric properties of brown dwarfs, such as effective temperature, T_{eff}, overlap with those of, on the low-mass end, gas giant planets, and, on the high-mass end, very-low mass stars, making them difficult to distinguish without mass/age measurements (e.g., Burrows et al. 2001).

These similarities suggest that magnetic phenomena may also change continually across the brown dwarf regime from planets to stars. Indeed, the underlying magnetic dynamos of giant planets, brown dwarfs and very-low mass stars may be very similar (Christensen, Holzwarth, and Reiners 2009; Morin et al. 2011); however this idea is currently being tested (see Kao et al. 2016). Nevertheless, the nature of the transition in magnetic activity across the brown dwarf regime is an open question. Because brown dwarfs have been identified and studied predominantly by the community of stellar astrophysicists, the view of their magnetic properties has been predominantly from the stellar-coronal perspective; however with the discovery of cooler and lower-mass brown dwarfs, and new evidence pointing to a breakdown of the coronal solar-like paradigm of magnetic activity, we are now motivated to consider the activity of brown dwarfs from the auroral-planet perspective. In Section 6.2, we discuss how the multi-wavelength trends in magnetic activity shift in the UCD regime. In

Section 6.3, we examine the activity data in the context of auroral phenomena in brown dwarf atmospheres. Lastly, in Section 6.4, we provide our conclusions, while summarizing our findings in Section 6.5

6.2 Trends in UCD Magnetic Activity

The multi-wavelength features of stellar magnetic activity change at the end of the main sequence, for late M dwarfs and UCDs. The shift in observational features are a consequence of significant differences between the stellar and sub-stellar regimes, reflecting changes in the internal structure, the large-scale magnetic field topology, and the atmospheric fractional ionization.

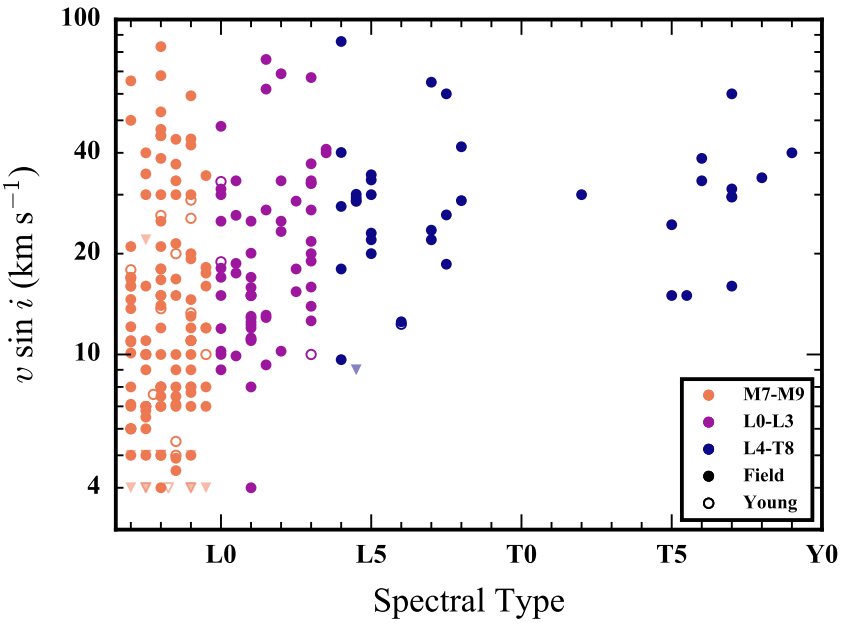

Figure 6.1: The $v \sin i$ of UCDs as a function of spectral type, as compiled from the literature (see Appendix). The brown dwarfs all show fast rotation rates, even at typical field ages. Circles are detections, with filled versus open indicating field ages and indications of youth, respectively. Upper limits are plotted as triangles, with points grouped in different colors according to expected regimes of atmospheric ionization, see Section 6.2

Convection, Dynamos, and Rotation

The lower mass and luminosity of very low-mass stars and brown dwarfs, relative to earlier type stars, have significant consequences for their internal structure. In contrast to early-M dwarfs, these objects have convective interiors extending from

their cores through to their outer layers. Consequently, a distinct dynamo mechanism must operate in this fully convective regime (mass $\lesssim$0.35 $M_\odot$, spectral type $\gtrsim$dM4; Chabrier and Baraffe 2000), in order to sustain the observed kG magnetic field strengths of these objects (Reiners and Basri 2007). The primary dynamo invoked is the α^2 dynamo, which generates and sustains the strong large-scale field through turbulent plasma motions (Browning 2008; Yadav et al. 2015).

This transition coincides with a change in the prevalent magnetic field topologies. ZDI observations of fully convective M-dwarfs show the emergence of strong large-scale, dipolar fields in mid M-dwarfs as compared to the multi-polar fields of earlier stars (Donati et al. 2006; Morin et al. 2010). This appears to persist into the UCD regime, where both kinds of field topologies have been observed, suggesting either a bi-stability of the dynamo mechanisms or potential phase transitions between dynamo modes (Morin et al. 2011; Kitchatinov, Moss, and Sokoloff 2014).

This change in topology had been thought to potentially drive changes in the angular momentum evolution of mid-to-late M-dwarfs as seen in the observed distribution of rotation periods and projected rotational velocities (Irwin and Bouvier 2009). However, recent results suggest that the rise in rotation rates of fully convective stars as compared to earlier stars may be driven predominantly by changes in the stellar radius (Reiners and Mohanty 2012). The increase in the observed rotation rates of very-low mass stars extends throughout the UCD regime where the object radius is nearly independent of mass, and is similar to the radius of Jupiter (e.g. Chabrier and Baraffe 2000). In Figure 6.1, we plot a compilation of numerous literature sources (see Appendix) of $v \sin i$ measurements, illustrating the large rotational velocities of UCDs. Indeed, most UCDs show signs of short rotation periods, with many showing periods of only a couple of hours, sustaining these fast rotation rates even at field ages (Hallinan et al. 2008; Metchev et al. 2015).

Atmospheric Ionization

The lower luminosities of very-low mass stars and brown dwarfs leads to much cooler T_{eff}, and correspondingly, much less ionized atmospheres. Mohanty et al. (2002) used atmospheric models to show that atmospheres below 2300 K are insufficiently ionized to sustain chromospheric activity. Recently, Rodriguez-Barrera et al. (2015), taking a similar approach with more recent atmospheric models, suggested that the corresponding threshold is closer to a temperature of 1400 K, with variations depending on the atmospheric gravity and metallicity. Moreover, they

show that, in these objects, significant portions of the atmosphere can be dominated by electromagnetic interactions, since the typical cyclotron frequency (assuming kG field strengths) far exceeds the collision frequency of electrons with neutrals (Rodriguez-Barrera et al. 2015).

These theoretical studies have important implications for the observed magnetic emissions of UCDs (see Section 6.2). We, thus, use these temperature thresholds as guides when considering the changes in the observed properties of UCDs with spectral type (T_{eff}), grouping the M-dwarfs (M7-M9), early L dwarfs (L0-L3) and late L dwarfs and T dwarfs (L4-T8) together (e.g. Figure 6.1). Although, a T_{eff} of 2300 K roughly coincides with the M/L transition, we base our groupings in spectral type additionally on the observational findings of Pineda et al. (2016) with regard to the prevalence of Hα emission across the UCD regime, which suggest the break below which ionization is too low to sustain chromospheres is closer to L4/L5, T_{eff} ~ 1600 K.

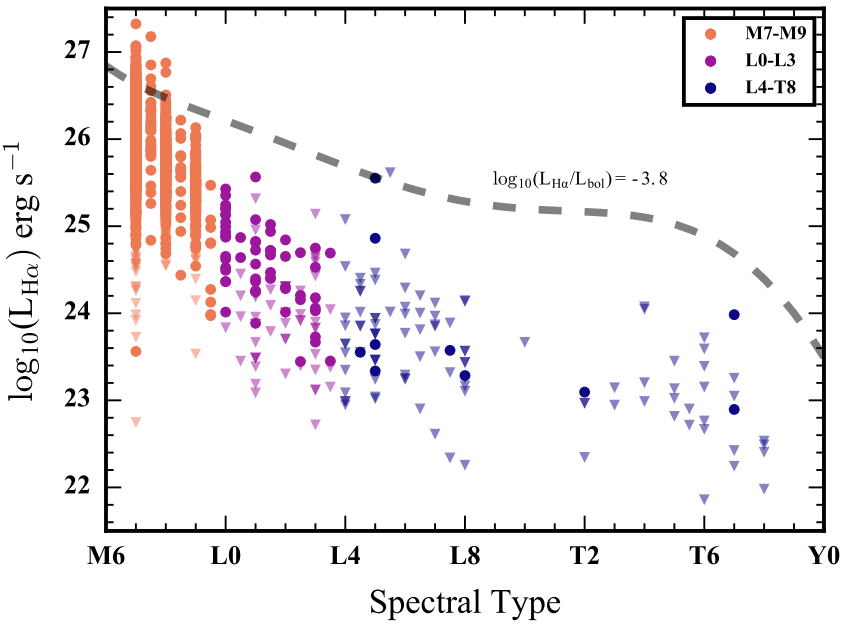

Figure 6.2: The luminosity in Hα in the UCD regime as a function of spectral type, spanning M7-T8. Detections are shown as filled circles and non-detections as triangles. We use the polynomial relations of Filippazzo et al. (2015) to determine the bolometric luminosity, L_{bol} as a function of spectral type. The different UCDs are further grouped in different colors according to expected regimes of atmospheric ionization; see Section 6.2. The data have been compiled from the literature (see Appendix).

Observed Magnetic Emission

Hα

The Hα emission of UCDs diverges from that observed in stellar atmospheres. For 'active' early M dwarfs, the strength of Hα emission is roughly in line with a normalized level of $\log_{10}(L_{H\alpha}/L_{bol}) = -3.8$ (Berger et al. 2010); however, the strength of emission in cooler objects is much weaker and declines more rapidly than the bolometric luminosity. In Figure 6.2, we show this decline by plotting the observed Hα luminosity as a function of spectral type in the UCD regime with a dashed line indicating a constant level of $L_{H\alpha}/L_{bol}$ for early M dwarfs. The typical emission level departs considerably from the expected chromospheric value based on the bolometric luminosity.

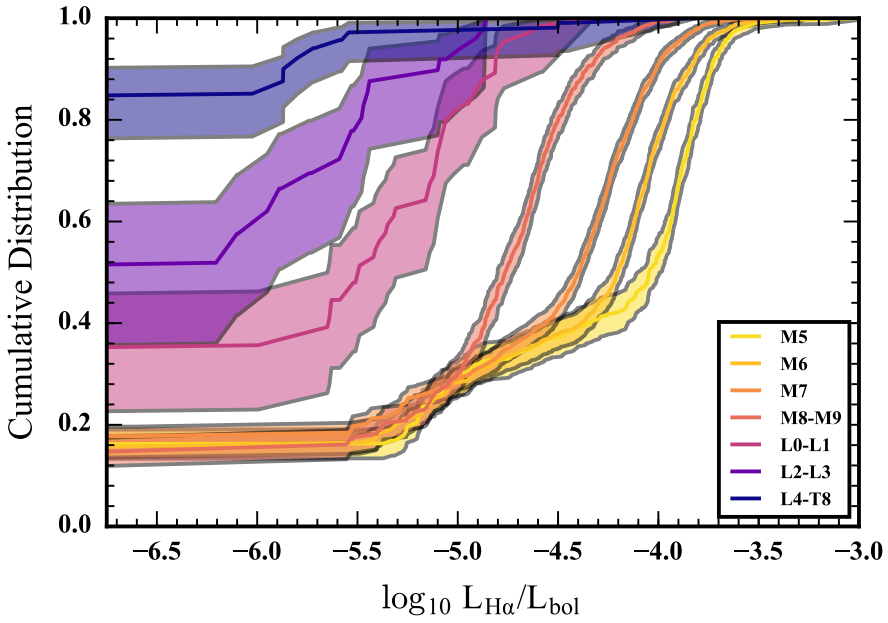

Figure 6.3: Empirical cumulative distribution functions of Hα luminosity normalized by the bolometric luminosity for late M-dwarfs and UCDs. Constructed using the Kaplan-Meier estimator, to account for non-detections, the curves illustrate the decline in the number of objects observed to be Hα active and the declining strength of the emission (also see Figure 6.2). The shaded regions represent 95% confidence intervals. The shape of the distributions are also distinct going from low-mass stars to cool brown dwarfs, see Section 6.2.

To better understand this divergence as a function spectral type, we have constructed the empirical cumulative distribution functions (ECDFs) for Hα emission in UCDs

and nearby mid M-dwarfs (from the Sloan Digital Sky Survey DR7 spectroscopic sample of West et al. 2011), using the Kaplan-Meier estimator, which takes into account non-detections. In Figure 6.3, we plot the ECDFs of $\log_{10}(L_{H\alpha}/L_{bol})$ for objects with spectral types later than M4. The trend of cooler objects showing weaker emission is evident in how the curves shift to the left for later spectral type objects. Where each curve meets the ordinate axis indicates the prevalence of Hα detections in each spectral type bin. Clearly, the cooler objects are less frequently observed in emission. The M5-M9 objects show similar rates of Hα detection, a consequence of restricting these bins to a height above the Galactic mid-plane, $|Z|$ <100 pc, where the typical ages are below the activity lifetimes of these stars (West et al. 2008). When including more distant objects, the mid M-dwarfs show fewer 'active' stars, and hence lower activity fractions (West et al. 2008; Pineda et al. 2013).

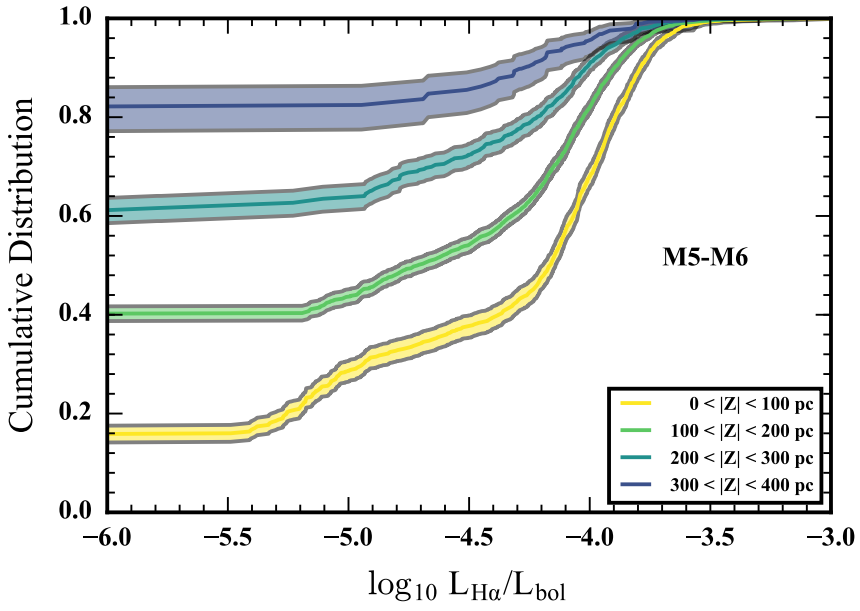

Figure 6.4: Empirical cumulative distribution functions of Hα luminosity normalized by the bolometric luminosity for M5-M6 dwarfs from the DR7 sample of West et al. (2011) for populations at different heights away from the Galactic mid-plane. The decline in emission at larger $|Z|$ reflects weakening chromospheric heating at older ages.

In Figure 6.3, when comparing the cool brown dwarfs relative to the M dwarfs, there is a stark change in the shape of the Hα distributions. As a comparison, we examined

how these distributions change for mid M-dwarfs with well defined chromospheres and differing levels of chromospheric heating. In Figure 6.4, we plot the ECDFs for M5-M6 dwarfs in the DR7 sample separated according to $|Z|$ (West et al. 2011). Objects farther away from the Galactic mid-plane are older and are rotating less rapidly than the younger stars near the Galactic mid-plane and hence show weaker magnetic heating. The weakening of chromospheric heating with slower rotation rates is seen in the way the curves shift up in Figure 6.4, with higher $|Z|$. However, for a given $|Z|$ bin the most active objects still achieve similar Hα luminosities. Comparing Figure 6.3 and Figure 6.4, it is evident that the contrast in Hα ECDF shapes between UCDs and the mid-M dwarfs, is different than the changes in the ECDF shapes observed in the weakening stellar activity of mid M-dwarfs. This suggests that the way the Hα distributions change in the cooler objects relative to M dwarfs is not the same as the changes that occur, specifically weaker heating, with age and slower rotation as seen within the M-dwarf stars.

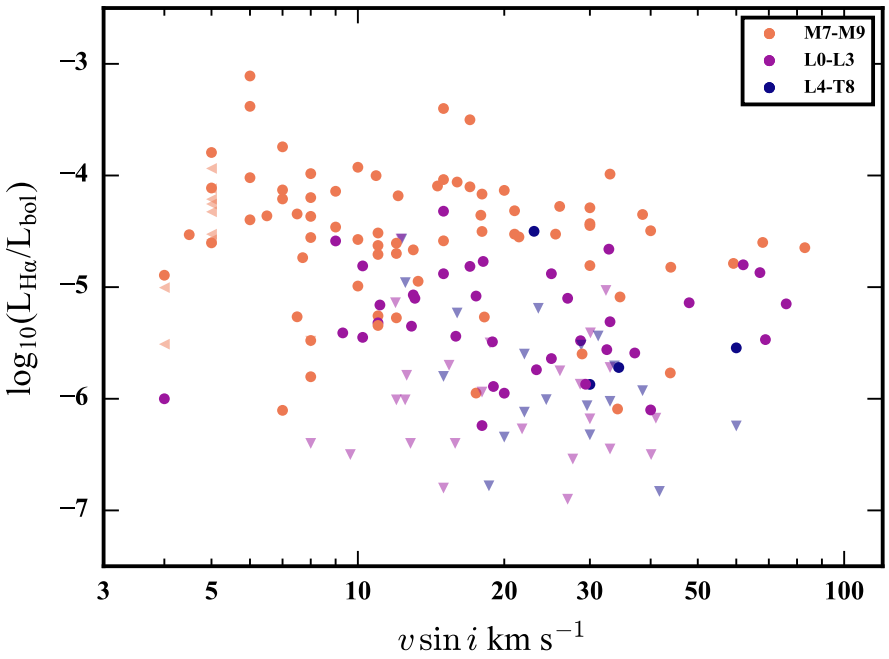

Figure 6.5: The Hα emission of UCDs normalized by their bolometric luminosity as a function of projected rotational velocity. For UCDs there does not appear to be a strong connection between Hα emission and rotation. The data have been compiled from the literature (see Appendix)

Moreover, observations explicitly show that in the UCD regime the Hα emission is not strongly correlated with the rotation distribution. In Figure 6.5, we show

the distribution of UCDs with both Hα measurements and $v \sin i$ measurements in the literature (see Appendix). There is no clear pattern of larger luminosities for faster rotators as has been observed in M dwarfs (e.g., McLean, Berger, and Reiners 2012; West et al. 2015). Thus, the emission in UCD atmospheres appears decoupled from the rotation distribution unlike warmer stars in which the rotation is strongly correlated with the level of non-thermal heating.

The change in the Hα ECDFs for UCD can thus mainly be attributed to the effects of atmospheric ionization (see Section 6.2). The cooler objects magnetically heat their atmospheres less efficiently despite maintaining large rotational velocities leading to distributions that show both weaker and less prevalent Hα emission. However, this chromospheric picture does not explain the distribution for the coolest brown dwarfs in Figure 6.3. Despite having atmospheres which are too cool to sustain much ionization, there appears to still be objects that have observed Hα emission (Burgasser et al. 2003; Pineda et al. 2016). Additionally, the shape of the distribution for L4-T8 dwarfs does not fit neatly in the chromospheric sequence of warmer objects. Whereas the bolometric luminosity declines throughout the L4-T8 bin, unlike for earlier spectral types, the typical emission levels appear to be independent of $L_{\rm bol}$ and hence T_{eff}, with multiple objects showing exceptionally strong emission relative to $L_{\rm bol}$.

These results suggest that a different mechanism is responsible for the Hα activity in these coldest brown dwarfs, distinct from the chromospheric emission seen in stars. The activity distribution across the UCD regime can thus be characterized as being predominantly chromospheric for late M dwarfs, transitory across the early L dwarf sequence, and not chromospheric for late L dwarfs and T dwarfs.

Radio

Unexpectedly, UCDs have also been observed to exhibit strong radio emission (Berger et al. 2001). Since the initial discovery, numerous surveys have looked for radio emission in very-low mass stars and brown dwarfs with very few detections (e.g., Berger 2006; McLean, Berger, and Reiners 2012; Antonova et al. 2013). In Figure 6.6, we plot a compilation of radio observations of UCDs in the literature (see Appendix) as a function of spectral type. The overall detection rate of unbiased radio surveys is ~7-10% (Route and Wolszczan 2016b). In Figure 6.7, we plot the measured detection fraction as a function of $v \sin i$ for all UCDs with both radio observations and $v \sin i$ measurements [1]. This plot shows an increase in objects with

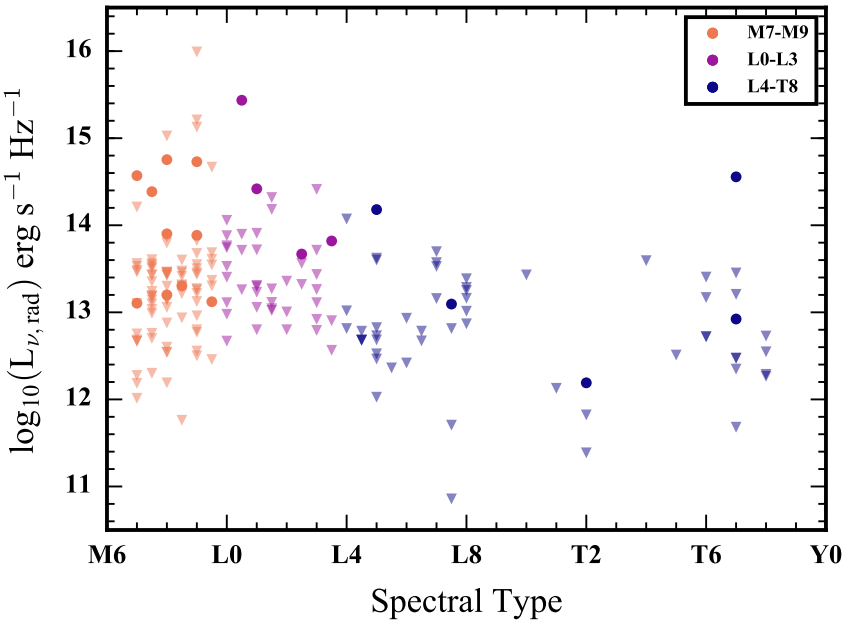

Figure 6.6: The radio luminosity of UCDs as a function of spectral type. Triangles denote upper limits and filled circles correspond to detections. The data are compiled from the literature (see Appendix). The different UCDs are grouped in different colors according to expected regimes of atmospheric ionization, see Section 6.2.

detected radio emission for objects rotating quickly, as first illustrated by McLean, Berger, and Reiners (2012). While fast rotators can be disguised with slow rotational broadening due to high inclinations, the faster rotators could be rotating even more quickly. Interestingly, we see a sharp rise in the detection fraction at a $v \sin i$ of ~40 km s^{-1}, which for objects with radii of 1 R_{Jup} and inclination close to 90°, corresponds to a period of 3.1 hr.

Significantly, the detected radio emission from these objects is morphologically distinct to that typically observed in low-mass stars. Quiescent stellar radio emission is likely dominated by a slowly varying gyro-synchrotron component at GHz frequencies, whereas stellar radio flares are highly energetic sporadic, impulsive events (see Güdel 2002, and references therein). The observations of UCDs have shown short duration strong radio emissions at GHz frequencies super imposed on a quiescent background (e.g., Route and Wolszczan 2012; Burgasser, Melis, et al. 2015). How-

[1]We used the Adaptive Kernel Density Estimation routine `akj` within the `quantreg` package in R to construct probability density functions (PDF) for detections and non-detections as a function of $v \sin i$ and combined them to construct the detection fraction (R Core Team 2016; Koenker 2016).

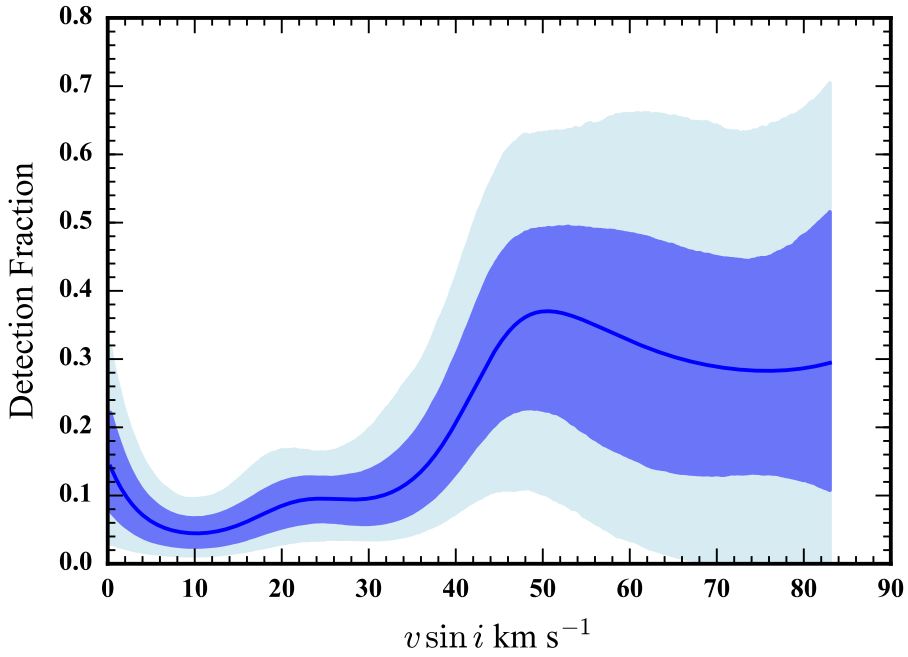

Figure 6.7: The detection fraction of UCDs, M7-T8, in the radio as a function of $v \sin i$. The fraction is computed by comparing the radio detections to the non-detections using a non-parametric adaptive kernel density estimation. The dark blue shaded region denotes the 68% confidence interval, while the light blue region denotes the 95% confidence interval using 5000 bootstrap samples of the set of targets with radio observations and $v \sin i$ measurements.

ever, studies that have observed individual UCDs, from M8.5-T6.5, for extended periods, have discovered periodic pulsations which are highly circularly polarized and have high brightness temperatures, indicative of coherent emission (e.g., Hallinan et al. 2008; Berger et al. 2009; Williams and Berger 2015). Although the radio light curves show varying morphologies, the pulses are consistently periodic and in agreement with the ECMI. Although the acceleration mechanism is unclear, the quiescent radio components of UCDs appear consistent with synchrotron emission (Williams et al. 2015).

The pulsed radio emission is distinct from typical stellar behavior and is related to the underlying mechanisms that generate the ECMI. Moreover, additional clues can be gathered from a comparison to other wavelength bands. We noted the low detection rate of radio UCDs, however, that rate is bolstered by the success of recent studies using a targeted sampled, based on Hα emission in late L dwarfs and T dwarfs, suggesting a link between these emissions in the coldest brown dwarfs (Kao

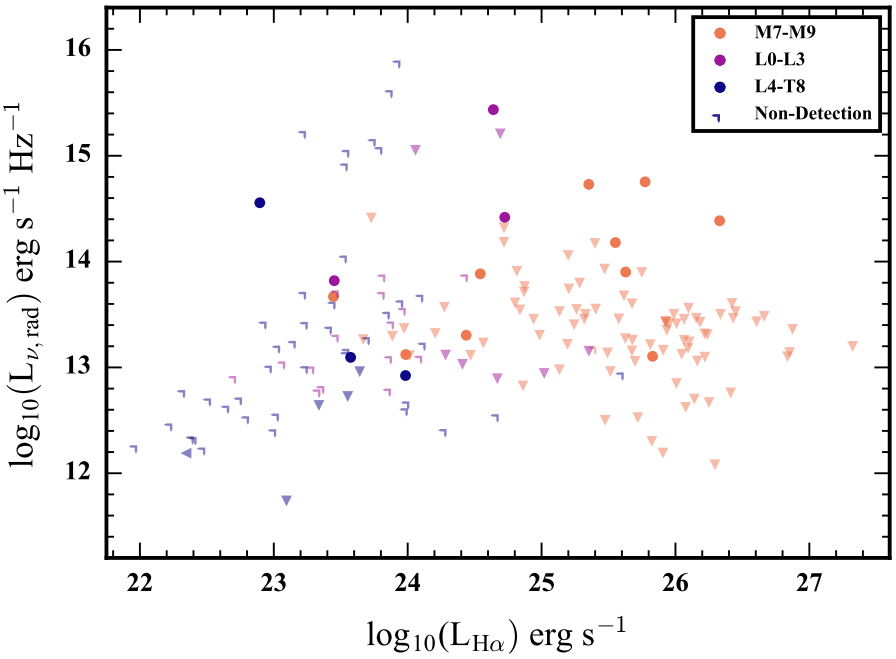

Figure 6.8: The radio luminosity plotted against the Hα luminosity in the UCD regime. Triangles denote upper limits and filled circles correspond to detections. Non-detections at both wavelengths are shown as corner symbols. The data are compiled from the literature (see Appendix). The different UCDs are grouped in different colors according to expected regimes of atmospheric ionization, see Section 6.2

et al. 2016). We compare these two samples in Figure 6.8, showing the luminosity in Hα versus the radio luminosity. For the majority of late M dwarfs, no radio emission is observed even when Hα emission is present. However, for L4-T8 objects, there is a significant overlap between objects showing both Hα and radio emissions.

The observations of pulsed ECMI radio emission throughout the UCD regime indicates the ability of these atmospheres to host conditions (see Equation 6.1) amenable to the production of ECM radio sources, independent of the nature of UCD chromospheres (see Section 6.2). Interestingly, most objects that exhibit a quiescent radio component also show strong periodic radio pulses when monitored for times exceeding their rotational periods. This results suggest that perhaps the pulses and the quiescent emission could be a consequence of the same underlying conditions.

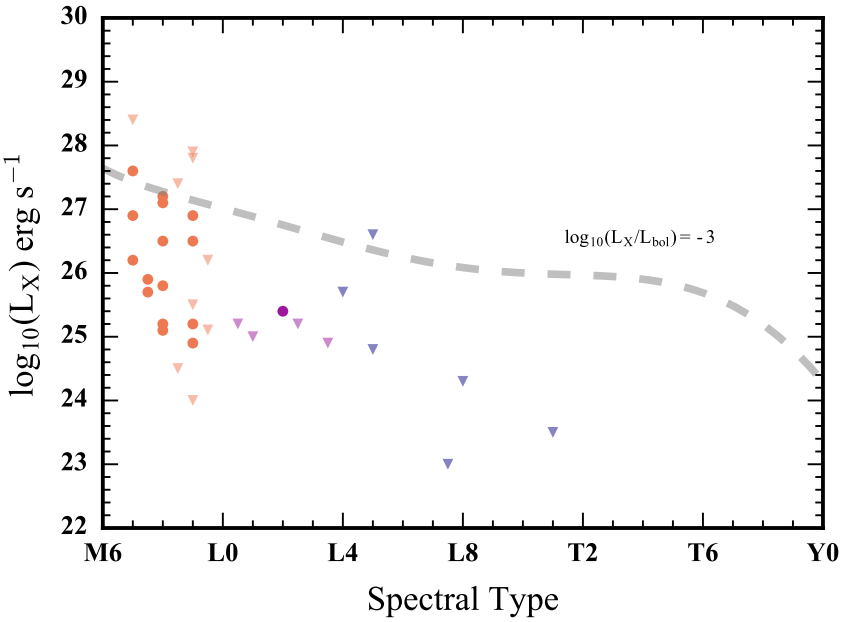

Figure 6.9: The X-ray luminosity of UCDs as a function of spectral type as compiled from the literature (see Appendix). Relative to earlier-type stars, there is a steep drop off in observed X-ray emission for UCDs, with only detection in objects later than L0. The dashed line indicates the typical X-ray emission level of active early M-dwarfs (Berger et al. 2010).

X-ray

The UCD regime also exhibits a steep drop in X-ray emission relative to earlier-type stars. In Figure 6.9, we plot X-ray luminosity of UCDs as a function of spectral type as compiled in the literature (see Appendix). The dashed line shows the typical level of emission observed in early-to-mid M dwarfs (Berger et al. 2010; Williams, Cook, and Berger 2014). Although there are only a handful of observations, especially for brown dwarfs, the observed limits on emissions are far below what would be expected from a standard stellar coronal perspective. This is evident when comparing the X-ray observations with the radio observations, as shown in Figure 6.10. Coronal X-ray and associated radio emissions, are expected to follow the Güdel-Benz relation (grey stripe), however, many observations of UCDs depart drastically from the empirical relation.

While the X-ray emission tracks the presence of hot coronal plasma, which disappears precipitously at the end of the main sequence, the persistent radio emission indicates that the processes producing these emissions are likely decoupled. Al-

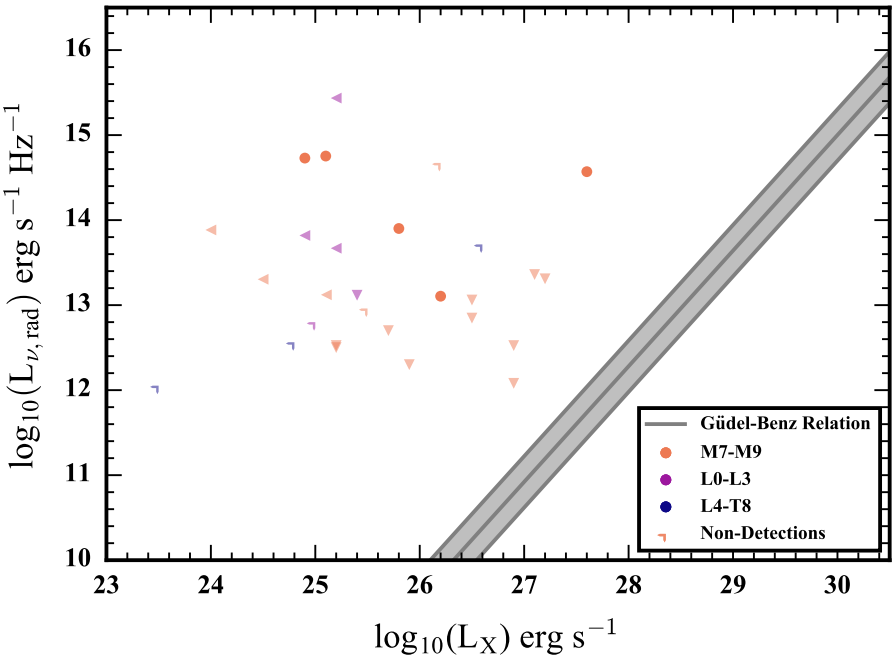

Figure 6.10: The radio luminosity versus the X-ray luminosity of UCDs for objects observed at both wavebands. The grey strip shows the Güdel-Benz relation and scatter for the tight X-ray–radio correlation in stellar coronal activity (Guedel and Benz 1993; Williams, Cook, and Berger 2014). The radio emitting UCDs strongly diverge from this empirical relation.

though these emissions may still be connected in the late M dwarfs, consistent with the portion of objects displaying Hα chromospheric emission (see Section 6.2), the detections of strong radio pulses far in excess of the expectation, based on any X-ray emission, indicates that the ECMI radio emission begins to emerge in M7-M9 dwarfs. Interestingly, if the X-ray is attributable to weak coronal emissions, the ECMI emission carries several orders of magnitude more energy than any synchrotron emission associated with the hot plasma, as predicted by the Güdel-Benz relation.

UV

Observations of UV emission in stars suggest that the at field ages, the UV chromospheric/coronal lines are very weak for spectral types later than M6 (France et al. 2016). Despite the limited observations, there have been a couple of results with regards to UV emission in UCDs. A matching of GALEX observations for late M dwarfs, did reveal a handful of NUV detections and only upper limits in the FUV

Jones and West (2016), amongst hundreds of targets. The lack of UV detections, despite the fast rotation rates of the objects in the sample, again points towards the diminishing ability of UCDs to sustain hot coronae.

However, some objects may still generate the heating necessary to power high temperature coronae. The flare star VB 10, an M8 dwarf star orbiting an early M dwarf, for example, has been observed both to flare in the UV and to exhibit quiescent EUV coronal emission (Linsky et al. 1995; Drake et al. 1996). Thus, although some individual objects, at the end of the main sequence, can generate strongly emitting coronae, the vast majority have only weak or non-existence coronae. Accordingly, these objects begin the transition away from the coronal paradigm. The UV emissions of even cooler objects, L dwarfs and later, have remained largely unexplored.

Stellar Winds

Stellar winds play a prominent role in the angular momentum evolution of stars. However, in the UCD regime, the emergence of large-scale field topologies would suggest that stellar winds could more efficiently remove angular momentum from the system due to the large lever arm (Reiners and Mohanty 2012). However, the fast rotation rates of most UCDs (see Figure 6.1) suggests that UCDs do not have strong stellar winds that remove angular momentum. This is likely a consequence of the largely neutral atmospheres (see Section 6.2) and diminished coronal activity.

White Light Flares

Observations of flare events in UCD atmospheres suggest that the same processes generating flares in M stars continues to operate in the UCD regime. These flare events are evident in the red optical data, noting the large increase in Balmer line emissions during short time intervals (e.g., Liebert et al. 1999; Schmidt et al. 2007). More recent monitoring of an L dwarf with *Kepler* and concurrent spectroscopic monitoring, revealed that these white light flare events resemble the same kinds of events on earlier type M dwarfs. The flares are just a energetic with energies as high a $\sim 10^{32}$ erg and potentially as strong as $\sim 10^{34}$ erg (Gizis et al. 2013; Schmidt et al. 2014). Gizis et al. (2013) also demonstrated that the frequency of energetic flares on the L dwarf is much less than what is observed on early M dwarf flare stars.

These observations may reflect the decreased ability of the cooler UCD atmospheres to build up and release energetic flaring magnetic loops from buoyant flux tubes that

have risen from the deep interior (Mohanty et al. 2002). Although, some brown dwarfs are still able to generate these flares, this trend would predict even fewer such flaring UCDs amongst the cooler late L dwarfs and T dwarfs, possible following the chromospheric breakdown of Hα (see Section 6.2).

Photometric Variability

Traditional stellar photometric variability has been interpreted as evidence for star spots. However, as the atmosphere cools and becomes more neutral, the ability of the atmosphere to sustain these magnetic features becomes less clear. Doppler imaging results suggests that magnetic spots could be important in late M dwarfs (Barnes et al. 2015). Concurrently, the low temperature of the atmospheres allows for the formation of dust condensates and clouds that influence the emergent stellar flux (e.g., Marley and Robinson 2015). Thus, in UCD atmospheres there is some ambiguity with regards to the dominant processes generating photometric variability, especially at the M/L transition, whether magnetic spots or clouds (Gizis et al. 2015).

Interestingly, photometric and spectroscopic monitoring of UCDs has revealed multi-wavelength broadband variability across the full range of spectral types from late M dwarfs to T dwarfs. Many of these observations have taken place in near IR wavebands, predominantly J and K, with monitoring observations of several hours. The results of these studies have revealed several large amplitude variables located at the transition between L dwarfs and T dwarfs and some additional lower amplitude and less frequent variability in spectral types away from this transition (Radigan et al. 2012, 2014). These observations have been interpreted as evidence for a patchy transition in cloud cover from L dwarfs to T dwarfs (e.g., Artigau et al. 2009; Buenzli et al. 2014). Additionally, *Spitzer* monitoring of UCDs indicates low-level variability is ubiquitous in the 3.6 and 4 μm bands, also interpreted as clouds (Metchev et al. 2015). Many of the IR variable objects also appear to display significant optical variability, with amplitudes of $\sim$10%, comparable to the highest amplitude IR variables (Biller et al. 2013; Heinze, Metchev, and Kellogg 2015)

The connection between optical and infrared variability is potentially significant in the context of magnetic activity because brown dwarfs with confirmed ECM radio emission also appear to show very clear long-term photometric variability at optical wavelengths (Harding, Hallinan, Boyle, et al. 2013). Moreover, Hallinan et al. (2015) demonstrated that the radio and optical variability may be linked (see Section 6.3). Although it is possible that many of these processes are connected,

both in optical and infrared, it also probable that UCDs may display both sets of phenomena in different objects. One potentially distinguishing feature is the nature of the photometric variability. While much of the variability is seen to evolve with time, leading to irregular periodicity in extended monitoring, other observations show long lived steady structures (Harding, Hallinan, Boyle, et al. 2013; Crossfield et al. 2014; Metchev et al. 2015; Gizis et al. 2015; Buenzli et al. 2015). This difference likely defines the distinction between variability caused by magnetic spots and heterogenous cloud cover; however the relative importance of each across the UCD regime remains unclear. Although, it is likely that clouds play a more important role for the coolest objects and that magnetic spots may only be significant in the warmest UCDs, the nature of the transition from one to the other is an open question.

6.3 Brown Dwarf Aurorae

Brown dwarf aurorae provide a natural explanation for many of the observational trends in UCD magnetism. The characteristics of the periodic radio pulses, that they are highly circularly polarized with large brightness temperatures, indicate that the ECMI must be the emission mechanism and that the aurorae, the consequence of energy dissipation from stable large-scale magnetospheric current systems, are present throughout the UCD regime. However, the physical conditions that power the aurorae remain an open question. Here, we discuss the implications of potential auroral scenarios on multi-wavelength brown dwarf emissions, how they fit within the observations of brown dwarf activity, and predictions based on the analogy with auroral systems in the gas giant planets of the Solar System.

The Electrodynamic Engines of Auroral Brown Dwarfs

We discussed the dominant auroral electrodynamic engines in Section 6.1. In the case of brown dwarfs, the the three engines, stellar wind, satellite induced and co-rotatoin breakdown, take on slightly different forms. Although we expect brown dwarfs in binary systems orbiting much larger stars to interact with the companion's stellar wind in much the same way planets do around the Sun, for these brown dwarfs the large orbital separations, precludes the generation of strong aurorae. Nevertheless, observationally many of the significant auroral brown dwarfs are isolated systems in the field. Consequently, a different mechanism must be at work. Alternatively, motion through the interstellar medium and reconnection in the large magnetosphere can provide a particle flux with which to generate auroral

processes. Work by Schrijver (2009) and Nichols et al. (2012), suggests that this mechanism would not be able to produce enough energy to power the auroral radio emission. Both of these sets of authors suggest that co-rotation breakdown can provide sufficient energy to power the aurorae, with Hallinan et al. (2015) further suggesting that a satellite interaction could also provide sufficient energy.

For the breakdown of co-rotation, the magnetospheric current and energy dissipated is dependent on the differential velocity between the co-rotating magnetosphere and an extended plasma disk, and dependent on the strength of the brown dwarf's magnetic field (Cowley and Bunce 2001; Nichols et al. 2012). Furthermore, the location of the auroral oval with respect to the magnetic axis, and hence particular flux tubes connected to the shearing layer, depend on the electron density of the plasma disk and the strength of the magnetic field (Cowley and Bunce 2001). When the magnetic energy density no longer dominates over the plasma energy density, the field can no longer drag the plasma with it and the large rotational velocities at distant radii are no longer maintained, creating the shearing layer. Thus, the magnetic field strength and rotational velocity play a crucial role in the generation mechanism and energy dissipation in this scenario. This electrodynamic engine would predict a strong dependence on rotational velocities and magnetic field strengths, both of which are much larger in brown dwarfs as compared to Jupiter, and could lead to much stronger aurorae in brown dwarfs (Hallinan et al. 2015). Additionally, co-rotation breakdown predicts that auroral atmospheric emission should be predominately confined to a narrow oval around the magnetic axis. However, a significant unknown for brown dwarfs is the existence of an extended equatorial plasma sheet that seeds the magnetospheric currents with plasma. In the Jovian system, Io's volcanic activity provides the material to load the plasma disk. Analogous systems have not yet been confirmed around very low-mass stars and brown dwarfs, however there have been recent detections of small, potentially rocky planets around UCDs (Udalski et al. 2015; Gillon et al. 2016).

Given these new planetary detections, the satellite induced scenario becomes an intriguing possibility. The satellite flux tube interaction is generated by the differential motion of an orbiting satellite through the brown dwarf's magnetosphere. In this scenario the auroral power is a function of this velocity, the magnetic field strength at the orbital location of the satellite, and the cross sectional area of interaction of the planet, usually defined be the size of the obstacle (Zarka 2007). For a rocky planet without an intrinsic magnetic field, the cross section is determined by the

planet's exo-ionosphere (e.g., Io), whereas for a system with it's own magnetosphere the area is determined by the magnetopause distance of the planet within the brown dwarf's magnetosphere (e.g., Ganymede, Zarka 2007). Thus, stronger emission is expected for closer in planetary systems, faster rotators and stronger magnetic field brown dwarfs. However, objects that are too close in, risk being tidally circularized and synchronizing the orbital period with the rotational period, as appears to be the case for the close-in planets of the TRAPPIST-1 system, a M8 dwarf orbited by 3 Earth-sized planets (Gillon et al. 2016). Interestingly, the size of flux tube foot point may also depend on the size of the orbital interaction area and may provide a separate constraint on the satellite radius, and provide a way to potentially confirm the existence and strength of the planetary magnetic field. Regardless, measurements of the surface feature and the emissions (see Section 6.3), associated with the flux tube can provide a way to distinguish the satellite scenario from co-rotation breakdown. Nevertheless, because the origin of the magnetospheric plasma is an open question, both the satellite and co-rotation breakdown scenarios may require the presence of planetary companions to brown dwarfs and can be overlapping in any given system. Consequently, the number of UCDs displaying significant auroral phenomena may be tied to the proportion of brown dwarfs with close-in planetary satellites.

Magnetic Field Topology

In Section 6.2, we described the evidence suggesting that brown dwarfs often exhibit axisymmetric dipolar large scale field topologies. The emergence of aurorae in brown dwarfs is enabled by this shift in the magnetic topologies toward largely dipolar from predominantly small-scale and multi-polar fields, although both may be possible in fully convective dwarfs (see Section 6.2). The extended dipolar fields provides the conditions to create the auroral electrodynamic engines (see Section 6.3). The stronger fields at large distances as compared to the smaller-scale fields enables the coupling between the ionosphere and the middle magnetosphere.

Previous studies have suggested that the magnetic field topology could be a critical component in defining which UCDs display which activity indicators. Amongst the group of objects with sensitive limits in both radio and X-ray, there appears to be two groups, radio loud (ECM) and X-ray quiet, and radio quiet and X-ray flaring, although X-ray only appear for warmest brown dwarfs (Stelzer et al. 2012; Williams, Cook, and Berger 2014). The connection of the magnetic field topology to the electrodynamic engines indicates that the radio loud objects are the ones which require strong large-scale field topologies, and the X-ray flaring objects are

the ones that likely display small-scale fields, in contrast to the ideas put forward by Williams, Cook, and Berger (2014). However, although a necessary component, the magnetic field topology may not be the distinguishing feature of the auroral emission processes. Even if strong dipolar fields are present, the generation of the electrodynamic engine may require additional underlying conditions (e.g., a close in satellite, see Section 6.3).

Impact on Atmosphere

If the ECMI is present, then a strong field-aligned current is driving an electron beam to precipitate into the atmosphere. This has a significant impact on the brown dwarf atmosphere, leading to the creation of multi-wavelength auroral emissions. The same physical processes that take place in the Jovian system should operate in the brown dwarfs (see Section 6.1); however important differences may arise due to the different atmospheric conditions and potentially due to the different properties of the auroral electron beams.

Emission Lines Features

The collision of high energy electrons with an atmosphere predominantly of neutral H/H_2, as is found in the brown dwarfs, leads to the ionization and excitation of the hydrogen gas. The de-excitation and recombination of the hydrogen will lead to considerable Balmer and Lyman series emission, as well as UV emission in the Lyman and Werner bands (Badman et al. 2015). Consequently, brown dwarfs hosting auroral radio emission are likely to generate surface features which are bright in Hα, Lyα and the FUV. Thus, the presence of these emissions should be correlated with the presence ECM radio emission. The statistics of radio detections and Hα emission in late L dwarfs and T dwarfs show evidence for this correlation (Kao et al. 2016; Pineda et al. 2016). The FUV emission of auroral brown dwarfs has not yet been searched for, but would be an important confirmation of the effects of auroral electron beams in brown dwarf atmospheres. Moreover, following the Jovian example, this FUV emission would be diagnostic of the total auroral energy and is sensitive to the auroral electron energy distribution (Bhardwaj and Gladstone 2000; Badman et al. 2015)

Additionally, the nature of the excitation mechanism for the hydrogen emission features, could potentially be used as a diagnostic of the auroral process. Detailed modeling is required to predict the Balmer line spectrum from the electron impacts

on the brown dwarf, however the emission ratios of the lines likely deviate from expectations from case B recombination and simple LTE gas models. An analysis of the Balmer series emission line ratios (decrement) by Stelzer et al. (2012), for one of the late M dwarfs with strong radio emission, showed that these models proved to be a poor fit to the data and did not follow the expectations from a standard stellar chromospheric perspective. An auroral NLTE origin for the Balmer series emission could account for this discrepancy.

Depending on the auroral electrodynamic engine, these features will appear as ovals around the magnetic axis or be localized to the satellite flux tube foot point, which have different observational signatures. The different morphologies of the surface features will be imprinted on emission lines, like Hα. In contrast to chromospheric emission which will be fully rotationally broadened, the line profile of the auroral Hα emission will be determined by the size and location of the auroral surface feature. Emission localized at a flux tube foot point would be narrow and centered at velocities set by the longitude of the surface feature. The emission features of an auroral oval, would be wider and span a range of velocities consistent with its L-shell [2] and the tilt of the magnetic axis relative to the rotational axis. The shape of the line would also deviate from a simple velocity broadened Gaussian profile because the emission at the center of the oval would be missing.

The observed variability also depends on the auroral engine. For an auroral oval, the feature rotates around as the magnetic axis rotates around. Depending on the viewing geometry, the auroral surface emission could rotate in and out of view creating a sinusoidal signal, like what is observed on LSR J1835+3259 (Hallinan et al. 2015). This variability is also imprinted on the velocity profile of the emission lines. In the case of a flux tube foot point the time variability of the emission is dominated by the orbital motion of the satellite instead of the rotational period of the object. This leads to long term variability of the emission features. Emission line variability in excess of the rotational period has already by confirmed in one auroral brown dwarf (Pineda et al. 2016).

Like the Jovian system, the auroral emission features are likely to be intrinsically variable on short timescales, reflecting changes in the electron beam energy distribution and auroral current system. Stellar chromospheric emission is also characterized by intermittent variability and can show enhanced emission within star spot regions

[2]The L-shell is the distance along the magnetic equator in units of the object radius of a given field line, which maps to a particular location on the stellar surface along that field line.

(Reiners and Basri 2008; Lee, Berger, and Knapp 2010). In contrast to sunspots and star spots, auroral surface features should not display enhanced magnetic field strengths relative to the unspotted photosphere, as they are not sites of clustered magnetic field.

As discussed in Section 6.1 the ionization of molecular hydrogen from the electron impacts leads to the creation of ionized triatomic hydrogen. H_3^+, however, is sensitive to the conditions in the atmosphere, and could be an important diagnostic with strong emission features at 2 μm and 4 μm (Tao, Badman, and Fujimoto 2011; Tao et al. 2012; Badman et al. 2015). The ro-vibrational features are thermally excited and depend on the atmospheric temperature. Additionally, the presence of H_3^+ is limited by the electron number density and the concentration of gas species, like CH_4 and H_2O that act to destroy the ion (Badman et al. 2015). Interestingly, although auroral electron beams in brown dwarfs are likely to create H_3^+, the concentration may not build up significantly if the ion is quickly destroyed. This would occur for large ionization fractions (higher in brown dwarfs relative to Jupiter but still mostly neutral, see Section 6.2), or a beam with high mean electron energies that penetrates to the deep atmospheric layers, below the homopause, where the concentration of molecules is high. Observations of these features could potentially be used to constrain the brown dwarf electron energy distribution.

Because these emission features depend on the atmospheric conditions, like the Jovian system, their intensity is diagnostic of the upper atmospheres of the brown dwarfs. If detected, features like the H_2 Werner band emission and H_3^+ lines would provide the only probe of these atmospheric regions well above the photosphere, however the effect will require detailed modeling to understand thoroughly.

Photometric Variability

The impact of the electron beam on the atmosphere deposits large amounts of energy, heating the atmosphere. In Jupiter, the bulk of the auroral energy emerges as thermal emission (see Section 6.1). The effect of this heating will depend on the atmospheric layers, where the bulk of the energy deposition takes place. Studies examining the effect of thermal perturbations in brown dwarf atmospheres have illustrated the wavelength dependence of the variable emission and demonstrated that stronger variability at IR wavelengths is generated when the energy is deposited higher in the atmosphere (Robinson and Marley 2014; Morley et al. 2014). In addition to changing the temperature profile, the auroral energy alters the chemical

structure and can impact the opacity of the auroral surface region. Hallinan et al. (2015) argues that this may be the mechanism generating the auroral surface features seen in broadband optical monitoring of auroral brown dwarfs (Harding, Hallinan, Boyle, et al. 2013).

Modeling the auroral electron beam impact is key to understanding these effects, however there are several expectations with regards to the photometric variability of auroral surface regions. The variability is generated near the magnetic axis and may be preferentially located near the rotational axis, generating sinusoidal variations as the feature moves into and out of view. The surface features are relatively steady and remain present on long time scales, far exceeding the transient signals expected from star spots and/or cloud structures. There should also be a strong correlation between objects displaying auroral radio emission and those showing long-term periodic variability. Comparing those objects with large NIR variability, J and K bands, to those with auroral radio emission and/or Hα emission shows a mixed record. The canonical L/T transition variables 2MASS J21392676+0220226 and SIMP J013656.5+093347.3, for example, do not display Hα emission. This is somewhat surprising, since SIMP 0136+09 was detected with highly circularly polarized radio emission; however this may point toward the influence of a satellite (see Section 6.3; Kao et al. 2016). Other objects like Luhman16 do show photometric variability and no sign of auroral activity (Osten et al. 2015). Some objects with IR variability from *Sptizer*, on the other hand, do show activity, like 2MASS J10430758+2225236 (Metchev et al. 2015; Pineda et al. 2016). Long-term monitoring of these objects may be needed to distinguishing the mechanisms producing the surface features, but there does not appear to be a one-to-one connection between the auroral activity and photometric variability. The data are consistent with two independent effects taking place on similar populations of objects, with general variability more common than auroral activity.

Auroral Beaming Geometry and Radio Emission

The different proposed electrodynamic engines of auroral emission produce different geometric beaming patterns. Modeling the brown dwarf radio emission on what is observed from Jupiter, we can use some basic properties of the emission to determine what to expect in the beaming pattern and variability from brown dwarfs. The Jovian radio aurorae are beamed into thin ($\sim$1-2°) hollow cones, emitting in directions nearly perpendicular to the local magnetic field direction, with cone half-angles $\sim$80-90° (Treumann 2006). The emission is highly circularly polarized and

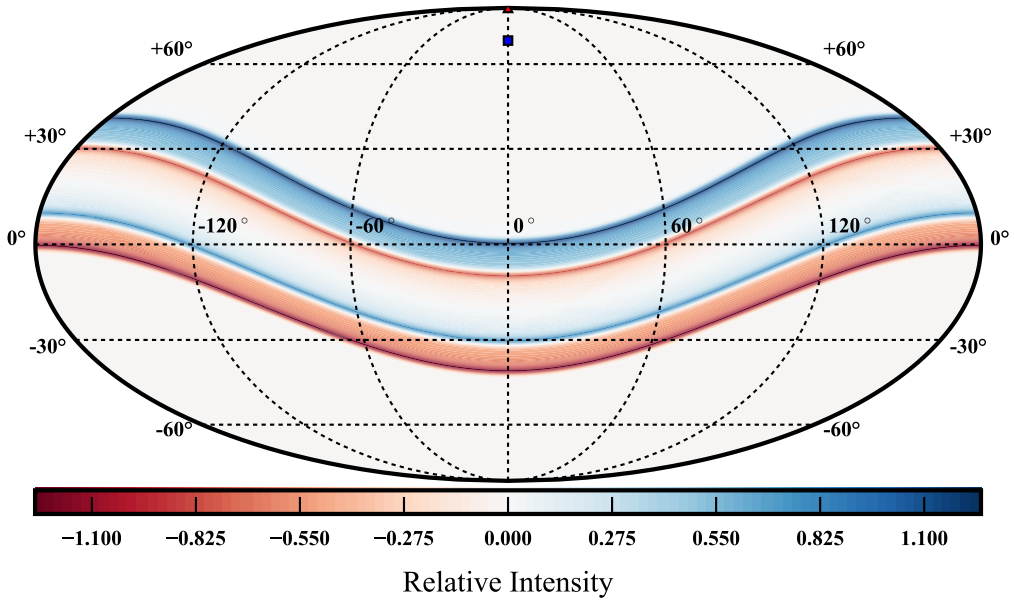

Figure 6.11: The beaming pattern of auroral radio emission in Stokes V, as seen from the emitting object, for a uniform auroral ring. The emission is normalized with positive values of the intensity corresponding right circular polarization and negative to left circular polarization. The emission model assumes that ECMI radio sources are located in a continuous ring around the magnetic axis near the stellar surface and that each emits in a hollow cone with an opening angle of 85° with a cone width of 2°. The sources are placed at an L-Shell of 30, or ∼10.5° from the magnetic axis. The magnetic axis is further defined to be 20° from the rotation axis, with its direction indicated by the blue square on the plot. As the object rotates, this beam pattern rotates to the right on a fixed sky.

appears to show different directions of polarization from the different magnetic poles, consistent with X mode waves in the plasma (Zarka 1998). The large-scale field is predominantly dipolar and can be used to map the acceleration regions to different locations in the magnetosphere. With these assumptions, we can examine the expected beam patterns for different systems and radiation sources (see also Yu et al. 2011; Lynch, Mutel, and Gudel 2015; Leto et al. 2016).

In the case of co-rotation breakdown, the ECMI sources are expected to be concentrated in a ring, near the object's surface, around the magnetic axis, with the location defined by the L-shell associated with the magnetospheric current system.

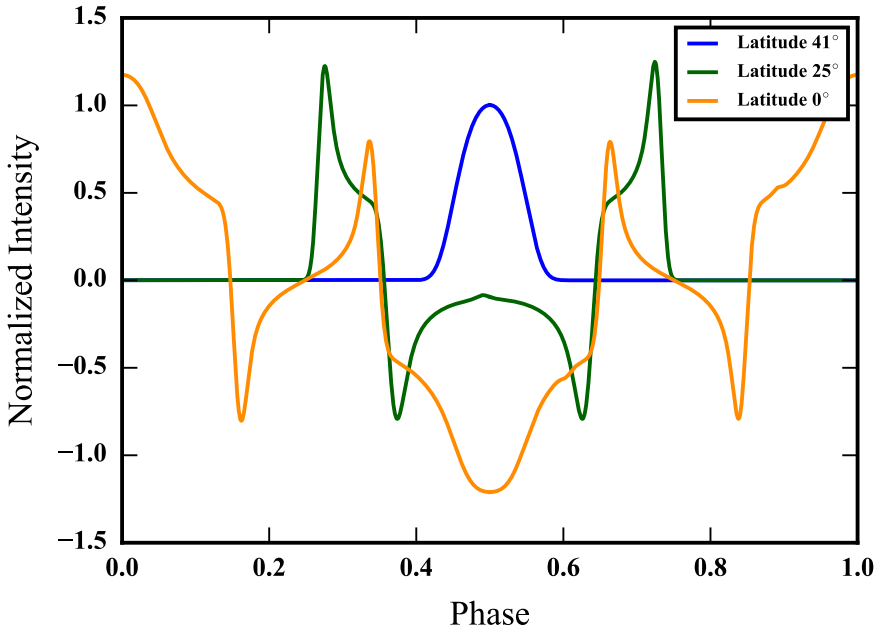

Figure 6.12: Intensity light curves from the variable ECM radio emission beam pattern of Figure 6.11. These light curves are latitudinal cuts in the intensity pattern created from the rotational variation of the emission. Phase 0 corresponds to longitude 0° in Figure 6.11. The beam pattern can generate a broad variety of light curves depending on the relative geometry of the object and the observer.

In Figure 6.11, we show a model beam pattern on the sky, in longitude and latitude, as viewed from the brown dwarf itself as a two-dimensional projection. The emission sources are from an auroral ring in the north and south hemispheres. The pattern shows the intensity as a function of position on the sky, using both right-hand circular polarization (positive intensities) and left-hand circular polarization (negative intensities). The inclination is set to 90° with the magnetic axis tilted at an angle of 20° in a uniform ring close to the surface (1.015 R_*) with an L-shell of 30, corresponding to sources located ~10.5° from the magnetic axis. The pattern of emission encompasses a large swath of the total sky. The peak emission intensities are generated at the edge of the beam pattern where the contributions from sources at multiple longitudes contribute constructively. As the object rotates, this pattern traverses the sky in longitude and generates the periodic variability of ECM emission.

For the observer, they would see very different light curves depending on their geometrical orientation with respect to this beaming pattern. As plotted in Figure 6.11,

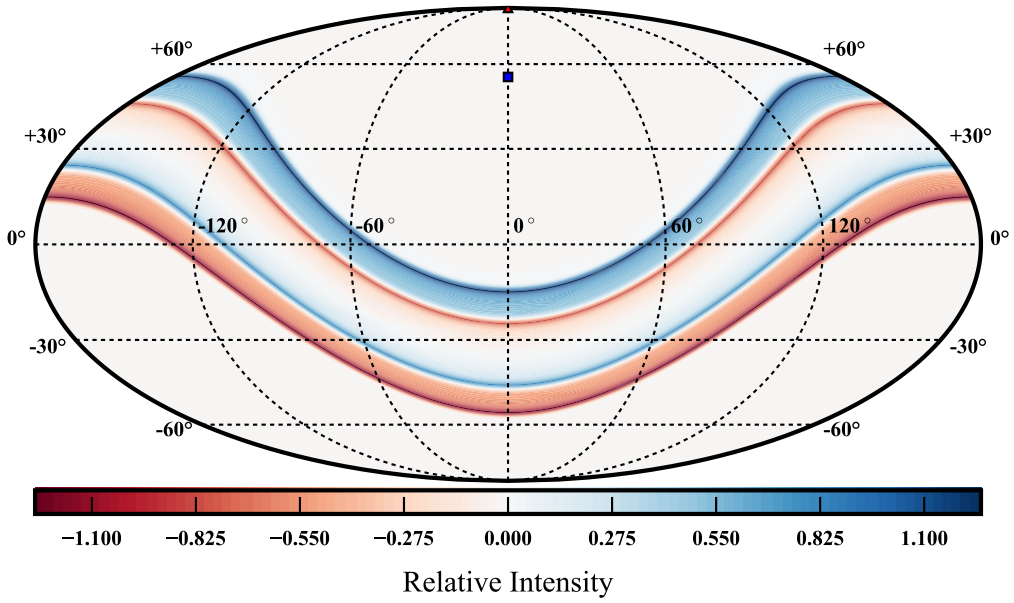

Figure 6.13: Same as Figure 6.11, but with the tilt of the magnetic axis set to 35°. With a larger angle between the rotational and magnetic axes, the proportion of the sky which is traversed by the auroral beam pattern increases.

the pattern uses an inclination of 90°, and the observer sees the light curve generated by the horizontal cut of this pattern at 0°. However, other inclination light curves can be read directly from these figures by looking at the latitudinal cut corresponding to $90 - i$. We plot some example light curves in Figure 6.12, for a selection of latitudes from Figure 6.11. If the object is viewed at an inclination of 0°, viewed above the rotational axis, there is no ECM emission visible. At other inclinations, the variability encompasses multiple pulses, a single pulse and/or multiple polarizations. Thus, a variety of light curve morphologies are possible and can change depending on the particular emission parameters, like cone width and cone opening angle. A narrower cone width, for example, would produce sharper pulse features. Comparing the morphology to the radio light curves produced in various surveys, we see a broad similarity between these shapes and the generic light curves of our model, based on basic assumptions about the emission process (Hallinan et al. 2008; Berger et al. 2009; Williams and Berger 2015; Kao et al. 2016). The beam pattern in Figure 6.11, uses a uniform ring of equal intensities, but observations of Jupiter

indicate that the auroral emission is intrinsically variable and the ring may not be populated uniformly with sources, leading to occasional gaps in the light curves and variable pulse intensities. Thus, although at many orientations an auroral ring would predict the detection of multiple pulses of both polarizations in a single period, they may not always be visible. However, if they are seen, then the separation of the pulses can be used to constrain the cone opening angle and the orientation of the magnetic axis relative to the rotational axis.

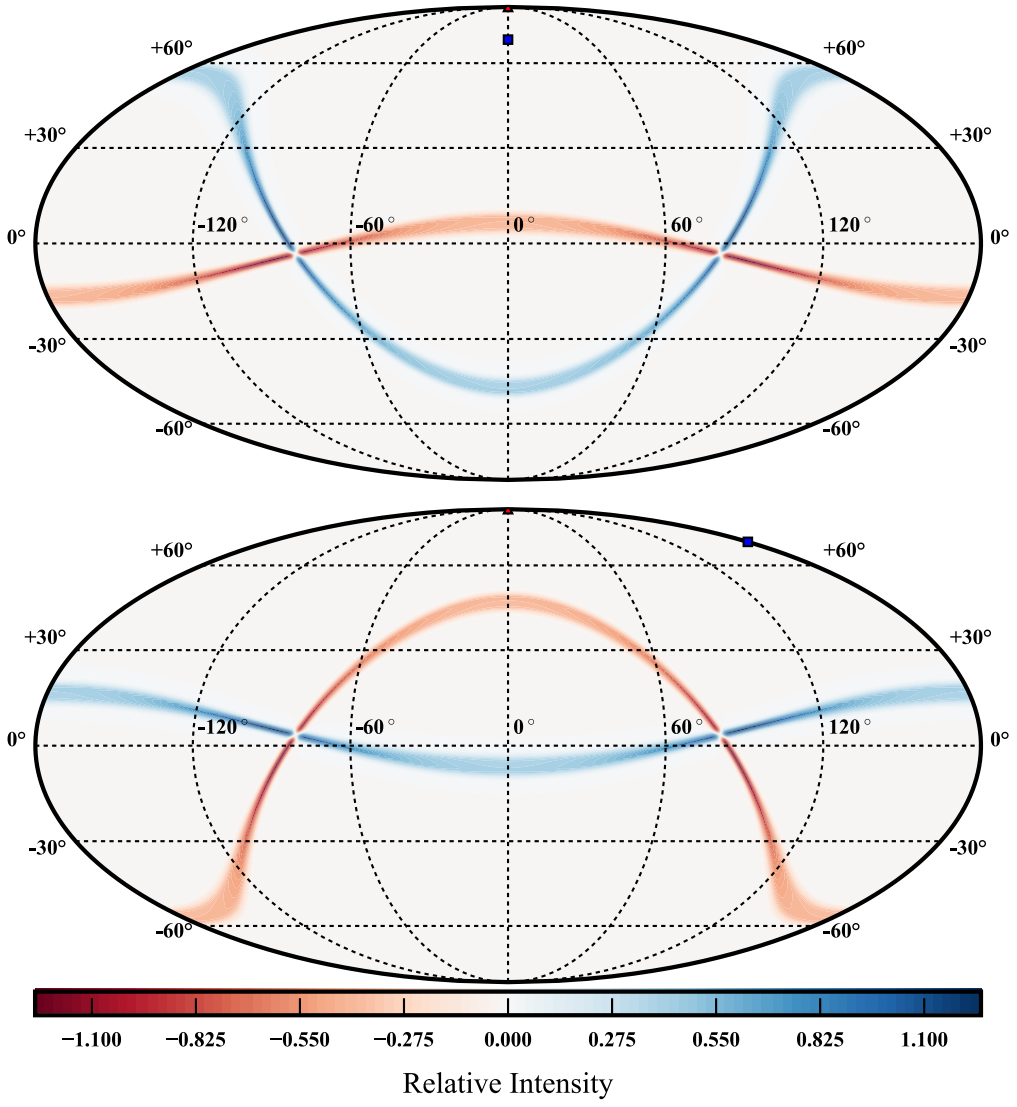

Figure 6.14: Emission beam patterns on the sky, as in Figure 6.11, for a set of ECMI radio sources at a fixed longitude associated with a current system fixed to a brown dwarf satellite flux tube. The range of sources span emission frequencies 3-12 GHz, for a dipolar field strength of 4.5 kG at the brown dwarf surface along the magnetic axis. The L-shell is set to 10 and the magnetic axis is tilted by 20°.

An examination of these beaming patterns, reveals that they encompass a large fraction of the sky as the object rotates around. Moreover, the fraction is larger when the magnetic axis is misaligned with respect to the rotational axis. In Figure 6.13, we show a beam pattern similar to that of Figure 6.11, but with a magnetic axis 35° misaligned instead of 20°, where the pattern encompasses 2/3 of the sky. The proportion depends on the L-shell of the radio sources, the source height and cone opening angle, but is large for reasonable values of these parameters, ∼50%. Pineda et al. (2016) and Kao et al. (2016) argue that the large overlap between radio auroral emissions and optical auroral emissions indicates that there may not much of a geometric selection effect biasing the radio detections. If this is the case, and the fraction of auroral objects is driven entirely by the proportion of objects with physical conditions amenable to the generation of auroral magnetospheric currents, then generically, the magnetic axes of brown dwarfs are likely to be misaligned. Given these considerations, the detection of quiescent radio emission from a pole-on L dwarf is unlikely to generate pulsed radio emission unless the magnetic axis is totally misaligned (Gizis et al. 2016). Similarly, the detection of variable circularly polarized emission in the data of WISEP J112254.73+255021.5, has been used to argue for a misaligned magnetic axis in that T dwarf (Williams, Gizis, and Berger 2016). This is particularly interesting because our model light curves predict, in these cases, some circularly polarized emission between the peak pulses with relatively uniform auroral rings.

In contrast to the auroral oval case, the generation of ECMI through currents in a flux tube connecting a satellite and a brown dwarf produces a very different beam pattern and variability signal. Under these circumstances, the radio source region is confined to the longitude associated with the flux tube of the satellite. However, the properties of the individual source region should be the same wide and thin hollow cone with different polarizations in the north and south hemispheres. In Figure 6.14, we show an example beam pattern for a satellite induced source region with L-shell of 10, spanning several heights analogous to multiple frequencies (e.g. 3 - 12 GHz), and two different instances of the rotational period, assuming the planet has remained relatively fixed at a longitude of 0°. In the top panel, the direction of the magnetic dipole is pointing toward the satellite and in the bottom panel it is pointing away, a 0.5 difference in rotational phase. There are several effects illustrated in this diagram. The inclusion of several frequencies, in contrast to the single frequency beam patterns of Figures 6.11-6.13, broadens the pulses when examined in broadband light curves. Since the different frequencies map to

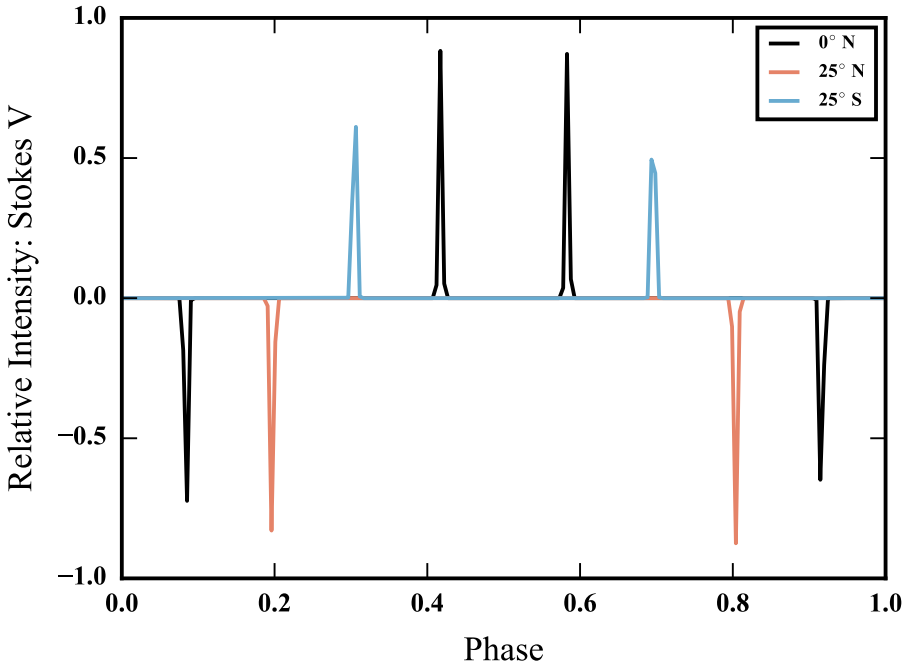

Figure 6.15: Radio light curves in stokes V intensity for different observers viewing a satellite induced auroral radio source, as in Figure 6.14. The observers see narrow pulses when the beam pattern traverses their line of sight, and depending on the viewing geometry, the observer may see only one polarization or the other, or both polarizations coming from the north and south hemispheres respectively.

different field strengths, the corresponding emission cones are pointed in slightly different directions, creating a slight broadening of the broadband ECMI pulse and slightly different arrival times for the emission at different frequencies as the emission cones sweep into view during the rotational period of the brown dwarf. Additionally, Figure 6.14 illustrates that when the magnetic axis is misaligned, the instantaneous beam pattern on the sky changes in shape and direction transforming continuously from the pattern in the top panel to the pattern in the bottom panel (for each fixed polarization) and back over the course of the brown dwarf's rotational period. In effect, the pattern can be considered as a result of the flux-tube tied to the satellite traversing multiple L-shells and longitudes, doing a circuit with respect to the magnetic axis during the rotational period. These rotational effects do not occur, if the magnetic field is well aligned with the rotational axis. Thus, for the auroral satellite scenario the radio emission can produce periodic light curves with both single and multiple polarization peaks, depending on the relative geometry of the observer and the source. I show some example light curves demonstrating this

effect for single frequency channels in Figure 6.15. The different lines correspond to different observers located at the indicated latitudes from Figure 6.14, along the longitude 0° line. Theses observed observe narrow pulses as the beam pattern sweeps over their lines of sight during the rotational modulation of the brown dwarf. Additionally, the changes in the magnetic field strength at the location of the satellite also contribute to variability in the observed intensity of the radio pulses. Super-imposed on this rotational variation, the satellite scenario further predicts a modulation of the radio emission on the orbital period of the planet around the brown dwarf. For a single object hosting both of these electrodynamic engines, co-rotation breakdown and a satellite flux-tube, depending on the relative viewing geometry and underlying parameters, the observer might intercept both, none or only one of the radio beam patterns of the ECM emission.

Pulsed vs. Quiescent Radio Emission

An important aspect of the detection of radio emission from UCDs, has been the distinction between the pulsed emission and a quiescent component at GHz frequencies. While the characteristics of the pulsed emission have identified it as due to the ECMI, there is no yet clear consensus on the nature of the quiescent component. Based on the beam patterns and light curves from Section 6.3, there could be ECMI emission between pulse peaks, although it would likely be much weaker and variable than the idealized emissions considered here. However, the polarization of the quiescent emission does not reflect a potential ECM origin (however, see Williams, Gizis, and Berger 2016). Quiescent radio emission typically shows low levels of circular polarization, however the constraints have not been particularly stringent (e.g., Kao et al. 2016). Other mechanisms have been examined. Based on radio detections at ~100 GHz, Williams et al. (2015) showed that the quiescent emission of TVLM 513-46546, one of the benchmark targets with periodic pulsations, was consistent with gyro-synchrotron emission. The polarization of the quiescent component is an important distinguishing feature. Although the low degree of circular polarization is used to argue against ECM, an important confirmation of the synchrotron nature of the emission will be the detection of significant linear polarization (Dulk 1985).

This, however, raises the question as to how these brown dwarfs energize the electrons responsible for this mildly relativistic emission. Stellar gyro-synchrotron emission is connected to the same heating and acceleration mechanisms that power the hot plasma of the coronae and stellar flares. However, the lack of X-ray emis-

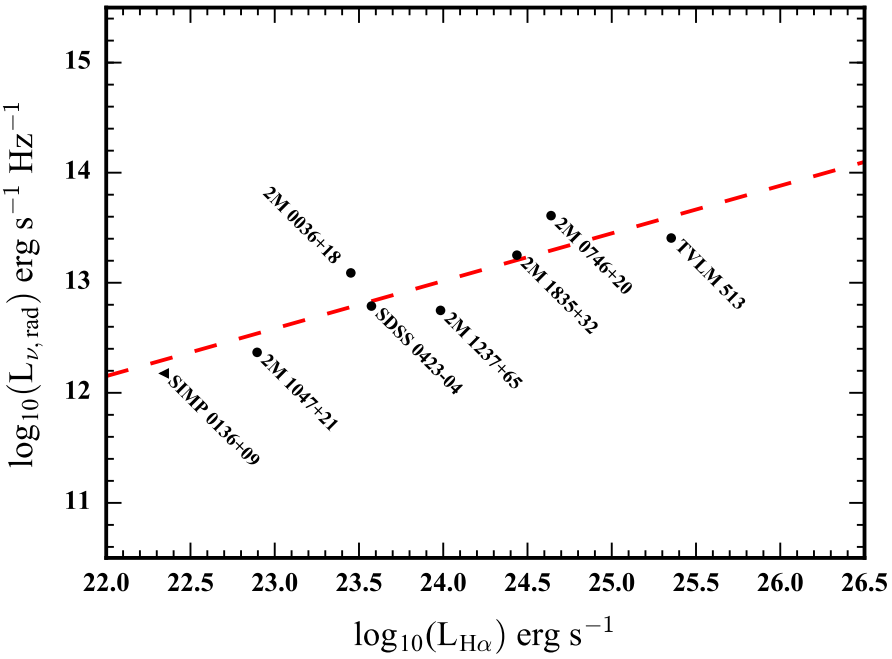

Figure 6.16: The observed quiescent radio luminosity of auroral brown dwarfs with confirmed period pulsations plotted against their Hα luminosities, plotted on a log-log scale. These properties of the emission appear correlated with linear regression line of slope 0.43 and ordinate intercept of 2.64, plotted as a dashed line. This suggests there may be a connection between the auroral processes and the quiescent radio emission.

sion (see Section 6.2) suggests these processes are weak in the cool atmospheres of UCDs, especially in late L dwarfs and T dwarfs, many of which have quiescent radio detections (e.g, Kao et al. 2016). Instead, one possibility for this emission is a brown dwarf counter part to the synchrotron radiation belts of the Jovian system. Jupiter exhibits a large population of magnetospherically confined energetic electrons (~1 MeV) in its equatorial regions that generate strong synchrotron emission at decimeter wavelengths (see Bagenal et al. 2014, and references therein). If similar structures exist on these brown dwarfs, they could generate the queiscent emission at GHz and higher frequencies, given the comparatively stronger magnetic field strength of brown dwarfs relative to Jupiter.

If this is indeed the source of the quiescent emission then this inner magnetospheric region must be loaded with energetic plasma. In the Jovian case, the major plasma source is the moon Io (e.g., Bolton et al. 2015). The material picked up from the moon is further ionized and energized by fast rotating magnetosphere, as the

ultimate source of energy for the system (Bolton et al. 2015). Given the potential requirements for the underlying electrodynamic engine of auroral magnetospheric currents, this supposes a potential connection between the quiescent and pulsed radio emissions. This is an intriguing possibility given that there is a large overlap between the population of objects with periodic pulsed ECMI emission and those with a detected quiescent radio component (e.g. Hallinan et al. 2008; Kao et al. 2016). Moreover, for many objects, initial radio detections come from short surveys of only 1-2 hr, which can be much less than the rotational periods (e.g. Route and Wolszczan 2013; McLean, Berger, and Reiners 2012). Follow-up efforts on these detections often confirm the presence of periodic pulsations on top of a quiescent radio background (e.g., Route and Wolszczan 2012; Williams and Berger 2015).

Interestingly, there appears to be a correlation between the quiescent radio emission and Hα emission. In Figure 6.16, we plot the quiescent radio luminosity against the Hα luminosity for objects with confirmed periodic pulsations. Whereas in the full set of observations there are not any clear trends (see Figure 6.8), for confirmed ECMI objects the brighter Hα sources correspond to the brighter quiescent radio sources. Although it is unclear how this connection originates, especially considering the uncertain nature of the quiescent radio component, it is possible that both mechanisms rely not only on the same conditions that make a particular brown dwarf amenable to host the auroral electrodynamic engine, but both become stronger when that engine is more energetic, e.g., faster rotation, higher magnetospheric plasma densities, and stronger field strengths. Alternatively, the acceleration mechanism of the electrons responsible for the quiescent emission may be the same as that which accelerates the auroral electrons. A deeper understanding of the quiescent emission is needed to disentangle these physical effects.

6.4 Conclusions

The observational shifts in stellar magnetic activity, into the ultracool dwarf regime, reflect the transition in physical properties in brown dwarfs going from stars to planets. The wide breadth of properties encompasses effects important in both the stellar and planetary cases. Our examination of the trends suggests that chromospheric and coronal heating begins to decay in very-low mass stars at the M/L transition, where the X-ray emission drops off dramatically. Relatively weaker heating continues into the L dwarfs, but is mostly suppressed in late L dwarfs and T dwarfs following the decline in atmospheric ionization fraction. While the heating declines gradually with spectral type, the change at the M/L transition may be accounted for by the end

of a contribution from flare heating, while the residual chromospheres of L dwarfs may be sustained by a continued gradual decline in MHD wave dissipation with cooler atmospheric temperatures.

Amidst this transition some brown dwarf systems exhibit the conditions required to power an auroral electrodynamic engine. Although the exact conditions are unclear, they require strong magnetic field strengths, large-scale magnetic field topologies, fast rotation rates, and the presence of significant magnetospheric plasma. The last condition is possibly associated with the presence of planets around brown dwarfs, in an analogy to the Jupiter-Io system, which seeds the magnetosphere with plasma through the moon's volcanic activity. Although the first three requirements are potentially met by most, if not all, brown dwarfs, the origins of the plasma and the role of a planetary satellite could be the underlying feature that distinguished aurorally active brown dwarfs from inactive ones. This could potentially tie the auroral detection statistics to the planet formation rates around brown dwarfs.

The ECM radio emission, periodically pulsed, coherent and with high degrees of circular polarization is the key observational indicator of the existence of the auroral magnetospheric processes. The aurorae are defined fundamentally by the presence of strong field aligned currents and a precipitating electron beam impacting the atmosphere. The consequences of this auroral beam include multi-wavelength surface emission features, like Hα and H_2 Werner band emission in addition to the pulsed radio emission. Furthermore, the various multi-wavelength emissions provide significant probes of the brown dwarf atmospheres: temperature, ionization, chemistry. Moreover, these emissions may provide the only probes of brown dwarf upper atmospheres and could provide constraints on the properties of the energetic electron distribution and strength of the auroral currents. Because the atmospheric and electrodynamic conditions deviate considerably from the Jovian example, the expected energy balance of the different processes could be very different; however more observations are required to establish the breakdown of total auroral energy dissipation. Furthermore, auroral brown dwarfs provide an opportunity to explore a new parameter space in auroral physics, relative to what is seen in the Solar System: stronger magnetic field strengths, faster rotation rates, and warmer and denser atmospheres.

Understanding these effects properly will require further investigation in both observations of brown dwarfs and modeling the impact of these processes in their atmospheres. Much remains uncertain but, like the Sun and stellar activity, Jupiter

and auroral activity will continue to provide important clues in deciphering the physics underlying the brown dwarf magnetism at the cross section of stars and planets.

6.5 Summary

In this article, we discussed how the trends in magnetic activity shift in the UCD regime and what the implications are for the underlying mechanisms powering magnetic phenomena in brown dwarf atmospheres, and in particular how auroral phenomena fit into these observations. Moreover, we applied the auroral paradigm to the multi-wavelength features of brown dwarf emission, illustrating the various processes and observational signatures indicative of UCD aurorae.

We summarize our main findings below:

- The distributions of Hα emission in the UCD regime show a transition across L spectral types from predominantly chromospheric to likely auroral.
- The predominant electrodynamic engine of auroral brown dwarfs may be co-rotation breakdown but likely involves the presence of close in planetary companions to the brown dwarfs.
- The auroral power is closely tied to the magnetic field strength and rotational velocity of the brown dwarf, regardless of the underlying engine.
- The presence of auroral emissions should be correlated with the presence of large-scale axisymmetric dipolar magnetic field topologies.
- Brown dwarf auroral atmospheric emissions like Hα, H_3^+, and H_2 Werner band emission are likely generated in auroral surface features but may be effected by atmospheric conditions.
- The auroral surface feature morphology is imprinted on the shape of the emission lines and depends on the electrodynamic engine powering the currents creating the auroral feature.
- Large amplitude NIR variability is likely dominated by transient cloud features and not magnetic effects, although the influence of auroral activity may be responsible the long-lived sinusoidal features observed in photometric monitoring of some objects.

- ECMI radio beaming patterns can produce a broad variety of observed light curves, accounting for the different morphologies of radio emissions from brown dwarfs hosting high polarized periodic radio pulses.
- The observed variability can be strongly dependent on the relative geometry of the source and the observer.
- The potentially low degree of geometric selection effect in the observed detections of radio pulses suggest that brown dwarf magnetic axes may be significantly misaligned in general.
- Most quiescent radio sources with extended monitoring observations have also been detected as sources of periodic highly circularly polarized radio sources.
- Quiescent radio luminosities are correlated with Hα luminosities for confirmed periodically pulsing UCDs.

Acknowledgments

J.S.P was supported by a grant from the National Science Foundation Graduate Research Fellowship under grant No. (DGE-11444469).

This research has benefitted from the M, L, T, and Y dwarf compendium housed at DwarfArchives.org. This research has benefitted from the Ultracool RIZzo Spectral Library maintained by Jonathan Gagné and Kelle Cruz. This researched has benefitted from the Database of Ultracool Parallaxes maintained by Trent Dupuy.

Appendix

Throughout this paper, we have compiled the results of many literature sources measuring the different properties of UCDs. Below, we report the sources for the data used in this compilation, according to the measurement referenced. In many cases there have been multiple observations of the same properties for individual stars. In this article, we use the values which are more recent and illustrate consistency between the reports of multiple groups.

Projected Rotational Velocities

Mohanty and Basri (2003), Blake, Charbonneau, and White (2010), Tanner et al. (2012), Prato et al. (2015), and Gizis et al. (2016); Crossfield (2014, and references therein)

Hα

Kirkpatrick et al. (1999), Gizis et al. (2000), Kirkpatrick et al. (2000), P. B. Hall (2002), Mohanty and Basri (2003), Burgasser et al. (2003), Liebert et al. (2003), Reiners and Basri (2007), Schmidt et al. (2007), Reiners and Basri (2008), Lee, Berger, and Knapp (2010), Burgasser et al. (2011), West et al. (2011), Gizis et al. (2013), Burgasser et al. (2015b), Metodieva et al. (2015), and Pineda et al. (2016)

Radio

Berger (2002), Berger et al. (2005), Berger (2006), Hallinan et al. (2007, 2008), Berger et al. (2009, 2010), McLean, Berger, and Reiners (2012), Route and Wolszczan (2012), Antonova et al. (2013), Route and Wolszczan (2013), Burgasser, Melis, et al. (2015), Osten et al. (2015), Williams and Berger (2015), Williams et al. (2015), Route and Wolszczan (2016a, 2016b), Kao et al. (2016), and Lynch et al. (2016)

X-ray

Berger et al. (2005), Audard et al. (2005), Berger et al. (2010), and Osten et al. (2015); Cook, Williams, and Berger 2014; Williams, Cook, and Berger 2014, and references therein

Chapter 7

CONCLUSION AND FUTURE DIRECTIONS

At the onset of this dissertation, I set out to investigate brown dwarf magnetic activity. It has become evident that brown dwarf magnetism represents a significant departure from the standard coronal picture of stellar activity and instead can be well described by a smooth transition from predominantly chromospheric and coronal to auroral and planet-like. In this way, like many of the other properties of brown dwarfs, they stand squarely at the cross section of stellar astrophysics and planetary science. It is important to emphasize that the aurorae are fundamentally defined by large-scale magnetospheric field-aligned current systems. Thus, although there are many manifestations of auroral phenomena in the Solar System, from the oxygen emission lines of Earth to the infrared H_3^+ lines of Saturn, the physical mechanism is tied to accelerated electron beams and their impact on the atmospheric gas. Accordingly, brown dwarf aurorae are not analogous to what is seen on Earth but instead to Jupiter with its hydrogen atmospheres and large rotationally dominated magnetosphere.

Brown dwarfs are capable of sustaining weak chromospheric activity at the M/L transition, which declines steadily in the cooler objects. Simultaneously, many of these objects have sufficiently cool atmospheres and large-scale magnetic fields coupled with fast rotation rates that permit the development of strong magnetospheric current systems. There is still an open question with regard to the exact processes of the electrodynamic engine; however the role of planetary satellites, could be instrumental. Moreover, like Jupiter, any given auroral brown dwarf may sustain both co-rotation breakdown and an auroral flux tube satellite interaction. Further study will be essential to confirm which of these processes are involved.

Indeed, the study of auroral brown dwarf activity has only just commenced. Although we have learned much with regards to the underlying processes of brown dwarf auroral physics, many questions remain. New brown dwarf discoveries and extended monitoring of known systems, in search of auroral emissions, will be important to provide a growing sample of auroral objects with which to study both the statistics of auroral phenomena and targets for follow-up observations. Key to further development will be detailed multi-wavelength observations of these brown

dwarfs. Because the aurorae are manifest at multiple different wavebands, its the connection of the different processes that will be crucial to solving remaining mysteries, like the electrodynamic engine, the breakdown of auroral energy dissipation and the auroral electron energy distribution. A complete understanding of individual systems, like LSR J1835+3259, will lead to further insights and provide the benchmarks for the brown dwarf auroral paradigm.

Observations with space-borne observatories could be critical in this endeavor. I have initiated a program with the *Hubble Space Telescope* to look for the FUV auroral emission features in the benchmark objects LSRJ 1835+3259 and TVLM 513-46546 (HST-14347). These data could provide the first direct confirmation of the impact of the energetic electron beam on the cool atmospheric gas. Additionally, the launch of the *James Webb Space Telescope* will provide the tools to initiate a deep search for H_3^+ emission features to examine the effect of the electron beam on the atmospheres and potentially provide precise constraints on the auroral electron energy distribution. The launch of the *Transiting Exoplanet Survey Satellite* will also provide a new look at the photometric variability of late M dwarfs, extending the long-term monitoring that was so successful with *Kepler* to even lower mass stars with its redder bandpass and large sky coverage. This will not only allow for a statistical look at the photometric variations to compare against other auroral activity indicators, it will began to establish the statistics of planet formation around brown dwarfs and provide one of the missing pieces of the brown dwarf electrodynamic engine. We have already begun investigating these possibilities with radio observations of the nearby brown dwarf system TRAPPIST-1 and its planets (VLA/16A-466).

Concurrently, it will be crucial to develop the theoretical modeling necessary to interpret these observations in the auroral context and uncover the physical atmospheric conditions of auroral browns, the electron beam energies and the dynamics of the auroral engine. Although, these have been developed for the gas giant planets of the Solar System, the opening of this field to extrasolar bodies provides a new opportunity to study auroral physics in a broader parameter space, with new conditions that will present additional challenges. Auroral electron beam modeling will provide the essential connection between the physical processes and the observations. Moreover, a deeper understanding of auroral physics from studies of the Jovian system will enable a more thorough understanding of the same processes outside of the Solar System. The *Juno* mission will be invaluable in the endeavor as it explores the Jovian magnetosphere and Jupiter's polar regions.

Despite the vast distances to astronomical objects, the astrophysical enterprise has managed to tease out some of the basic truths of nature. Although many mysteries in understanding brown dwarf magnetism remain, with a few key observations and the judicious application of physics it is possible to continue to uncover these underlying truths about nature. There is much work to be done.

"It is well to remember that all forms of scientific research represent a very real service to the state. Astronomy is not so remote from the practical affairs of life as a superficial estimate might conceive it. Poincaré has shown this most clearly in his book on *The Value of Science*, where he asks how far advanced the world's civilization would be if the stars had always been hidden by clouds. It is interesting to observe that in demonstrating the part played by astronomy in the world's progress he does not even mention such important matters as navigation and the determination of time, because of their insignificance as compared with far more impressive contributions. Thanks to observatories in all quarters of the earth, the picture of the universe still continues to unfold and to influence progress in every field of thought."

George Ellery Hale

Annual Report of Director of the Mount Wilson Observatory

1917

BIBLIOGRAPHY

Allard, F., P. H. Hauschildt, D. R. Alexander, and S. Starrfield. 1997. "Model Atmospheres of Very Low Mass Stars and Brown Dwarfs." *ARA&A* 35:137–177. doi:10.1146/annurev.astro.35.1.137.

Antonova, A., G. Hallinan, J. G. Doyle, S. Yu, A. Kuznetsov, Y. Metodieva, A. Golden, and K. L. Cruz. 2013. "Volume-limited radio survey of ultracool dwarfs." *A&A* 549, A131 (January): A131. doi:10.1051/0004-6361/201118583. arXiv: 1212.3464 [astro-ph.SR].

Apai, D., J. Radigan, E. Buenzli, A. Burrows, I. N. Reid, and R. Jayawardhana. 2013. "HST Spectral Mapping of L/T Transition Brown Dwarfs Reveals Cloud Thickness Variations." *ApJ* 768, 121 (May): 121. doi:10.1088/0004-637X/768/2/121. arXiv: 1303.4151 [astro-ph.EP].

Artigau, É., S. Bouchard, R. Doyon, and D. Lafreniere. 2009. "Photometric Variability of the T2.5 Brown Dwarf SIMP J013656.5+093347: Evidence for Evolving Weather Patterns." *ApJ* 701 (August): 1534–1539. doi:10.1088/0004-637X/701/2/1534. arXiv: 0906.3514 [astro-ph.SR].

Artigau, É., R. Doyon, D. Lafreniere, D. Nadeau, J. Robert, and L. Albert. 2006. "Discovery of the Brightest T Dwarf in the Northern Hemisphere." *ApJ* 651 (November): L57–L60. doi:10.1086/509146. eprint: astro-ph/0609419.

Aschwanden, M. J., A. I. Poland, and D. M. Rabin. 2001. "The New Solar Corona." *ARA&A* 39:175–210. doi:10.1146/annurev.astro.39.1.175.

Audard, M., A. Brown, K. R. Briggs, M. Güdel, A. Telleschi, and J. E. Gizis. 2005. "A Deep Look at the T-Type Brown Dwarf Binary ϵ Indi Bab with Chandra and the Australia Telescope Compact Array." *ApJ* 625 (May): L63–L66. doi:10.1086/430881. eprint: astro-ph/0504424.

Badman, S. V., G. Branduardi-Raymont, M. Galand, S. L. G. Hess, N. Krupp, L. Lamy, H. Melin, and C. Tao. 2015. "Auroral Processes at the Giant Planets: Energy Deposition, Emission Mechanisms, Morphology and Spectra." *Space Sci. Rev.* 187 (April): 99–179. doi:10.1007/s11214-014-0042-x.

Bagenal, F., A. Adriani, F. Allegrini, S. J. Bolton, B. Bonfond, E. J. Bunce, J. E. P. Connerney, et al. 2014. "Magnetospheric Science Objectives of the Juno Mission." *Space Sci. Rev.* (February). doi:10.1007/s11214-014-0036-8.

Baraffe, I., G. Chabrier, F. Allard, and P. H. Hauschildt. 1998. "Evolutionary models for solar metallicity low-mass stars: mass-magnitude relationships and color-magnitude diagrams." *A&A* 337 (September): 403–412. eprint: arXiv:astro-ph/9805009.

Baraffe, I., D. Homeier, F. Allard, and G. Chabrier. 2015. "New evolutionary models for pre-main sequence and main sequence low-mass stars down to the hydrogen-burning limit." *A&A* 577, A42 (May): A42. doi:10.1051/0004-6361/201425481. arXiv: 1503.04107 [astro-ph.SR].

Bardalez Gagliuffi, D. C., A. J. Burgasser, C. R. Gelino, D. L. Looper, C. P. Nicholls, S. J. Schmidt, K. Cruz, A. A. West, J. E. Gizis, and S. Metchev. 2014. "SpeX Spectroscopy of Unresolved Very Low Mass Binaries. II. Identification of 14 Candidate Binaries with Late-M/Early-L and T Dwarf Components." *ApJ* 794, 143 (October): 143. doi:10.1088/0004-637X/794/2/143. arXiv: 1408.3089 [astro-ph.SR].

Barnes, J. R., S. V. Jeffers, H. R. A. Jones, Y. V. Pavlenko, J. S. Jenkins, C. A. Haswell, and M. E. Lohr. 2015. "Starspot Distributions on Fully Convective M Dwarfs: Implications for Radial Velocity Planet Searches." *ApJ* 812, 42 (October): 42. doi:10.1088/0004-637X/812/1/42. arXiv: 1509.05284 [astro-ph.SR].

Basri, G., and G. W. Marcy. 1995. "A surprise at the bottom of the main sequence: Rapid rotation and NO H-alpha emission." *AJ* 109 (February): 762–773. doi:10.1086/117319.

Bastian, T. S., A. O. Benz, and D. E. Gary. 1998. "Radio Emission from Solar Flares." *ARA&A* 36:131–188. doi:10.1146/annurev.astro.36.1.131.

Batalha, N. M., et al. 2012. "Planetary Candidates Observed by Kepler, III: Analysis of the First 16 Months of Data." *ArXiv e-prints* (February). arXiv: 1202.5852 [astro-ph.EP].

Bean, J. L., C. Sneden, P. H. Hauschildt, C. M. Johns-Krull, and G. F. Benedict. 2006. "Accurate M Dwarf Metallicities from Spectral Synthesis: A Critical Test of Model Atmospheres." *ApJ* 652 (December): 1604–1616. doi:10.1086/508321. eprint: arXiv:astro-ph/0608093.

Berger, E. 2002. "Flaring up All Over-Radio Activity in Rapidly Rotating Late M and L Dwarfs." *ApJ* 572 (June): 503–513. doi:10.1086/340301. eprint: astro-ph/0111317.

———. 2006. "Radio Observations of a Large Sample of Late M, L, and T Dwarfs: The Distribution of Magnetic Field Strengths." *ApJ* 648 (September): 629–636. doi:10.1086/505787. eprint: astro-ph/0603176.

Berger, E., S. Ball, K. M. Becker, M. Clarke, D. A. Frail, T. A. Fukuda, I. M. Hoffman, et al. 2001. "Discovery of radio emission from the brown dwarf LP944-20." *Nature* 410 (March): 338–340. eprint: astro-ph/0102301.

Berger, E., G. Basri, T. A. Fleming, M. S. Giampapa, J. E. Gizis, J. Liebert, E. Martin, N. Phan-Bao, and R. E. Rutledge. 2010. "Simultaneous Multi-Wavelength Observations of Magnetic Activity in Ultracool Dwarfs. III. X-ray, Radio, and Hα Activity Trends in M and L dwarfs." *ApJ* 709 (January): 332–341. doi:10.1088/0004-637X/709/1/332. arXiv: 0909.4783 [astro-ph.SR].

Berger, E., G. Basri, J. E. Gizis, M. S. Giampapa, R. E. Rutledge, J. Liebert, E. Martin, et al. 2008. "Simultaneous Multiwavelength Observations of Magnetic Activity in Ultracool Dwarfs. II. Mixed Trends in VB 10 and LSR 1835+32 and the Possible Role of Rotation." *ApJ* 676, 1307-1318 (April): 1307–1318. doi:10.1086/529131. arXiv: 0710.3383.

Berger, E., R. E. Rutledge, N. Phan-Bao, G. Basri, M. S. Giampapa, J. E. Gizis, J. Liebert, E. Martin, and T. A. Fleming. 2009. "Periodic Radio and Hα Emission from the L Dwarf Binary 2MASSW J0746425+200032: Exploring the Magnetic Field Topology and Radius Of An L Dwarf." *ApJ* 695 (April): 310–316. doi:10.1088/0004-637X/695/1/310. arXiv: 0809.0001.

Berger, E., R. E. Rutledge, I. N. Reid, L. Bildsten, J. E. Gizis, J. Liebert, E. Martin, et al. 2005. "The Magnetic Properties of an L Dwarf Derived from Simultaneous Radio, X-Ray, and Hα Observations." *ApJ* 627 (July): 960–973. doi:10.1086/430343. eprint: astro-ph/0502384.

Berry, D. S. 1993. "MEMSYS – A Maximum Entropy image reconstruction package." *Starlink User Note* 117.

Bhardwaj, A., and G. R. Gladstone. 2000. "Auroral emissions of the giant planets." *Reviews of Geophysics* 38:295–354. doi:10.1029/1998RG000046.

Biller, B. A., I. J. M. Crossfield, L. Mancini, S. Ciceri, J. Southworth, T. G. Kopytova, M. Bonnefoy, et al. 2013. "Weather on the Nearest Brown Dwarfs: Resolved Simultaneous Multi-wavelength Variability Monitoring of WISE J104915.57-531906.1AB." *ApJ* 778, L10 (November): L10. doi:10.1088/2041-8205/778/1/L10. arXiv: 1310.5144 [astro-ph.SR].

Blake, C. H., D. Charbonneau, and R. J. White. 2010. "The NIRSPEC Ultracool Dwarf Radial Velocity Survey." *ApJ* 723 (November): 684–706. doi:10.1088/0004-637X/723/1/684. arXiv: 1008.3874 [astro-ph.SR].

Bolton, S. J., F. Bagenal, M. Blanc, T. Cassidy, E. Chané, C. Jackman, X. Jia, et al. 2015. "Jupiter's Magnetosphere: Plasma Sources and Transport." *Space Sci. Rev.* 192 (October): 209–236. doi:10.1007/s11214-015-0184-5.

Bonfils, X., et al. 2012. "A hot Uranus transiting the nearby M dwarf GJ 3470. Detected with HARPS velocimetry. Captured in transit with TRAPPIST photometry." *A&A* 546, A27 (October): A27. doi:10.1051/0004-6361/201219623. arXiv: 1206.5307 [astro-ph.EP].

Bonfils, X., T. Forveille, X. Delfosse, S. Udry, M. Mayor, C. Perrier, F. Bouchy, F. Pepe, D. Queloz, and J.-L. Bertaux. 2005a. "The HARPS search for southern extra-solar planets. VI. A Neptune-mass planet around the nearby M dwarf Gl 581." *A&A* 443 (December): L15–L18. doi:10.1051/0004-6361:200500193. eprint: arXiv:astro-ph/0509211.

Bonfils, X., T. Forveille, X. Delfosse, S. Udry, M. Mayor, C. Perrier, F. Bouchy, F. Pepe, D. Queloz, and J.-L. Bertaux. 2005b. "The HARPS search for southern extra-solar planets. VI. A Neptune-mass planet around the nearby M dwarf Gl 581." *A&A* 443 (December): L15–L18. doi:10.1051/0004-6361:200500193. eprint: arXiv:astro-ph/0509211.

Borucki, W. J., et al. 2011. "Characteristics of Planetary Candidates Observed by Kepler. II. Analysis of the First Four Months of Data." *ApJ* 736 (July): 19–+. doi:10.1088/0004-637X/736/1/19. arXiv: 1102.0541 [astro-ph.EP].

Bouy, H., G. Duchêne, R. Köhler, W. Brandner, J. Bouvier, E. L. Martin, A. Ghez, et al. 2004. "First determination of the dynamical mass of a binary L dwarf." *A&A* 423 (August): 341–352. doi:10.1051/0004-6361:20040551. eprint: astro-ph/0405111.

Bowler, B. P., M. C. Liu, and T. J. Dupuy. 2010. "SDSS J141624.08+134826.7: A Nearby Blue L Dwarf From the Sloan Digital Sky Survey." *ApJ* 710 (February): 45–50. doi:10.1088/0004-637X/710/1/45. arXiv: 0912.3796 [astro-ph.SR].

Boyajian, T. S., et al. 2012. "Stellar Diameters and Temperatures. II. Main-sequence K- and M-stars." *ApJ* 757, 112 (October): 112. doi:10.1088/0004-637X/757/2/112. arXiv: 1208.2431 [astro-ph.SR].

Browning, M. K. 2008. "Simulations of Dynamo Action in Fully Convective Stars." *ApJ* 676, 1262-1280 (April): 1262–1280. doi:10.1086/527432. arXiv: 0712.1603.

Browning, M. K., G. Basri, G. W. Marcy, A. A. West, and J. Zhang. 2010. "Rotation and Magnetic Activity in a Sample of M-Dwarfs." *AJ* 139 (February): 504–518. doi:10.1088/0004-6256/139/2/504.

Browning, M. K., M. S. Miesch, A. S. Brun, and J. Toomre. 2006. "Dynamo Action in the Solar Convection Zone and Tachocline: Pumping and Organization of Toroidal Fields." *ApJ* 648 (September): L157–L160. doi:10.1086/507869. eprint: astro-ph/0609153.

Buchhave, L. A., et al. 2012. "An abundance of small exoplanets around stars with a wide range of metallicities." *Nature* 486 (June): 375–377. doi:10.1038/nature11121.

Buenzli, E., D. Apai, J. Radigan, I. N. Reid, and D. Flateau. 2014. "Brown Dwarf Photospheres are Patchy: A Hubble Space Telescope Near-infrared Spectroscopic Survey Finds Frequent Low-level Variability." *ApJ* 782, 77 (February): 77. doi:10.1088/0004-637X/782/2/77. arXiv: 1312.5294 [astro-ph.SR].

Buenzli, E., M. S. Marley, D. Apai, D. Saumon, B. A. Biller, I. J. M. Crossfield, and J. Radigan. 2015. "Cloud Structure of the Nearest Brown Dwarfs. II. High-amplitude Variability for Luhman 16 A and B in and out of the 0.99 μm FeH feature." *ApJ* 812, 163 (October): 163. doi:10.1088/0004-637X/812/2/163. arXiv: 1509.06148 [astro-ph.SR].

Burgasser, A. J., A. Burrows, and J. D. Kirkpatrick. 2006. "A Method for Determining the Physical Properties of the Coldest Known Brown Dwarfs." *ApJ* 639 (March): 1095–1113. doi:10.1086/499344. eprint: astro-ph/0510707.

Burgasser, A. J., K. L. Cruz, M. Cushing, C. R. Gelino, D. L. Looper, J. K. Faherty, J. D. Kirkpatrick, and I. N. Reid. 2010. "SpeX Spectroscopy of Unresolved Very Low Mass Binaries. I. Identification of 17 Candidate Binaries Straddling the L Dwarf/T Dwarf Transition." *ApJ* 710 (February): 1142–1169. doi:10.1088/0004-637X/710/2/1142. arXiv: 0912.3808 [astro-ph.SR].

Burgasser, A. J., T. R. Geballe, S. K. Leggett, J. D. Kirkpatrick, and D. A. Golimowski. 2006. "A Unified Near-Infrared Spectral Classification Scheme for T Dwarfs." *ApJ* 637 (February): 1067–1093. doi:10.1086/498563. eprint: astro-ph/0510090.

Burgasser, A. J., M. Gillon, J. K. Faherty, J. Radigan, A. H. M. J. Triaud, P. Plavchan, R. Street, E. Jehin, L. Delrez, and C. Opitom. 2014. "A Monitoring Campaign for Luhman 16AB. I. Detection of Resolved Near-infrared Spectroscopic Variability." *ApJ* 785, 48 (April): 48. doi:10.1088/0004-637X/785/1/48. arXiv: 1402.2342 [astro-ph.SR].

Burgasser, A. J., J. D. Kirkpatrick, M. E. Brown, I. N. Reid, A. Burrows, J. Liebert, K. Matthews, et al. 2002. "The Spectra of T Dwarfs. I. Near-Infrared Data and Spectral Classification." *ApJ* 564 (January): 421–451. doi:10.1086/324033. eprint: astro-ph/0108452.

Burgasser, A. J., J. D. Kirkpatrick, M. E. Brown, I. N. Reid, J. E. Gizis, C. C. Dahn, D. G. Monet, et al. 1999. "Discovery of Four Field Methane (T-Type) Dwarfs with the Two Micron All-Sky Survey." *ApJ* 522 (September): L65–L68. doi:10.1086/312221. eprint: astro-ph/9907019.

Burgasser, A. J., J. D. Kirkpatrick, J. Liebert, and A. Burrows. 2003. "The Spectra of T Dwarfs. II. Red Optical Data." *ApJ* 594 (September): 510–524. doi:10.1086/376756. eprint: astro-ph/0305139.

Burgasser, A. J., J. D. Kirkpatrick, I. N. Reid, J. Liebert, J. E. Gizis, and M. E. Brown. 2000. "Detection of Hα Emission in a Methane (T Type) Brown Dwarf." *AJ* 120 (July): 473–478. doi:10.1086/301423. eprint: astro-ph/0003291.

Burgasser, A. J., J. Liebert, J. D. Kirkpatrick, and J. E. Gizis. 2002. "A Search for Variability in the Active T Dwarf 2MASS 1237+6526." *AJ* 123 (May): 2744–2753. doi:10.1086/339836. eprint: astro-ph/0201382.

Burgasser, A. J., S. E. Logsdon, J. Gagne, J. J. Bochanski, J. K. Faherty, A. A. West, E. E. Mamajek, S. J. Schmidt, and K. L. Cruz. 2015a. "The Brown Dwarf Kinematics Project (BDKP). IV. Radial Velocities of 85 Late-M and L Dwarfs with MagE." *ApJS* 220, 18 (September): 18. doi:10.1088/0067-0049/220/1/18. arXiv: 1507.00057 [astro-ph.SR].

Burgasser, A. J., S. E. Logsdon, J. Gagne, J. J. Bochanski, J. K. Faherty, A. A. West, E. E. Mamajek, S. J. Schmidt, and K. L. Cruz. 2015b. "The Brown Dwarf Kinematics Project (BDKP). IV. Radial Velocities of 85 Late-M and L Dwarfs with MagE." *ApJS* 220, 18 (September): 18. doi:10.1088/0067-0049/220/1/18. arXiv: 1507.00057 [astro-ph.SR].

Burgasser, A. J., C. Melis, J. Todd, C. R. Gelino, G. Hallinan, and D. Bardalez Gagliuffi. 2015. "Radio Emission and Orbital Motion from the Close-encounter Star-Brown Dwarf Binary WISE J072003.20-084651.2." *AJ* 150, 180 (December): 180. doi:10.1088/0004-6256/150/6/180. arXiv: 1508.06332 [astro-ph.SR].

Burgasser, A. J., I. N. Reid, S. K. Leggett, J. D. Kirkpatrick, J. Liebert, and A. Burrows. 2005. "SDSS J042348.57-041403.5AB: A Brown Dwarf Binary Straddling the L/T Transition." *ApJ* 634 (December): L177–L180. doi:10.1086/498866. eprint: astro-ph/0510580.

Burgasser, A. J., B. N. Sitarski, C. R. Gelino, S. E. Logsdon, and M. D. Perrin. 2011. "The Hyperactive L Dwarf 2MASS J13153094-2649513: Continued Emission and a Brown Dwarf Companion." *ApJ* 739, 49 (September): 49. doi:10.1088/0004-637X/739/1/49. arXiv: 1107.1484 [astro-ph.SR].

Burgasser, A. J., J. C. Wilson, J. D. Kirkpatrick, M. F. Skrutskie, M. R. Colonno, A. T. Enos, J. D. Smith, et al. 2000. "Discovery of a Bright Field Methane (T-Type) Brown Dwarf by 2MASS." *AJ* 120 (August): 1100–1105. doi:10.1086/301475. eprint: astro-ph/0004239.

Burrows, A., A. J. Burgasser, J. D. Kirkpatrick, J. Liebert, J. A. Milsom, D. Sudarsky, and I. Hubeny. 2002. "Theoretical Spectral Models of T Dwarfs at Short Wavelengths and Their Comparison with Data." *ApJ* 573 (July): 394–417. doi:10.1086/340584. eprint: astro-ph/0109227.

Burrows, A., W. B. Hubbard, J. I. Lunine, and J. Liebert. 2001. "The theory of brown dwarfs and extrasolar giant planets." *Reviews of Modern Physics* 73 (July): 719–765. doi:10.1103/RevModPhys.73.719. eprint: astro-ph/0103383.

Burrows, A., W. B. Hubbard, D. Saumon, and J. I. Lunine. 1993. "An expanded set of brown dwarf and very low mass star models." *ApJ* 406 (March): 158–171. doi:10.1086/172427.

Butler, R. P., S. S. Vogt, G. W. Marcy, D. A. Fischer, J. T. Wright, G. W. Henry, G. Laughlin, and J. J. Lissauer. 2004. "A Neptune-Mass Planet Orbiting the Nearby M Dwarf GJ 436." *ApJ* 617 (December): 580–588. doi:10.1086/425173. eprint: arXiv:astro-ph/0408587.

Chabrier, G., and I. Baraffe. 2000. "Theory of Low-Mass Stars and Substellar Objects." *ARA&A* 38:337–377. doi:10.1146/annurev.astro.38.1.337. eprint: arXiv:astro-ph/0006383.

Charbonneau, P. 2014. "Solar Dynamo Theory." *ARA&A* 52 (August): 251–290. doi:10.1146/annurev-astro-081913-040012.

Chiu, K., X. Fan, S. K. Leggett, D. A. Golimowski, W. Zheng, T. R. Geballe, D. P. Schneider, and J. Brinkmann. 2006. "Seventy-One New L and T Dwarfs from the Sloan Digital Sky Survey." *AJ* 131 (June): 2722–2736. doi:10.1086/501431. eprint: astro-ph/0601089.

Christensen, U. R., V. Holzwarth, and A. Reiners. 2009. "Energy flux determines magnetic field strength of planets and stars." *Nature* 457 (January): 167–169. doi:10.1038/nature07626.

Cook, B. A., P. K. G. Williams, and E. Berger. 2014. "Trends in Ultracool Dwarf Magnetism. II. The Inverse Correlation Between X-Ray Activity and Rotation as Evidence for a Bimodal Dynamo." *ApJ* 785, 10 (April): 10. doi:10.1088/0004-637X/785/1/10. arXiv: 1310.6758 [astro-ph.SR].

Cooper, M. C., J. A. Newman, M. Davis, D. P. Finkbeiner, and B. F. Gerke. 2012. *spec2d: DEEP2 DEIMOS Spectral Pipeline.* Astrophysics Source Code Library, March. ascl: 1203.003.

Coughlin, J. L., M. López-Morales, T. E. Harrison, N. Ule, and D. I. Hoffman. 2011. "Low-mass Eclipsing Binaries in the Initial Kepler Data Release." *AJ* 141, 78 (March): 78. doi:10.1088/0004-6256/141/3/78. arXiv: 1007.4295 [astro-ph.SR].

Covey, K. R., M. A. Agüeros, J. J. Lemonias, N. M. Law, A. L. Kraus, and Palomar Transient Factory Collaboration. 2011. "The Age-Rotation-Activity Relation: From Myrs to Gyrs." In *16th Cambridge Workshop on Cool Stars, Stellar Systems, and the Sun,* edited by C. Johns-Krull, M. K. Browning, and A. A. West, 448:269. Astronomical Society of the Pacific Conference Series. December. arXiv: 1012.0061 [astro-ph.SR].

Cowley, S. W. H., and E. J. Bunce. 2001. "Origin of the main auroral oval in Jupiter's coupled magnetosphere-ionosphere system." *Planet. Space Sci.* 49 (August): 1067–1088. doi:10.1016/S0032-0633(00)00167-7.

Cowley, S., E. Bunce, and R. Prangé. 2004. "Saturn's polar ionospheric flows and their relation to the main auroral oval." *Annales Geophysicae* 22 (April): 1379–1394. doi:10.5194/angeo-22-1379-2004.

Crossfield, I. J. M. 2014. "Doppler imaging of exoplanets and brown dwarfs." *A&A* 566, A130 (June): A130. doi:10.1051/0004-6361/201423750. arXiv: 1404.7853 [astro-ph.SR].

Crossfield, I. J. M., T. Barman, B. M. S. Hansen, and A. W. Howard. 2013. "Warm ice giant GJ 3470b. I. A flat transmission spectrum indicates a hazy, low-methane, and/or metal-rich atmosphere." *A&A* 559, A33 (November): A33. doi:10.1051/0004-6361/201322278. arXiv: 1308.6580 [astro-ph.EP].

Crossfield, I. J. M., B. Biller, J. E. Schlieder, N. R. Deacon, M. Bonnefoy, D. Homeier, F. Allard, et al. 2014. "A global cloud map of the nearest known brown dwarf." *Nature* 505 (January): 654–656. doi:10.1038/nature12955. arXiv: 1401.8145 [astro-ph.EP].

Cruz, K. L., I. N. Reid, J. D. Kirkpatrick, A. J. Burgasser, J. Liebert, A. R. Solomon, S. J. Schmidt, P. R. Allen, S. L. Hawley, and K. R. Covey. 2007. "Meeting the Cool Neighbors. IX. The Luminosity Function of M7-L8 Ultracool Dwarfs in the Field." *AJ* 133 (February): 439–467. doi:10.1086/510132. eprint: astro-ph/0609648.

Cruz, K. L., I. N. Reid, J. Liebert, J. D. Kirkpatrick, and P. J. Lowrance. 2003. "Meeting the Cool Neighbors. V. A 2MASS-Selected Sample of Ultracool Dwarfs." *AJ* 126 (November): 2421–2448. doi:10.1086/378607. eprint: astro-ph/0307429.

Cushing, M. C., J. D. Kirkpatrick, C. R. Gelino, R. L. Griffith, M. F. Skrutskie, A. Mainzer, K. A. Marsh, et al. 2011. "The Discovery of Y Dwarfs using Data from the Wide-field Infrared Survey Explorer (WISE)." *ApJ* 743, 50 (December): 50. doi:10.1088/0004-637X/743/1/50. arXiv: 1108.4678 [astro-ph.SR].

Cushing, M. C., M. S. Marley, D. Saumon, B. C. Kelly, W. D. Vacca, J. T. Rayner, R. S. Freedman, K. Lodders, and T. L. Roellig. 2008. "Atmospheric Parameters of Field L and T Dwarfs." *ApJ* 678 (May): 1372–1395. doi:10.1086/526489. arXiv: 0711.0801.

Cushing, M. C., J. T. Rayner, and W. D. Vacca. 2005. "An Infrared Spectroscopic Sequence of M, L, and T Dwarfs." *ApJ* 623 (April): 1115–1140. doi:10.1086/428040. eprint: astro-ph/0412313.

Cutri, R. M., et al. 2003. "2MASS All-Sky Catalog of Point Sources (Cutri+ 2003)." *VizieR Online Data Catalog* 2246 (March): –+.

Dahn, C. C., H. C. Harris, F. J. Vrba, H. H. Guetter, B. Canzian, A. A. Henden, S. E. Levine, et al. 2002. "Astrometry and Photometry for Cool Dwarfs and Brown Dwarfs." *AJ* 124 (August): 1170–1189. doi:10.1086/341646. eprint: astro-ph/0205050.

Deacon, N. R., M. C. Liu, E. A. Magnier, B. P. Bowler, B. Goldman, J. A. Redstone, W. S. Burgett, et al. 2011. "Four New T Dwarfs Identified in Pan-STARRS 1 Commissioning Data." *AJ* 142, 77 (September): 77. doi:10.1088/0004-6256/142/3/77. arXiv: 1106.3105 [astro-ph.SR].

Delfosse, X., T. Forveille, C. Perrier, and M. Mayor. 1998. "Rotation and chromospheric activity in field M dwarfs." *A&A* 331 (March): 581–595.

Delfosse, X., T. Forveille, D. Ségransan, J.-L. Beuzit, S. Udry, C. Perrier, and M. Mayor. 2000. "Accurate masses of very low mass stars. IV. Improved mass-luminosity relations." *A&A* 364 (December): 217–224. eprint: arXiv:astro-ph/0010586.

Delfosse, X., C. G. Tinney, T. Forveille, N. Epchtein, E. Bertin, J. Borsenberger, E. Copet, et al. 1997. "Field brown dwarfs found by DENIS." *A&A* 327 (November): L25–L28.

Delorme, P., C. J. Willott, T. Forveille, X. Delfosse, C. Reyle, E. Bertin, L. Albert, et al. 2008. "Finding ultracool brown dwarfs with MegaCam on CFHT: method and first results." *A&A* 484 (June): 469–478. doi:10.1051/0004-6361:20078843. arXiv: 0804.1477.

Demory, B.-O., G. Torres, V. Neves, L. Rogers, M. Gillon, E. Horch, P. Sullivan, et al. 2013. "Spitzer Observations of GJ3470b: a Very Low-density Neptune-size Planet Orbiting a Metal-rich M dwarf." *ArXiv e-prints* (January). arXiv: 1301.6555 [astro-ph.EP].

Donati, J.-F., T. Forveille, A. Collier Cameron, J. R. Barnes, X. Delfosse, M. M. Jardine, and J. A. Valenti. 2006. "The Large-Scale Axisymmetric Magnetic Topology of a Very-Low-Mass Fully Convective Star." *Science* 311 (February): 633–635. doi:10.1126/science.1121102. eprint: astro-ph/0602069.

Donati, J.-F., J. Morin, P. Petit, X. Delfosse, T. Forveille, M. Aurière, R. Cabanac, et al. 2008. "Large-scale magnetic topologies of early M dwarfs." *MNRAS* 390 (October): 545–560. doi:10.1111/j.1365-2966.2008.13799.x. arXiv: 0809.0269.

Drake, J. J., R. A. Stern, G. Stringfellow, M. Mathioudakis, J. M. Laming, and D. L. Lambert. 1996. "Detection of Quiescent Extreme Ultraviolet Emission from the Very Low Mass Dwarf van Biesbroeck 8: Evidence for a Turbulent Field Dynamo." *ApJ* 469 (October): 828. doi:10.1086/177830.

Dulk, G. A. 1985. "Radio emission from the sun and stars." *ARA&A* 23:169–224. doi:10.1146/annurev.aa.23.090185.001125.

Dupuy, T. J., and M. C. Liu. 2012. "The Hawaii Infrared Parallax Program. I. Ultracool Binaries and the L/T Transition." *ApJS* 201, 19 (August): 19. doi:10.1088/0067-0049/201/2/19. arXiv: 1201.2465 [astro-ph.SR].

Dupuy, T. J., M. C. Liu, S. K. Leggett, M. J. Ireland, K. Chiu, and D. A. Golimowski. 2015. "The Mass-Luminosity Relation in the L/T Transition: Individual Dynamical Masses for the New J-band Flux Reversal Binary SDSSJ105213.51+442255.7AB." *ApJ* 805, 56 (May): 56. doi:10.1088/0004-637X/805/1/56. arXiv: 1503.06212 [astro-ph.SR].

Dyudina, U. A., A. P. Ingersoll, S. P. Ewald, and D. Wellington. 2016. "Saturn's aurora observed by the Cassini camera at visible wavelengths." *Icarus* 263 (January): 32–43. doi:10.1016/j.icarus.2015.05.022. arXiv: 1506.00664 [astro-ph.EP].

Epchtein, N., et al. 1997. "The deep near-infrared southern sky survey (DENIS)." *The Messenger* 87 (March): 27–34.

Faber, S. M., et al. 2003. "The DEIMOS spectrograph for the Keck II Telescope: integration and testing." In *Instrument Design and Performance for Optical/Infrared Ground-based Telescopes,* edited by M. Iye and A. F. M. Moorwood, 4841:1657–1669. Society of Photo-Optical Instrumentation Engineers (SPIE) Conference Series. March. doi:10.1117/12.460346.

Faherty, J. K., Y. Beletsky, A. J. Burgasser, C. Tinney, D. J. Osip, J. C. Filippazzo, and R. A. Simcoe. 2014. "Signatures of Cloud, Temperature, and Gravity from Spectra of the Closest Brown Dwarfs." *ApJ* 790, 90 (August): 90. doi:10.1088/0004-637X/790/2/90. arXiv: 1406.1518 [astro-ph.SR].

Faherty, J. K., A. J. Burgasser, F. M. Walter, N. Van der Bliek, M. M. Shara, K. L. Cruz, A. A. West, F. J. Vrba, and G. Anglada-Escude. 2012. "The Brown Dwarf Kinematics Project (BDKP). III. Parallaxes for 70 Ultracool Dwarfs." *ApJ* 752, 56 (June): 56. doi:10.1088/0004-637X/752/1/56. arXiv: 1203.5543 [astro-ph.SR].

Filippazzo, J. C., E. L. Rice, J. Faherty, K. L. Cruz, M. M. Van Gordon, and D. L. Looper. 2015. "Fundamental Parameters and Spectral Energy Distributions of Young and Field Age Objects with Masses Spanning the Stellar to Planetary Regime." *ApJ* 810, 158 (September): 158. doi:10.1088/0004-637X/810/2/158. arXiv: 1508.01767 [astro-ph.SR].

Fleming, T. A., J. Liebert, I. M. Gioia, and T. Maccacaro. 1988. "M dwarfs from the Einstein extended medium sensitivity survey." *ApJ* 331 (August): 958–973. doi:10.1086/166613.

France, K., C. S. Froning, J. L. Linsky, A. Roberge, J. T. Stocke, F. Tian, R. Bushinsky, et al. 2013. "The Ultraviolet Radiation Environment around M dwarf Exoplanet Host Stars." *ApJ* 763, 149 (February): 149. doi:10.1088/0004-637X/763/2/149. arXiv: 1212.4833 [astro-ph.EP].

France, K., R. O. Parke Loyd, A. Youngblood, A. Brown, P. C. Schneider, S. L. Hawley, C. S. Froning, et al. 2016. "The MUSCLES Treasury Survey. I. Motivation and Overview." *ApJ* 820, 89 (April): 89. doi:10.3847/0004-637X/820/2/89. arXiv: 1602.09142 [astro-ph.SR].

Geballe, T. R., et al. 2002. "Toward Spectral Classification of L and T Dwarfs: Infrared and Optical Spectroscopy and Analysis." *ApJ* 564 (January): 466–481. doi:10.1086/324078. eprint: astro-ph/0108443.

Geballe, T. R., M.-F. Jagod, and T. Oka. 1993. "Detection of H3(+) infrared emission lines in Saturn." *ApJ* 408 (May): L109–L112. doi:10.1086/186843.

Geballe, T. R., S. R. Kulkarni, C. E. Woodward, and G. C. Sloan. 1996. "The Near-Infrared Spectrum of the Brown Dwarf Gliese 229B." *ApJ* 467 (August): L101. doi:10.1086/310203. eprint: astro-ph/9606056.

Gillon, M., E. Jehin, S. M. Lederer, L. Delrez, J. de Wit, A. Burdanov, V. Van Grootel, et al. 2016. "Temperate Earth-sized planets transiting a nearby ultracool dwarf star." *Nature* 533 (May): 221–224. doi:10.1038/nature17448. arXiv: 1605.07211 [astro-ph.EP].

Gizis, J. E., A. J. Burgasser, E. Berger, P. K. G. Williams, F. J. Vrba, K. L. Cruz, and S. Metchev. 2013. "Kepler Monitoring of an L Dwarf I. The Photometric Period and White Light Flares." *ApJ* 779, 172 (December): 172. doi:10.1088/0004-637X/779/2/172. arXiv: 1310.5940 [astro-ph.SR].

Gizis, J. E., K. G. Dettman, A. J. Burgasser, S. Camnasio, M. Alam, J. C. Filippazzo, K. L. Cruz, S. Metchev, E. Berger, and P. K. G. Williams. 2015. "Kepler Monitoring of an L Dwarf. II. Clouds with Multi-year Lifetimes." *ApJ* 813, 104 (November): 104. doi:10.1088/0004-637X/813/2/104. arXiv: 1509.07186 [astro-ph.SR].

Gizis, J. E., D. G. Monet, I. N. Reid, J. D. Kirkpatrick, J. Liebert, and R. J. Williams. 2000. "New Neighbors from 2MASS: Activity and Kinematics at the Bottom of the Main Sequence." *AJ* 120 (August): 1085–1099. doi:10.1086/301456. eprint: astro-ph/0004361.

Gizis, J. E., P. K. G. Williams, A. J. Burgasser, M. Libralato, D. Nardiello, G. Piotto, L. R. Bedin, E. Berger, and R. Paudel. 2016. "WISEP J060738.65+242953.4: A Nearby. Pole-On L8 Brown Dwarf with Radio Emission." *ArXiv e-prints* (July). arXiv: 1607.00943 [astro-ph.SR].

Gladstone, G. R., J. H. Waite, D. Grodent, W. S. Lewis, F. J. Crary, R. F. Elsner, M. C. Weisskopf, et al. 2002. "A pulsating auroral X-ray hot spot on Jupiter." *Nature* 415 (February): 1000–1003.

Grodent, D., J. T. Clarke, J. Kim, J. H. Waite, and S. W. H. Cowley. 2003. "Jupiter's main auroral oval observed with HST-STIS." *Journal of Geophysical Research (Space Physics)* 108, 1389 (November): 1389. doi:10.1029/2003JA009921.

Grodent, D., J. H. Waite Jr., and J.-C. Gérard. 2001. "A self-consistent model of the Jovian auroral thermal structure." *J. Geophys. Res.* 106 (July): 12933–12952. doi:10.1029/2000JA900129.

Güdel, M. 2002. "Stellar Radio Astronomy: Probing Stellar Atmospheres from Protostars to Giants." *ARA&A* 40:217–261. doi:10.1146/annurev.astro.40.060401.093806. eprint: astro-ph/0206436.

Guedel, M., and A. O. Benz. 1993. "X-ray/microwave relation of different types of active stars." *ApJ* 405 (March): L63–L66. doi:10.1086/186766.

Gustin, J., J.-C. Gérard, D. Grodent, G. R. Gladstone, J. T. Clarke, W. R. Pryor, V. Dols, et al. 2013. "Effects of methane on giant planet's UV emissions and implications for the auroral characteristics." *Journal of Molecular Spectroscopy* 291 (September): 108–117. doi:10.1016/j.jms.2013.03.010.

Haisch, B., K. T. Strong, and M. Rodono. 1991. "Flares on the sun and other stars." *ARA&A* 29:275–324. doi:10.1146/annurev.aa.29.090191.001423.

Hall, J. C. 2008. "Stellar Chromospheric Activity." *Living Reviews in Solar Physics* 5 (March). doi:10.12942/lrsp-2008-2.

Hall, P. B. 2002. "2MASSI J1315309-264951: An L Dwarf with Strong and Variable Hα Emission." *ApJ* 564 (January): L89–L92. doi:10.1086/339020. eprint: astro-ph/0112241.

Hallinan, G., A. Antonova, J. G. Doyle, S. Bourke, C. Lane, and A. Golden. 2008. "Confirmation of the Electron Cyclotron Maser Instability as the Dominant Source of Radio Emission from Very Low Mass Stars and Brown Dwarfs." *ApJ* 684 (September): 644–653. doi:10.1086/590360. arXiv: 0805.4010.

Hallinan, G., S. Bourke, C. Lane, A. Antonova, R. T. Zavala, W. F. Brisken, R. P. Boyle, F. J. Vrba, J. G. Doyle, and A. Golden. 2007. "Periodic Bursts of Coherent Radio Emission from an Ultracool Dwarf." *ApJ* 663 (July): L25–L28. doi:10.1086/519790. arXiv: 0705.2054.

Hallinan, G., S. P. Littlefair, G. Cotter, S. Bourke, L. K. Harding, J. S. Pineda, R. P. Butler, et al. 2015. "Magnetospherically driven optical and radio aurorae at the end of the stellar main sequence." *Nature* 523 (July): 568–571. doi:10.1038/nature14619. arXiv: 1507.08739 [astro-ph.SR].

Hamuy, M., N. B. Suntzeff, S. R. Heathcote, A. R. Walker, P. Gigoux, and M. M. Phillips. 1994. "Southern spectrophotometric standards, 2." *PASP* 106 (June): 566–589. doi:10.1086/133417.

Harding, L. K., G. Hallinan, R. P. Boyle, A. Golden, N. Singh, B. Sheehan, R. T. Zavala, and R. F. Butler. 2013. "Periodic Optical Variability of Radio-detected Ultracool Dwarfs." *ApJ* 779, 101 (December): 101. doi:10.1088/0004-637X/779/2/101. arXiv: 1310.1367 [astro-ph.SR].

Harding, L. K., G. Hallinan, Q. M. Konopacky, K. M. Kratter, R. P. Boyle, R. F. Butler, and A. Golden. 2013. "Spin-orbit alignment in the very low mass binary regime. The L dwarf tight binary 2MASSW J0746425+200032AB." *A&A* 554, A113 (June): A113. doi:10.1051/0004-6361/201220865. arXiv: 1304.5290 [astro-ph.SR].

Hauschildt, P. H., F. Allard, and E. Baron. 1999. "The NextGen Model Atmosphere Grid for 3000<= T_eff <=10,000 K." *ApJ* 512 (February): 377–385. doi:10.1086/306745. eprint: arXiv:astro-ph/9807286.

Heinze, A. N., S. Metchev, D. Apai, D. Flateau, R. Kurtev, M. Marley, J. Radigan, A. J. Burgasser, É. Artigau, and P. Plavchan. 2013. "Weather on Other Worlds. I. Detection of Periodic Variability in the L3 Dwarf DENIS-P J1058.7-1548 with Precise Multi-wavelength Photometry." *ApJ* 767, 173 (April): 173. doi:10.1088/0004-637X/767/2/173. arXiv: 1303.2948 [astro-ph.SR].

Heinze, A. N., S. Metchev, and K. Kellogg. 2015. "Weather on Other Worlds. III. A Survey for T Dwarfs with High-amplitude Optical Variability." *ApJ* 801, 104 (March): 104. doi:10.1088/0004-637X/801/2/104. arXiv: 1412.6733 [astro-ph.SR].

Helling, C., and S. Casewell. 2014. "Atmospheres of brown dwarfs." *A&A Rev.* 22 (November): 80. doi:10.1007/s00159-014-0080-0. arXiv: 1410.6029 [astro-ph.SR].

Hill, C. A., C. A. Watson, D. Steeghs, V. S. Dhillon, and T. Shahbaz. 2016. "Roche tomography of cataclysmic variables - VII. The long-term magnetic activity of AE Aqr." *MNRAS* 459 (June): 1858–1874. doi:10.1093/mnras/stw766. arXiv: 1603.09368 [astro-ph.SR].

Hilton, E. J., A. A. West, S. L. Hawley, and A. F. Kowalski. 2010. "M Dwarf Flares from Time-resolved Sloan Digital Sky Survey Spectra." *AJ* 140 (November): 1402–1413. doi:10.1088/0004-6256/140/5/1402. arXiv: 1009.1158 [astro-ph.SR].

Howard, A. W., et al. 2010. "The California Planet Survey. I. Four New Giant Exoplanets." *ApJ* 721 (October): 1467–1481. doi:10.1088/0004-637X/721/2/1467. arXiv: 1003.3488 [astro-ph.EP].

Hui, Y., D. R. Schultz, V. A. Kharchenko, P. C. Stancil, T. E. Cravens, C. M. Lisse, and A. Dalgarno. 2009. "The Ion-induced Charge-exchange X-ray Emission of the Jovian Auroras: Magnetospheric or Solar Wind Origin?" *ApJ* 702 (September): L158–L162. doi:10.1088/0004-637X/702/2/L158. arXiv: 0907.1672 [astro-ph.HE].

Ingersoll, A. P., A. R. Vasavada, B. Little, C. D. Anger, S. J. Bolton, C. Alexander, K. P. Klaasen, W. K. Tobiska, and Galileo SSI Team. 1998. "Imaging Jupiter's Aurora at Visible Wavelengths." *Icarus* 135 (September): 251–264. doi:10.1006/icar.1998.5971.

Irwin, J., and J. Bouvier. 2009. "The rotational evolution of low-mass stars." In *The Ages of Stars,* edited by E. E. Mamajek, D. R. Soderblom, and R. F. G. Wyse, 258:363–374. IAU Symposium. June. doi:10.1017/S1743921309032025.

James, D. J., M. M. Jardine, R. D. Jeffries, S. Randich, A. Collier Cameron, and M. Ferreira. 2000. "X-ray emission from nearby M-dwarfs: the super-saturation phenomenon." *MNRAS* 318 (November): 1217–1226. doi:10.1046/j.1365-8711.2000.03838.x. eprint: astro-ph/0007159.

Johnson, J. A., et al. 2012a. "Characterizing the Cool KOIs. II. The M Dwarf KOI-254 and Its Hot Jupiter." *AJ* 143, 111 (May): 111. doi:10.1088/0004-6256/143/5/111. arXiv: 1112.0017 [astro-ph.EP].

Johnson, J. A., and K. Apps. 2009. "On the Metal Richness of M Dwarfs with Planets." *ApJ* 699 (July): 933–937. doi:10.1088/0004-637X/699/2/933. arXiv: 0904.3092 [astro-ph.EP].

Johnson, J. A., K. Apps, J. Z. Gazak, J. R. Crepp, I. J. Crossfield, A. W. Howard, G. W. Marcy, T. D. Morton, C. Chubak, and H. Isaacson. 2011. "LHS 6343 C: A Transiting Field Brown Dwarf Discovered by the Kepler Mission." *ApJ* 730, 79 (April): 79. doi:10.1088/0004-637X/730/2/79. arXiv: 1008.4141 [astro-ph.EP].

Johnson, J. A., J. Z. Gazak, K. Apps, P. S. Muirhead, J. R. Crepp, I. J. M. Crossfield, T. Boyajian, et al. 2012b. "Characterizing the Cool KOIs. II. The M Dwarf KOI-254 and Its Hot Jupiter." *AJ* 143, 111 (May): 111. doi:10.1088/0004-6256/143/5/111. arXiv: 1112.0017 [astro-ph.EP].

Jones, D. O., and A. A. West. 2016. "A Catalog of GALEX Ultraviolet Emission from Spectroscopically Confirmed M Dwarfs." *ApJ* 817, 1 (January): 1. doi:10.3847/0004-637X/817/1/1. arXiv: 1509.03645 [astro-ph.SR].

Jones, H. R. A., Y. Pavlenko, S. Viti, R. J. Barber, L. A. Yakovina, D. Pinfield, and J. Tennyson. 2005. "Carbon monoxide in low-mass dwarf stars." *MNRAS* 358 (March): 105–112. doi:10.1111/j.1365-2966.2005.08736.x. eprint: astro-ph/0412387.

Kaiser, N., et al. 2002. "Pan-STARRS: A Large Synoptic Survey Telescope Array." In *Survey and Other Telescope Technologies and Discoveries,* edited by J. A. Tyson and S. Wolff, 4836:154–164. Society of Photo-Optical Instrumentation Engineers (SPIE) Conference Series. December. doi:10.1117/12.457365.

Kao, M. M., G. Hallinan, J. S. Pineda, I. Escala, A. Burgasser, S. Bourke, and D. Stevenson. 2016. "Auroral Radio Emission from Late L and T Dwarfs: A New Constraint on Dynamo Theory in the Substellar Regime." *ApJ* 818, 24 (February): 24. doi:10.3847/0004-637X/818/1/24. arXiv: 1511.03661 [astro-ph.SR].

Keiling, A., E. Donovan, F. Bagenal, and T. Karlsson. 2012. "Auroral Phenomenology and Magnetospheric Processes: Earth and Other Planets." *Washington DC American Geophysical Union Geophysical Monograph Series* 197. doi:10.1029/GM197.

Kendall, T. R., H. R. A. Jones, D. J. Pinfield, R. S. Pokorny, S. Folkes, D. Weights, J. S. Jenkins, and N. Mauron. 2007. "New nearby, bright southern ultracool dwarfs." *MNRAS* 374 (January): 445–454. doi:10.1111/j.1365-2966.2006.11026.x. eprint: astro-ph/0609396.

Kirkpatrick, J. D. 2005. "New Spectral Types L and T." *ARA&A* 43 (September): 195–245. doi:10.1146/annurev.astro.42.053102.134017.

Kirkpatrick, J. D., et al. 2011. "The First Hundred Brown Dwarfs Discovered by the Wide-field Infrared Survey Explorer (WISE)." *ApJS* 197, 19 (December): 19. doi:10.1088/0067-0049/197/2/19. arXiv: 1108.4677 [astro-ph.SR].

Kirkpatrick, J. D., T. S. Barman, A. J. Burgasser, M. R. McGovern, I. S. McLean, C. G. Tinney, and P. J. Lowrance. 2006. "Discovery of a Very Young Field L Dwarf, 2MASS J01415823-4633574." *ApJ* 639 (March): 1120–1128. doi:10.1086/499622. eprint: astro-ph/0511462.

Kirkpatrick, J. D., K. L. Cruz, T. S. Barman, A. J. Burgasser, D. L. Looper, C. G. Tinney, C. R. Gelino, et al. 2008. "A Sample of Very Young Field L Dwarfs and Implications for the Brown Dwarf "Lithium Test" at Early Ages." *ApJ* 689 (December): 1295–1326. doi:10.1086/592768. arXiv: 0808.3153.

Kirkpatrick, J. D., C. R. Gelino, M. C. Cushing, G. N. Mace, R. L. Griffith, M. F. Skrutskie, K. A. Marsh, et al. 2012. "Further Defining Spectral Type "Y" and Exploring the Low-mass End of the Field Brown Dwarf Mass Function." *ApJ* 753, 156 (July): 156. doi:10.1088/0004-637X/753/2/156. arXiv: 1205.2122 [astro-ph.SR].

Kirkpatrick, J. D., T. J. Henry, and D. W. McCarthy Jr. 1991. "A standard stellar spectral sequence in the red/near-infrared - Classes K5 to M9." *ApJS* 77 (November): 417–440. doi:10.1086/191611.

Kirkpatrick, J. D., T. J. Henry, and D. A. Simons. 1995. "The solar neighborhood. 2: The first list of dwarfs with spectral types of M7 and cooler." *AJ* 109 (February): 797–807. doi:10.1086/117323.

Kirkpatrick, J. D., I. N. Reid, J. Liebert, R. M. Cutri, B. Nelson, C. A. Beichman, C. C. Dahn, D. G. Monet, J. E. Gizis, and M. F. Skrutskie. 1999. "Dwarfs Cooler than "M": The Definition of Spectral Type "L" Using Discoveries from the 2 Micron All-Sky Survey (2MASS)." *ApJ* 519 (July): 802–833. doi:10.1086/307414.

Kirkpatrick, J. D., I. N. Reid, J. Liebert, J. E. Gizis, A. J. Burgasser, D. G. Monet, C. C. Dahn, B. Nelson, and R. J. Williams. 2000. "67 Additional L Dwarfs Discovered by the Two Micron All Sky Survey." *AJ* 120 (July): 447–472. doi:10.1086/301427. eprint: astro-ph/0003317.

Kitchatinov, L. L., D. Moss, and D. Sokoloff. 2014. "Magnetic fields in fully convective M-dwarfs: oscillatory dynamos versus bistability." *MNRAS* 442 (July): L1–L4. doi:10.1093/mnrasl/slu041. arXiv: 1401.1764 [astro-ph.SR].

Knapp, G. R., et al. 2004. "Near-Infrared Photometry and Spectroscopy of L and T Dwarfs: The Effects of Temperature, Clouds, and Gravity." *AJ* 127 (June): 3553–3578. doi:10.1086/420707. eprint: astro-ph/0402451.

Koenker, Roger. 2016. *quantreg: Quantile Regression.* R package version 5.24. https://CRAN.R-project.org/package=quantreg.

Kumar, S. S. 1963a. "The Helmholtz-Kelvin Time Scale for Stars of Very Low Mass." *ApJ* 137 (May): 1126. doi:10.1086/147590.

———. 1963b. "The Structure of Stars of Very Low Mass." *ApJ* 137 (May): 1121. doi:10.1086/147589.

Lacy, C. H., T. J. Moffett, and D. S. Evans. 1976. "UV Ceti stars - Statistical analysis of observational data." *ApJS* 30 (January): 85–96. doi:10.1086/190358.

Lam, H. A., N. Achilleos, S. Miller, J. Tennyson, L. M. Trafton, T. R. Geballe, and G. E. Ballester. 1997. "A Baseline Spectroscopic Study of the Infrared Auroras of Jupiter." *Icarus* 127 (June): 379–393. doi:10.1006/icar.1997.5698.

Law, N. M., et al. 2009. "The Palomar Transient Factory: System Overview, Performance, and First Results." *PASP* 121 (December): 1395–1408. doi:10.1086/648598. arXiv: 0906.5350 [astro-ph.IM].

Lawrence, A., et al. 2007. "The UKIRT Infrared Deep Sky Survey (UKIDSS)." *MNRAS* 379 (August): 1599–1617. doi:10.1111/j.1365-2966.2007.12040.x. eprint: astro-ph/0604426.

Lee, K.-G., E. Berger, and G. R. Knapp. 2010. "Short-term Hα Variability in M Dwarfs." *ApJ* 708 (January): 1482–1491. doi:10.1088/0004-637X/708/2/1482. arXiv: 0905.3182 [astro-ph.SR].

Leggett, S. K., T. R. Geballe, X. Fan, D. P. Schneider, J. E. Gunn, R. H. Lupton, G. R. Knapp, et al. 2000. "The Missing Link: Early Methane ("T") Dwarfs in the Sloan Digital Sky Survey." *ApJ* 536 (June): L35–L38. doi:10.1086/312728. eprint: astro-ph/0004408.

Lenz, L. F., A. Reiners, A. Seifahrt, and H. U. Käufl. 2016. "A CRIRES-search for H_3^+ emission from the hot Jupiter atmosphere of HD 209458 b." *A&A* 589, A99 (May): A99. doi:10.1051/0004-6361/201525675. arXiv: 1604.00792 [astro-ph.EP].

Leto, P., C. Trigilio, C. S. Buemi, G. Umana, A. Ingallinera, and L. Cerrigone. 2016. "3D modelling of stellar auroral radio emission." *MNRAS* 459 (June): 1159–1169. doi:10.1093/mnras/stw639. arXiv: 1603.02423 [astro-ph.SR].

Liebert, J., and A. J. Burgasser. 2007. "On the Nature of the Unique Hα-emitting T Dwarf 2MASS J12373919+6526148." *ApJ* 655 (January): 522–527. doi:10.1086/509882. eprint: astro-ph/0609793.

Liebert, J., J. D. Kirkpatrick, K. L. Cruz, I. N. Reid, A. Burgasser, C. G. Tinney, and J. E. Gizis. 2003. "A Flaring L5 Dwarf: The Nature of Hα Emission in Very Low Mass (Sub)Stellar Objects." *AJ* 125 (January): 343–347. doi:10.1086/345514. eprint: astro-ph/0210348.

Liebert, J., J. D. Kirkpatrick, I. N. Reid, and M. D. Fisher. 1999. "A 2MASS Ultracool M Dwarf Observed in a Spectacular Flare." *ApJ* 519 (July): 345–353. doi:10.1086/307349.

Linsky, J. L. 1980. "Stellar chromospheres." *ARA&A* 18:439–488. doi:10.1146/annurev.aa.18.090180.002255.

Linsky, J. L., P. L. Bornmann, K. G. Carpenter, E. K. Hege, R. F. Wing, M. S. Giampapa, and S. P. Worden. 1982. "Outer atmospheres of cool stars. XII - A survey of IUE ultraviolet emission line spectra of cool dwarf stars." *ApJ* 260 (September): 670–694. doi:10.1086/160288.

Linsky, J. L., B. E. Wood, A. Brown, M. S. Giampapa, and C. Ambruster. 1995. "Stellar Activity at the End of the Main Sequence: GHRS Observations of the M8 Ve Star VB 10." *ApJ* 455 (December): 670. doi:10.1086/176614.

Littlefair, S. P., V. S. Dhillon, T. R. Marsh, T. Shahbaz, E. L. Martín, and C. Copperwheat. 2008. "Optical variability of the ultracool dwarf TVLM 513-46546: evidence for inhomogeneous dust clouds." *MNRAS* 391 (November): L88–L92. doi:10.1111/j.1745-3933.2008.00562.x. arXiv: 0809.2193.

Liu, M. C., T. J. Dupuy, and S. K. Leggett. 2010. "Discovery of a Highly Unequal-mass Binary T Dwarf with Keck Laser Guide Star Adaptive Optics: A Coevality Test of Substellar Theoretical Models and Effective Temperatures." *ApJ* 722 (October): 311–328. doi:10.1088/0004-637X/722/1/311. arXiv: 1008.2200 [astro-ph.SR].

Lodders, K. 1999. "Alkali Element Chemistry in Cool Dwarf Atmospheres." *ApJ* 519 (July): 793–801. doi:10.1086/307387.

López-Morales, M., and I. Ribas. 2005. "GU Bootis: A New 0.6 M_{solar} Detached Eclipsing Binary." *ApJ* 631 (October): 1120–1133. doi:10.1086/432680. eprint: arXiv:astro-ph/0505001.

Lynch, C., T. Murphy, V. Ravi, G. Hobbs, K. Lo, and C. Ward. 2016. "Radio detections of southern ultracool dwarfs." *MNRAS* 457 (April): 1224–1232. doi:10.1093/mnras/stw050. arXiv: 1601.01749 [astro-ph.SR].

Lynch, C., R. L. Mutel, and M. Gudel. 2015. "Wideband Dynamic Radio Spectra of Two Ultra-cool Dwarfs." *ApJ* 802, 106 (April): 106. doi:10.1088/0004-637X/802/2/106. arXiv: 1405.3516 [astro-ph.SR].

Mace, G. N., et al. 2013. "A Study of the Diverse T Dwarf Population Revealed by WISE." *ApJS* 205, 6 (March): 6. doi:10.1088/0067-0049/205/1/6. arXiv: 1301.3913 [astro-ph.SR].

Maillard, J., and S. Miller. 2011. "The Molecular Ion H_3^+ in Emission in Planetary Atmospheres." In *Molecules in the Atmospheres of Extrasolar Planets,* edited by J. P. Beaulieu, S. Dieters, and G. Tinetti, 450:19–21. Astronomical Society of the Pacific Conference Series. December.

Manjavacas, E., B. Goldman, J. M. Alcala, M. R. Zapatero-Osorio, V. J. S. Bejar, D. Homeier, M. Bonnefoy, R. L. Smart, T. Henning, and F. Allard. 2015. "Hunting for brown dwarf binaries and testing atmospheric models with X-Shooter." *ArXiv e-prints* (September). arXiv: 1509.01714 [astro-ph.SR].

Marley, M. S., D. Saumon, and C. Goldblatt. 2010. "A Patchy Cloud Model for the L to T Dwarf Transition." *ApJ* 723 (November): L117–L121. doi:10.1088/2041-8205/723/1/L117. arXiv: 1009.6217 [astro-ph.SR].

Marley, M.S., and T.D. Robinson. 2015. "On the Cool Side: Modeling the Atmospheres of Brown Dwarfs and Giant Planets." *Annual Review of Astronomy and Astrophysics* 53 (1): 279–323. doi:10.1146/annurev-astro-082214-122522. eprint: http://dx.doi.org/10.1146/annurev-astro-082214-122522. http://dx.doi.org/10.1146/annurev-astro-082214-122522.

Massey, P., and C. Gronwall. 1990. "The Kitt Peak spectrophotometric standards - Extension to 1 micron." *ApJ* 358 (July): 344–349. doi:10.1086/168991.

Mayor, M., et al. 2003. "Setting New Standards with HARPS." *The Messenger* 114 (December): 20–24.

McLean, I. S., M. R. McGovern, A. J. Burgasser, J. D. Kirkpatrick, L. Prato, and S. S. Kim. 2003. "The NIRSPEC Brown Dwarf Spectroscopic Survey. I. Low-Resolution Near-Infrared Spectra." *ApJ* 596 (October): 561–586. doi:10.1086/377636. eprint: astro-ph/0309257.

McLean, I. S., C. C. Steidel, H. W. Epps, N. Konidaris, K. Y. Matthews, S. Adkins, T. Aliado, et al. 2012. "MOSFIRE, the multi-object spectrometer for infrared exploration at the Keck Observatory." In *Ground-based and Airborne Instrumentation for Astronomy IV,* vol. 8446, 84460J. Proc. SPIE. September. doi:10.1117/12.924794.

McLean, I. S., C. C. Steidel, H. Epps, K. Matthews, S. Adkins, N. Konidaris, B. Weber, et al. 2010. "Design and development of MOSFIRE: the multi-object spectrometer for infrared exploration at the Keck Observatory." In *Ground-based and Airborne Instrumentation for Astronomy III,* vol. 7735, Proc. SPIE. July. doi:10.1117/12.856715.

McLean, M., E. Berger, and A. Reiners. 2012. "The Radio Activity-Rotation Relation of Ultracool Dwarfs." *ApJ* 746, 23 (February): 23. doi:10.1088/0004-637X/746/1/23. arXiv: 1108.0415 [astro-ph.SR].

Melin, H., S. Miller, T. Stallard, and D. Grodent. 2005. "Non-LTE effects on H3+ emission in the jovian upper atmosphere." *Icarus* 178 (November): 97–103. doi:10.1016/j.icarus.2005.04.016.

Melin, H., S. Miller, T. Stallard, L. M. Trafton, and T. R. Geballe. 2007. "Variability in the H_3^+ emission of Saturn: Consequences for ionisation rates and temperature." *Icarus* 186 (January): 234–241. doi:10.1016/j.icarus.2006.08.014.

Metchev, S. A., A. Heinze, D. Apai, D. Flateau, J. Radigan, A. Burgasser, M. S. Marley, E. Artigau, P. Plavchan, and B. Goldman. 2015. "Weather on Other Worlds. II. Survey Results: Spots are Ubiquitous on L and T Dwarfs." *ApJ* 799, 154 (February): 154. doi:10.1088/0004-637X/799/2/154. arXiv: 1411.3051 [astro-ph.SR].

Metodieva, Y., A. Antonova, V. Golev, D. Dimitrov, D. García-Álvarez, and J. G. Doyle. 2015. "Low-resolution optical spectra of ultracool dwarfs with OSIRIS/GTC." *MNRAS* 446 (February): 3878–3884. doi:10.1093/mnras/stu2370. arXiv: 1412.2736 [astro-ph.SR].

Miller, S., R. D. Joseph, and J. Tennyson. 1990. "Infrared emissions of H3(+) in the atmosphere of Jupiter in the 2.1 and 4.0 micron region." *ApJ* 360 (September): L55–L58. doi:10.1086/185811.

Mohanty, S., and G. Basri. 2003. "Rotation and Activity in Mid-M to L Field Dwarfs." *ApJ* 583 (January): 451–472. doi:10.1086/345097. eprint: astro-ph/0201455.

Mohanty, S., G. Basri, F. Shu, F. Allard, and G. Chabrier. 2002. "Activity in Very Cool Stars: Magnetic Dissipation in Late M and L Dwarf Atmospheres." *ApJ* 571 (May): 469–486. doi:10.1086/339911. eprint: astro-ph/0201518.

Morales, J. C., J. Gallardo, I. Ribas, C. Jordi, I. Baraffe, and G. Chabrier. 2010. "The Effect of Magnetic Activity on Low-Mass Stars in Eclipsing Binaries." *ApJ* 718 (July): 502–512. doi:10.1088/0004-637X/718/1/502. arXiv: 1005.5720 [astro-ph.SR].

Morin, J., J.-F. Donati, P. Petit, X. Delfosse, T. Forveille, and M. M. Jardine. 2010. "Large-scale magnetic topologies of late M dwarfs." *MNRAS* 407 (October): 2269–2286. doi:10.1111/j.1365-2966.2010.17101.x. arXiv: 1005.5552 [astro-ph.SR].

Morin, J., E. Dormy, M. Schrinner, and J.-F. Donati. 2011. "Weak- and strong-field dynamos: from the Earth to the stars." *MNRAS* 418 (November): L133–L137. doi:10.1111/j.1745-3933.2011.01159.x. arXiv: 1106.4263 [astro-ph.SR].

Morley, C. V., M. S. Marley, J. J. Fortney, and R. Lupu. 2014. "Spectral Variability from the Patchy Atmospheres of T and Y Dwarfs." *ApJ* 789, L14 (July): L14. doi:10.1088/2041-8205/789/1/L14. arXiv: 1406.0863 [astro-ph.SR].

Morton, T. D., and J. N. Winn. 2014. "Obliquities of Kepler Stars: Comparison of Single- and Multiple-transit Systems." *ApJ* 796, 47 (November): 47. doi:10.1088/0004-637X/796/1/47. arXiv: 1408.6606 [astro-ph.EP].

Muirhead, P. S., et al. 2012a. "Characterizing the Cool KOIs. III. KOI 961: A Small Star with Large Proper Motion and Three Small Planets." *ApJ* 747, 144 (March): 144. doi:10.1088/0004-637X/747/2/144. arXiv: 1201.2189 [astro-ph.SR].

Muirhead, P. S., K. Hamren, E. Schlawin, B. Rojas-Ayala, K. R. Covey, and J. P. Lloyd. 2012b. "Characterizing the Cool Kepler Objects of Interests. New Effective Temperatures, Metallicities, Masses, and Radii of Low-mass Kepler Planet-candidate Host Stars." *ApJ* 750, L37 (May): L37. doi:10.1088/2041-8205/750/2/L37. arXiv: 1109.1819 [astro-ph.SR].

Nakajima, T., B. R. Oppenheimer, S. R. Kulkarni, D. A. Golimowski, K. Matthews, and S. T. Durrance. 1995. "Discovery of a cool brown dwarf." *Nature* 378 (November): 463–465. doi:10.1038/378463a0.

Neale, L., S. Miller, and J. Tennyson. 1996. "Spectroscopic Properties of the H 3 + Molecule: A New Calculated Line List." *ApJ* 464 (June): 516. doi:10.1086/177341.

Neves, V., X. Bonfils, N. C. Santos, X. Delfosse, T. Forveille, F. Allard, C. Natário, C. S. Fernandes, and S. Udry. 2012. "Metallicity of M dwarfs. II. A comparative study of photometric metallicity scales." *A&A* 538, A25 (February): A25. doi:10.1051/0004-6361/201118115. arXiv: 1110.2694 [astro-ph.SR].

Newman, J. A., et al. 2013. "The DEEP2 Galaxy Redshift Survey: Design, Observations, Data Reduction, and Redshifts." *ApJS* 208, 5 (September): 5. doi:10.1088/0067-0049/208/1/5. arXiv: 1203.3192.

Nichols, J. D., M. R. Burleigh, S. L. Casewell, S. W. H. Cowley, G. A. Wynn, J. T. Clarke, and A. A. West. 2012. "Origin of Electron Cyclotron Maser Induced Radio Emissions at Ultracool Dwarfs: Magnetosphere-Ionosphere Coupling Currents." *ApJ* 760, 59 (November): 59. doi:10.1088/0004-637X/760/1/59. arXiv: 1210.1864 [astro-ph.SR].

Oke, J. B., J. G. Cohen, M. Carr, J. Cromer, A. Dingizian, F. H. Harris, S. Labrecque, et al. 1995. "The Keck Low-Resolution Imaging Spectrometer." *PASP* 107 (April): 375. doi:10.1086/133562.

Önehag, A., U. Heiter, B. Gustafsson, N. Piskunov, B. Plez, and A. Reiners. 2012. "M-dwarf metallicities. A high-resolution spectroscopic study in the near infrared." *A&A* 542, A33 (June): A33. doi:10.1051/0004-6361/201118101. arXiv: 1112.0141 [astro-ph.SR].

Oppenheimer, B. R., S. R. Kulkarni, K. Matthews, and T. Nakajima. 1995. "Infrared Spectrum of the Cool Brown Dwarf Gl 229B." *Science* 270 (December): 1478–1479. doi:10.1126/science.270.5241.1478.

Ossendrijver, M. 2003. "The solar dynamo." *A&A Rev.* 11:287–367. doi:10.1007/s00159-003-0019-3.

Osten, R. A., C. Melis, B. Stelzer, K. W. Bannister, J. Radigan, A. J. Burgasser, A. Wolszczan, and K. L. Luhman. 2015. "The Deepest Constraints on Radio and X-Ray Magnetic Activity in Ultracool Dwarfs from WISE J104915.57-531906.1." *ApJ* 805, L3 (May): L3. doi:10.1088/2041-8205/805/1/L3. arXiv: 1504.06514 [astro-ph.SR].

Patil, Anand, David Huard, and Christopher J. Fonnesbeck. 2010. "PyMC: Bayesian Stochastic Modelling in Python." *Journal of Statistical Software* 35, no. 4 (July 16): 1–81. ISSN: 1548-7660. http://www.jstatsoft.org/v35/i04.

Perry, J. J., Y. H. Kim, J. L. Fox, and H. S. Porter. 1999. "Chemistry of the Jovian auroral ionosphere." *J. Geophys. Res.* 104 (July): 16541–16566. doi:10.1029/1999JE900022.

Perryman, M. A. C., and others. 1997. "The HIPPARCOS Catalogue." *A&A* 323 (July): L49–L52.

Pineda, J. S., G. Hallinan, J. D. Kirkpatrick, G. Cotter, M. M. Kao, and K. Mooley. 2016. "A Survey for Hα Emission from Late L Dwarfs and T Dwarfs." *ApJ* 826, 73 (July): 73. doi:10.3847/0004-637X/826/1/73. arXiv: 1604.03941 [astro-ph.SR].

Pineda, J. S., A. A. West, J. J. Bochanski, and A. J. Burgasser. 2013. "The Sloan Digital Sky Survey Data Release 7 Spectroscopic M Dwarf Catalog. III. The Spatial Dependence of Magnetic Activity in the Galaxy." *AJ* 146, 50 (September): 50. doi:10.1088/0004-6256/146/3/50. arXiv: 1306.6330 [astro-ph.SR].

Pizzolato, N., A. Maggio, G. Micela, S. Sciortino, and P. Ventura. 2003. "The stellar activity-rotation relationship revisited: Dependence of saturated and non-saturated X-ray emission regimes on stellar mass for late-type dwarfs." *A&A* 397 (January): 147–157. doi:10.1051/0004-6361:20021560.

Prato, L., G. N. Mace, E. L. Rice, I. S. McLean, J. D. Kirkpatrick, A. J. Burgasser, and S. S. Kim. 2015. "Radial Velocity Variability of Field Brown Dwarfs." *ApJ* 808, 12 (July): 12. doi:10.1088/0004-637X/808/1/12. arXiv: 1506.02771 [astro-ph.SR].

R Core Team. 2016. *R: A Language and Environment for Statistical Computing*. Vienna, Austria: R Foundation for Statistical Computing. https://www.R-project.org/.

Radigan, J., R. Jayawardhana, D. Lafreniere, E. Artigau, M. Marley, and D. Saumon. 2012. "Large-amplitude Variations of an L/T Transition Brown Dwarf: Multi-wavelength Observations of Patchy, High-contrast Cloud Features." *ApJ* 750, 105 (May): 105. doi:10.1088/0004-637X/750/2/105. arXiv: 1201.3403 [astro-ph.SR].

Radigan, J., D. Lafreniere, R. Jayawardhana, and E. Artigau. 2014. "Strong Brightness Variations Signal Cloudy-to-clear Transition of Brown Dwarfs." *ApJ* 793, 75 (October): 75. doi:10.1088/0004-637X/793/2/75. arXiv: 1404.3247 [astro-ph.SR].

Rayner, J. T., M. C. Cushing, and W. D. Vacca. 2009. "The Infrared Telescope Facility (IRTF) Spectral Library: Cool Stars." *ApJS* 185 (December): 289–432. doi:10.1088/0067-0049/185/2/289. arXiv: 0909.0818 [astro-ph.SR].

Rebolo, R., M. R. Zapatero Osorio, and E. L. Martín. 1995. "Discovery of a brown dwarf in the Pleiades star cluster." *Nature* 377 (September): 129–131. doi:10.1038/377129a0.

Reid, I. N., A. J. Burgasser, K. L. Cruz, J. D. Kirkpatrick, and J. E. Gizis. 2001. "Near-Infrared Spectral Classification of Late M and L Dwarfs." *AJ* 121 (March): 1710–1721. doi:10.1086/319418. eprint: astro-ph/0012275.

Reid, I. N., K. L. Cruz, S. P. Laurie, J. Liebert, C. C. Dahn, H. C. Harris, H. H. Guetter, et al. 2003. "Meeting the Cool Neighbors. IV. 2MASS 1835+32, a Newly Discovered M8.5 Dwarf within 6 Parsecs of the Sun." *AJ* 125 (January): 354–358. doi:10.1086/344946.

Reid, I. N., S. L. Hawley, and J. E. Gizis. 1995. "The Palomar/MSU Nearby-Star Spectroscopic Survey. I. The Northern M Dwarfs -Bandstrengths and Kinematics." *AJ* 110 (October): 1838. doi:10.1086/117655.

Reid, I. N., J. D. Kirkpatrick, J. E. Gizis, C. C. Dahn, D. G. Monet, R. J. Williams, J. Liebert, and A. J. Burgasser. 2000. "Four Nearby L Dwarfs." *AJ* 119 (January): 369–377. doi:10.1086/301177. eprint: astro-ph/9909336.

Reiners, A., and G. Basri. 2007. "The First Direct Measurements of Surface Magnetic Fields on Very Low Mass Stars." *ApJ* 656 (February): 1121–1135. doi:10.1086/510304. eprint: astro-ph/0610365.

———. 2008. "Chromospheric Activity, Rotation, and Rotational Braking in M and L Dwarfs." *ApJ* 684 (September): 1390–1403. doi:10.1086/590073. arXiv: 0805.1059.

———. 2010. "A Volume-Limited Sample of 63 M7-M9.5 Dwarfs. II. Activity, Magnetism, and the Fade of the Rotation-Dominated Dynamo." *ApJ* 710 (February): 924–935. doi:10.1088/0004-637X/710/2/924. arXiv: 0912.4259 [astro-ph.SR].

Reiners, A., and S. Mohanty. 2012. "Radius-dependent Angular Momentum Evolution in Low-mass Stars. I." *ApJ* 746, 43 (February): 43. doi:10.1088/0004-637X/746/1/43. arXiv: 1111.7071 [astro-ph.SR].

Ribas, I. 2006. "Masses and Radii of Low-Mass Stars: Theory Versus Observations." *Ap&SS* 304 (August): 89–92. doi:10.1007/s10509-006-9081-4. eprint: arXiv:astro-ph/0511431.

Rivera, E. J., J. J. Lissauer, R. P. Butler, G. W. Marcy, S. S. Vogt, D. A. Fischer, T. M. Brown, G. Laughlin, and G. W. Henry. 2005. "A ~7.5 $M_\oplus$ Planet Orbiting the Nearby Star, GJ 876." *ApJ* 634 (November): 625–640. doi:10.1086/491669. eprint: arXiv:astro-ph/0510508.

Robinson, T. D., and M. S. Marley. 2014. "Temperature Fluctuations as a Source of Brown Dwarf Variability." *ApJ* 785, 158 (April): 158. doi:10.1088/0004-637X/785/2/158. arXiv: 1403.2438 [astro-ph.SR].

Rockosi, C., et al. 2010. "The low-resolution imaging spectrograph red channel CCD upgrade: fully depleted, high-resistivity CCDs for Keck." In *Society of Photo-Optical Instrumentation Engineers (SPIE) Conference Series,* vol. 7735, Society of Photo-Optical Instrumentation Engineers (SPIE) Conference Series. July. doi:10.1117/12.856818.

Rodriguez-Barrera, M. I., C. Helling, C. R. Stark, and A. M. Rice. 2015. "Reference study to characterize plasma and magnetic properties of ultracool atmospheres." *MNRAS* 454 (December): 3977–3995. doi:10.1093/mnras/stv2090. arXiv: 1509.02769 [astro-ph.EP].

Rojas-Ayala, B., K. R. Covey, P. S. Muirhead, and J. P. Lloyd. 2010. "Metal-rich M-Dwarf Planet Hosts: Metallicities with K-band Spectra." *ApJ* 720 (September): L113–L118. doi:10.1088/2041-8205/720/1/L113. arXiv: 1007.4593 [astro-ph.SR].

Rojas-Ayala, B., K. R. Covey, P. S. Muirhead, and J. P. Lloyd. 2012. "Metallicity and Temperature Indicators in M Dwarf K-band Spectra: Testing New and Updated Calibrations with Observations of 133 Solar Neighborhood M Dwarfs." *ApJ* 748, 93 (April): 93. doi:10.1088/0004-637X/748/2/93. arXiv: 1112.4567 [astro-ph.SR].

Route, M., and A. Wolszczan. 2012. "The Arecibo Detection of the Coolest Radio-flaring Brown Dwarf." *ApJ* 747, L22 (March): L22. doi:10.1088/2041-8205/747/2/L22. arXiv: 1202.1287 [astro-ph.SR].

———. 2013. "The 5 GHz Arecibo Search for Radio Flares from Ultracool Dwarfs." *ApJ* 773, 18 (August): 18. doi:10.1088/0004-637X/773/1/18. arXiv: 1306.1152 [astro-ph.SR].

———. 2016a. "Radio Flaring from the T6 Dwarf WISEPC J112254.73+255021.5 with a Possible Ultra-short Periodicity." *ApJ* 821, L21 (April): L21. doi:10.3847/2041-8205/821/2/L21. arXiv: 1604.04543 [astro-ph.SR].

———. 2016b. "The Second Arecibo Search for 5 GHz Radio Flares from Ultracool Dwarfs." *ArXiv e-prints* (August). arXiv: 1608.02480 [astro-ph.SR].

Saur, J., F. M. Neubauer, J. E. P. Connerney, P. Zarka, and M. G. Kivelson. 2004. "Plasma interaction of Io with its plasma torus." In *Jupiter. The Planet, Satellites and Magnetosphere,* edited by F. Bagenal, T. E. Dowling, and W. B. McKinnon, 537–560.

Schlaufman, K. C., and G. Laughlin. 2010. "A physically-motivated photometric calibration of M dwarf metallicity." *A&A* 519, A105 (September): A105. doi:10.1051/0004-6361/201015016. arXiv: 1006.2850 [astro-ph.EP].

Schmidt, S. J., K. L. Cruz, B. J. Bongiorno, J. Liebert, and I. N. Reid. 2007. "Activity and Kinematics of Ultracool Dwarfs, Including an Amazing Flare Observation." *AJ* 133 (May): 2258–2273. doi:10.1086/512158. eprint: astro-ph/0701055.

Schmidt, S. J., S. L. Hawley, A. A. West, J. J. Bochanski, J. R. A. Davenport, J. Ge, and D. P. Schneider. 2015. "BOSS Ultracool Dwarfs. I. Colors and Magnetic Activity of M and L Dwarfs." *AJ* 149, 158 (May): 158. doi:10.1088/0004-6256/149/5/158. arXiv: 1410.0014 [astro-ph.SR].

Schmidt, S. J., A. A. West, J. J. Bochanski, S. L. Hawley, and C. Kielty. 2014. "Calibrating Ultracool Dwarfs: Optical Template Spectra, Bolometric Corrections, and χ Values." *PASP* 126 (July): 642–659. doi:10.1086/677403. arXiv: 1406.1228 [astro-ph.SR].

Schrijver, C. J. 2009. "On a Transition from Solar-Like Coronae to Rotation-Dominated Jovian-Like Magnetospheres in Ultracool Main-Sequence Stars." *ApJ* 699 (July): L148–L152. doi:10.1088/0004-637X/699/2/L148. arXiv: 0905.1354 [astro-ph.SR].

Schweitzer, A., J. E. Gizis, P. H. Hauschildt, F. Allard, and I. N. Reid. 2001. "Analysis of Keck HIRES Spectra of Early L-Type Dwarfs." *ApJ* 555 (July): 368–379. doi:10.1086/321486. eprint: astro-ph/0103402.

Shkolnik, E. L., and T. S. Barman. 2014. "HAZMAT. I. The Evolution of Far-UV and Near-UV Emission from Early M Stars." *AJ* 148, 64 (October): 64. doi:10.1088/0004-6256/148/4/64. arXiv: 1407.1344 [astro-ph.SR].

Shkolnik, E., E. Gaidos, and N. Moskovitz. 2006. "No Detectable H_3^+ Emission from the Atmospheres of Hot Jupiters." *AJ* 132 (September): 1267–1274. doi:10.1086/506476. eprint: astro-ph/0605708.

Skrutskie, M. F., et al. 2006. "The Two Micron All Sky Survey (2MASS)." *AJ* 131 (February): 1163–1183. doi:10.1086/498708.

Skumanich, A. 1972. "Time Scales for CA II Emission Decay, Rotational Braking, and Lithium Depletion." *ApJ* 171 (February): 565. doi:10.1086/151310.

Solanki, S. K., B. Inhester, and M. Schüssler. 2006. "The solar magnetic field." *Reports on Progress in Physics* 69 (March): 563–668. doi:10.1088/0034-4885/69/3/R02. arXiv: 1008.0771 [astro-ph.SR].

Stelzer, B., J. Alcalá, K. Biazzo, B. Ercolano, I. Crespo-Chacón, J. López-Santiago, R. Martínez-Arnáiz, et al. 2012. "The ultracool dwarf DENIS-P J104814.7-395606. Chromospheres and coronae at the low-mass end of the main-sequence." *A&A* 537, A94 (January): A94. doi:10.1051/0004-6361/201118097. arXiv: 1111.6880 [astro-ph.SR].

Stephens, D. C., S. K. Leggett, M. C. Cushing, M. S. Marley, D. Saumon, T. R. Geballe, D. A. Golimowski, X. Fan, and K. S. Noll. 2009. "The 0.8-14.5 μm Spectra of Mid-L to Mid-T Dwarfs: Diagnostics of Effective Temperature, Grain Sedimentation, Gas Transport, and Surface Gravity." *ApJ* 702 (September): 154–170. doi:10.1088/0004-637X/702/1/154. arXiv: 0906.2991 [astro-ph.SR].

Stevenson, D. J. 1991. "The search for brown dwarfs." *ARA&A* 29:163–193. doi:10.1146/annurev.aa.29.090191.001115.

Strauss, M. A., et al. 1999. "The Discovery of a Field Methane Dwarf from Sloan Digital Sky Survey Commissioning Data." *ApJ* 522 (September): L61–L64. doi:10.1086/312218. eprint: astro-ph/9905391.

Swift, J. J., J. A. Johnson, T. D. Morton, J. R. Crepp, B. T. Montet, D. C. Fabrycky, and P. S. Muirhead. 2013. "Characterizing the Cool KOIs IV: Kepler-32 as a prototype for the formation of compact planetary systems throughout the Galaxy." *ArXiv e-prints* (December). arXiv: 1301.0023 [astro-ph.EP].

Tanner, A., R. White, J. Bailey, C. Blake, G. Blake, K. Cruz, A. J. Burgasser, and A. Kraus. 2012. "Keck NIRSPEC Radial Velocity Observations of Late-M Dwarfs." *ApJS* 203, 10 (November): 10. doi:10.1088/0067-0049/203/1/10. arXiv: 1209.1772 [astro-ph.SR].

Tao, C., S. V. Badman, and M. Fujimoto. 2011. "UV and IR auroral emission model for the outer planets: Jupiter and Saturn comparison." *Icarus* 213 (June): 581–592. doi:10.1016/j.icarus.2011.04.001.

Tao, C., S. V. Badman, T. Uno, and M. Fujimoto. 2012. "On the feasibility of characterizing jovian auroral electrons via H3+ infrared line-emission analysis." *Icarus* 221 (September): 236–247. doi:10.1016/j.icarus.2012.07.015.

Terrien, R. C., S. Mahadevan, C. F. Bender, R. Deshpande, L. W. Ramsey, and J. J. Bochanski. 2012. "An H-band Spectroscopic Metallicity Calibration for M Dwarfs." *ApJ* 747, L38 (March): L38. doi:10.1088/2041-8205/747/2/L38. arXiv: 1202.1800 [astro-ph.SR].

Testa, P., S. H. Saar, and J. J. Drake. 2015. "Stellar activity and coronal heating: an overview of recent results." *Philosophical Transactions of the Royal Society of London Series A* 373 (April): 20140259–20140259. doi:10.1098/rsta.2014.0259. arXiv: 1502.07401 [astro-ph.SR].

Thorstensen, J. R., and J. D. Kirkpatrick. 2003. "Serendipitous Discovery and Parallax of a Nearby L Dwarf." *PASP* 115 (October): 1207–1210. doi:10.1086/378080. eprint: astro-ph/0307295.

Tinney, C. G., A. J. Burgasser, J. D. Kirkpatrick, and M. W. McElwain. 2005. "The 2MASS Wide-Field T Dwarf Search. IV. Hunting Out T Dwarfs with Methane Imaging." *AJ* 130 (November): 2326–2346. doi:10.1086/491734. eprint: astro-ph/0508150.

Tinney, C. G., J. R. Mould, and I. N. Reid. 1993. "The faintest stars - Infrared photometry, spectra, and bolometric magnitude." *AJ* 105 (March): 1045–1059. doi:10.1086/116492.

Tonry, J., and M. Davis. 1979. "A survey of galaxy redshifts. I - Data reduction techniques." *AJ* 84 (October): 1511–1525. doi:10.1086/112569.

Treumann, R. A. 2006. "The electron-cyclotron maser for astrophysical application." *A&A Rev.* 13 (August): 229–315. doi:10.1007/s00159-006-0001-y.

Udalski, A., Y. K. Jung, C. Han, A. Gould, S. Kozłowski, J. Skowron, R. Poleski, et al. 2015. "A Venus-mass Planet Orbiting a Brown Dwarf: A Missing Link between Planets and Moons." *ApJ* 812, 47 (October): 47. doi:10.1088/0004-637X/812/1/47. arXiv: 1507.02388 [astro-ph.EP].

Vasavada, A. R., A. H. Bouchez, A. P. Ingersoll, B. Little, C. D. Anger, and Galileo SSI Team. 1999. "Jupiter's visible aurora and Io footprint." *J. Geophys. Res.* 104:27133–27142. doi:10.1029/1999JE001055.

Vernazza, J. E., E. H. Avrett, and R. Loeser. 1981. "Structure of the solar chromosphere. III - Models of the EUV brightness components of the quiet-sun." *ApJS* 45 (April): 635–725. doi:10.1086/190731.

Voges, W., B. Aschenbach, T. Boller, H. Bräuninger, U. Briel, W. Burkert, K. Dennerl, et al. 1999. "The ROSAT all-sky survey bright source catalogue." *A&A* 349 (September): 389–405. eprint: arXiv:astro-ph/9909315.

Vogt, S. S., S. L. Allen, B. C. Bigelow, L. Bresee, B. Brown, T. Cantrall, A. Conrad, et al. 1994. "HIRES: the high-resolution echelle spectrometer on the Keck 10-m Telescope." In *Instrumentation in Astronomy VIII,* edited by D. L. Crawford and E. R. Craine, 2198:362. Proc. SPIE. June.

Vrba, F. J., A. A. Henden, C. B. Luginbuhl, H. H. Guetter, J. A. Munn, B. Canzian, A. J. Burgasser, et al. 2004. "Preliminary Parallaxes of 40 L and T Dwarfs from the US Naval Observatory Infrared Astrometry Program." *AJ* 127 (May): 2948–2968. doi:10.1086/383554. eprint: astro-ph/0402272.

Walkowicz, L. M., C. M. Johns-Krull, and S. L. Hawley. 2008. "Characterizing the Near-UV Environment of M Dwarfs." *ApJ* 677 (April): 593–606. doi:10.1086/526421. arXiv: 0711.1861.

Weinberger, A. J., A. P. Boss, S. A. Keiser, G. Anglada-Escudé, I. B. Thompson, and G. Burley. 2016. "Trigonometric Parallaxes and Proper Motions of 134 Southern Late M, L, and T Dwarfs from the Carnegie Astrometric Planet Search Program." *AJ* 152, 24 (July): 24. doi:10.3847/0004-6256/152/1/24. arXiv: 1604.05611 [astro-ph.SR].

West, A. A., S. L. Hawley, J. J. Bochanski, K. R. Covey, I. N. Reid, S. Dhital, E. J. Hilton, and M. Masuda. 2008. "Constraining the Age-Activity Relation for Cool Stars: The Sloan Digital Sky Survey Data Release 5 Low-Mass Star Spectroscopic Sample." *AJ* 135 (March): 785–795. doi:10.1088/0004-6256/135/3/785. arXiv: 0712.1590.

West, A. A., D. P. Morgan, J. J. Bochanski, J. M. Andersen, K. J. Bell, A. F. Kowalski, J. R. A. Davenport, et al. 2011. "The Sloan Digital Sky Survey Data Release 7 Spectroscopic M Dwarf Catalog. I. Data." *AJ* 141, 97 (March): 97. doi:10.1088/0004-6256/141/3/97. arXiv: 1101.1082 [astro-ph.SR].

West, A. A., K. L. Weisenburger, J. Irwin, Z. K. Berta-Thompson, D. Charbonneau, J. Dittmann, and J. S. Pineda. 2015. "An Activity-Rotation Relationship and Kinematic Analysis of Nearby Mid-to-Late-Type M Dwarfs." *ApJ* 812, 3 (October): 3. doi:10.1088/0004-637X/812/1/3. arXiv: 1509.01590 [astro-ph.SR].

Williams, P. K. G., and E. Berger. 2015. "The Rotation Period and Magnetic Field of the T Dwarf 2MASSI J1047539+212423 Measured from Periodic Radio Bursts." *ApJ* 808, 189 (August): 189. doi:10.1088/0004-637X/808/2/189. arXiv: 1502.06610 [astro-ph.SR].

Williams, P. K. G., S. L. Casewell, C. R. Stark, S. P. Littlefair, C. Helling, and E. Berger. 2015. "The First Millimeter Detection of a Non-Accreting Ultracool Dwarf." *ApJ* 815, 64 (December): 64. doi:10.1088/0004-637X/815/1/64. arXiv: 1511.05559 [astro-ph.SR].

Williams, P. K. G., B. A. Cook, and E. Berger. 2014. "Trends in Ultracool Dwarf Magnetism. I. X-Ray Suppression and Radio Enhancement." *ApJ* 785, 9 (April): 9. doi:10.1088/0004-637X/785/1/9. arXiv: 1310.6757 [astro-ph.SR].

Williams, P. K. G., J. E. Gizis, and E. Berger. 2016. "Variable and polarized radio emission from the T6 brown dwarf WISEP J112254.73+255021.5." *ArXiv e-prints* (August). arXiv: 1608.04390 [astro-ph.SR].

Winn, J. N. 2010. "Exoplanet Transits and Occultations." In *Exoplanets,* edited by S. Seager, 55–77. December.

Wolszczan, A., and M. Route. 2014. "Timing Analysis of the Periodic Radio and Optical Brightness Variations of the Ultracool Dwarf, TVLM 513-46546." *ApJ* 788, 23 (June): 23. doi:10.1088/0004-637X/788/1/23. arXiv: 1404.4682 [astro-ph.SR].

Woolf, V. M., and G. Wallerstein. 2005. "Metallicity measurements using atomic lines in M and K dwarf stars." *MNRAS* 356 (January): 963–968. doi:10.1111/j.1365-2966.2004.08515.x. eprint: arXiv:astro-ph/0410452.

Wright, E. L., et al. 2010. "The Wide-field Infrared Survey Explorer (WISE): Mission Description and Initial On-orbit Performance." *AJ* 140, 1868 (December): 1868–1881. doi:10.1088/0004-6256/140/6/1868. arXiv: 1008.0031 [astro-ph.IM].

Wu, C. S., and L. C. Lee. 1979. "A theory of the terrestrial kilometric radiation." *ApJ* 230 (June): 621–626. doi:10.1086/157120.

Yadav, R. K., U. R. Christensen, J. Morin, T. Gastine, A. Reiners, K. Poppenhaeger, and S. J. Wolk. 2015. "Explaining the Coexistence of Large-scale and Small-scale Magnetic Fields in Fully Convective Stars." *ApJ* 813, L31 (November): L31. doi:10.1088/2041-8205/813/2/L31. arXiv: 1510.05541 [astro-ph.SR].

York, D. G., et al. 2000. "The Sloan Digital Sky Survey: Technical Summary." *AJ* 120 (September): 1579–1587. doi:10.1086/301513. eprint: astro-ph/0006396.

Yu, S., G. Hallinan, J. G. Doyle, A. L. MacKinnon, A. Antonova, A. Kuznetsov, A. Golden, and Z. H. Zhang. 2011. "Modelling the radio pulses of an ultracool dwarf." *A&A* 525, A39 (January): A39. doi:10.1051/0004-6361/201015580. arXiv: 1009.1548 [astro-ph.SR].

Zapatero Osorio, M. R., E. L. Martin, H. Bouy, R. Tata, R. Deshpande, and R. J. Wainscoat. 2006. "Spectroscopic Rotational Velocities of Brown Dwarfs." *ApJ* 647 (August): 1405–1412. doi:10.1086/505484. eprint: astro-ph/0603194.

Zarka, P. 1998. "Auroral radio emissions at the outer planets: Observations and theories." *J. Geophys. Res.* 103 (September): 20159–20194. doi:10.1029/98JE01323.

Zarka, P. 2000. “Radio Emissions from the Planets and their Moons.” *Washington DC American Geophysical Union Geophysical Monograph Series* 119:167–178.

———. 2007. “Plasma interactions of exoplanets with their parent star and associated radio emissions.” *Planet. Space Sci.* 55 (April): 598–617. doi:10.1016/j.pss.2006.05.045.

Zhang, M., and B. C. Low. 2005. “The Hydromagnetic Nature of Solar Coronal Mass Ejections.” *ARA&A* 43 (September): 103–137. doi:10.1146/annurev.astro.43.072103.150602.

Appendix A

USING HIGH-RESOLUTION OPTICAL SPECTRA TO MEASURE INTRINSIC PROPERTIES OF LOW-MASS STARS: NEW PROPERTIES FOR KOI-314 AND GJ 3470

Pineda, J. S., M. Bottom, and J. A. Johnson. 2013. "Using High-resolution Optical Spectra to Measure Intrinsic Properties of Low-mass Stars: New Properties for KOI-314 and GJ 3470." *ApJ* 767, 28 (April): 28. doi:10.1088/0004-637X/767/1/28. arXiv: 1302.6231 [astro-ph.SR].

We construct high signal-to-noise "template" spectra by co-adding hundreds of spectra of nearby dwarfs spanning K7 to M4, taken with Keck/HIRES as part of the California Planet Search. We identify several spectral regions in the visible (370 - 800 nm) that are sensitive to the stellar luminosity and metallicity. We use these regions to develop a spectral calibration method to measure the mass, metallicity, and distance of low-mass stars, without the requirement of geometric parallaxes. Testing our method on a sample of nearby M dwarfs we show that we can reproduce stellar masses to about 8 - 10%, metallicity to $\sim$ 0.15 dex and distance to 11%. We were able to make use of HIRES spectra obtained as part of the radial velocity monitoring of the star KOI-314 to derive a new mass estimate of $0.57 \pm 0.05\ M_{\odot}$, a radius of $0.54 \pm 0.05\ R_{\odot}$, a metallicity, [Fe/H], of -0.28 ± 0.10 and a distance of 66.5 ± 7.3 pc. Using HARPS archival data and combining our spectral method with constraints from transit observations, we are also able to derive the stellar properties of GJ 3470, a transiting planet hosting M dwarf. We estimate a mass of 0.53 ± 0.05 $M_{\odot}$, a radius of $0.50 \pm 0.05\ R_{\odot}$, a metallicity, [Fe/H], of 0.12 ± 0.12 and a distance of $29.9 \pm^{3.7}_{3.4}$ pc.

A.1 Introduction

M-type dwarf stars are poorly understood compared to higher-mass FGK stars because of the difficulty in modeling both their atmospheres and interior structures (Hauschildt, Allard, and Baron 1999; Chabrier and Baraffe 2000). The cool atmospheres of these stars contain many molecular species such as VO and TiO, which dominate both the line and continuum opacity in their photospheres (Kirkpatrick, Henry, and McCarthy 1991). Due to the millions of molecular transitions, many of

the opacity sources have yet to be accounted for, making it difficult to synthesize M-dwarf spectra. Modeling has also proven challenging in this mass regime because convection plays an important role in the structure of the star (Baraffe et al. 1998; Ribas 2006; Morales et al. 2010). Much of the input physics for low-mass stars remains approximate, and consequently, the physical properties of M dwarfs outside of binary systems are difficult to measure (for example studies of binaries see López-Morales and Ribas 2005; Coughlin et al. 2011).

Despite these challenges, there have been many attempts to discern the intrinsic properties of isolated M dwarfs. These efforts have focused on using observational properties to either aid the theoretical treatments or to develop empirical calibrations based on stars of known physical properties. Delfosse et al. (2000) demonstrated a tight relation between absolute magnitudes in the infrared passbands (J, H, and K_s) and stellar mass as determined from binary systems. As the metallicity of these stars increases, their colors redden and the bolometric luminosity decreases. These effects balance in the infrared to produce relatively tight mass-luminosity relations.

Delfosse et al. (2000) also suggested that the large scatter in the color-magnitude diagram, $(V - K_s) - M_{K_s}$, was due to this same effect. Bonfils et al. (2005a) took advantage of this sensitivity to metallicity to develop a photometric calibration based on wide binaries with an M-dwarf secondary and an FGK primary of known [Fe/H]. The Bonfils et al. (2005a) photometric calibration has since been revised using improved V-band photometry (Johnson and Apps 2009, Neves et al. 2012) and by using a physical model based guide (Schlaufman and Laughlin 2010). Schlaufman and Laughlin (2010) and Neves et al. (2012) parameterize the metallicity as a function of $\Delta(V - K_s)$, which measures how much a given star deviates from the main sequence. These efforts represent significant progress in determining the intrinsic properties of M dwarfs; however they require precise photometry and a parallax measurement. Although these requirements are met for nearby M dwarfs ($d \lesssim 15$ pc), the lack of parallaxes for fainter, more distant stars severely limits our knowledge of M dwarfs beyond the Solar neighborhood.

Additionally, spectral synthesis has been used to measure M-dwarf metallicities (Woolf and Wallerstein 2005; Bean et al. 2006; Önehag et al. 2012). For higher-mass stars, spectral line comparisons based on equivalent width measurements can be used to compute abundances. However, the line blanketing in low-mass stars makes this extremely difficult, as individual lines blend and completely dominate any thermal continuum . Bean et al. (2006) applied atmospheric models to binary

systems composed of an FGK primary and an M-dwarf secondary. Assuming a co-evolutionary system, the metallicity of the primary can be determined accurately and used to calibrate the modeling of M-dwarf spectra. However, Bean et al. (2006) were off by $\sim$ 0.3 dex compared to later photometric calibrations, likely due to deficiencies in the low-mass atmospheric models. Woolf and Wallerstein (2005) were successful, but only because they used extremely metal-poor M dwarfs with minimal molecular line blanketing. More recently, Önehag et al. (2012) matched synthetic spectra to their high-resolution J-band spectra to measure metallicities to within 0.09 dex of the best photometric calibrations.

Instead of relying on atmospheric models, recent, more accurate methods have made use of observation-based calibrations. Rojas-Ayala et al. (2010) used moderate-resolution infrared spectra to develop metallicity indicators based on Ca I and Na I features in the K-band. Similarly, Terrien et al. (2012) used Ca I and K I features in the H-band to measure metallicity. These near-IR spectroscopic calibrations agree well with current photometric calibrations (Rojas-Ayala et al. 2012; Terrien et al. 2012).

Accurately measuring the properties of low-mass stars has gained renewed urgency because of the discovery of a multitude of planets around M dwarfs (Butler et al. 2004; Rivera et al. 2005; Bonfils et al. 2005b). There are also many M dwarfs among the hosts of planet candidates discovered by the *Kepler* Mission (Borucki 2011; Batalha 2012 ; Muirhead et al. 2012b). Additionally, these stars may host a multitude of terrestrial planets (Muirhead 2012a; Buchhave 2012; Swift et al. 2013). For radial velocity and transit detected planets, determining the physical properties of the planets requires an accurate measurement of the physical properties of their host stars.

In this contribution we develop a method to measure the physical properties of low-mass stars using spectroscopic indices from high-resolution optical spectra. Specifically, our technique provides estimates of the absolute NIR magnitudes (M_J, M_H, M_K), distances d, and $\Delta(V - K_s)$ for M dwarfs without parallaxes. Using known observational calibrations these quantities can be converted to estimate both mass and metallicity (Delfosse et al. 2000; Schlaufman and Laughlin 2010; Neves et al. 2012). We create a library of high signal-to-noise, high-resolution "template" low-mass dwarf spectra with known photometric properties to develop calibration curves based on the strength of various absorption features. By measuring the strength of these features in the spectrum of a star with unknown properties and

using the calibration curves, the photometric properties of the low-mass star can be estimated which in turn can be used to estimate the star's physical properties. In Section 2, we describe the data sample used to develop our library. In Section 3, we cover our analysis methods to construct and develop our calibration curves. In Section 4, we apply our methods to a distant M-dwarf listed among the host stars containing *Kepler* exoplanet candidates and another star with a recently discovered transiting neptune-mass planet. Lastly, in Section 5, we discuss the utility of our methods.

A.2 Data

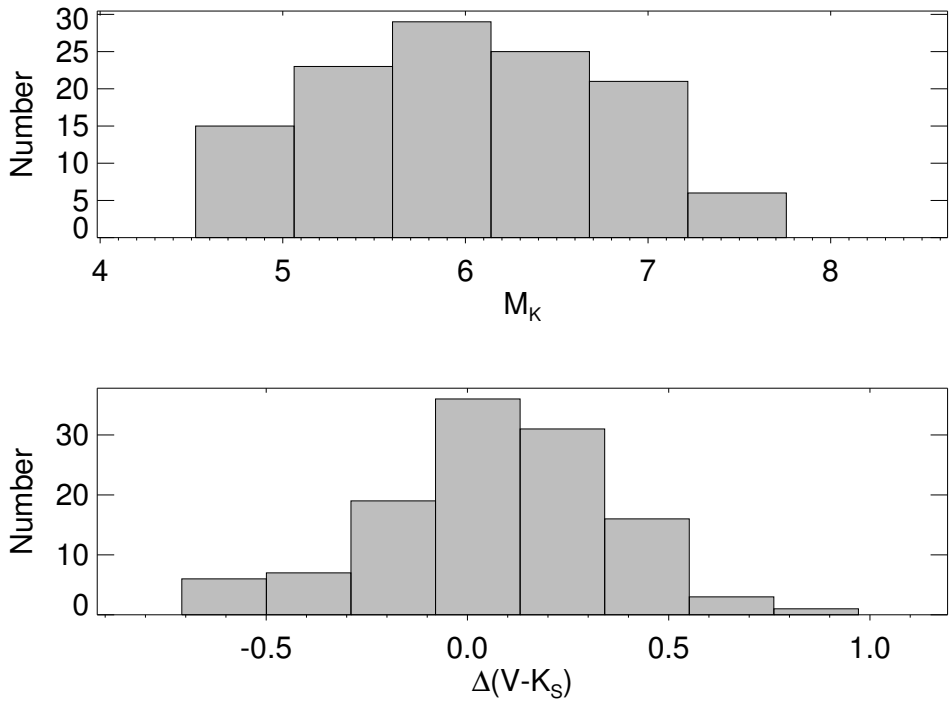

Figure A.1: Distribution of stellar properties in sample. Top panel is $\mathcal{M}_{Ks}$, and bottom is $\Delta(V - K_s)$. The calibration sample thus spans a broad range or stellar properties

Sample

Over the past decade the California Planet Survey (CPS) has obtained spectroscopic measurements of more than 2,500 stars at Keck Observatory, monitoring their radial velocities for the characteristic signature on the host star induced by the presence of a planet (Howard 2010). We make use of their High-Resolution Echelle Spectrometer (HIRES ; Vogt et al. 1994) observations of 155 M dwarfs to build a high-resolution,

high signal-to-noise "template" spectrum of each star. The typical CPS program HIRES set-up gives a resolving power $R = \lambda/\Delta\lambda \approx 50,000$ and uses an iodine-cell for precise wavelength calibration of radial velocity measurements (Howard 2010). In our application the iodine lines are contaminants, so we can only make use of the blue and red chips of the HIRES detector, where there are no lines from the iodine cell. The blue portion of the spectrum allows us to examine between 370 nm and 480 nm, while the red portion of the spectrum covers between 650 nm and 800 nm.

The M dwarfs in the CPS sample have well defined 2MASS photometry and parallaxes from *Hipparcos* (Perryman and others. 1997; Cutri 2003). This allows us to characterize the stellar sample in terms of their absolute near-IR magnitudes, (M_{JHKs}) and color, ($V - K_s$). We culled stars from the sample that were overly active or young, selected on the basis of having published rotation periods less than 5 days, high X-ray luminosities with a X-ray count rate > 1 count s^{-1} in ROSAT (Voges et al. 1999) or as being members of a young open cluster or moving group. We also culled stars that were known to be unresolved binaries or turned out to be missing geometric parallax measurements. We also limited the sample to stars brighter than $M_{Ks} = 8$, so that the range of properties is well sampled by the CPS stars. This left us with 119 calibration stars. The sample spans a range of M_{Ks} from 4.5 to 7.5 as shown in the top panel of Figure A.1. Using the Johnson and Apps (2009) solar-metallicity main sequence relation, defined as $M_{Ks} = \sum a_i (V - K_s)^i$, where $a = \{-9.58933, 17.3952, -8.88365, 2.22598, -0.258854, 0.0113399\}$, we can calculate the quantity, $\Delta(V - K_s)$, the difference between the observed color and the main-sequence color for a star of the same M_{Ks} such that positive values of $\Delta(V - K_s)$ correspond to redder objects. We will henceforth refer to $\Delta(V - K_s)$ as the color offset, which can be used as a proxy for metallicity (Schlaufman and Laughlin 2010). The bottom panel of Figure A.1 shows that our sample spans a broad range in color offset and hence a broad range in metallicity.

Spectral Library

Since our sample of calibration stars have been monitored for radial velocity shifts indicative of planets over the past 10-15 years, each star has an average of 25 observations. By combining the individual observations we can produce high signal-to-noise, high-resolution template spectra for each of the calibration stars in our sample. We rebinned each star's spectrum onto a wavelength scale that is evenly spaced in $\ln \lambda$ (cadence of 1.9×10^{-6}), which allows us to properly Doppler shift the spectra with respect to one another (Tonry and Davis 1979). We also corrected for

small differences in the wavelength solution from night to night (on the order of a couple of pixels) for every spectral order due to changes between the cross-disperser angle and the echelle angle as well as changes in the slit illumination for any given observation.

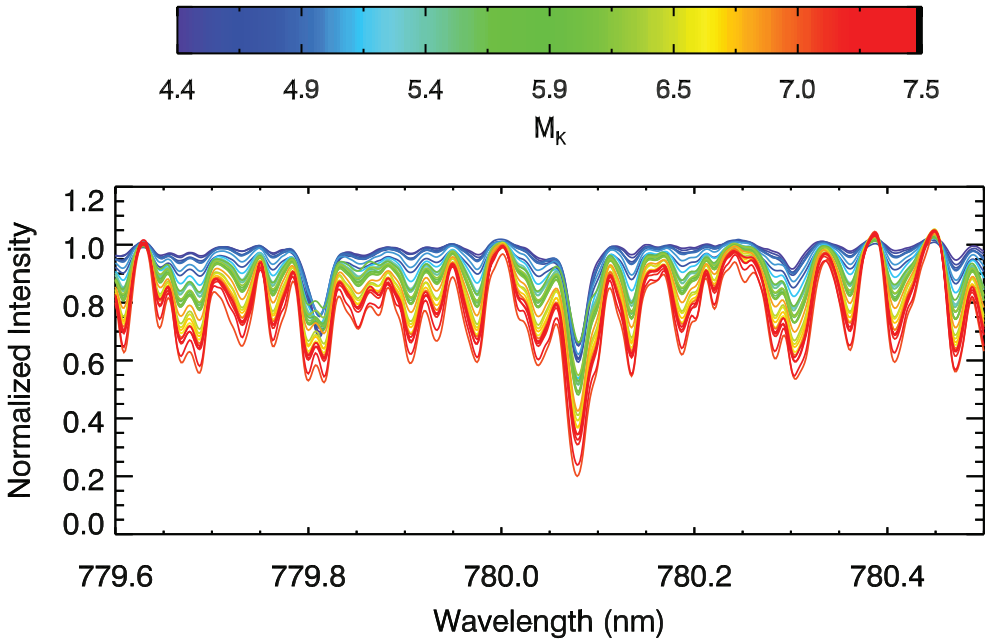

Figure A.2: Normalized Intensity as a function of wavelength for sensitive regions with bin-averaged spectra of width 0.1 mags in $\mathcal{M}_{Ks}$. Colors correspond to $\mathcal{M}_{Ks}$ in the range 4.5 to 7.5, with red being fainter stars and blue being brighter.

Having aligned the spectra and removed defects (cosmic ray hits etc.), we simply co-added the flux to produce a high signal-to-noise ratio spectrum for each star. The red portions of the spectrum yield a typical signal-to-noise ratio (SNR) per resolution element ranging from $\sim$ 800 to $\sim$ 4000, depending on the number of observations for the particular star. For the blue-chip spectra the SNR ranges from $\sim$ 100 up to $\sim$ 600. The SNR of the red side is higher primarily because the peak of the M dwarfs' spectral energy distribution lies closer to near-infrared wavelengths than to the blue portion of the spectrum.

In order to compare the spectra it was necessary to normalize each order to remove the effect of the blaze function of the spectrometer and to account for a pseudo-continuum. We normalize each spectral order individually. First, we separate the order into tens of "chunks", masking out telluric regions, and take the top 1-2% of points of each chunk as representing the "continuum". We then fit a low-order polynomial to the continuum points across the full extent of the order. Lastly,

we divide the spectral order by this polynomial, ignoring problematic points at the ends of the orders, to get the normalized spectrum (see Appendix for further details). Since the echelle spectra are not flux calibrated and the blaze function distorts the shape of the spectra, a pseudo-continuum is not well defined through our normalization procedure. However, because we use the same continuum regions for all stars, this process allows for reliable, differential comparisons among stars of different types.

In Figure A.2, we plot the template spectra averaged in M_{Ks} bins with width of 0.1 mag. The different colors correspond to different values of M_{Ks} with red corresponding to cooler stars and blue to hotter stars. In the Figure, we see that the absorption features are quite distinct from the “continuum" , which match across the different stars. It is clear in the high signal-to-noise spectra that features such as these are quite sensitive to M_{Ks} and we can use the strength of the absorption for a given spectrum as indicative of the stars intrinsic luminosity. Deviations from a strict sequence are primarily due to metallicity effects. At a given M_{Ks} changes in metallicity will affect the strength of certain absorption features. Accounting for this second-order effect will provide us with a valuable indicator of stellar metallicity.

A.3 Analysis

Spectral Calibration

The presence of spectral regions sensitive to changes in M_{JHKs} motivates the development of a quantitative relationship between the strength of each region and the physical properties of a star. The regions that were found to be sensitive and useful for calibration are listed in Table A.1. We identified these regions by eye looking across the full spectrum, ignoring telluric regions, and requiring the continuous regions of the spectrum to have have monotonically increasing absorption with decreasing stellar effective temperatures (see Figure A.2). The useful regions consist predominately of portions of TiO and VO bands. Note that the spectral indices listed in the table are all in the red portion of the spectrum. Although there also appeared to be sensitive regions at blue wavelengths, the lower overall flux level limits their usefulness, both for the calibration procedure and for future observations. In addition to the regions listed in Table A.1 there were other regions that we identified as sensitive to the physical stellar properties. However, we selected a subset that when combined provided the optimal calibration (see Section A.3).

The CPS sample spans a representative range of properties for low-mass stars,

Table A.1: Spectral Indices

Center Wavelength (nm)	Total Width (nm)	Molecule/Line [a]
658.24	0.820	TiO
660.35	0.59	TiO
663.89	0.81	TiO
668.82	1.71	TiO
710.27	2.91	TiO
713.64	2.48	TiO [b]
727.01	0.06	TiO
770.04	0.79	TiO / KI
770.83	0.50	TiO
776.92	2.38	TiO
780.13	0.92	TiO
787.30	0.85	TiO / VO
791.04	0.51	VO
792.26	1.67	VO
793.26	0.30	VO
794.87	0.24	VO

[a] Predominant Molecules and Lines based on spectra of Kirkpatrick, Henry, and McCarthy 1991

[b] This region is closely related to the TiO4/5 bands defined in Reid, Hawley, and Gizis 1995

making it useful for our calibration procedure. Since the sample is limited in size and individual stars only represent discrete points in the mass-metallicity plane, comparing the spectra directly is less than ideal, giving poor parameter resolution. Instead, it is preferable to compare the strength of sensitive features, measured from their integrated fluxes (equivalent widths, EWs), allowing us to fit smooth functions to observed trends in EW and providing a continuous relationship between the integrated flux and the stellar properties. The integrated flux is defined as

$$\mathrm{EW} = \Delta\lambda - \int S(\lambda) d\lambda \tag{A.1}$$

$$\approx \Delta\lambda - \sum_i S_i h_\lambda \,, \tag{A.2}$$

where $\Delta\lambda$ is the width over which the integral is computed and $S(\lambda)$ is the normalized spectrum as a function of wavelength λ. Equation A.2 gives the approximation for discretely sampled spectra over pixels that span $\Delta\lambda$ evenly sampled with width h_λ. To determine the errors on our equivalent width measurements we randomly

simulate the spectral observation using poisson statistics with a mean in each spectral bin given by the photon counts of the actual data. We take the error on the equivalent width measurement to be the standard deviation of the distribution of EW values in the simulation. The typical error on the EW measurements are $\sim 1-5\%$.

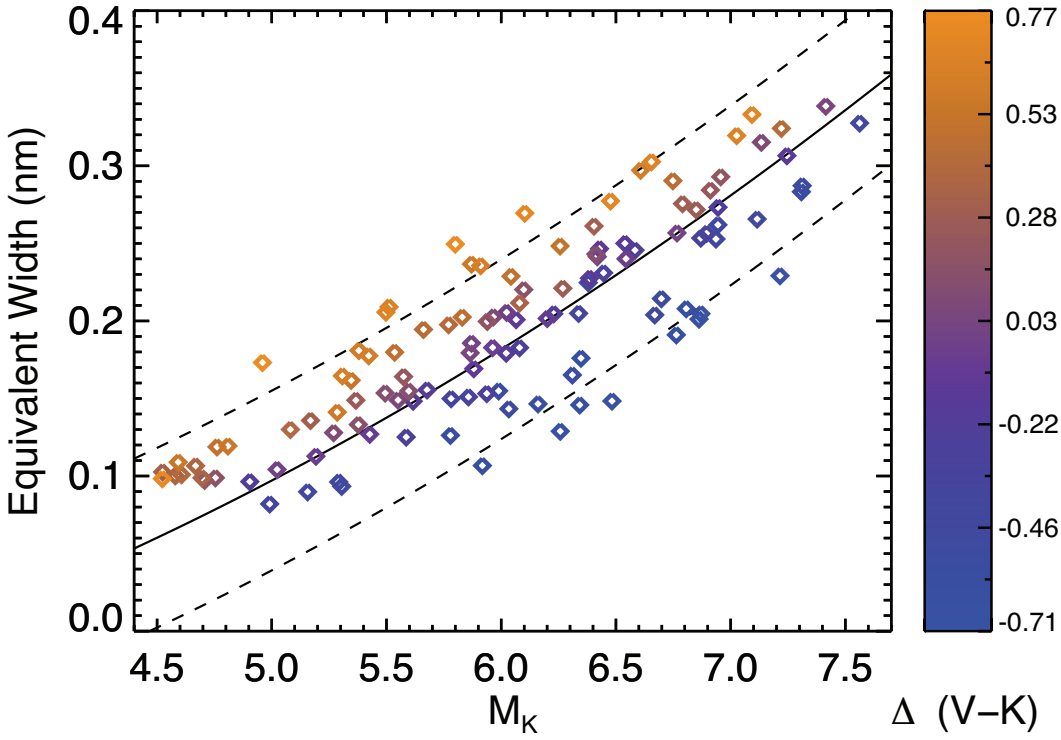

Figure A.3: EW plotted as a function of $\mathcal{M}_{Ks}$ for all stars in the sample. The colors are ordered according to the $\Delta(V-K_s)$ of the stars in the sample. There is a clear gradient that corresponds to differences in metallicity. The lines correspond to contours in our polynomial model of constant color offset, $\Delta(V-K_s)$, with values 0.5, 0.0 and -0.5 going from top to bottom respectively. This region is centered at 770.04 nm with a width of 0.50 nm

In Figure A.3 we plot the behavior of EW as a function of $\mathcal{M}_{Ks}$ and $\Delta(V-K_s)$ for a particular spectral region. The colors correspond to $\Delta(V-K_s)$ with red corresponding to stars that are more metal-rich and blue corresponding to stars that are more metal-poor. For spectral regions such as this one, the strength of the feature increases with increasing metal content as well as decreasing luminosity. The behavior, expressed in Figure A.3, motivates the parameterization of each EW in terms of $\mathcal{M}_{JHKs}$ and $\Delta(V-K_s)$. For a given region, l, we calibrate the equivalent widths against each of the absolute magnitudes and the color offset. Our calibration EW, which allows us to interpolate between the discrete sample star properties, is given by

$$\mathrm{EW}_{l,\alpha} = (b + c\mathcal{M}_\alpha)\Delta(V - K_s) + \sum_{i=0}^{2} a_i \mathcal{M}_\alpha^i \,, \tag{A.3}$$

where $\alpha \in \{\ J,\ H,\ Ks\ \}$, so there is a separate calibration for each passband using the same spectral region.

We fit each passband separately instead of going directly to mass, despite tight mass-luminosity relations, because the infrared colors (ex. $J - K$) are not simply functions of mass and can change with metallicity; this is in contrast to other broadband photometric studies of low-mass stars (Johnson et al. 2011, 2012a). In addition to the simple polynomial terms expressed in Equation A.3, we include a cross term governed by the coefficient c that accounts for differences between brighter and fainter stars in how their absorption strength responds to the addition of metals. The need for such a term is evident in how TiO features are known to saturate in late-type M dwarfs and that VO features are not apparent in early M dwarfs but appear in late-type M dwarfs (Kirkpatrick, Henry, and McCarthy 1991).

Fitting Broadband Photometry

We used a Bayesian method to fit Equation A.3 to each set of EWs. In addition to the coefficients in Equation A.3, we also incorporated an additional parameter, σ, to take into account intrinsic scatter in our choice of parameterization. Using a Markov Chain Monte Carlo (MCMC) technique with a Metropolis-Hastings algorithm, we explore the posterior distribution for the best parameters in the calibration conditioned on the known properties of the stars in the sample. The best calibration parameters are those that maximize their respective marginal distributions, and thus maximize the probability of each parameter reproducing the stellar properties of the stars in the sample with our simple model. We report the parameter values of our calibration in Table A.2. For a given spectral index the first row of the table corresponds to the parameters for the calibration with $\mathcal{M}_J$, the second row for $\mathcal{M}_H$, and the third for $\mathcal{M}_{Ks}$.

Table A.2: Calibration Parameters [a]

Center (nm)	a_0 (nm)	a_1 (nm)	a_2 (nm)	b (nm)	c (nm)	σ (nm)
658.24	-0.4501058	0.09198486	-0.001427114	0.07882096	0.002933661	0.01270252
	-0.3490226	0.07719585	-0.0005361921	0.06294231	0.006100980	0.01208604
	-0.3486802	0.07969309	-0.0005093491	0.07282996	0.005513314	0.01123767
660.35	-0.1596480	0.01916057	0.001997996	0.001896713	0.008210727	0.007939490
	-0.1520269	0.02420063	0.001671400	0.003454885	0.009034893	0.007594586
	-0.1553699	0.02603111	0.001767160	0.01073864	0.008722165	0.007079715
663.89	-0.4226041	0.08017676	-0.00008847487	0.07432834	0.003435445	0.01253907
	-0.3302306	0.06765508	0.0007076964	0.05919351	0.006587219	0.01168440
	-0.3803160	0.08669426	-0.0005393973	0.08166828	0.004118372	0.01082510
668.82	-2.836934	0.7375158	-0.03934088	0.6871808	-0.06801754	0.03053437
	-2.196094	0.6257768	-0.03455122	0.5937715	-0.05868804	0.02922317
	-2.374936	0.7089150	-0.04205847	0.6733981	-0.07173435	0.02711429
710.27	-5.145841	1.292010	-0.06165890	1.147429	-0.08640261	0.06357273
	-4.044212	1.116565	-0.05456582	1.010953	-0.07058973	0.06100981
	-4.307040	1.244481	-0.06565496	1.162449	-0.09311087	0.05549368
713.64	-6.357848	1.673048	-0.08776160	1.399011	-0.1214399	0.05989609

Continues on next page ...

Center (nm)	a_0 (nm)	a_1 (nm)	a_2 (nm)	b (nm)	c (nm)	σ (nm)
	-5.054271	1.471289	-0.08102439	1.272483	-0.1101706	0.05812801
	-5.253722	1.593891	-0.09263240	1.423004	-0.1339820	0.05169340
727.01	-0.1138363	0.02944591	-0.001551650	0.02305361	-0.001910082	0.001294007
	-0.09486709	0.02712001	-0.001531907	0.02163241	-0.001814339	0.001242313
	-0.09856623	0.02938447	-0.001748182	0.02431960	-0.002235494	0.001166170
770.04	-0.1598857	0.008933704	0.006038753	0.1399386	-0.004808356	0.01121777
	-0.1181027	0.008006942	0.006416439	0.1134480	-0.0005393014	0.01118438
	-0.1085764	0.004873543	0.007252633	0.1158942	-0.000001015819	0.009809055
770.83	-0.3815610	0.07699559	-0.001319326	0.04795545	0.003966268	0.009098964
	-0.2753433	0.05733777	-0.00003557394	0.03629728	0.006487797	0.008746648
	-0.3191640	0.07383029	-0.001163489	0.05463092	0.004446250	0.007962008
776.92	-1.408374	0.2440679	0.001240992	0.1658279	0.02825762	0.04063114
	-1.204047	0.2346570	0.001405473	0.1440118	0.03585729	0.03961519
	-1.302366	0.2751659	-0.0008869298	0.2068376	0.03001058	0.03584416
780.13	-0.3511850	0.05775816	0.001359554	0.05715288	0.007504470	0.01079916
	-0.2988942	0.05584809	0.001437870	0.05035518	0.009766074	0.01034952
	-0.2972508	0.05705502	0.001681733	0.06221154	0.009053781	0.009174584
787.30	-0.07969772	-0.01437250	0.005574401	0.009402555	0.01204589	0.01161012

Continues on next page ...

Center (nm)	a_0 (nm)	a_1 (nm)	a_2 (nm)	b (nm)	c (nm)	σ (nm)
	-0.04158101	-0.02027625	0.006402968	-0.003833748	0.01558149	0.01126873
	-0.06175869	-0.01473584	0.006440116	0.005074938	0.01547640	0.01026771
791.04	0.01844099	-0.02735590	0.004700167	-0.02789386	0.01186093	0.006290352
	0.01743679	-0.02505636	0.004849061	-0.02857221	0.01330172	0.006062947
	-0.0009558277	-0.02019831	0.004791414	-0.02164277	0.01312965	0.005528097
792.26	0.2785090	-0.1369218	0.01704969	-0.1025768	0.03602162	0.01778133
	0.2310036	-0.1224368	0.01723172	-0.09838984	0.03933845	0.01729166
	0.2100510	-0.1211605	0.01818554	-0.09387771	0.04123889	0.01595478
793.26	0.1454432	-0.04912226	0.004548514	-0.01954720	0.006100179	0.003336126
	0.1161707	-0.04273733	0.004429765	-0.02024410	0.006868234	0.003257263
	0.1180228	-0.04515902	0.004855676	-0.02172495	0.007529807	0.003095342
794.87	0.04278556	-0.02045305	0.002583565	-0.004188786	0.004094394	0.002292025
	0.03241636	-0.01713182	0.002513652	-0.002884554	0.004370116	0.002306728
	0.02124669	-0.01420778	0.002431369	-0.0002786377	0.004293440	0.002088636

[a] The first row for a given index center corresponds to parameters for the J calibration, the second row for H calibration and third row for K_s calibration

These curves provide a calibration, which we can apply to stars of unknown properties with measured EWs and estimate $\mathcal{M}_{JHKs}$ and $\Delta(V-K_s)$. Taking the errors in the integrated flux as normally distributed, we minimize a χ^2 statistic to get the stellar photometric properties. The statistic is split up into a couple components,

$$\chi^2 = \sum_l \chi^2_l + \chi^2_{\rm p}\,, \tag{A.4}$$

where the first term comes from the spectral calibration and is summed over the different indices, l, and the last term correspond to photometric constraints. The sum over all the different indices allows us to partially break the degeneracy between metallicity and mass inherent in the individual indices.

For each spectral region, l, the fitting statistic is

$$\chi^2_l \;=\; \sum_\alpha \frac{[{\rm EW}^{obs}_l - {\rm EW}_{l,\alpha}(\Delta(V-K_s),\mathcal{M}_\alpha)]^2}{2(\sigma^2_{obs,l}+\sigma^2_{l,\alpha})}\,, \tag{A.5}$$

where ${\rm EW}_{obs,l}$ is the measured EW, with uncertainty $\sigma_{obs,l}$, and ${\rm EW}_{l,\alpha}$ is from Equation A.3, using the best calibration parameters; here the scatter parameter, $\sigma_{l,\alpha}$, is added in quadrature to the measurement error. The sum is over each of the three infrared passbands, $\alpha \in \{\ J,\ H,\ Ks\ \}$, which have separate calibrations for the given spectral region (see Table A.2).

Since many nearby stars have 2MASS photometry, we can use the distance, d, as an additional parameter by requiring that our estimates of $\mathcal{M}_{JHKs}$ reproduce the observed photometry.

$$\chi^2_{\rm p} = \sum_\alpha \frac{\{\alpha - [\mathcal{M}_\alpha + 5\log_{10}(d/10{\rm pc})\ ]\}^2}{2\sigma^2_{p,\alpha}}\,, \tag{A.6}$$

where α corresponds to the observed infrared magnitudes and $\sigma_{p,\alpha}$ is the corresponding measurement uncertainty.

Summing over all of the indices and the additional constraints gives the total χ^2 of Equation A.4, which we minimize as a function of $\mathcal{M}_{JHKs}$, $\Delta(V-K_s)$ and d to determine the best-fit stellar properties and the distance to the star.

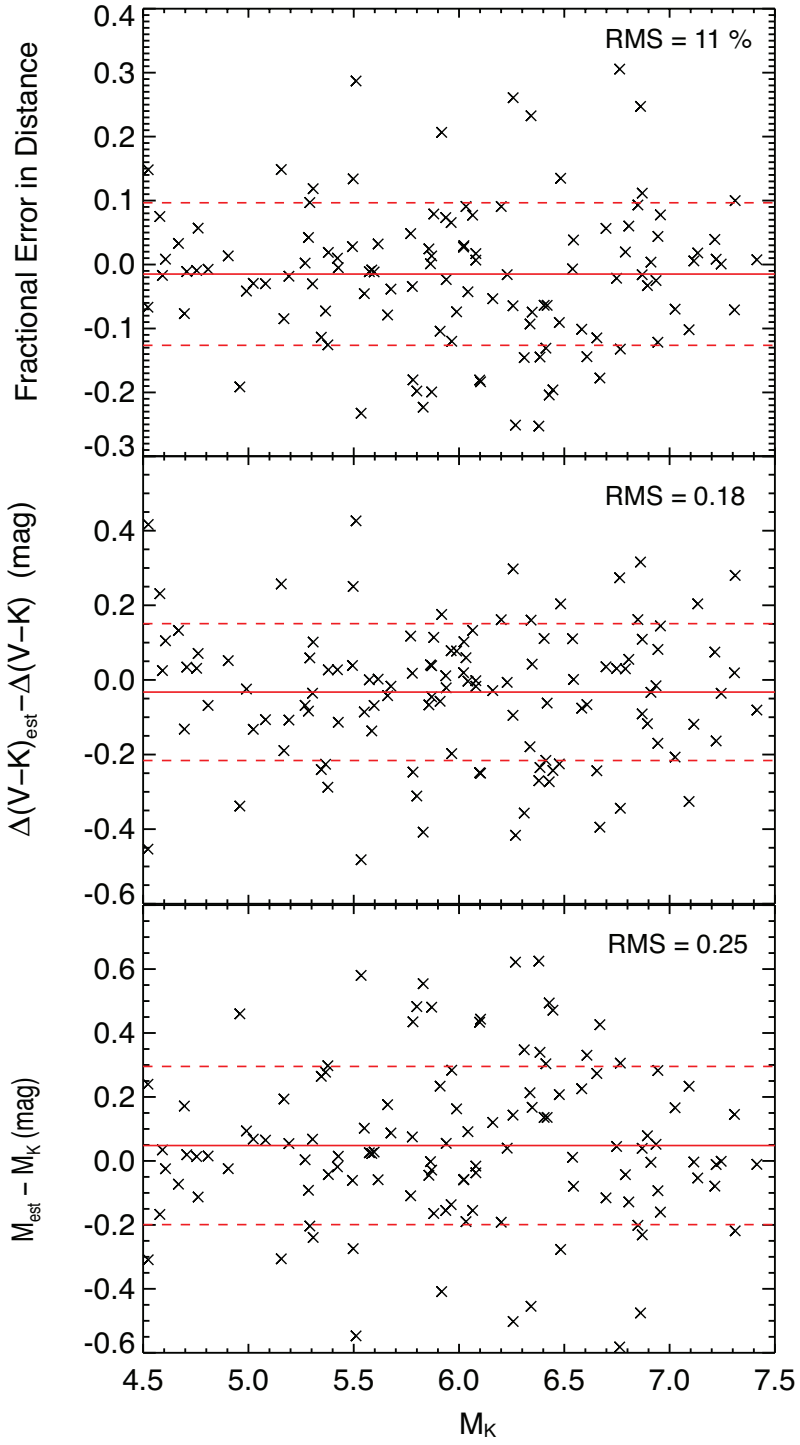

Figure A.4: The error in the distance (top panel), color offset (middle panel) and $\mathcal{M}_{Ks}$ (bottom panel) as a function of the intrinsic brightness of the star. We can reproduce the distances to an accuracy of 11%, the color offset to 0.18 dex and $\mathcal{M}_{Ks}$ to 0.25 dex. The RMS in the absolute magnitudes for J and H band closely match the RMS in the K band absolute magnitude. There is no clear trend, as the method appears to be uniformly applicable between $4.5 < \mathcal{M}_{Ks} < 7.5$. The solid lines mark the mean of the example set and the dashed lines mark the 1σ levels about the mean.

Accuracy

In Figure 4 we show the results of our assessment of how well we can recover the properties of the stars in our calibration sample. The top panel of the Figure shows the percentage error in reproducing the observed distance of the stars, the middle panel shows the error on the color offset and the bottom panel shows the error in $\mathcal{M}_{Ks}$. The root-mean-scatter (RMS) for the distance, color offset and absolute K-band magnitude are 11%, 0.18 dex and 0.25 dex respectively. Using established photometric relations, this scatter would correspond to 0.10-0.15 dex in [Fe/H] (depending on the literature calibration) and $\sim 0.05\ M_{\odot}$ in mass (Schlaufman and Laughlin 2010 ; Delfosse et al. 2000).

As an additional test, we examined what SNR is necessary to get consistent parameter estimates from any given stellar spectrum using our methods. We simulated a given SNR by adding noise to our template spectra using a pseudo-random number generator. Repeating this many times for each SNR, we saw what effect the noise had on our parameter estimates. In Figure A.5, we plot the dispersion in our estimates as a function of SNR. The top panel is for $\Delta(V - K_s)$ and bottom for $\mathcal{M}_{Ks}$. As the SNR increases, the initial improvements are significant. But after about a SNR of $\sim$ 70, the improvements with greater signal are marginal.

Spectral Resolution

We also examined how spectral resolution affects the utility of our calibrations. By measuring EWs consistent with our original measurements we would be able to use our calibration to recover the same set of stellar properties using lower resolution spectra. To test this, we first took the template spectra for our calibration sample and convolved the spectra down to lower resolutions (5,000-45,000) in increments of 5,000 from our original resolution of 50,000. We then normalized the spectra in the same manner as we did our original template spectra (see Section A.2) and computed the EW for each of the indices of Table A.1 and all of the sample stars. In Figure A.6, we plot the average fractional difference in EW measurements, across all the calibration stars, between the convolved spectra and the unconvolved spectra as a function of spectral resolution, where each panel corresponds to a different index as listed in Table A.1. The error bars in the plot represent the scatter in the deviation across the sample of calibration stars. For each index the EW measurements are consistent with the original measurements for spectral resolutions above 30,000. Therefore our calibration should not be used below this threshold without accounting for the systematic effects demonstrated in Figure A.6.

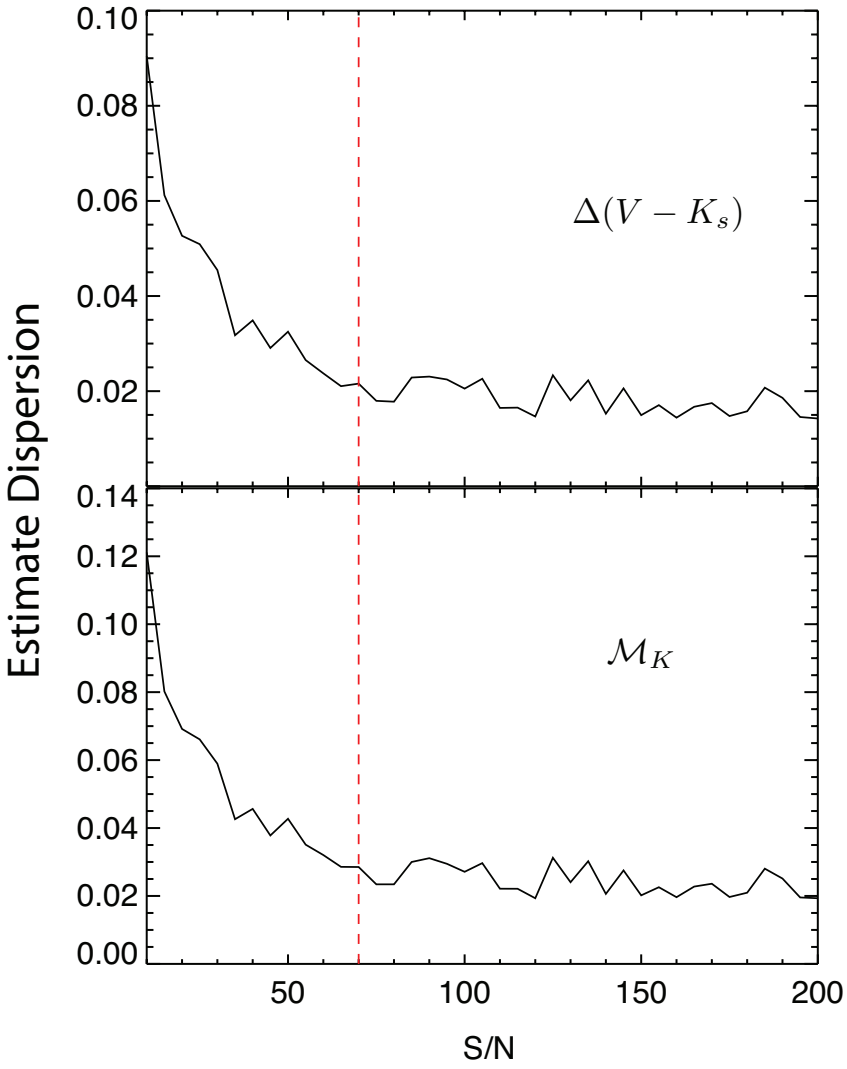

Figure A.5: The degree to which the parameter estimates vary as a function of the median signal-to-noise ratio of the input spectrum measured across the red chip of the HIRES detector. When the input spectrum has a SNR above ~70 (marked by dashed line), the parameter estimates settle down to a well defined value. See text for analysis procedure.

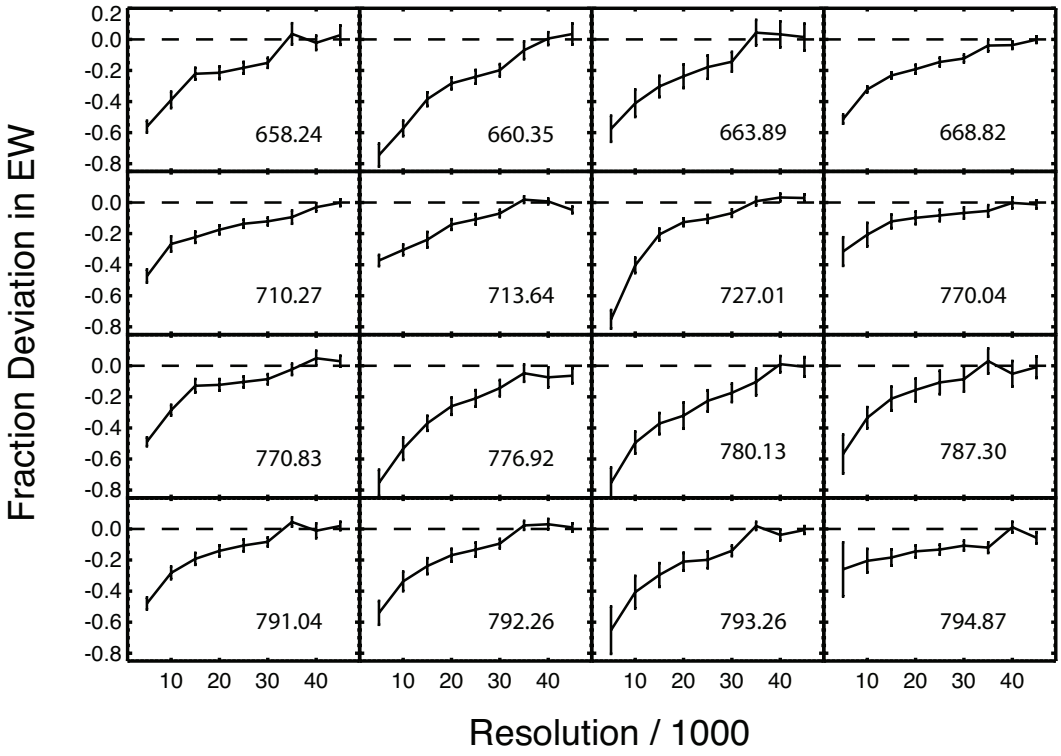

Figure A.6: The average fractional deviation in measured EW compared to our original HIRES spectra as a function of spectral resolution for each spectral index designated by the central wavelength (nm) listed in Table A.1. Each point represents the mean deviation across the full calibration sample with the error bars given by the corresponding scatter. There are considerable deviations for resolutions below ~30,000.

Although the integrated flux of a spectrum should not change at lower resolutions, the blending of pseudo-continuum with the many absorption band-heads complicates our EW measurements.

To consider higher resolution data we examined a subsample within our set of calibration stars that also had publicly available data from the ESO data archive using the HARPS spectrograph at a resolution of 115,000 (Mayor 2003). For this subsample of 43 stars we combined multiple observations and put together template spectra similar to our HIRES spectra (see Section A.2). This produced a set of HARPS spectra with high SNRs, all greater than 70. We then convolved the spectra down to the HIRES resolution of 50,000 to compare EW measurements. Normalizing the spectra in the usual manner we then measured the EWs for the first four indices of Table A.1; because of the small overlap between the HARPS spectrograph and the

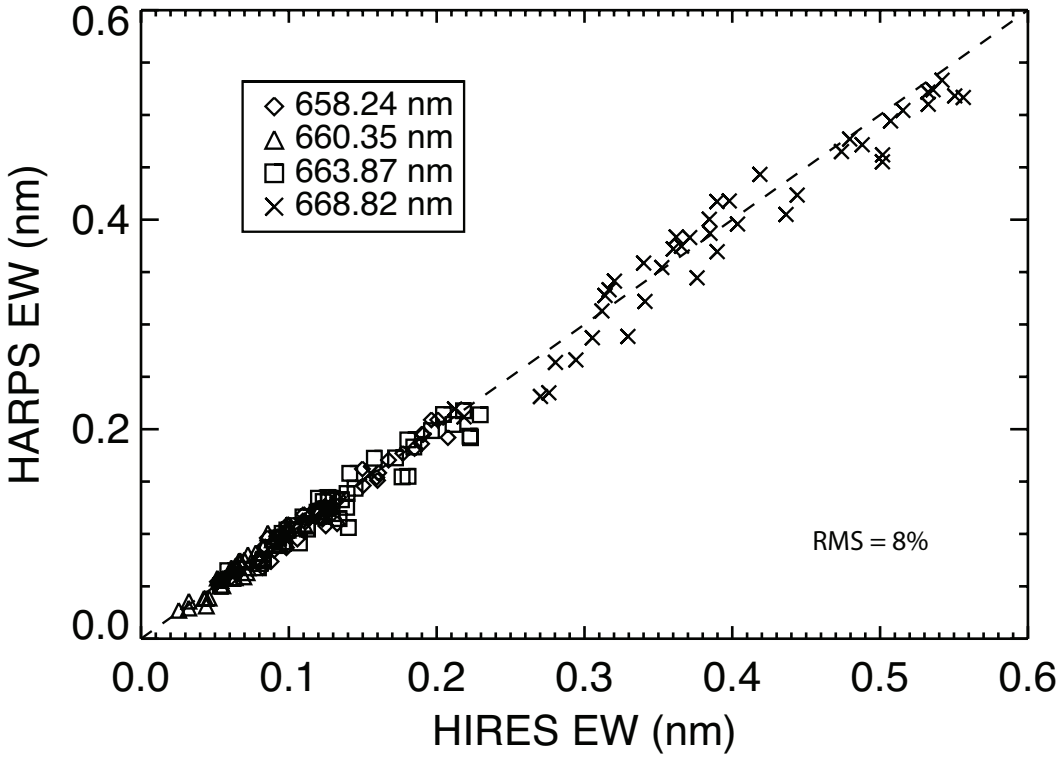

Figure A.7: A comparison of the EW measurements for the subsample with HARPS spectra. The different symbols correspond to the four different indices available and the line indicates a 1:1 correspondence. The scatter about the line is at the 8% level consistent with the measurement uncertainties.

HIRES red chip only these four indices were available. In Figure A.7, we compare equivalent width measurements from the HARPS subsample to the measurements from our HIRES spectral templates. The straight line in the plot corresponds to exact agreement. The measurements agreed rather well with an RMS of $\sim 8\%$, in line with the combined errors between the two measurements.

A.4 Applications

KOI-314

We applied our methods to the case of the *Kepler* object of interest KOI-314. This M-dwarf, with a visual magnitude ~ 14 with a Kepler-band magnitude $K_p = 12.93$, received Keck Observatory HIRES follow-up to confirm the planetary nature of the two transit signals observed in its *Kepler* light curve. We were able to make use of 6 CPS observations to construct a high-resolution spectral template to apply our method. The co-addition procedure, as discussed in Section A.2, yielded a spectrum with a typical signal-to-noise ratio of ~ 250 in the red portion, plenty for

our purposes. Figure A.8 shows the results of our analysis with the contours for each pairing in our five parameter fit, $\mathcal{M}_{JHKs}$, $\Delta(V-K_s)$, and d.

Each parameter is highly correlated, leading to the oblong shaped contours of the figure. This is predominately because the absorption strength of the spectral indices is degenerate in mass and metallicity; the absorption strength can increase with a drop in the effective temperature or an increase in the metal content. Additionally, the shape of the contours between the infrared magnitudes must be consistent with the observed colors ($J-H, H-K$ etc.).

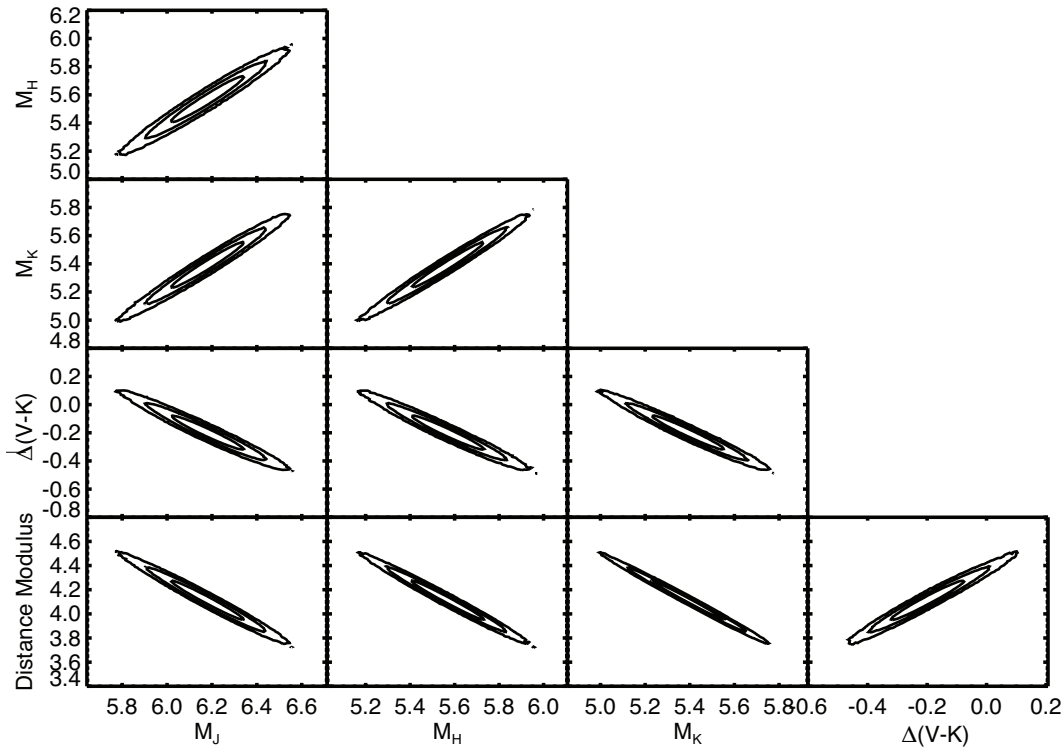

Figure A.8: Contour plots of the posterior probability distribution from the five parameter MCMC analysis of KOI-314. The contour levels represent the 1σ, 2σ, and 3σ confidence levels. The oblong contours come from spectral indices being degenerate in $\mathcal{M}_{Ks}$ and $\Delta(V-K_s)$

We can then marginalize over the full posterior probability for the five parameters to get probability distributions for the likelihood of each of the parameters. Our estimates are shown in Table A.3 where we have adopted for our uncertainties the scatter we have in reproducing the stellar parameters as demonstrated in Section A.3. We have additionally added an empirical estimate of the stellar radius based on the single star mass-radius relation of Boyajian (2012) established from interferometric radii measurements of nearby low-mass stars. The table also includes select estimates

from Muirhead et al. (2012b), which uses infrared spectra in conjunction with stellar models to derive properties. Additionally, in Figure A.9, we plot the marginalized distributions for the stellar properties, after converting the photometric properties, $\mathcal{M}_{Ks}$ and $\Delta(V-K_s)$ to the physical properties of mass and [Fe/H]. The top left panel shows our distribution for the distance. The top right panel shows the distribution for [Fe/H], using the calibration of Neves et al. (2012) to make the conversion from $\Delta(V-K_s)$. The accompanying dashed line is a Gaussian representing the Muirhead et al. (2012b) estimate. The bottom left panel shows the distribution for mass, the solid line being our estimate, employing the Delfosse et al. (2000) relation for $\mathcal{M}_{Ks}$ with the dashed line representing the Muirhead et al. (2012b) estimate. Finally, the bottom right panel uses our mass estimate and the mass-radius relation of Boyajian (2012) to estimate the radius of the star with the dash-dot line again representing the Muirhead et al. (2012b) estimate. Our measurements match those in Muirhead et al. (2012b) within the respective uncertainties, giving us confidence in the accuracy of our derived parameters. Combining our estimates with theirs gives a mass estimate of $0.55 \pm 0.04\ M_\odot$, a radius estimate of $0.52 \pm 0.04\ R_\odot$ and a metallicity of -0.29 ± 0.08 dex .

Table A.3: Properties: KOI-314

Attribute	Muirhead et al. (2012b)	This Study
M_J	...	6.18 ± 0.25
M_H	...	5.57 ± 0.25
$\mathcal{M}_{Ks}$	...	5.39 ± 0.25
$\Delta(V-K_s)$	...	-0.20 ± 0.18
d	...	66.5 ± 7.3 pc
Mass [a]	$0.51 \pm 0.06\ M_\odot$	$0.57 \pm 0.05\ M_\odot$
Radius[b]	$0.48 \pm 0.06\ R_\odot$	$0.54 \pm 0.05\ R_\odot$
[Fe/H][c]	-0.31 ± 0.13	-0.28 ± 0.10

[a] For this work the estimate uses the relations of Delfosse et al. (2000) to convert $\mathcal{M}_{Ks}$ to mass.

[b] For this work the estimate uses the relations of Boyajian (2012) to convert mass to radius.

[c] In converting $\Delta(V-K_s)$ to [Fe/H], the estimate uses the relation of Neves et al. (2012): [Fe/H] = $0.57\Delta(V-K_s) - 0.17$. The listed uncertainty does not include the scatter in their relation.

GJ 3470

As an additional application of our methods we consider the exoplanet hosting

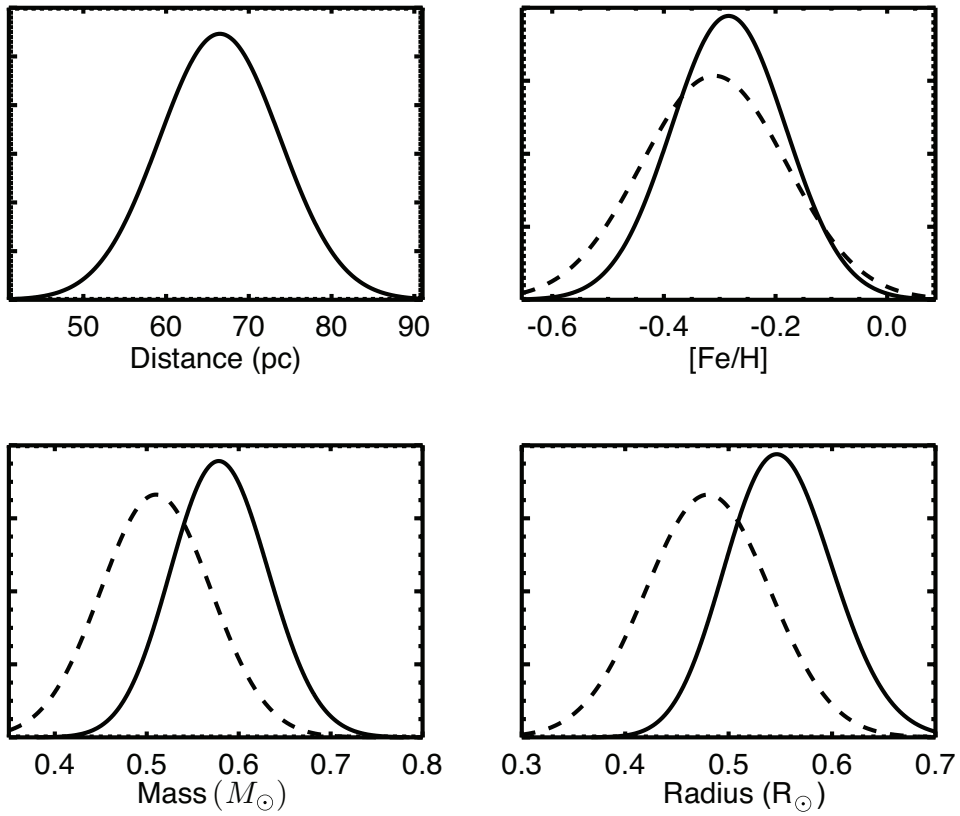

Figure A.9: Marginalized probability distributions for the properties of KOI=314, using photometric calibrations to convert to mass and [Fe/H]. The Delfosse et al. (2000) is used to convert to mass and the Neves et al. (2012) relation is used for metallicity. The distributions from Muirhead et al. (2012b) are over plotted with a dashed line, assuming normal distributions with a standard deviation given by the reported uncertainties

Table A.4: Properties: GJ 3470 System

Attribute	Bonfils (2012)	This Study
J[a]	...	8.794 ± 0.019
H[a]	...	8.206 ± 0.023
K[a]	...	7.989 ± 0.023
$a/R_\star$	14.9 ± 1.2	...
Period	3.33714 days	...
$R_p/R_\star$	0.0755 ± 0.0031	...
d	...	$29.9\pm^{3.7}_{3.4}$ pc
Mass	0.54 ± 0.07 $M_\odot$	0.53 ± 0.05 $M_\odot$
Radius	0.50 ± 0.06 $R_\odot$	0.50 ± 0.05 $R_\odot$
[Fe/H]	...	0.12 ± 0.12

[a] 2MASS photometry of Cutri (2003)

star GJ 3470. In the discovery paper Bonfils (2012) used HARPS radial velocities and a photometric transit detection to constrain the mass and radius of the planet, adding the system to three other M dwarfs (GL 436, GJ 1214 and KOI-254) with planets that have well-measured mass and radius estimates. The precision of the planet properties for GJ 3470b however was limited by the uncertainty in the stellar properties. Previous studies of GJ 3470 suggested that it is a typical field star on the main sequence, making the methods of this paper applicable (Bonfils 2012).

In Section A.3 we showed how HARPS archival spectra could be used to measure EWs compatible with the spectral index calibrations of Table A.2. We applied the procedures of Section A.3 on the HARPS spectra of GJ 3470 to obtain a spectrum with a typical signal-to-noise of 72 near the spectral indices. We measured the EWs and were able to independently estimate the distance, mass, [Fe/H] and radius of the star using entirely empirical methods; we used the mass-radius relation of Boyajian (2012) to determine the radius from the mass. However, only the first four of the indices of Table A.1 are useable with the HARPS spectra, reducing the precision of our measurements. Using just the four indices we reproduced the properties of the calibration sample to a RMS of 0.38 in $\mathcal{M}_{JHKs}$, 0.27 dex in $\Delta(V - K_s)$ and 18% in distance (see methods in Section A.3). This RMS corresponds to 0.08 $M_\odot$ in mass and 0.15 dex in metallicity using the calibrations of Delfosse et al. (2000) and Neves et al. (2012) respectively. To improve the precision of our estimates we look for additional constraints to apply to the stellar properties.

The broadband photometric methods of Johnson et al. (2012b) showed how photometric observations could be combined with transit light curve observables to provide precise estimates of the stellar properties. Following their example we include the reduced semi-major axis of the planet orbit as an additional constraint:

$$\frac{a}{R_\star}(M_\star, P) = \left(\frac{G}{4\pi^2}\right)^{1/3} \frac{M_\star^{1/3}}{R_\star(M_\star)} P^{2/3}\,, \tag{A.7}$$

where the radius is given as a function of mass using the mass-radius relation of Boyajian (2012) and we neglect the mass of the planet as very small compared to the stellar mass. The transit light-curve observable, $d_p/R_\star$, gives the planet-star separation at the time of transit and for the case of a circular orbit matches the reduced semi-major axis of Equation A.7. We take the period to be well defined as 3.33714 days and the observed $(a/R_\star)_o$ as 14.9 ± 1.2 from Bonfils (2012). We

incorporated this constraint by adding an additional term to the total χ^2 of Equation A.4,

$$\chi^2_a = \frac{[(a/R_\star)_o - a/R_\star(M_\star, P)]^2}{2\sigma^2_{ar}} \ . \tag{A.8}$$

In implementing the MCMC methods of Section A.3 we use the relations of Delfosse et al. (2000) to go from $\mathcal{M}_{Ks}$ to $M_\star$ in Equation A.8. Our estimates, shown in Table A.4, agree well with the output values derived by the planet-discovery team which combined a transit detection with radial velocity measurements, $0.54 \pm 0.07\ M_\odot$ for the mass and $0.50 \pm 0.06\ R_\odot$ for the radius, however our stellar properties are more precise. They are also consistent with stellar parameter estimates incorporating a new infrared transit analysis (Demory et al. 2013). In Figure A.10 we plot the contours for the total probability distribution in our estimate of the stellar mass as a function of observed quantities at the fixed distance and metallicity of our estimates shown in Table A.4. The filled overlays show the 3σ constraints provided by each observation with blue corresponding to $a/R_\star$, green to the joint constraint in JHK and orange given by the combined constraints of the EWs.

We can combine our stellar radius measurement with the estimate from Bonfils (2012) to get a precise stellar radius of $0.50 \pm 0.04\ R_\odot$. Using the transit observable $R_p/R_\star = 0.0755 \pm 0.0031$ from Bonfils (2012), we get a planet radius estimate of $R_p = 4.12 \pm 0.37\ R_\oplus$, slightly smaller than their estimate of $R_p = 4.2 \pm 0.6\ R_\oplus$.

A.5 Summary and Discussion

Using high-resolution spectra of nearby M-dwarfs we have developed a new spectroscopic calibration for the physical properties of low-mass stars of types K7-M4. With a high signal-to-noise spectrum and 2MASS photometry we can estimate the mass and the metallicity of the star as well as the distance to the star.

Our methods are based on the integrated spectral flux (EW) at a series of spectral regions sensitive to the known photometric properties of the stars. By measuring the corresponding EWs from the spectra of low-mass stars and making use of the observed infrared magnitudes, we can estimate the photometric properties, $\mathcal{M}_{JHKs}$ and $\Delta(V - K_s)$, as well as the distance. Additionally, using known photometric calibrations, these can be converted to mass and metallicity. Our estimates are strongly dependent on the accuracy of the assumed parameters for our calibration stars; however, the sample comprises a set of well studied nearby stars with accurate

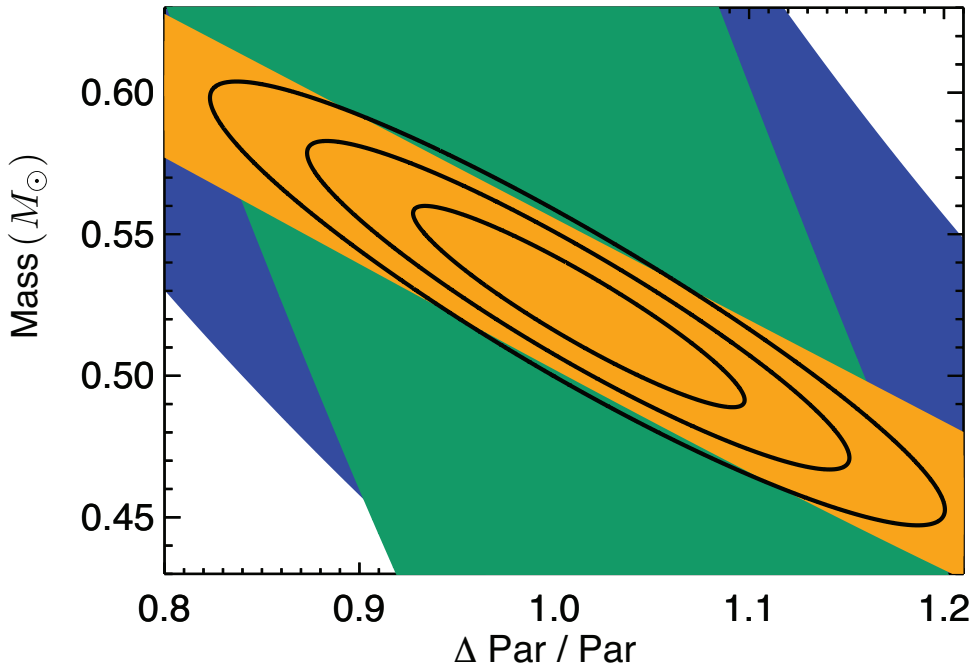

Figure A.10: Contours of the probability distribution for our mass estimate of GJ 3470 as a function of observed parameters with the metallicity and distance fixed to their best estimates, 0.12 dex and 29.9 pc respectively. The outer (blue) region defines the 3σ constraint applied by the measurement of $a/R_\star$. The middle (green) regions applies the combined 3σ constraint of the infrared passbands JHK. The thin (orange) region is the combined 3σ constraint using our calibration on the measured EWs of the HARPS spectra. The black contours represent the 1σ, 2σ, and 3σ contour levels for the entire set of constraints.

properties. We are thus able to estimate the intrinsic physical properties of low-mass stars without having parallax measurements, independently of stellar models.

We applied our methods to a particular star KOI-314, one of the *Kepler* objects of interest and estimated a mass of 0.58 ± 0.05 $M_\odot$, a radius of $0.55\pm^{0.06}_{0.05}$ $R_\odot$, a metallicity, [Fe/H], of -0.28 ± 0.10 and a distance of 66.5 ± 7.3 pc, where we have adopted for our uncertainties the representative scatter of Section A.3 and propagated those uncertainties through the empirical calibrations to the uncertainties of the desired physical properties. These estimates are in good agreement with the approach taken by Muirhead et al. (2012b), providing additional observational evidence in corroboration of their model-dependent methods. We were also able to apply our methods to the planet host GJ 3470, making use of archival HARPS spectra and taking advantage of the transit observable $a/R_\star$ to narrow in on the

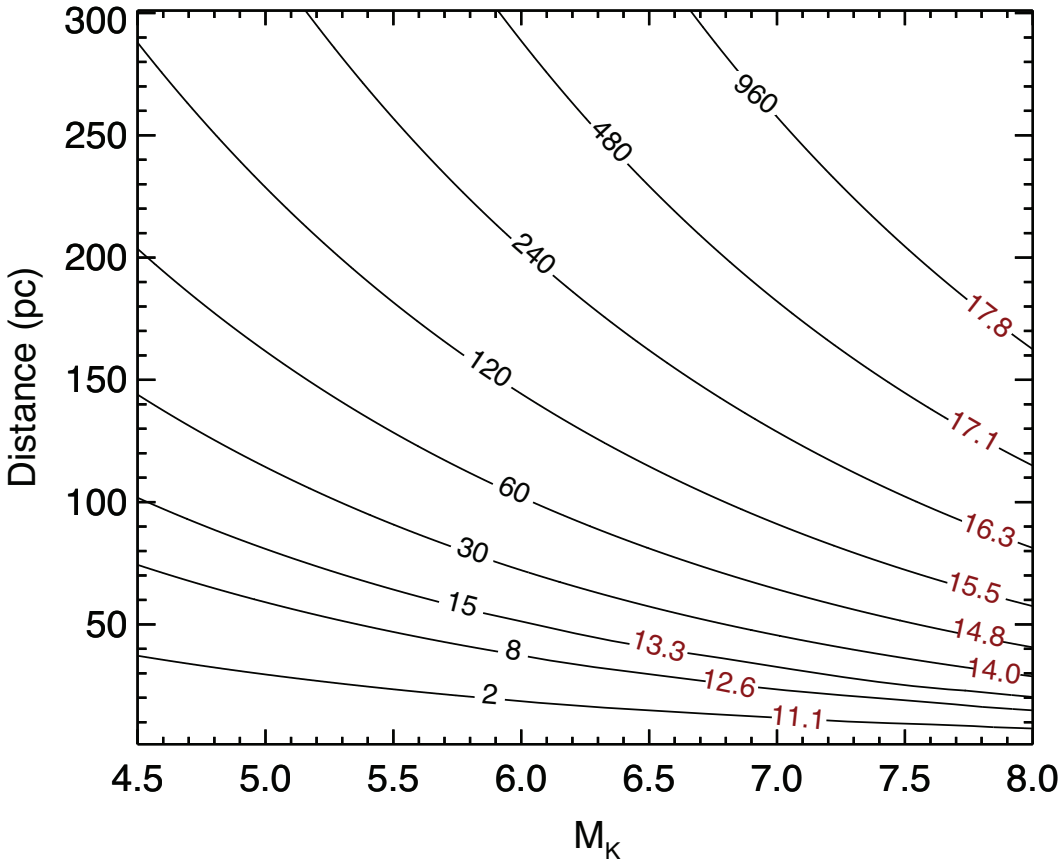

Figure A.11: Contours indicate the approximate minimum total integration time with HIRES, in minutes, for typical low-mass star required to utilize our methods to obtain stellar properties (achieve S/N ~ 70). The time is shown in the black labels and the corresponding approximate V-band magnitude is shown with the red labels

stellar properties. We estimated a mass of 0.53 ± 0.05 $M_{\odot}$, a radius of 0.50 ± 0.05 $R_{\odot}$, a metallicity, [Fe/H], of 0.12 ± 0.12 and a distance of $29.9\pm^{3.7}_{3.4}$ pc. These properties are very similar to those determined by Bonfils (2012) who then estimate an approximate mass of ~14 $M_{\oplus}$ and radius of ~4.2 $R_{\oplus}$ for GJ 3470b.

Although our calibration provides estimates for stellar properties, there are some limitations. We examined the effect of spectral resolution and found that we could use the calibration only for spectral resolutions greater than ~30,000. We also demonstrated how to use the calibration with higher resolution data (>50,000) by making use of HARPS archival spectra. Additionally, our calibration sample only spans a particular range of $\mathcal{M}_{Ks}$ (see Figure A.1) and should only be used outside that range with caution. This restricts applicability to mostly early type M dwarfs, earlier than about M4, and late K dwarfs. This still spans a fairly broad range of masses from about ~ 0.7 to ~ 0.2 $M_{\odot}$.

Our method requires a high-signal, high-resolution, spectrum of the star. To quantify the necessary signal-to-noise, we used the observations of KOI-314 as a guide in our noise analysis (see Section A.3). In Figure A.11, we show the approximate minimum total integration time needed, in minutes (on left side), to achieve a signal-to-noise of ~ 70 and use the techniques presented in this contribution. The corresponding V-band magnitudes are also shown on the contours towards the right side of the plot. As a benchmark, a star with a V-band magnitude of 14 would need a total integration time of 30 minutes. It is possible to build up this signal over time by building a composite spectrum. This makes it an ideal method to complement radial velocity surveys of M dwarfs. Many spectra are needed to sample the radial velocities of these stars, so as a byproduct of those observations the physical stellar properties can be determined simultaneously. Additionally, this method can also be applied immediately to archival HIRES data of low-mass stars[1].

Appendix

Continuum Normalization

The continuum normalization procedure was briefly explained in Section A.2 however, we expand upon the details here. The reduced spectra from the HIRES detector include several orders, ten of those corresponding to the red chip of the detector, spanning between 650 nm and 800 nm. Each spectral order is affected by the blaze function of the detector and the overall shape of the stellar spectrum, and we therefore normalize each order separately. For each order, the spectral regions listed in Table A.5, we first masked out any telluric regions. We then equally divided each region into 10 or 20 (see 'Divisions' in Table A.5) different sections. For each section we ordered the flux and took the top 1% or 2% (see 'Percentage' in Table A.5) level as representative of a pseudo-continuum. We then fit these points with a polynomial of order 2 or 3 (see 'Polynomial Order' in Table A.5) to define our normalization. The number of points in the fit therefore matches the number of bins we used. For each order we divided the spectrum by this polynomial to get the normalized spectrum (see example in Figure A.12). Changes in the normalization properties attempt to account for differences in the curvature/symmetry of the spectral continuum/blaze function to achieve an appropriate normalization. To this end the fifth spectral order in Table A.5 does not use the full order in the normalization and instead we applied a narrower range of wavelengths when applying our normalization methods in order

[1] Keck Observatory Archive:
http://www2.keck.hawaii.edu/koa/public/koa.php

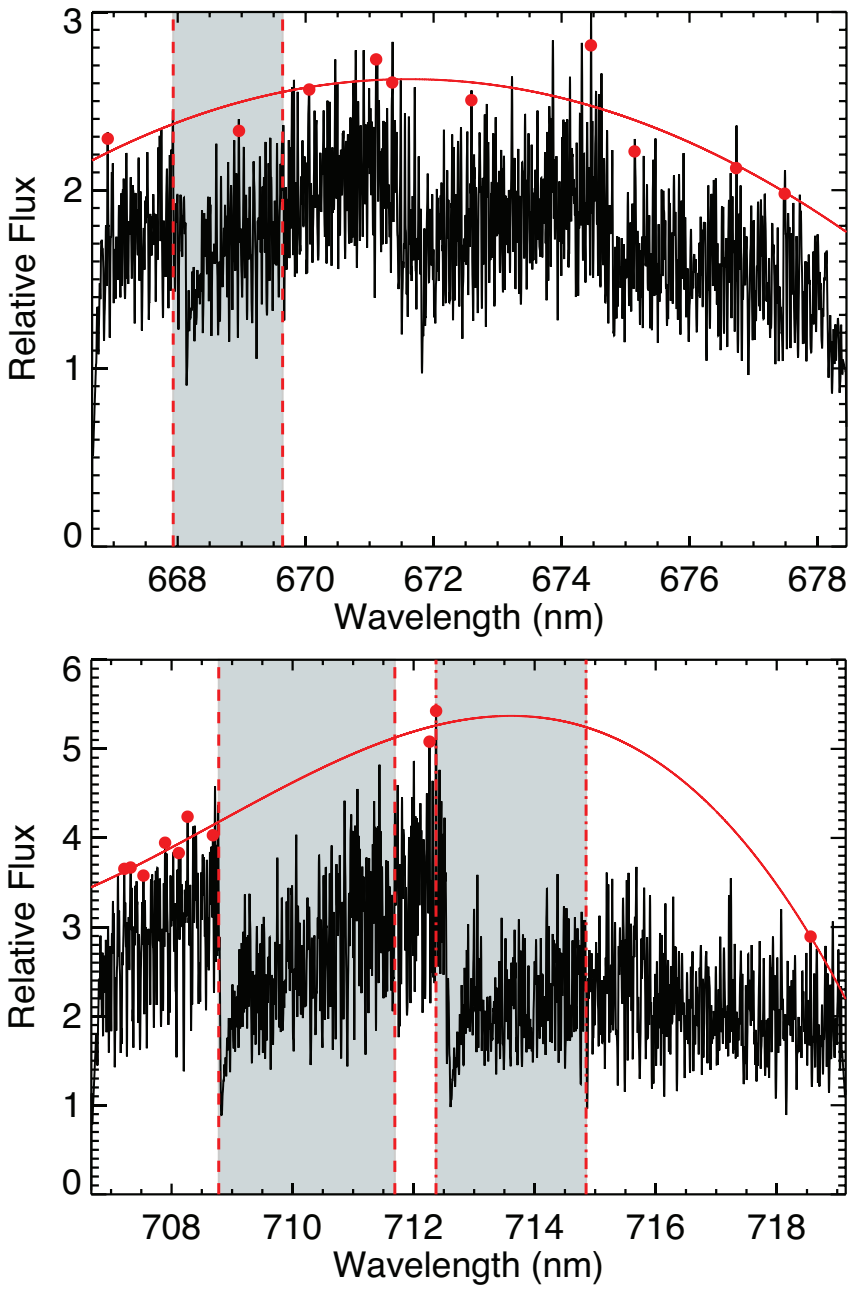

Figure A.12: Example spectrum with normalization plotted overtop. Each plot comprises a full order and shows the regions used as spectral indices for computing equivalent widths. Points used for the continuum normalization are shown as filled circles. Chosen points assure that the normalization addresses the convex shape of instrument profile. All of the wiggles are real features in the spectra.

to account for the broad and deep absorption bands (see bottom panel of Figure A.12). Despite the lack of pseudo-continuum points toward greater wavelengths in the lower panel, the chosen points assure that our normalization accounts for the generally convex shape of the blaze function for each the order. Although there can be issues at the edge of each order, the spectral indices are all located near the central regions so this does not affect the calculated equivalent widths.

Table A.5: Normalization Properties

Region (nm)	Divisions	Percentage %	Polynomial Order
654.35 - 665.92	10	1	3
666.69 - 678.49	10	1	2
679.52 - 691.53	10	1	3
692.85 - 705.08	10	1	3
706.71 - 719.17 [a]	10	1	3
721.14 - 733.84	10	1	3
736.17 - 749.12	10	1	3
751.84 - 765.05	20	2	2
768.19 - 781.67	10	1	3
785.28 - 796.55	10	1	2

[a] Within region only the following sections are used for computing normalization: 707.04-708.79 nm, 712.19-712.58 nm, 718.35-718.63 nm

We opted not to use continuum regions defined as the linear interpolation of points flanking the absorption region because the spectral regions we identified as sensitive to stellar properties were not always bounded by points of minimal absorption. Our procedure also addresses the difficulties introduced by the shape of the blaze function on the spectrum and by taking a broader region into account for the continuum calculation we can get consistent pseudo-continua across many different spectra. Our application of this procedure to the HARPS data was able to produce equivalent width measurements for several indices in accord with our HIRES measurements, showing how our methods can be used for different data samples (see Section A.3).

Acknowledgments

The authors would like to thank the California Planet Search team for the use of the data, the Keck telescopes support staff for their assistance, Philip Muirhead for his

support in this endeavor. The authors would also like to thank the native Hawaiians for the use of their mountain in the advancement of science.

The authors would also like to acknowledge the referee for providing useful comments that strengthened this work.

JSP was supported by a grant from the National Science Foundation Graduate Research Fellowship under Grant No. (DGE-1144469).

JAJ acknowledges support from the Sloan Foundation and the David & Lucile Packard Foundation.

Based on data obtained from the ESO Science Archive Facility under request number(s): mbottom 48576, jspineda 49793, 49870, 49872, 49874-91, 49893-914, 49916-26.

This publication makes use of data products from the Two Micron All Sky Survey, which is a joint project of the University of Massachusetts and the Infrared Processing and Analysis Cen- ter/California Institute of Technology, funded by the National Aeronautics and Space Administra- tion and the National Science Foundation.